
Quantitative evaluation of ozone and selected climate parameters in the chemistry-climate model EMAC

Carolin Klinger



Munich 2011

Ludwig-Maximilians-Universität München
Faculty of Physics
Meteorological Institute Munich

Quantitative evaluation of ozone and selected climate parameters in the chemistry-climate model EMAC

Carolin Klinger

MASTER THESIS

Examiners: Priv.-Doz. Dr. habil. Veronika Eyring (DLR)
Prof. Dr. Bernhard Mayer (LMU)

Deutsches Zentrum für Luft- und Raumfahrt (DLR)
Institut für Physik der Atmosphäre

December 2011

*Geological change usually takes thousands of years to happen
but we are seeing the climate changing not just in our lifetimes
but also year by year.*

James Lovelock

Abstract

Four present-day simulations performed with different setups of the ECHAM/MESy Atmospheric Chemistry (EMAC) model have been evaluated in this thesis through a comprehensive comparison with different observational datasets. In particular, the results from a previous EMAC evaluation of a model simulation with a weak nudging towards realistic meteorology in the troposphere have been compared to new simulations with different model setups and updated emission datasets in free-running timeslice and nudged Quasi Chemistry-Transport Mode (QCTM). The focus of the evaluation was to identify differences in simulated ozone and selected climate parameters that resulted from (a) the different setups of the EMAC model (nudged versus free-running) and (b) different boundary conditions (emissions and sea surface temperatures (SSTs)).

The boundary conditions of the 2000 timeslice simulations (EMAC-TS2000 and EMAC-ACCMIP) differ from each other in their emission inventories and SSTs, which are prescribed in all simulations. The boundary conditions in the nudged simulations (EMAC2-EVAL and EMAC-QCTM) are similar to those in the EMAC-TS2000 timeslice simulation, except that the emissions and SSTs datasets are transient (i.e. varying from year to year) rather than specifying a single year (year 2000) as in the timeslice simulations.

With the exception of some particular features which are detailed in this thesis, no large differences that could be related particularly to the different setups of the EMAC simulations (nudged versus free-running) were found, which opens the possibility to evaluate and improve the overall model with the help of shorter nudged simulations in comparison to observations. This is beneficial since the evaluation of the free-running simulation has to be performed in a statistical manner and requires longer simulations and observations. However, in many cases the two corresponding simulations of one setup (nudged or free-running) are more alike. The main differences between the two setups is a better representation of the temperature in the nudged simulations, also in the stratosphere, and according to an improved simulation of the temperature in the tropical tropopause layer, a better simulation of stratospheric water vapour concentrations. Ozone and ozone precursor concentrations as well as transport characteristics on the other hand are very similar in the different model setups if similar boundary conditions are used.

Boundary conditions lead to significant differences in the four simulations. In particular, prescribed SSTs play a key role in the representation of the ozone hole, which is significantly better represented in the EMAC-ACCMIP simulation than in the EMAC-TS2000 simulation. Another improvement in the EMAC-ACCMIP simulation that is related to the boundary conditions is a better representation of tropospheric ozone precursors. While the two nudged simulations and the EMAC-TS2000 simulation underestimate species like carbon monoxide (CO) and some non-methane hydrocarbons (NMHCs), the higher total emissions used in the EMAC-ACCMIP simulation improve the representation of these species, although biases compared to observations still remain.

The developed diagnostics and observations have been implemented into the CCMVal Diagnostic Tool, an open source tool for chemistry-climate model evaluation. This tool can now be used for the routine evaluation of EMAC and can be further extended with additional diagnostics and observations. The tool will significantly facilitate the complex evaluation of EMAC on the long-term. In addition, the results of the EMAC evaluation will guide future model improvements.

Content

1	Introduction	5
1.1	Background and Motivation	5
1.2	Goals and Methods of the Thesis	7
1.3	Structure of the Thesis	8
2	Scientific Background	9
2.1	The Climate System of the Earth	9
2.2	Global Chemistry-Climate Models	10
2.3	Chemistry – Climate Model Evaluation	11
2.4	Ozone and Basic Climate Parameters	12
2.4.1	Temperature and Radiation	13
2.4.2	Geopotential Height	14
2.4.3	Specific Humidity	15
2.4.4	Tropospheric and Stratospheric Dynamics	15
2.4.5	Ozone and Ozone Chemical Reactions in the Stratosphere and Troposphere	19
3	Model and Model Simulations	23
3.1	ECHAM/MESSy Atmospheric Chemistry Model (EMAC)	23
3.2	Model Simulations	24
3.2.1	Simulation in Nudged Mode: EMAC2-EVAL	24
3.2.2	Simulation in Nudged Mode: EMAC-QCTM	26
3.2.3	Timeslice Simulation: EMAC-TS2000	27
3.2.4	Timeslice Simulation: EMAC-ACCMIP	27
4	Strategy for Model Evaluation	31
4.1	Model Evaluation Strategy	31
4.2	Statistical Methods and Specific Choices for Quantitative Model Evaluation	38
5	Observational Data and the CCMVal-Diagnostic Tool	43
5.1	Diagnostics and Performance Metrics Evaluation Tool for EMAC	43
5.1.1	The CCMVal Diagnostic Tool	43
5.1.2	Extension of the CCMVal Diagnostic Tool	44
5.2	Observational Data for Model Evaluation	46
5.2.1	Observational Data for the Evaluation of Basic Climate Parameters	47
5.2.1.1	Temperature, Winds, Geopotential Height and Specific Humidity	47
5.2.1.2	Radiation	47
5.2.2	Observational Data for the Evaluation Stratospheric Ozone	48
5.2.2.1	Datasets for Stratospheric Ozone	48
5.2.2.2	Datasets for Key Processes that Determine Stratospheric Ozone	48
5.2.3	Observational Data for the Evaluation Tropospheric Ozone	49
5.2.3.1	Datasets for Tropospheric Ozone	49

5.2.3.2	Datasets for Ozone Precursors and the Hydroxyl Radical	50
6	Results and Discussion of Model Evaluation.....	51
6.1	Basic Climate Parameters.....	51
6.1.1	Temperature	51
6.1.1.1	Detecting Temperature Biases	51
6.1.1.2	Understanding Temperature Biases.....	54
6.1.2	Zonal Mean Wind.....	58
6.1.2.1	Detecting Zonal Mean Wind Biases.....	58
6.1.2.2	Understanding Zonal Mean Wind Biases	59
6.1.3	Meridional Wind, Specific Humidity, Geopotential Height and Radiation	62
6.1.4	Quantifying Biases in Basic Climate Parameters.....	65
6.2	Tropospheric Ozone	70
6.2.1	Detecting Tropospheric Ozone Biases	70
6.2.2	Understanding Tropospheric Ozone Biases.....	76
6.2.3	Quantifying Biases in Tropospheric Ozone and its Precursors.....	84
6.3	Stratospheric Ozone.....	87
6.3.1	Detecting Stratospheric Ozone Biases	88
6.3.2	Understanding Stratospheric Ozone Biases	90
6.3.3	Quantifying Biases in Stratospheric Ozone and Related Processes.....	100
7	Summary and Outlook.....	105
7.1	Summary	105
7.2	Conclusion and Outlook	108
	References	111
	Abbreviations.....	iii
	List of Figures.....	vi
	List of Tables	xii
	Appendix.....	xiii

1 Introduction

1.1 Background and Motivation

Ozone (O_3) plays an important role in two regions of the Earth's atmosphere. In the troposphere, ozone is considered to be "bad" as it affects human health and acts as a greenhouse gas. In the stratosphere, on the other hand, ozone has a positive effect, because it absorbs ultra-violet (UV) radiation which would be harmful to life on Earth.

Tropospheric ozone burden has increased during the last century. The rise in tropospheric

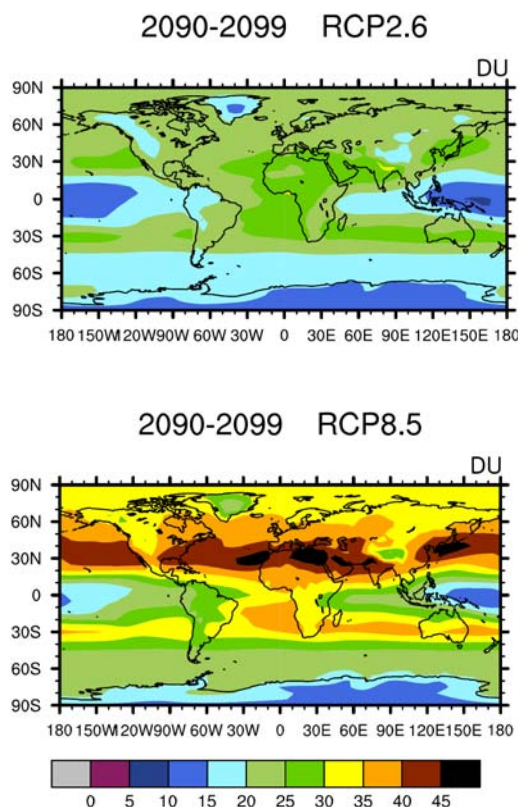


Figure 1. Decadal mean tropospheric column ozone, in the RCPs 2.6 and 8.5 at the end of the 21st century. From Cionni et al. (2011), their Figure 9.

ozone was particularly strong in the northern hemispheric midlatitudes due to an increase in anthropogenic emissions. As tropospheric ozone is a greenhouse gas, a rise in tropospheric ozone also contributes to global warming and has led to a global mean radiative forcing (RF) of around 0.35 Wm^{-2} [$+0.25$ to $+0.65 \text{ Wm}^{-2}$] in 2005 (IPCC 2007). In the future, tropospheric ozone is projected to change, depending on the emission scenario, in particular the evolution of ozone precursors such as nitrogen oxides ($\text{NO}_x = \text{NO} + \text{NO}_2$), carbon monoxide (CO), methane (CH_4), and non-methane hydrocarbons (NMHCs). As an example, Figure 1 shows decadal means of tropospheric ozone in the 2090s under two out of the four *Representative Concentration Pathways* (RCPs, Moss et al., 2010). Cionni et al. (2011) found that the future development of total tropospheric column ozone strongly depends on the RCPs. These scenarios differ in the emissions of important ozone precursors.

The ozone hole in the stratosphere was discovered in the 1980s. Stratospheric ozone depletion is caused by emissions of ozone-depleting substances (ODSs). The *Montreal Protocol* and its Amendments and Adjustments controls the emissions of these substances leading to a recovery of the ozone layer, which is projected by state-of-the art *Chemistry-Climate Models* (CCMs) participating in the second round of the *Chemistry-Climate Model Validation* (CCMVal) activity (Figure 2). In the southern hemisphere, the ozone hole has been identified as the primary driver of changes in summertime high-latitude surface climate over the past few decades (Thompson and Solomon 2002, Thompson and Solomon 2005, Thompson et al., 2005). In addition, the projected strengthening of the *Brewer-Dobson circulation* could result in a decrease in tropical ozone and an increase in extratropical ozone in the lower stratosphere, with impacts on RF (SPARC CCMVal, 2010, Eyring et al., 2007, Shepherd 2008).

ozone was particularly strong in the northern hemispheric midlatitudes due to an increase in anthropogenic emissions. As tropospheric ozone is a greenhouse gas, a rise in tropospheric ozone also contributes to global warming and has led to a global mean radiative forcing (RF) of around 0.35 Wm^{-2} [$+0.25$ to $+0.65 \text{ Wm}^{-2}$] in 2005 (IPCC 2007). In the future, tropospheric ozone is projected to change, depending on the emission scenario, in particular the evolution of ozone precursors such as nitrogen oxides ($\text{NO}_x = \text{NO} + \text{NO}_2$), carbon monoxide (CO), methane (CH_4), and non-methane hydrocarbons (NMHCs). As an example, Figure 1 shows decadal means of tropospheric ozone in the 2090s under two out of the four *Representative Concentration Pathways* (RCPs, Moss et al., 2010). Cionni et al. (2011) found that the future development of total tropospheric column ozone strongly depends on the RCPs. These scenarios differ in the emissions of important ozone precursors.

The ozone hole in the stratosphere was discovered in the 1980s. Stratospheric ozone depletion is caused by emissions of ozone-

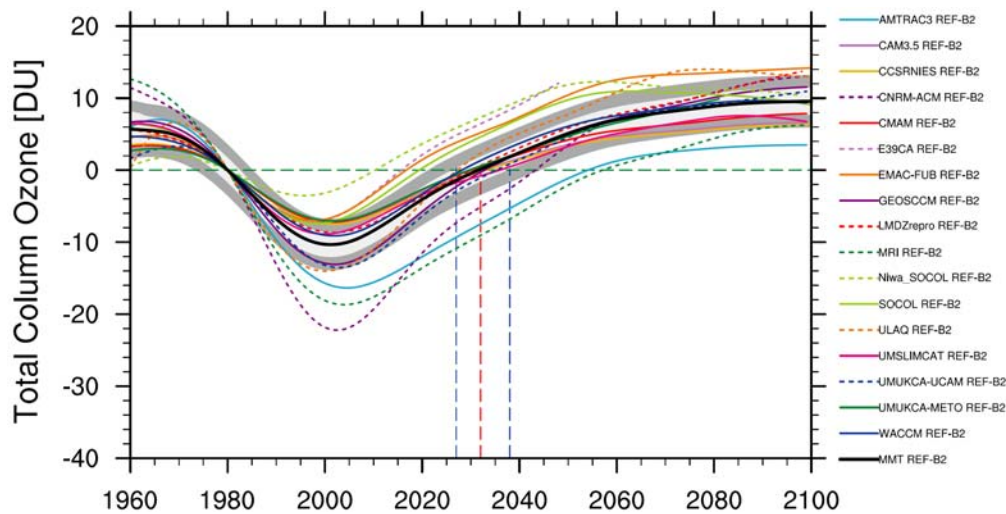


Figure 2. 1980 baseline-adjusted annual mean global total ozone column from 17 CCM simulations. The thick black line shows the multi-model mean and the light- and dark-grey shaded regions show the 95% confidence and 95% prediction intervals, respectively. The red vertical dashed line indicates the year when the multi-model mean returns to 1980 values and the blue vertical dashed lines indicate the uncertainty in these return dates. The green horizontal dashed line refers to the 1980 baseline. From Eyring et al. (2010b), their Figure 1.

For all the above mentioned reasons, it is important to simulate ozone and related key processes correctly in CCMs that are used to understand past and to project future ozone. Here, the *ECHAM/MESSy Atmospheric Chemistry* (EMAC) model is evaluated. EMAC is a numerical chemistry and climate simulation system that includes submodels describing tropospheric and middle atmosphere processes and their interaction with oceans, land and human influences (Jöckel et al., 2006). It uses the *Modular Earth Submodel System* (MESSy) to link multi-institutional computer codes. The core atmospheric model is the 5th generation European Centre Hamburg general circulation model (ECHAM5, Roeckner et al., 2006). The chemical mechanism of this model is integrated in the entire model domain, i.e., consistently from the surface to the stratosphere. In the EMAC model, dynamic, radiation and chemistry are coupled, meaning that feedback mechanisms between these important aspects of a model can develop.

The model is driven by prescribed input parameters such as sea surface temperatures (SSTs) and sea ice concentrations (SICs), emissions, greenhouse gases and natural processes (e.g. volcanic eruptions). In transient simulations, radiatively active gases as well as other emissions and boundary conditions (e.g. SSTs) vary from year to year, while in timeslice simulations a single year (e.g. 2000) is repeatedly simulated under fixed boundary conditions to account for interannual variability. In free-running mode CCMs simulate a statistical relationship to the real atmosphere, and so a comparison of model results with measurements must be performed in a statistical manner. This is problematic, because it takes many decades of observations to define a robust stratospheric climatology, especially in the Arctic winter (Eyring et al., 2005). To allow a more direct comparison of the model output with observations, so-called nudged simulations are performed. In these simulations, meteorological parameters (e.g., temperature, surface pressure, vorticity and divergence) are „nudged” towards a realistic meteorology. This setup makes comparisons of

shorter simulation periods to observations of a specific year possible. This is beneficial, because observational data often only cover short time periods. For the EMAC model, an additional setup, the *Quasi Chemistry-Transport Mode* (QCTM, Deckert et al., 2011) is available. In this mode, chemistry is decoupled from radiation and the dynamics, thus omitting feedback mechanisms. With this mode, small chemical perturbations can be evaluated.

1.2 Goals and Methods of the Thesis

The outputs from four simulations with the EMAC model under the different setups described briefly in Section 1.1 were made available for a comprehensive evaluation with observational data in this thesis.

The four present-day EMAC simulations have a T42-L90MA resolution, i.e. with a spherical truncation of T42 (corresponding to a quadratic Gaussian grid of approximately $2.8^\circ \times 2.8^\circ$ degrees in latitude and longitude) with 90 vertical hybrid pressure levels up to 0.01 hPa, but differ from each other in their setup. Two nudged, transient simulations (EMAC2-EVAL and EMAC-QCTM) driven by the same (where available transient) SSTs and emission inventories are compared to two free-running timeslice simulations. One of the nudged simulations is a previously evaluated simulation (EMAC2-EVAL) that covers the time period 1998-2009 (Jöckel et al., 2010) and serves as the reference simulation. The other nudged simulation is in the QCTM mode (EMAC-QCTM). The setups of the free-running timeslice simulations (EMAC-TS2000 and EMAC-ACCMIP) differ from each other in the emission inventories and the SSTs. To follow the specification of the *Atmospheric Chemistry and Climate Model Intercomparison Project* (ACCMIP), emissions from Lamarque et al. (2010) and modeled SSTs and SICs from the *Centro Euro-Mediterraneo per i Cambiamenti Climatici* (CMCC) climate model are prescribed in the EMAC-ACCMIP simulation instead of observational SSTs / SICs in the EMAC-TS2000 simulation. The boundary conditions of the EMAC-TS2000 simulation are more similar to the nudged simulations, except that emissions and SSTs are climatological mean datasets instead of transient datasets.

The focus of this thesis is to assess strengths and weaknesses of these different setups in the EMAC model. In particular, conclusions from the previously evaluated EMAC2-EVAL simulation in nudged mode that uses a Newtonian relaxation technique in the troposphere (Jöckel et al., 2010) are compared to the new simulations with different model setups and boundary conditions in free-running timeslice and Quasi Chemistry-Transport Mode.

The evaluation strategy in this thesis follows the concept of process-oriented evaluation that has been established and applied by CCMVal (Eyring et al., 2005, SPARC CCMVal, 2010). The basic concept behind is that the evaluation does not only focus on the quantity of interest, which in the case of CCMVal is stratospheric ozone, but focuses on the processes that determine it. This includes the evaluation of mean climate and transport characteristics, which are important for a realistic simulation of stratospheric ozone (SPARC CCMVal, 2010). Here, in addition a process-oriented evaluation is also applied in the troposphere, although promising diagnostics that have been published so far in this area are much more limited. The evaluation of tropospheric ozone is therefore focused on ozone itself and its precursors (NO_x , CO and NMHCs). Additionally, an evaluation of basic cli-

mate parameters (temperature, wind, geopotential height, specific humidity, and radiation) is performed to assess the different setups of EMAC simulations against each other.

The statistical analysis in the quantitative part of the evaluation focuses on the evaluation of the annual cycle of different basic climate parameters, following Gleckler et al. (2008) and selected diagnostics for tropospheric and stratospheric ozone and related processes. Statistical measures like the root mean square difference, the overall mean bias and Taylor diagrams (Taylor 2001) are used for this quantitative evaluation.

As part of this thesis, different observations were collected, including reanalysis-data, satellite data, ground-based measurements and insitu measurements from aircraft campaigns. The newly developed diagnostics and external observations have been implemented into the CCMVal-Diagnostic tool, an open source tool for chemistry-climate model evaluation (Gettleman et al., 2011, in prep). For the use of this tool, the observational data as well as the EMAC model output needed to be brought into a standard format. Furthermore, a variety of diagnostics, mostly those related to the troposphere and the basic climate parameters were added to the tool. For the quantitative evaluation, new routines for the statistical measures were implemented as well.

1.3 Structure of the Thesis

Chapter 2 provides a brief overview of the scientific background for this work divided into climate change (Section 2.1), chemistry-climate models (Section 2.2), climate model evaluation (Section 2.3) and main characteristics of selected climate variables (Section 2.4). The EMAC model and model simulations with their different setups and boundary conditions are described in Chapter 3. The model evaluation strategy and statistical methods for a quantitative evaluation are addressed in Chapter 4. Chapter 5 describes the evaluation tool for EMAC, which is based on the CCMVal-Diagnostic tool (Section 5.1) and observational data that have been implemented for the model evaluation as part of this thesis (Section 5.2). Chapter 6 presents the qualitative and quantitative results of the model evaluation. Finally, Chapter 7 closes with a summary and outlook.

2 Scientific Background

This chapter provides a short summary of the scientific background on which this thesis is based. A short overview of the Earth's climate system and climate change is given in Section 2.1, followed by an introduction to chemistry-climate modelling in Section 2.2 and chemistry-climate model evaluation in Section 2.3. Finally, the main characteristics of the climate parameters selected for the evaluation in this thesis are summarized in Section 2.4.

2.1 The Climate System of the Earth

The climate system of the Earth is a complex, non-linear system. Different constituents determine its characteristics as for example atmosphere, ocean, ice and land surfaces and

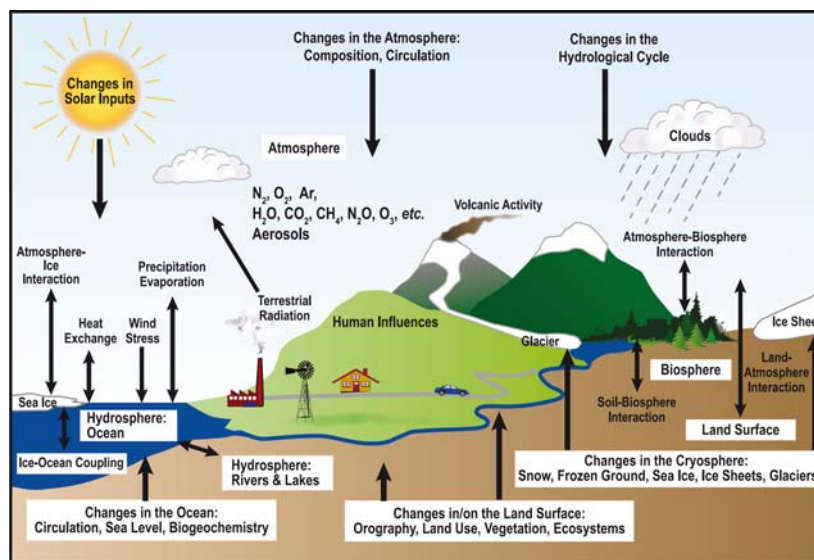


Figure 3. Components of the Earth's system, interactions and processes. From IPCC 2007, Chapter 1, FAQ 1.2, Figure 1.

the biosphere (Figure 3). Additionally, different forcings which can be of natural or anthropogenic origin affect the climate system. The climate system is mainly driven by solar radiation entering the Earth's atmosphere. Changes in radiation lead to an imbalance in the energy budget of the Earth. Alterations in the radiation budget are related to changes in the incoming solar radiation, in the reflected radiation and in the outgoing longwave radiation. About 1370 W/m^2 of solar radiation reach the top of the atmosphere, but only a fraction of this radiation reaches the Earth's surface. During its way through the atmosphere, radiation interacts with its constituents (molecules, clouds, aerosols, etc.) via scattering, absorption and emission processes. About 70% of the incoming solar radiation is absorbed by the ground and the atmosphere, while the remaining 30% of solar radiation is reflected back to space. The absorbed solar radiation is re-emitted as thermal longwave radiation. Outgoing longwave radiation is absorbed by greenhouse gases (e.g. CO_2 , CH_4 , H_2O or O_3) in the atmosphere, resulting in a warming of the atmosphere (Figure 4). This process, known as the greenhouse effect, is a natural atmospheric process. Due to the natural greenhouse effect the temperature on the Earth is about 15°C , while it would be about -19°C without it (Fourier 1824, Arrhenius 1896b). Increased concentrations in greenhouse gases, mainly caused by industries and traffic emissions, strengthen this effect which is then known as anthropogenic greenhouse effect.

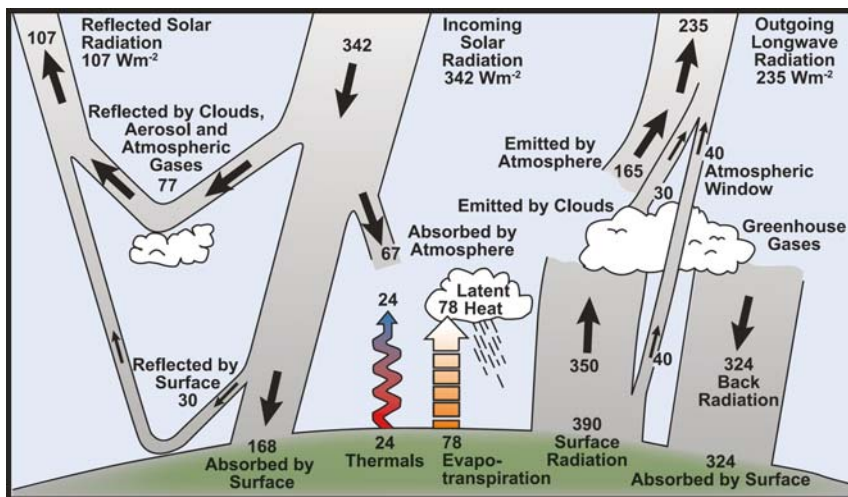


Figure 4. Global mean energy balance showing the equilibrium between incoming solar and outgoing longwave radiation. About half of the incoming solar radiation is absorbed by the Earth's surface. This energy is transferred to the atmosphere by warming the air in contact with the surface (thermals), by evapotranspiration and by longwave radiation that is absorbed by clouds and greenhouse gases. The atmosphere in turn radiates longwave energy back to Earth as well as out to space. From IPCC 2007, Chapter 1, FAQ 1.1, Figure 1.

Due to the rotation of the Earth and the associated Coriolis force, these transport processes do not remain north-southward, but change into a west-east direction. Additionally, these transport processes are perturbed by local phenomena such as orography or temperature contrasts between land and sea.

The climate system with its own dynamics and complexity is perturbed by human activities. Since the industrialization, the concentration of greenhouse gases in the atmosphere has steadily increased, thus strengthening the anthropogenic greenhouse effect. As there is less thermal radiation leaving the atmosphere, the energy balance is no longer given and the temperature on Earth is rising to establish a new equilibrium state. This increase in temperature in turn causes other feedbacks in the climate system which can additionally contribute to temperature increase or act in the opposite direction (IPCC 2007). Anthropogenic emissions do not only lead to an increase in greenhouse gas concentration but alter the chemical composition of the atmosphere and the interaction between these components. This leads to changes in the atmospheric chemical composition which can be seen for example in a rise in tropospheric ozone or ozone depletion in the stratosphere.

2.2 Global Chemistry-Climate Models

Climate models describe the complex, interactive, nonlinear physical processes of the Earth system mathematically. Today, they are a common tool for Earth-scientists to study the causes and effects of the complex Earth system, including interactions between the atmosphere, the biosphere and the ocean. They are also useful in order to understand changes in the climate system. Climate models solve the physical laws that govern the evolution of the climate and are therefore able to predict its future behaviour. The principle laws that gov-

As the Earth is, to a good approximation, a sphere and its axis is tilted, the incoming solar radiation is not spread equally over the globe. In the tropics more energy arrives per surface area than in polar regions. This imbalance forces circulations in the atmosphere and the oceans, trying to establish equilibrium by transporting energy from the tropics to higher latitudes.

ern the atmospheric processes and dynamics are the so-called primitive equations, including dynamic, thermodynamic, and conservation equations (e.g. Schlesinger 1988).

Over the last decades, climate models have improved mainly due to the increasing computational capacity of supercomputers on which climate model simulations are performed. Such an increase in computational power has led to more complex models which include more and more processes and components that determine climate. Additionally, spatial and temporal resolution has increased as well.

A variety of different climate models exist, ranging from so called simple models to very complex ones. Important aspects that are considered in climate models are radiation, dynamics, surface processes, and the resolution in time and space. Radiation is related to the absorption of the incoming solar radiation, its interaction with the atmosphere and the emission of infrared radiation. Dynamics is related to the transport of energy around the globe in form of winds, ocean currents or wave propagation. Surface processes include e.g. the effects of ice, vegetation and moisture exchanges. Chemistry covers the chemical composition of the atmosphere, chemical reactions of these components and their exchange processes with e.g. land and ocean. CCMs, like the one used in this thesis, are complex, three-dimensional models where radiation, dynamics and chemistry are coupled to each other. This means that CCMs represent radiative, dynamical and chemical processes and corresponding interactions in the atmosphere. Chemical reactions, for example, change the chemical composition which can change the radiative balance of the atmosphere and also the dynamics. In turn, changes in the dynamics or the radiation can have feedback effects on the chemistry (Eyring et al., 2010b, Eyring et al., 2006). The development of the Earth system is driven by forcings, which are of natural and anthropogenic origin. Natural forcings include the solar cycle or volcanic activity; anthropogenic forcings are related to emissions of pollutants by human activities (e.g. industries and traffic). CCMs are driven by pre-described input data such as sea surface temperatures, greenhouse gases, emissions and natural effects.

In order to achieve reliable future projections, a number of different scenarios are usually simulated in climate models. Formerly, each of these scenarios was related to a particular development of the emissions of climate relevant substances (e.g. CO₂). These former scenarios, the so-called SRES (*Special Report on Emissions Scenarios*, Nakicenovic et al., 2000) where based on economic and social developments like the growth of population, economy or traffic. Political regulations concerning the resulting emission were not considered. More recent scenarios, so called RCPs (*Representative Concentration Pathways*, Moss et al., 2010) in support of the *Intergovernmental Panel on Climate Change Assessment Report 5* (IPCC AR5), are no longer based on CO₂-equivalent emissions but on the resulting radiative forcing at the end of the 21st century with respect to pre-industrial conditions. In this way, not only greenhouse gas emissions, but also land use changes (resulting e.g. in changes in the albedo), and political strategies to reduce greenhouse gas emissions are considered (Moss et al., 2010, van Vuuren et al., 2009).

2.3 Chemistry – Climate Model Evaluation

Climate model evaluation is the procedure of comparing model output with observations or other models. Occasionally, recent model versions are compared to former ones, in or-

der to assess information about the improvement of the models development (Knutti et al., 2010b).

Within international intercomparison projects, such as the *Climate Model Intercomparison Project* (CMIP), the *Atmospheric Model Intercomparison Project* (AMIP) or CCMVal, climate models are tested against each other as well as against observations and thus outlining the skills and weaknesses of each climate model. For climate model evaluations, projections of the past and present are evaluated on the basis of available observations. In multi-model evaluation, the multi-model mean (a weighted or un-weighted average of model predictions) has become a common approach. The multi-model mean often agrees better with observations than the individual models, because individual weaknesses of the models cancel out. However, it is not clear whether the multi-model mean is really the best estimate and further investigations are encouraged (Knutti et al., 2010b).

Climate models can be evaluated by simply comparing model projections of a certain variable to corresponding observations using so called diagnostics¹. This approach shows the ability of a model to project this particular variable but does not show whether all the processes within the model, which are needed to make the prediction of a certain variable, are solved correctly. Deficiencies in processes may cancel each other out, leading to a wrong impression of the model's ability to simulate the responsible processes for the prediction of the particular variable. Therefore, evaluation on the process level is required (Eyring et al., 2005, Knutti et al., 2010a).

Additionally, models can be graded by means of performance metrics (Knutti et al., 2010b). A metric is a statistical quantitative measure of agreement between a simulated and observed quantity and can be used to give "grades" to individual models (Knutti et al., 2010b). A performance metric is usually derived from a diagnostic and relates to a certain process and shows the agreement between a simulated and observed quantity (Knutti et al., 2010b). The application of a metric has to be done with caution. Gleckler et al. (2008) showed that applying different metrics leads to different model rankings. Also, model abilities can be overestimated if important processes are missing or if model errors, uncertainties in observations and the robustness of a statistical assumption are not carefully looked at (Knutti 2010, Knutti et al., 2010a).

One possible approach for the evaluation of chemistry-climate models is a process-oriented evaluation as performed within CCMVal. This approach takes into account physical, dynamical and chemical processes related to chemical species. Certain diagnostics are chosen, specifying regions or height levels which are of interest for the variable to be evaluated. A closer description on the evaluation of the model used in this thesis is given in Section 4.1.

2.4 Ozone and Basic Climate Parameters

This thesis focuses on atmospheric variables, in particular on the representation of ozone in the chemistry-climate model EMAC. For a process oriented evaluation in the troposphere and in the stratosphere, other variables have to be considered as well. These variables include temperature (as low temperatures in the stratosphere are one of the meteor-

¹ Diagnostic: A quantity derived from model output, used for comparison with observations or other model outputs, e.g. maps, trends or time-series (Knutti et al., 2010b).

logical conditions for the depletion of ozone), ozone precursors, ozone depleting substances and tracers (such as methane) to characterise transport properties.

2.4.1 Temperature and Radiation

Temperature is a key climate variable. Radiative processes affect the thermal structure of

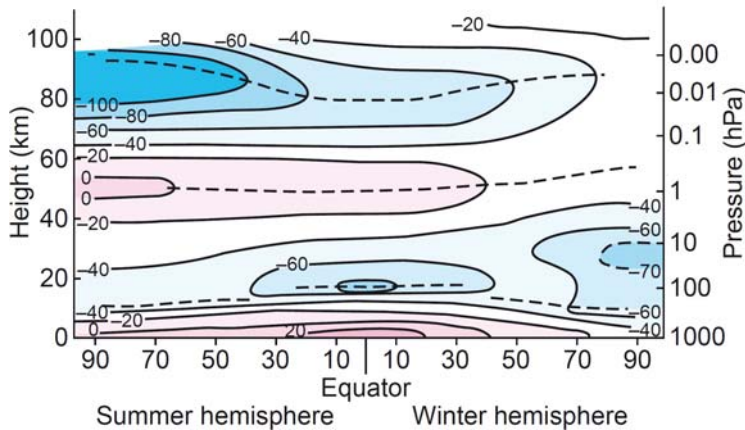


Figure 5. Idealized meridional cross section of the temperature distribution (schematic). Contour intervals of 20°C, pink regions show warmer, blue regions cooler areas. From Wallace and Hobbs (2006), their Figure 1.11.

the atmosphere. Hence, any perturbation of these processes can cause alterations in the temperature profile of the Earth-atmospheric system and thus induce climate change (Santer et al., 1996). The temperature profile of the atmosphere is the result of the interaction of radiative, convective, dynamical and chemical processes. Figure 5 shows the climatological mean zonal mean temperature profile of the atmosphere as a function of

latitude and height. Highest temperatures are found at the ground. The tropical tropopause (~10 km) as well as the lower stratosphere (~20 km) of the winter hemisphere show lower temperatures while the summer stratosphere is characterized by higher temperatures. In the summer mesosphere (~90 km), the lowest temperatures of the atmosphere are observed.

The prime source of energy for the Earth system is the incoming solar radiation which interacts with the atmosphere and the Earth's surface (Hartmann 1994). In general, the amount of incoming solar radiation and outgoing longwave radiation at top of the atmosphere is in balance, i.e. a radiative equilibrium is maintained. If this equilibrium state is perturbed by forcings, the atmosphere will warm or cool in order to arrange a new equilibrium state. Forcings can be of natural (variations in the solar cycle, volcanic eruptions, etc.) or anthropogenic (e.g. rise in greenhouse gas concentrations) origin and lead to different temperature trends in different parts of the atmosphere.

About 70% of the incoming solar radiation is absorbed by the Earth-system (~50% from the surface and ~20% from the atmosphere), whereas the remaining 30% is reflected (~20% by the atmosphere, e.g. through interaction with molecules or aerosols and ~10% by the ground, see Figure 4). Therefore, the highest temperatures are usually found at the ground (Figure 5 and Figure 6). As warm air tends to rise, the warming of the surface causes the air near the surface to rise and convective processes start, leading to a mixing of air masses with different temperatures in the troposphere.

Temperatures at the ground vary with latitude, season and with the properties of the surface (ice, water, soil etc.). These horizontal variations are only dominant at the ground, as the mixing of air masses due to atmospheric motions smooths the differences at higher altitudes. Generally, temperature decreases with height until the tropopause is reached (Figure 6). Above the tropopause, in the stratosphere, most of the UV-solar radiation is absorbed by ozone, wherefore the temperature increases with height throughout the stratosphere. However, the stratospheric temperature varies with latitude and season, because the incoming solar UV-radiation is latitude and season dependent. Particularly at the winter poles, within the polar vortex, the temperature is very low (c.f. 2.4.4). Above the tropopause, through the mesosphere, temperature decreases until the mesopause is reached. Above the mesopause, temperature increases again in the so-called thermosphere where high-energy photons are absorbed.

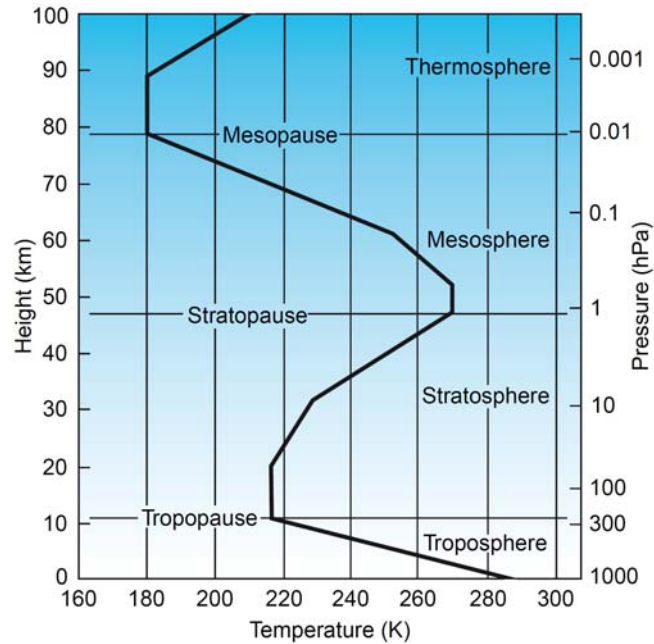


Figure 6. Midlatitude temperature profile from U.S. Standard Atmosphere. From Wallace and Hobbs (2006), their Figure 1.09.

In the last decades, a warming at the surface and in the troposphere and a cooling in the stratosphere has been observed by different observation systems (satellites, radiosondes, etc.) and has also been predicted by climate models. Hence it is important to assess the performance of climate models with respect to radiative processes and temperature.

In this thesis, temperature is evaluated with respect to stratospheric ozone and to test the performance of the different EMAC setups. Radiation processes also affect stratospheric and tropospheric ozone, but in this work they are only regarded to assess the performance of the EMAC simulations in general. A further investigation of the radiation processes connected to ozone would be beyond the scope of this thesis.

2.4.2 Geopotential Height

The *geopotential* (Φ) is defined as the work that has to be done against the Earth's gravitational field to raise a mass of 1 kg from sea level to a certain point in the Earth's atmosphere, usually given in [J/kg] or [m^2/s^2]. In other words, it is the gravitational potential per unit mass. Φ is shown in Eq. 1, where z corresponds to the height above sea level, g is the gravitational acceleration and dz denotes the change in height. The geopotential at sea level has been taken 0 by convention (Wallace and Hobbs, 2006):

$$\Phi(z) = \int_0^z g dz . \quad (1)$$

The geopotential only depends on the height itself and not on the path that an air parcel takes to get into that height. One can also define the *geopotential height* (Z) (Eq. 2), with g_0 being the globally averaged acceleration due to gravity at the Earth's surface:

$$Z = \frac{\Phi(z)}{g_0} . \quad (2)$$

Geopotential height is often used as a vertical coordinate in applications where energy plays an important role (Wallace and Hobbs, 2006).

2.4.3 Specific Humidity

Water vapour is a key climate variable as it is the most important greenhouse gas. Water vapour strongly absorbs infrared radiation and about 60% of the natural greenhouse effect is caused by water vapour (IPCC 2007). In the lower troposphere (boundary layer), water vapour determines the flux of thermal radiation to the ground and absorbs a significant part of direct solar radiation. In the middle and upper troposphere, water vapour mainly acts as a greenhouse gas. The amount of water vapour in the atmosphere changes the radiative equilibrium and influences the formation of clouds. The water vapour feedback is one of the most important feedbacks in the climate system. The warming of the Earth due to an increase of greenhouse gases in the atmosphere leads to an increase in water vapour concentrations in the atmosphere, because more water vapour can be stored in warmer air. In turn, an increase in water vapour advances cloud formation which has a cooling effect (IPCC 2001).

The amount of water vapour in the atmosphere can be determined by a variety of different variables. One of these variables is the *specific humidity* (q , Eq. 3). The specific humidity is the mass of water vapour (m_v) in a unit mass of air (dry air (m_d) plus water vapour) typically measured in [kg/kg] (Wallace and Hobbs, 2006):

$$q = \frac{m_v}{m_v + m_d} . \quad (3)$$

Specific humidity and geopotential height are evaluated in this thesis in order to see how the different setups of the model simulations (nudged and free-running) perform compared to each other.

2.4.4 Tropospheric and Stratospheric Dynamics

In general wind is a motion of air caused by pressure differences (pressure gradient force). Wind blows from high pressure regions to low pressure regions trying to establish an equilibrium state. The stronger the pressure gradient, the higher the speed of the wind. The general wind pattern on the Earth's surface can be described by the atmospheric general circulation. Wind is described as a three-dimensional vector. The three components refer to the zonal component (u , Eq. 4), the meridional component (v , Eq. 4) and the vertical component (w , Eq. 4):

$$u \equiv \frac{dx}{dt}; \quad v \equiv \frac{dy}{dt}; \quad w \equiv \frac{dz}{dt} . \tag{4}$$

Winds on the Earth are primarily caused by the different solar heating of the equatorial re-

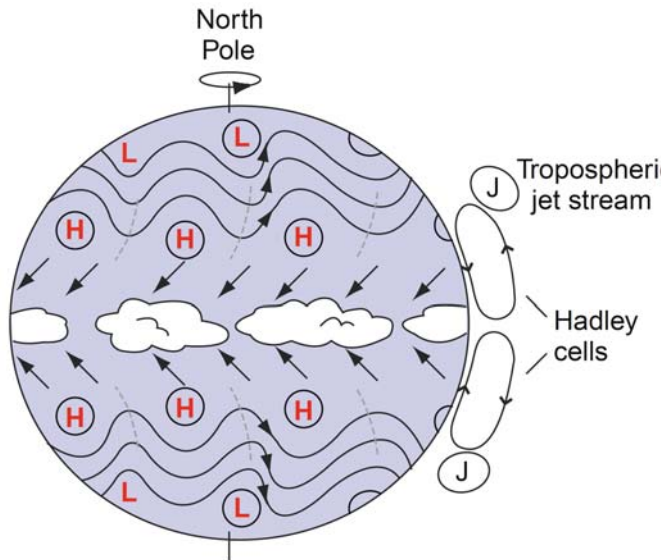


Figure 7. Schematic description of the Earth’s wind patterns and pressure belts. Hadley cell and subtropical jets (J) are shown as well. From Wallece and Hobbs (2006), their Figure 1.15.

gions and the poles, and by the rotation of the planet (*Coriolis Effect*). The resulting general wind pattern on the surface is shown in Figure 7. The high intensity of solar radiation at the equator warms the surface; air rises and diverges in the upper troposphere. This results in a pole-ward transport of air masses in the upper levels (~10-15 km). At subtropical latitudes (30°N/S), the cooled air masses descend and diverge again at the surface, causing an equator-ward wind at the surface (see the *Hadley Cell* in Figure 7 and Figure 8). These surface winds are referred to as *trade winds*. The *Coriolis force* acting on these winds leads to their westward deflection. There-

fore, trade winds are named north-easterly trade winds (northern hemisphere) and south-easterly trade winds (southern hemisphere). At the Equator, the trade winds converge, forming the *Inter Tropical Convergence Zone* (ITCZ). At subtropical latitudes, where the air masses descend, high pressure regions form. Next to the Hadley Cell, other wind cells exist, i.e. the *Ferrel Cell* at mid-latitudes and the *Polar Cell* at the poles (Figure 8).

Cooling at the poles forces the air to subside and thus form a high pressure area. The resulting equator-ward outflow of air is then turned to an east-ward direction by the Coriolis Force. These winds are usually dry, cold, weak and irregular and directed toward low pressure systems of the west-wind region in the higher mid-latitudes (Figure 7). The polar cell is the weakest of all cells and covers the smallest area.

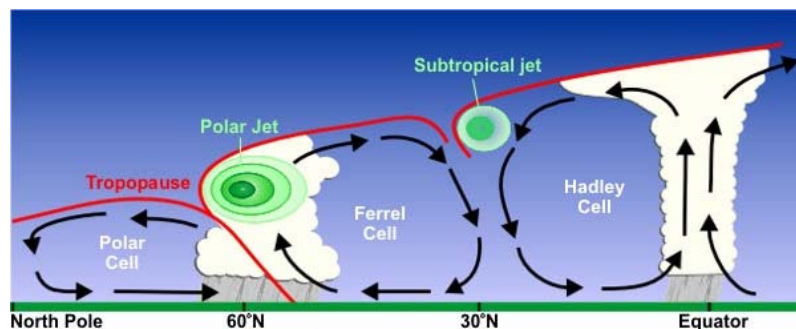


Figure 8. Meridional cross section of the atmospheric cells and jet streams (web2).

Within the Ferrel cell, the air flows pole- and east-ward near the surface and equator- and west-ward at higher levels (Figure 7 and Figure 8). In the low-level west-wind zone between 30° and 60°N/S (also called frontal zone), which is a zone of strong horizontal tem-

perature gradients, low-pressure systems (cyclones) form caused by baroclinic instabilities (instabilities due to non-aligned planes of constant temperature and pressure, respectively). The trade winds and the west wind zone are separated by a high pressure zone at about 30°N/S .

At higher levels in the atmosphere ($\sim 7\text{-}15$ km), so-called *jet streams* can be found. Jet streams are narrow channels of strong winds (faster than 30 m/s) which are usually found near the tropopause. In general, there are two kinds of jet streams as shown in Figure 9. At about 30°N/S the *Subtropical Jet Stream*, which is a westerly stream, is observed. Its existence results from the Hadley Circulation and thermal winds caused by the lower temperatures at latitudes higher than 30°N/S . The *Mesospheric Jet Stream* which changes its direction with season (west wind jet in winter month and east wind jet in summer month) has its maximum wind speeds at about 60 km height (Figure 9).

In the middle atmosphere (stratosphere and mesosphere), the main wind characteristics are an easterly jet in the summer hemisphere and a westerly jet (known as polar night jet) in the winter hemisphere.

In the polar regions, a large circumpolar circulation, the so called *polar vortex* with strong westerly winds at its boundary is the dominant feature. The vortex is caused by the temperature gradient between the poles and lower

latitudes. Thus, it is strongest in the hemisphere's winter and weakens or disappears in the summer. It is stronger, more symmetric, and colder in the Antarctic. In the southern hemisphere, orography disturbs the westerlies less than in the northern hemisphere, wherefore less atmospheric waves propagate the troposphere into the stratosphere and perturb the vortex. Atmospheric wave propagation into the stratosphere and the breaking of these waves on the zonal mean flow causes the polar vortex to slow down, followed by a change from westerlies to easterlies and a sudden rise in temperature (stratospheric warming).

Within the vortex, downward transport of ozone and other trace-gases takes place (Eyring et al., 2005, Jacob 1999, WMO 2002). The strong winds at the edge of the vortex act as a transport barrier. This results in an isolation of the Antarctic stratosphere from the lower mid-latitudes.

In the middle equatorial stratosphere the QBO (*Quasi-Biannual Oscillation*), a variation from easterlies to westerlies about every two years, caused by breaking of tropical waves is the main characteristics of the wind pattern.

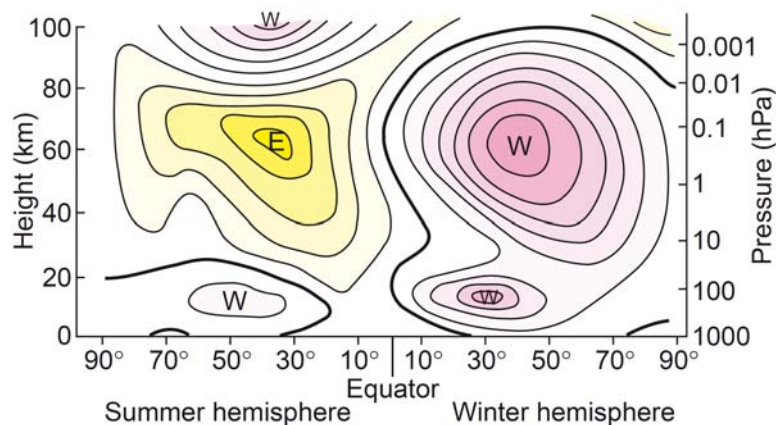


Figure 9. Idealized meridional cross section of the wind strength and direction (contours of 10 m/s) for the summer and winter hemisphere. Yellow areas indicate regions of easterlies, red areas regions of westerlies. The more intensive the color, the stronger the winds are. Small differences in northern and southern hemispheric seasons are neglected. From Wallece and Hobbs (2006), their Figure 1.11.

Another important transport feature of the stratosphere is the *Brewer-Dobson-Circulation* (Figure 10). This circulation describes the global vertical and meridional transport and mixing of ozone and other trace gases in the stratosphere and troposphere-stratosphere exchanges. In the tropics, warm air masses rise through the troposphere into the stratosphere where meridional transport of these air masses to the poles takes place. The mixing of air masses in the stratosphere is not homogeneous, as barriers in the subtropics and at the boundaries of the polar vortices prevent transport of air into these regions. The Brewer-Dobson Circulation is stronger in the northern hemisphere, because the *Rosby waves*, which drive the Brewer-Dobson Circulation, are stronger in the northern hemisphere. Therefore, more ozone and warmer temperatures are found in the northern polar regions than in the southern (Jacob 1999, WMO 2002).

For the evaluation of ozone, it is important to look at transport properties and certain features related to wind (e.g. the polar vortex) that are connected with the depletion and formation of ozone. This will be addressed more closely in the following section. For the comparison of the different EMAC simulations, the zonal and meridional wind components are evaluated.

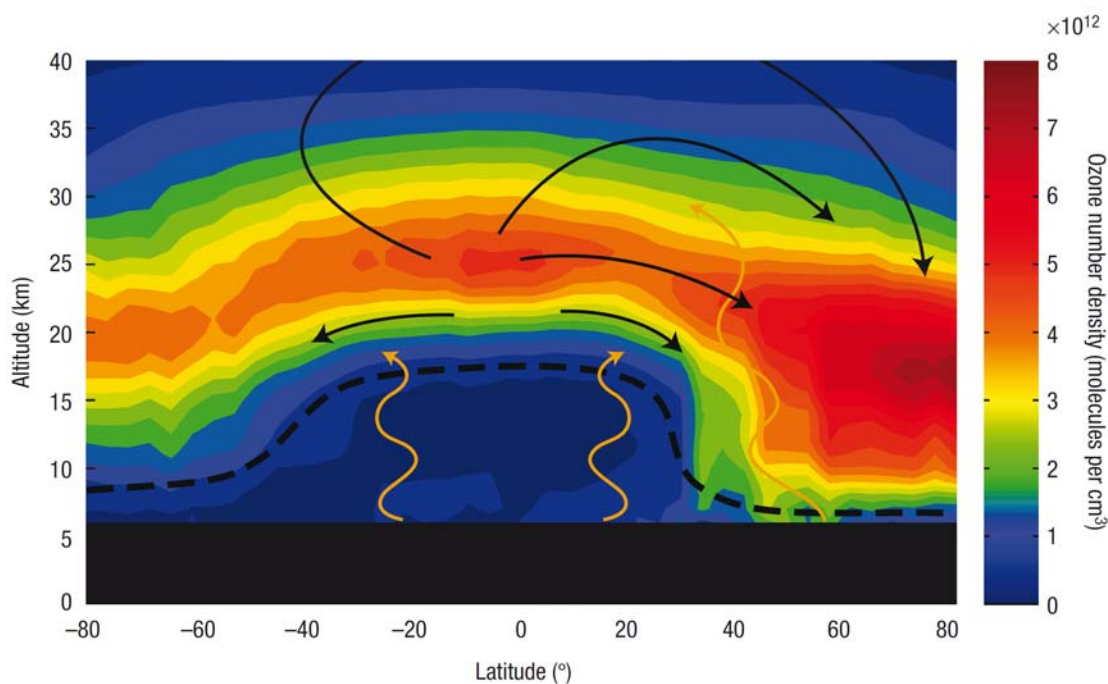


Figure 10. Longitudinally averaged cross-section of the atmosphere showing the Brewer-Dobson circulation (black arrows), and the ozone distribution as measured by the OSIRIS² satellite instrument in March 2004. The circulation is forced by waves propagating up from the troposphere (orange arrows), especially in the winter hemisphere, and it strongly shapes the distribution of ozone by transporting it from its source region in the tropical upper stratosphere to the high-latitude lower stratosphere. The dashed line represents the tropopause. From Shaw and Shepherd (2008), their Figure 1.

² OSIRIS: Optical Spectrograph and InfraRed Imager System

2.4.5 Ozone and Ozone Chemical Reactions in the Stratosphere and Troposphere

Ozone (O_3) is a reactive gas which is naturally present in the atmosphere. About 10% of the total amount of atmospheric ozone is found in the troposphere. The remaining 90% is located in the stratosphere, where it forms the so called *ozone layer* (at a height of ca. 20-25km). The total amount of ozone in the atmosphere, compared to other constituents, is rather low and makes less than 1% by mass. Still, ozone plays an important role in the atmosphere. While stratospheric ozone (“good ozone”) is stated beneficial, because it absorbs UV-radiation which is harmful to humans (e.g. skin cancer), tropospheric ozone (“bad ozone”) in concentration higher than natural, is stated as dangerous because it can cause damage to the lungs and the heart. However, in natural concentrations, ozone in the troposphere is also rather beneficial because it reacts with many pollutants and thus “cleans” the atmosphere (Fahey and Hegglin, 2011, Jacob 1999, Wallace and Hobbs, 2006, WMO 2011).

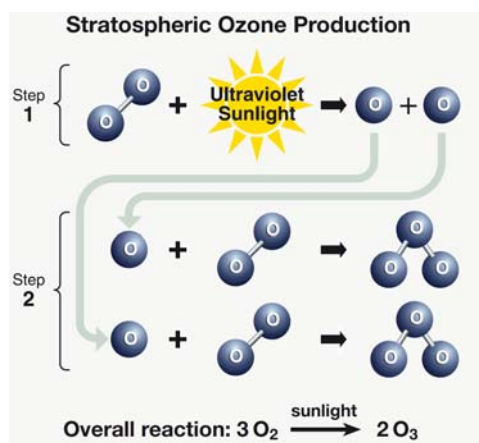


Figure 11. Stratospheric ozone production. Fahey and Hegglin (2011), their Figure Q2-1.

Stratospheric ozone is formed by chemical reactions from oxygen molecules in the presence of UV-radiation. The simplest ozone reaction is the so called *Chapman Cycle* (Chapman 1930), named after Sydney Chapman, who discovered this photolysis reaction in 1930. Solar UV-radiation ($\lambda < 240$ nm) breaks an oxygen molecule (O_2) into two highly reactive oxygen atoms (O). Each of these two atoms reacts, with the help of a third body M (e.g. O_2 or N_2), with an oxygen molecule and forms an ozone molecule (Figure 11, Equation 5-7). These first two reactions of the Chapman Cycle serve as a source of ozone:



The second two reactions of the cycle form the sink of ozone: UV-radiation ($\lambda < 320$ nm) breaks an O_3 molecule into an oxygen atom and an oxygen molecule. Another ozone molecule then reacts with the oxygen atom to form two further oxygen molecules (Equation 8-10):



The Chapman Cycle results then in a steady-state³ concentration of O_3 , which will depend on the intensity of the UV-radiation and further sources and sinks of ozone. As the UV-intensity is highest in the tropics, this is the region where most of the ozone is formed. From there it is transported via the Brewer-Dobson Circulation (c.f. 2.4.4) to the poles where the highest ozone concentrations are found.

The full ozone chemistry is much more complex than the basic Chapman Cycle. The Chapman reactions above cannot explain the observed ozone concentrations, particularly, they cannot fully explain the ozone depletion. Additionally to Eq. 10, atmospheric ozone is destroyed in the presence of certain catalysts, according to Eqs. 11-14, where X denotes the catalyst:



Ozone is destroyed by these reactions either with natural or human produced catalysts. In the stratosphere, these catalysts include hydrogen- and nitrogen oxides (HO_x and NO_x), chlorines (Cl_x), bromines (Br_x) and are called ozone depleting substances (ODS).

In springtime, a decrease in ozone concentrations in the polar regions, particularly in the Antarctic, is observed. This so-called ‘‘ozone hole’’ was first discovered in the 1980s. This decrease in ozone can be explained by catalytic reactions of O_3 with the already mentioned ODSs. Many of these ODSs are formed by chemical reactions of so called *source gases*⁴ with UV-radiation in the stratosphere. Three catalytic cycles with bromines and chlorines are known, each containing two or more separate reactions. One of these three cycles is shown in Eqs. 15-17.



These catalytic reactions of ODSs with O_3 take place in the whole stratosphere, but special conditions in the polar regions of the stratosphere cause a more severe ozone depletion. Low autumn temperatures ($\approx -78^\circ\text{C}$) in the polar stratosphere lead to the formation of polar stratospheric clouds (PSC). The air in the polar region is separated from mid-latitude air by the polar vortex (c.f. 2.4.4), thus the transfer of warmer air to the poles is inhibited.

³ Steady state: production and loss terms of a species (here O_3 , and thus its concentration) are nearly constant with times.

⁴ Source gases include ozone depleting substances and are emitted at the Earth’s surface by human induced or natural processes. In the stratosphere, these gases chemically react with UV-radiation and release reactive substances like bromine and chlorine.

At these special conditions, source gases react on the PSCs forming Cl and thus causing the ozone hole. The ozone hole is more severe in the Antarctic, because the vortex is stronger and temperatures are lower in the southern hemisphere (c.f. 2.4.4). Additionally to the importance of low temperatures for the formation of PSCs, many chemical reactions are temperature-dependent. Changes in the chemical composition cause changes in radiative heating of the stratosphere and can in turn impact the chemical reactions. Also, changes in water vapour concentrations can have significant effects on the stratosphere, e.g. changes in radiation balance or the formation of PSCs.

Tropospheric ozone, like stratospheric ozone, is not directly emitted. It is transported into the troposphere from the stratosphere or is produced by photochemical reactions with ozone precursors. Since the beginning of the industrialization, ozone concentrations in the troposphere have risen. Due to the short lifetime of ozone it is not equally distributed in the atmosphere.

Ozone chemistry in the troposphere is very complex and depends on precursors like NO_x , CO, CH_4 and non-methane hydrocarbons (NMHCs).

Anthropogenic pollutants which influence ozone reactions in the troposphere are mostly produced by the combustion of fossil fuels; natural pollutants are for example formed by lightning (NO_x). In contrast to the stratosphere, UV-radiation in the troposphere is rather weak. Tropospheric ozone is mainly produced by scission of NO_x . In the thus induced photochemical reactions other species like CO, CH_4 or NMHC are important.

NO_2 reacts with sunlight to produce NO and an oxygen atom. The latter one reacts with O_2 and forms ozone (Eqs. 18-19, Figure 12)



The just formed NO in turn reacts with O_3 to NO_2 and O_2 (Eq. 20, Figure 12). Thus an equilibrium state of ozone depletion and formation exists.



NMHCs, CO and other substances can interact and thus disturb the natural equilibrium between ozone production and depletion. However, these species do not disturb the ozone cycle directly, but are removed from the atmosphere via oxidation processes. The products formed by these oxidation reactions advance the reaction from NO to NO_2 . Therefore less

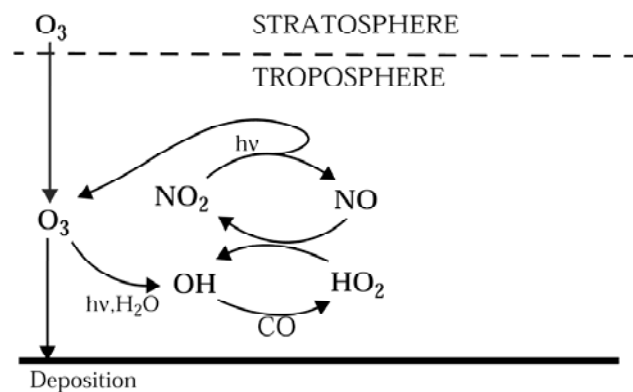


Figure 12. Schematic illustration of tropospheric O_3 chemistry showing the coupling between the chemical cycles of ozone, HO_x and NO_x . From Jacob (1999), their Figure 1 (modified).

NO exists for ozone depletion while at the same time NO_2 concentrations rise and advance the formation of ozone.

Concentrations of NO_x and CO are highest in the lower troposphere at northern mid-latitudes due to fossil fuel combustion. In the upper troposphere, lightning is an additional source of NO_x . Ozone concentrations in the troposphere therefore generally increase with altitude and are higher in the northern hemisphere than in the southern, due to the abundance of NO_x (Jacob 1999).

Still, ozone concentrations are not rising to infinity. This is due to the reaction of ozone with UV-radiation, which splits the ozone molecule into an oxygen atom and an oxygen molecule. The majority of the oxygen atoms react again with an oxygen molecule, forming ozone again. However, some oxygen atoms react with water vapour and form the hydroxyl radical (OH). OH is an important oxidant in the troposphere which determines the lifetime of many important greenhouse gases (e.g. CH_4) (Jacob 1999).

3 Model and Model Simulations

The ECHAM/MESSy Atmospheric Chemistry Model (EMAC) and the four model simulations that were made available for this thesis are described in this section. Section 3.1 gives a description of EMAC. Section 3.1 describes the setups of the EMAC simulations used in this thesis and is therefore divided into four subsections, each referring to one of the model simulations.

3.1 ECHAM/MESSy Atmospheric Chemistry Model (EMAC)

The *ECHAM/MESSy Atmospheric Chemistry* (EMAC) model is a numerical chemistry and climate simulation system that includes submodels describing tropospheric and middle atmosphere processes and their interaction with oceans, land and human influences (Jöckel et al., 2006). It uses the *Modular Earth Submodel System* (MESSy) to link multi-institutional computer codes. The core atmospheric model is the 5th generation European Centre Hamburg general circulation model (ECHAM5, Roeckner et al., 2006). For the present study EMAC (ECHAM 5.3.02/MESSy 2.41 and ECHAM 5.3.01/MESSy 1.10) is applied in the T42L90MA-resolution, i.e. with a spherical truncation of T42 (corresponding to a quadratic Gaussian grid of approximately $2.8^\circ \times 2.8^\circ$ degrees in latitude and longitude) with 90 vertical hybrid pressure levels up to 0.01 hPa.

The current version of MESSy includes more than 50 submodels, with different functions and purposes. The submodels that are used in the simulations evaluated in the present study are summarized in Table 1 and are mostly common to the two versions of MESSy (2.41 and 1.10). Additional and more detailed information can be found in Jöckel et al. (2006), Jöckel et al. (2010) and on the MESSy project webpage (www.messy-interface.org).

Gas-phase chemistry is calculated with the submodel MECCA (Sander et al., 2005), which deals with both tropospheric and stratospheric chemistry. The chemical mechanism is integrated in the entire model domain, i.e., consistently from the surface to the stratosphere. It is important to highlight that no arbitrary or artificial “intermediate boundary conditions” (for instance at the tropopause or between layers) are prescribed. This means that in particular the stratosphere-to-troposphere transport of ozone is simulated self-consistently, i.e., with a single ozone tracer. Chemical species are advected according to the algorithm of Lin and Rood (1996), which is part of ECHAM5. The chemical mechanism in the model setup used here consists of 228 gas phase reactions (including ozone tropospheric chemistry, non-methane hydrocarbons up to isoprene and stratospheric chemistry for bromine and chlorine), 70 photolysis reactions and 22 heterogeneous reactions, involving a total of 134 species. Additional heterogeneous, acid-base and aqueous-phase reactions are included in the submodel SCAV (Tost et al., 2006). The convection processes are simulated following the Tiedtke scheme (Tiedtke 1989) with the Nordeng closure (Nordeng 1994), as in ECHAM5 (Roeckner et al., 2006). The radiation calculations take into account prognostic cloud cover, cloud water, cloud ice (from the CLOUD submodel) and prognostic specific humidity. Forcings from radiatively active gases (CO_2 , CH_4 , O_3 , N_2O , CFCl_3 (CFC-11) and CF_2Cl_2 (CFC-12)) and aerosols are computed from the corresponding prognostic tracers within the RAD4ALL submodel.

3.2 Model Simulations

In this thesis four different EMAC simulations of the recent past are evaluated. As a reference, a nudged simulation described in Jöckel et al. (2010) is used, which is an update using the recently-released version 2.41 of MESSy of the S2 experiment discussed by Jöckel et al. (2006) and Pozzer et al. (2007). The setup of this simulation (hereafter referred to as EMAC2-EVAL) is described in Section 3.2.1. The other three simulations are performed using MESSy version 1.10. A second nudged simulation (EMAC-QCTM) is run using the so-called Quasi Chemistry-Transport Mode (QCTM), developed by Deckert et al. (2011), and is described in Section 3.2.2. Finally, two additional simulations in timeslice mode under 2000 conditions are performed, one (EMAC-TS2000) using observed sea surface temperatures (SSTs) and seaice concentrations (SICs) and one (hereafter called EMAC-ACCMIP) using modeled SSTs and SICs. These are described in Sections 3.2.3 and 3.2.4, respectively.

The basic features of these four simulations summarized in Table 2 and the corresponding emission inventories and offline data in Table 3. The description of the simulations starts with details on the EMAC2-EVAL simulation. For the other three model simulations, only the differences with respect to the EMAC2-EVAL are highlighted.

3.2.1 Simulation in Nudged Mode: EMAC2-EVAL

This simulation covers 12 years (1998-2009), with the first year used for spin-up and therefore not considered in the model analysis. Boundary conditions are as much as possible taken from observations. It is performed in nudged mode, applying a weak nudging towards realistic meteorology (Jeuken et al., 1996), i.e. to data from the ECMWF operational analysis, through the Newtonian relaxation of four prognostic model variables: temperature, divergence, vorticity and the logarithm of surface pressure (van Aalst et al., 2004). SSTs are prescribed from ECMWF operational analysis data as well. The nudging in this method is applied only in the free troposphere, so that stratospheric dynamics are calculated freely and inconsistencies between the boundary layer representation of ECMWF and ECHAM5 model are avoided. The nudging (relaxation e-folding time in parentheses) of temperature (12 h), surface pressure (12 h), divergence (48 h), and vorticity (6 h) in spectral representation is applied between model levels 63 (~97 hPa) and 84 (~706 hPa), with additional transition zones (intermediate stepwise reduced nudging coefficients) between levels 58 (~62 hPa) and 62 (~89 hPa), and 85 (~775 hPa) and 87 (~909 hPa). The nudging is then further reduced (similar to the S2 model simulation in Jöckel et al., 2006) in the vertical down to level 71, i.e., to approximately 204 hPa, with a transition zone from level 65 (~116 hPa) to 70 (~185 hPa).

Online emissions for isoprene, monoterpene, soil NO and Br from sea-salt are simulated by the model. Offline emissions for various sources are also included. As listed in Table 1, several MESSy submodels allow for external fields to be used by the model as offline data. These include natural and anthropogenic emissions (via the OFFEMIS/OFFLEM submodel), boundary condition data for tracers (via TNUDGE) as well as specific information required by other submodels (like AIRSEA, QBO, RAD4ALL and JVAL, in the configuration used for this study). In the current setup, emissions of NO, CO, SO₂, NH₃ and NMHCs (C₂H₄, C₂H₆, C₃H₆, C₃H₈, C₄H₁₀, CH₃CHO, CH₃COCH₃, CH₃COOH, CH₃OH, HCHO, HCOOH, methyl ethyl ketone (MEK)) are supplied to the model from external

inventories. Emissions from both natural (biomass burning, volcanoes, biogenic sources) and anthropogenic (traffic and non-traffic) sources are considered.

This experiment should approximately reproduce meteorology and atmospheric composition for the individual years. Therefore emissions are transient (i.e. varying year by year) where possible. For anthropogenic non-traffic emissions the inventory developed by Lamarque et al. (2010) in support of the International Panel for Climate Change (IPCC) Fifth Assessment Report (AR5) for the year 2000 is used, which provides fluxes on a $0.5^\circ \times 0.5^\circ$ grid, with a time resolution of 1 year. This source is also used for shipping emissions (in this case with a time resolution of 1 month) and the emissions are rescaled using the scaling factors from Eyring et al. (2010a) in order to get a transient set. For the road traffic sector the QUANTIFY dataset (Borken-Kleefeld et al., 2010) is used, which has a spatial resolution of $1^\circ \times 1^\circ$ degree and a time resolution of 1 year. The aviation emissions come from Schmitt and Brunner (1997, SB97) and are available for the period 1960-2009, distributed on a $3.7^\circ \times 3.7^\circ$ grid with a time resolution of 1 month.

Biomass burning emissions are taken from GFED 3.1 (van der Werf et al., 2010). These emissions are gridded with a resolution of $0.5^\circ \times 0.5^\circ$, for the period 1997-2009. For NH_3 the EDGAR3.2FT database (van Aardenne et al., 2005) is considered as well. Additional emissions include volcanic SO_2 (from AeroCom, Dentener et al., 2006), terrestrial DMS (Spiro et al., 1992) and biogenic sources (Ganzeveld et al., 2006). NO_x production from lightning activity is computed according to the scheme of Price and Rind (1994), based on the correlation between the convective cloud top height and the occurrence of flashes derived from regional observations.

NMHC speciation is realized according to the speciation fraction by von Kuhlmann et al. (2003). Different fractions are used for biomass burning and anthropogenic emissions. NMHC mass (usually $\text{kg}(\text{NMHC})$) is converted to carbon mass ($\text{kg}(\text{C})$) assuming a ratio of 161/210, as suggested in the IPCC third assessment report (see also Hoor et al., 2009). The speciation provided in the inventory by Lamarque et al. (2010) has also been considered, but due to its inconsistency with the chemical mechanism of the model, it led to unrealistic results in comparison with the tropospheric vertical profiles from Emmons et al. (2000). Therefore the above method was preferred and applied in all of the simulations presented here (see also Jöckel et al., 2006, 2010). Emission totals for all species in each sector are summarized in Table 8 and Table 9.

Anthropogenic (except aviation) and biomass burning emissions are distributed in the vertical using 6 layers (45, 140, 240, 400, 600, 800 m) following the suggestions of Ganzeveld et al. (2006, mostly based on EMEP). Aviation emission levels are provided by the corresponding inventory (in the range 0-15 km). Volcanic emissions are distributed according to the volcano height. Other sources are emitted as two-dimensional surface fluxes and no assumption on the injection height is therefore required.

Boundary conditions for long-lived species are supplied to the model via the TNUDGE submodel. Greenhouse gases (CO_2 , N_2O , CH_4 , SF_6), chlorofluorocarbons (CFCl_3 , CF_2Cl_2 , CH_3CCl_3 , CCl_4), hydrochlorofluorocarbons (CH_3Cl , CH_3Br), halons (CF_2ClBr , CF_3Br) and H_2 are included. The observed mixing ratios in the AGAGE database (Prinn et al., 2000) are used. The fields are provided on a monthly basis and zonally-averaged.

As mentioned above, some of the MESSy submodels require offline fields. The AIRSEA submodel, which simulates the exchange of species between the ocean and the atmosphere, reads in the concentration of isoprene (Broadgate et al., 1997), oceanic DMS (Kettle and Andreae 2000) as well as the ocean salinity (Boyer et al., 2002). The solar cycle data, used by JVAL for the computation of photolysis rates, are taken from Lean (2000). For the simulation in nudged mode (EMAC2-EVAL and EMAC-QCTM), the quasi-biennial oscillation (QBO) data are also needed. In these model simulations the QBO is forced externally by relaxation of the stratospheric equatorial zonal wind to observed equatorial zonal wind profiles (Giorgetta and Bengtsson, 1999). The externally driven QBO is therefore synchronized with the observed QBO.

3.2.2 Simulation in Nudged Mode: EMAC-QCTM

The Quasi Chemistry-Transport Mode (QCTM) simulation covers a period of 10 years (1998-2007, 1 year spin-up) and is based on a recently-developed setup for EMAC (Deckert et al., 2011) in which chemical effects are decoupled from the dynamics (i.e., any feedback between chemistry and dynamics is switched off). This configuration is particularly useful when analyzing the effect of small chemical perturbation (like the addition of a specific emission source, e.g. shipping) on the climate system. Investigating such effects is usually hampered by the internal variability of the model, which induces very low signal-to-noise ratio and makes extremely hard to extract the desired signal. In the QCTM mode, the dynamical differences between different simulations are eliminated and the signal-to-noise ratio can be significantly improved, allowing studying small chemical perturbations even with a limited amount of simulated years.

In order to realize such setup, the model has to be run in offline mode, to ensure identical meteorological conditions in different experiments. Furthermore, radiation must be driven by external climatological fields for the radiatively active gases (CO_2 , CH_4 , O_3 , N_2O and chlorofluorocarbons). Water vapour must not affect the dynamics of the system nor the cloud properties, therefore water vapour tendencies must be decoupled from the chemical processes simulated by the model (via the MECCA submodel).

Four submodels are involved in the QCTM configuration. In RAD4ALL, constant mixing ratios are assumed for CO_2 (367 ppm), CH_4 (1.75 ppm), N_2O (316 ppb), CFC-11 and CFC-12 (262 ppt and 540 ppt, respectively), whereas a climatology (Fortuin and Kelder 1998) is used for O_3 . Water vapour tendencies are managed by the H2O submodel: here only external climatologies are used, switching off any connection with the online chemistry calculations. The data from a simulation by Steil et al. (2003), using the MAECHAM4/CHEM model, as suggested by Deckert et al. (2011) is used. In the HETCHEM submodel, the effect of thermodynamic repartitioning of water phases on water tendencies is switched off. The PSC submodel also introduces feedbacks between chemistry and dynamics, by determining heterogeneous reaction rates via HETCHEM, by changing H_2O and HNO_3 mixing ratio from ice particle sedimentation and by setting the PSC-relevant regions according to the distribution of HNO_3 (see Deckert et al. (2011) for a more thorough description of the processes). These processes are switched off in this configuration and climatologies for HNO_3 and H_2SO_4 from a corresponding coupled simulation are used in input.

Similarly to EMAC2-EVAL, this simulation was carried out to approximate meteorology and atmospheric composition for individual years, hence it is performed in nudged mode and using transient emissions. The same emissions setup as in the EMAC2-EVAL simulation is adopted, with the exception of aircraft emissions which were taken from QUANTIFY (Hoor et al., 2009), with a spatial resolution of $1^\circ \times 1^\circ$ grid and a time resolution of 1 month. Aerosols are prescribed using the standard ECHAM5 climatology (Tanre et al., 1984). See Table 3 for a summary.

3.2.3 Timeslice Simulation: EMAC-TS2000

The EMAC-TS2000 timeslice simulation is performed in free mode and encompasses a period of 10 years under 2000 conditions with one additional year for spin-up.

The distributions for SSTs and SICs are prescribed using the HadISST1 dataset from the Met Office Hadley Centre (Rayner et al., 2003), containing monthly global fields on a $1^\circ \times 1^\circ$ grid. Here a 10-year climatology from 1995 to 2004 is used. Since this is a timeslice experiment, only year 2000 emissions are considered and otherwise the same emission setup as in the EMAC-QCTM simulation is used. Lightning NO_x production is computed following the parameterization by Grewe et al. (2001), which links the updraft velocity (as a measure of convective strength) and the associated cloud electrification with flash frequency.

3.2.4 Timeslice Simulation: EMAC-ACCMIP

The timeslice simulation EMAC-ACCMIP was performed in support of the *Atmospheric Chemistry & Climate Model Intercomparison Project* (ACC-MIP). The simulation is equal to the EMAC-TS2000 setup, except that slightly different emission inventories were used (see Table 3), which were chosen to conform to the project requirements. The 2000 timeslice simulation is only one out of the ACCMIP series of experiments, covering the period 1850 to 2100.

To allow a consistent use of SSTs/SICs that cover the full period without discontinuities, simulated SSTs/SICs from a continuous climate model simulation were prescribed instead of observations as in EMAC-TS2000. Monthly mean SSTs and SICs are prescribed as a 10-year climatological mean around the base year 2000 using the historical CMIP5 experiment carried out with the CMCC Climate Model. The CMCC SSTs/SICs on the ORCA coordinates are interpolated to a T42 grid using the ECHAM land mask. Similar to EMAC, the atmospheric component of the CMCC climate model is based on ECHAM5 (Roeckner et al., 2006), but in contrast to EMAC the OASIS3 coupler (Fogli and Coauthors 2009, Valek 2006) and the OPA8.2/LIM ocean and sea ice components (Fichefet and Maqueda 1997, Madec et al., 1999) are used. The incorporation of the resolved stratospheric component implies the use of the Middle Atmosphere (MA-ECHAM5) setup of the atmospheric model (Manzini et al., 2006). Such setup has a top at 80 km (0.01 hPa) and includes the parameterization of momentum conserving orographic and non-orographic gravity wave drag. The SW radiation scheme covers the 185-4000 nm spectral interval with a spectral resolution of 6 bands separating the UV and visible ozone absorption (Cagnazzo et al., 2007), so is different to the one that was used here. In the atmospheric component, a source of water vapour in the stratosphere and mesosphere by methane oxidation is con-

sidered. The oceanic component has a resolution of about 2 degrees in the horizontal and 31 vertical levels.

Table 1 List of the MESSy submodels that have been used in the simulations of this thesis

Submodel	Function	Reference
AIRSEA	calculates the deposition and emissions over the ocean using a two-layer model, depending on the concentrations both in the air and on the oceanic surface	(Pozzer et al., 2006)
CLOUD	calculates the cloud cover and the cloud microphysical processes (including precipitations), implementing the original cloud routines of ECHAM5 in the MESSy framework.	(Roeckner et al., 1996)
CONVECT	Deals with the convection process and includes several different parameterizations.	(Roeckner et al., 1996)
CVTRANS	Calculates the transport of tracers due to convection, following the approach described by Lawrence and Rasch (2005).	(Lawrence and Rasch 2005)
DRYDEP (DDEP in MESSy2)	Calculates gas phase and aerosol tracer dry deposition according to the big leaf approach	(Kerkweg et al., 2006a)
H2O	Defines H ₂ O as a tracer, provides its initialisation in the stratosphere and in the mesosphere using satellite data, and controls the consistent feedback with specific humidity of the base model	(Jöckel et al., 2006)
HETCHEM	Deals with the heterogeneous chemistry, by calculating heterogeneous reaction rates on stratospheric nitric acid trihydrate (NAT), ice and super-cooled ternary solutions (STS) and on stratospheric and tropospheric (sulfate) aerosols.	(Jöckel et al., 2006)
JVAL	Provides online calculation of photolysis rate coefficients (J-values), according to	(Landgraf and Crutzen 1998)
LNOX	Calculates NO _x production from lightning activity, including four different parameterizations.	(Allen and Pickering 2002, Grewe et al., 2001, Price and Rind 1994)
MECCA	Calculates tropospheric and stratospheric chemistry: The integration of the set of stiff differential equations is performed by the Kinetic Preprocessor (KPP), using a 3 rd order Rosenbrock sparse-matrix technique with adaptive time step.	(Fahey and Hegglin 2011, Sander et al., 2005, Sander et al., 2011, Sandu and Sander 2006)
OFFEMIS / OFFLEM	Manages the prescribed emission field	(Kerkweg et al., 2006b)

ONEMIS / ONLEM	Calculates online emission fluxes	(Kerkweg et al., 2006b)
PSC	Simulates micro-physical processes that lead to the formation of super-cooled ternary solutions (STS), nitric acid trihydrate (NAT), and ice particles in the polar stratosphere as well as heterogeneous chemical reaction coefficients of halogens and dinitrogen pentoxide (N ₂ O ₅) on liquid and solid aerosol particles	(Buchholz 2005, Kirner et al., 2011)
PTRAC	Uses user-defined initialised prognostic tracers to test mass conservation, monotonicity and positive definiteness of Eulerian and Lagrangian advection algorithms	(Jöckel et al., 2008)
QBO	Assimilates quasi-biennial oscillation (QBO) zonal wind observations and is required only when the model is run in nudged mode (like in the QCTM and MESSy2 runs).	(Giorgetta and Bengtsson 1999, Naujokat 1986)
RAD4ALL	Implements the original radiation scheme from ECHAM5, including some additional features like the online coupling of radiation with trace gases and the possibility to read input quantities from external climatologies.	(Roeckner et al. 1996)
SCAV	Simulates wet deposition and liquid phase chemistry in precipitation fluxes, considering gas-phase and aerosol species in large-scale as well as in convective clouds and precipitation events	(Tost et al., 2006)
SEDI	Calculates sedimentation of aerosol particles and their components	(Kerkweg et al., 2006a)
TNUDGE	Used for nudging user-defined tracers with arbitrary user-defined fields	(Kerkweg et al., 2006b)
TROPOP	Diagnoses the tropopause, according to various definitions, and the height of the planetary boundary layer	(Jöckel et al., 2006)

Table 2 Details of the four EMAC simulations evaluated in this thesis

Name	Resolution	Time period	Running mode
EMAC2-EVAL	T42-L90MA	1998-2009	Nudged
EMAC-QCTM	T42-L90MA	1998-2007	Nudged
EMAC-TS2000	T42-L90MA	10 years under 2000 conditions	Free-running timeslice
EMAC-ACCMIP	T42-L90MA	12 years under 2000 conditions	Free-running timeslice

Table 3 Boundary conditions and emission datasets for the simulations considered in this thesis. References to each dataset/inventory are given in the text. Below a specification whether data are used in transient or in constant (2000) mode, is given for each dataset. The Lamarque et al. (2010) inventory is abbreviated with L2010.

Species / Sector	Submodel	EVAL	QCTM	TS2000	ACCMIP
Greenhouse gases	TNUDGE	AGAGE			
		Transient	Transient	2000	2000
Chlorofluoro-carbon	TNUDGE	AGAGE			
		Transient	Transient	2000	2000
Hydrochloro-fluorocarbon	TNUDGE	AGAGE			
		Transient	Transient	2000	2000
Halons	TNUDGE	AGAGE			
		Transient	Transient	2000	2000
H ₂	TNUDGE	AGAGE			
		Transient	Transient	2000	2000
Biomass burning	OFFLEM / OFFFEMIS	GFED	GFED	GFED	L2010
		Transient	Transient	2000	2000
Agricultural waste burning	OFFLEM / OFFFEMIS	L2010	L2010	L2010	L2010
		2000	2000	2000	2000
Anthropogenic (non-traffic)	OFFLEM / OFFFEMIS	L2010	L2010	L2010	L2010
		2000	2000	2000	2000
Road transportation	OFFLEM / OFFFEMIS	QUANTIFY	QUANTIFY	QUANTIFY	L2010
		2000	2000	2000	2000
Shipping	OFFLEM / OFFFEMIS	L2010	L2010	L2010	L2010
		Transient	Transient	2000	2000
Aviation	OFFLEM / OFFFEMIS	SB97	QUANTIFY	QUANTIFY	L2010
		Transient	2000	2000	2000
Biogenic sources	OFFLEM / OFFFEMIS	Ganzeveld et al., 2006			
		2000			
Volcanic SO ₂	OFFLEM / OFFFEMIS	AeroCom			
		2000			
Terrestrial DMS	OFFLEM / OFFFEMIS	Spiro et al., 1992			
		2000			
NH ₃	OFFLEM / OFFFEMIS	EDGAR	EDGAR	EDGAR	L2010
		2000	2000	2000	2000

4 Strategy for Model Evaluation

When evaluating a climate model, specific choices have to be made for example on the adopted diagnostics, observations and statistical measures. In this chapter, the model evaluation strategy is described in Section 4.1, followed by a description of the statistical measures in Section 4.2.

4.1 Model Evaluation Strategy

As noted in the Introduction, the focus of this thesis is to evaluate and understand the performance of different configurations of the EMAC model (nudged versus free-running) with respect to how well they simulate ozone. The evaluation follows the concept of process-oriented model evaluation established by the Chemistry-Climate Model (CCMVal) Activity of the World Climate Research Programme's *Stratospheric Processes and their Role in Climate* (SPARC) project (SPARC CCMVal, 2010). The basic idea is that the evaluation does not only focus on the quantity of interest, which in the case of CCMVal is stratospheric ozone, but also on the processes that determine it.

Since the main differences between the free-running and nudged simulations are introduced due to differences in meteorology, basic climate parameters are first compared to observations. For the evaluation of such parameters (temperature, wind, geopotential height, specific humidity, and radiation), the same diagnostics, performance metrics and observational datasets are applied as those used by Gleckler et al. (2008), except that products and time periods were updated where available. As in Gleckler et al. (2008), the evaluation focuses primarily on the global scales of the simulated mean annual cycle. Since a chemistry-climate model with prescribed SSTs is evaluated, the ocean parameters are not applied, and also no longwave and shortwave cloud radiative forcing, cloud cover, precipitation and precipitable water, since it is difficult to relate biases in these parameters to ozone, which is the focus of the analysis here.

In the troposphere, promising process-oriented diagnostics that have been published so far are much more limited than for the stratosphere. The tropospheric evaluation therefore mostly focuses on a statistical analysis for the comparison of ozone precursors to observations from numerous field campaigns. For comparison with previous EMAC evaluation paper, the same locations and periods as in Pozzer et al. (2007) and Jöckel et al. (2006) were chosen. In the stratosphere, the diagnostics that were applied by Eyring et al. (2006) as part of the CCMVal-1 comparison are chosen. While many more diagnostics have been applied to CCMVal-2 simulations as part of the SPARC CCMVal (2010) report, applying them all here is beyond the scope of this thesis. Therefore, in a first step, ozone is compared to observational data followed by a process-oriented evaluation covering stratospheric temperature distribution (as it affects chemical reactions related to ozone), stratospheric winds (as they provide information about the polar vortex and the polar vortex transport barrier), transport processes and the distribution of ozone depletion substances (see Section 2.4.4 and 2.4.5).

A summary of the list of diagnostics that are applied in this thesis along with the variable, corresponding observations, short name, period and domain for the performance metric and references is given in Table 4, Table 5 and Table 6. The evaluation is done in two

steps: qualitatively by applying the diagnostics, and quantitatively by applying statistical measures.

Table 4 List of core processes to evaluate basic mean climate state. Diagnostics for the evaluation are given along with the variable, observations, the short name and period / domain for the performance metric and references.

Basic Climate Parameters	Diagnostic	Variable	Observations	Short name for performance metric	Period / domain for performance metric	Reference
Basic climate parameters						
Tropospheric temperature climatologies	Annual cycle of climatological mean tropospheric temperatures	Temperature (K), 5 hPa, 30 hPa, 200 hPa and 850 hPa	ERA-Interim (1995-2005), NCEP (1995-2005)	ta5-Glob ta30-Glob ta200-Glob ta850-Glob	Glob (90°S-90°N)	(Gleckler et al., 2008) Sums of grades accumulated over all months and over the domain of interest
				ta5-EQ ta30-EQ ta200-EQ ta850-EQ	Tropics (20°S-20°N),	
				ta5-NHExt ta30-NHExt ta200-NHExt ta850-NHExt	NHExt (20°N-90°N)	
				ta5-SHExt ta30-SHExt ta200-SHExt ta850-SHExt	SHExt (20°S-90°S)	
Tropospheric wind climatologies	Annual cycle of climatological mean zonal mean tropospheric winds	Zonal mean wind (m/s), 5 hPa, 30 hPa, 200 hPa and 850 hPa	ERA-Interim (1995-2005), NCEP (1995-2005)	ua5-Glob ua30-Glob ua200-Glob ua850-Glob	Glob (90°S-90°N)	(Gleckler et al., 2008)
				ua5-EQ ua30-EQ ua200-EQ ua850-EQ	Tropics (20°S-20°N),	
				ua5-NHExt ua30-NHExt ua200-NHExt ua850-NHExt	NHExt (20°N-90°N)	
				ua5-SHExt ua30-SHExt ua200-SHExt ua850-SHExt	SHExt (20°S-90°S)	
	Annual cycle of climatological mean meridional tropospheric winds	Meridional wind (m/s), 5 hPa, 30 hPa, 200 hPa and 850 hPa	ERA-Interim (1995-2005), NCEP (1995-2005)	va5-Glob va30-Glob va200-Glob va850-Glob	Glob (90°S-90°N)	(Gleckler et al., 2008)
				va5-EQ va30-EQ va200-EQ	Tropics (20°S-20°N),	

				va850-EQ		
				va5-NHExt va30-NHExt va200-NHExt va850-NHExt	NHExt (20°N- 90°N)	
				va5-SHExt va30-SHExt va200-SHExt va850-SHExt	SHExt (20°S-90°S)	
Geopotential height	Annual cycle of climatological mean geopotential height	Geopotential height (m), 5 hPa, 30 hPa, 500 hPa, 850 hPa	ERA-Interim (1995-2005), NCEP (1995-2005)	zg5-Glob zg30-Glob zg500-Glob zg850-Glob	Glob (90°S-90°N)	(Gleckler et al., 2008)
				zg5-EQ zg30-EQ zg500-EQ zg850-EQ	Tropics (20°S-20°N),	
				zg5-NHExt zg30-NHExt zg500-NHExt zg850-NHExt	NHExt (20°N-90°N)	
				zg5-SHExt zg30-SHExt zg500-SHExt zg850-SHExt	SHExt (20°S-90°S)	
Specific humidity	Annual cycle of climatological mean specific humidity	Specific humidity (kg/kg), 5 hPa, 30 hPa, 400 hPa and 850 hPa	ERA-Interim (1995-2005), NCEP (1995-2005)	hus5-Glob hus30-Glob hus400-Glob hus850-Glob	Glob (90°S-90°N)	(Gleckler et al., 2008)
				hus5-EQ hus30-EQ hus400-EQ hus850-EQ	Tropics (20°S-20°N),	
				hus5-NHExt hus30-NHExt hus400-NHExt hus850-NHExt	NHExt (20°N-90°N)	
				hus5-SHExt hus30-SHExt hus400-SHExt hus850-SHExt	SHExt (20°S-90°S)	
Radiation	Climatological mean TOA reflected shortwave radiation	TOA reflected shortwave radiation (W/m ²)	SRB (1995-2005), CERES (2001-2005)	rsut-Glob	Glob (90°S-90°N)	(Gleckler et al., 2008)
				rsut-EQ	Tropics (20°S-20°N),	
				rsut-NHExt	NHExt (20°N-90°N)	
				rsut-SHExt	SHExt (20°S-90°S)	
	Clima-	TOA outgo-	SRB (1995-	rlutcs-Glob	Glob (90°S-	Gleckler et

	tological mean TOA longwave clear-sky radiation	ing longwave clear-sky radiation (W/m ²)	2005), CERES (2001-2005)		90°N)	al. 2008)
				rlutcs-EQ	Tropics (20°S-20°N),	
				rlutcs-NHExt	NHExt (20°N-90°N)	
				rlutcs-SHExt	SHExt (20°S-90°S)	
	Climatological mean TOA longwave radiation	TOA outgoing longwave radiation (W/m ²)	SRB (1995-2005), CERES (2001-2005)	rlut-Glob	Glob (90°S-90°N)	Gleckler et al. 2008)
				rlut-EQ	Tropics (20°S-20°N),	
				rlut-NHExt	NHExt (20°N-90°N)	
				rslut-SHExt	SHExt (20°S-90°S)	

Table 5 List of core processes to evaluate tropospheric ozone. Diagnostics for the evaluation are given along with the variable, observations, the short name and period / domain for the performance metric and references.

Tropospheric Ozone / Process	Dagnostic	Variable	Observations	Short name for performance metric	Period / domain for performance metric	Reference
Tropospheric Ozone						
Evaluation of ECV: Tropospheric Ozone						
Tropospheric Ozone	Vertical profiles of ozone	O ₃ (ppm) for selected latitudes and longitudes (depending on ozone sonde station)	Campaign measurements (different time periods) (Emmons et al., 2000)	o3trop-ALL-regions	Emmons – data levels, all available observations considered	(Emmons et al., 2000)
		O ₃ (ppm) for selected latitudes and longitudes (depending on aircraft campaign) 1000-200 hPa	Ozonesondes (different time periods) (Tilmes et al., 2011)	o3trop-VP-region	Scatterplot 0-200 ppb	(Logan 1999)
	Global tropospheric column ozone climatology	Zonal mean monthly mean tropospheric column ozone annual cycle (DU)	MLS/OMI	toz-trop-Glob-AC	Averaged over all month	Ziemke et al., 2011

		Zonal mean monthly mean tropospheric column ozone (DU)	MLS/OMI	toz-trop-Glob	90°N – 90°S	Ziemke et al., 2011
Process-oriented evaluation of tropospheric ozone						
Tropospheric ozone formation and destruction by ozone precursors	Vertical profiles of CH ₄ , NO _x , CO, and NMHCs	CH ₄ (ppt), NO _x (ppt), CO (ppb), and NMHCs (depending) For selected latitudes and longitudes (depending on aircraft campaign)	Campaign measurements (different time periods) (Emmons et al., 2000)	ch4trop-ALL-regions noxtrop-ALL-regions cotrop-ALL-regions nmhtrop-ALL-regions	Emmons – data levels (varies for different stations)	(Emmons et al., 2000)
	Annual Cycle of CO	CO (ppb), for selected latitudes and longitudes (depending on GLOBALVIEW station)	NOAA GLOBALVIEW W (1991-2009)	cotrop-AC-station	Averaged over all month	GLOBALVIEW-CO (2009)
Oxidation capacity	Vertical profiles of OH	OH (molec/cm) for selected latitudes and longitudes (depending on aircraft campaign)	Campaign measurements (different time periods) (Emmons et al., 2000)	ohtrop-ALL-regions	Emmons – data levels	(Emmons et al., 2000)

Table 6 List of core processes to evaluate stratospheric ozone. Diagnostics for the evaluation are given along with the variable, observations, the short name and period / domain for the performance metric and references.

Stratospheric Ozone / Process	Diagnostic	Variable	Observations	Short name for performance metric	Period / domain for performance metric	Reference	
Stratospheric Ozone							
Evaluation of ECV: stratospheric ozone							
Stratospheric ozone	Climatological zonal mean, meridional ozone profiles	O ₃ (ppm) at 50 hPa, March	HALOE (1991-2005)	o3strat50-NH	60°-90°N	(Eyring et al., 2006)	
		O ₃ (ppm) at 50 hPa, October		o3strat50-SH	60°-90°S		
	Climatological zonal mean, vertical ozone profiles	O ₃ (ppm) at 80°S October	HALOE (1991-2005)	o3strat-80S-VP	30-50 hPa	Eyring et al. (2006); Karpetchko et al. (2010)	
		O ₃ (ppm) in the tropics (25°N-25°S) in March		o3strat-Trop-VP			
				o3strat-80N-VP	No Grading		
	Global total column ozone climatology	Zonal mean monthly mean total column ozone (DU)	NIWA (1995-2005)	toz-Glob-AC	90°S-90°N	Eyring et al. (2006); Karpetchko et al., 2010	
				toz-SP-AC	60°-90°S		
	Climatological zonal mean meridional total column ozone profile	Zonal mean seasonal and annual mean total column ozone (DU)	NIWA (1995-2005)	toz-MAM-zon	90°S-90°N	Loyola et al., 2009	
				toz-JJA-zon	90°S-90°N		
			GOME (1996-2006)	toz-SON-zon	90°S-90°N		
toz-DJF-zon				90°S-90°N			
toz-ANN-zon				90°S-90°N			
Process-oriented evaluation of stratospheric ozone							
Stratospheric temperature climatologies	North- and South-polar climatological mean temperature biases	Climatological mean temperature (K), SON, 60°-90°S	ERA-Interim (1995-2005), NCEP (1995-2005)	ta-SP-SON	30-50 hPa	(Eyring et al., 2006); Waugh and Eyring (2008)	
				Climatological mean temperature (K), JJA, 60°-90°S	ta-SP-JJA		30-50 hPa
				Climatological mean temperature (K), DJF, 60°-90°N	ta-NP-DJF		30-50 hPa
				Climatological mean temperature (K), MAM, 60°-90°N	ta-NP-MAM		30-50 hPa

Stratospheric temperature climatologies	Temperature climatologies	Temperature (K) 60°S, 30 hPa	ERA-Interim (1995-2005)	ta30-60S	for each month	Dameris et al. (2005)
		Temperature (K) 60°N, 30 hPa		ta30-60N		
Stratospheric wind climatologies	Zonal mean wind climatologies	Zonal mean wind (m/s) 60°S, 30 hPa	ERA-Interim (1995-2005)	ua30-60S		
		Zonal mean wind (m/s) 60°N, 30 hPa		ua30-60N		
Break up of polar vortex	Transition to easterlies, mean zonal wind	Zonal mean wind (m/s) at 60°S, OCT - JAN	ERA-Interim (1995-2005)	No grading	No grading	(Eyring et al., 2006) Butchart et al. (2010)
Subtropical and polar stratospheric mixing barriers	Climatological zonal mean, meridional tracer profiles	CH ₄ (ppm), 50 hPa, March / October	HALOE (1991-2005)	ch4-Subt	0°N-30°N, for March 0°-30°S for October; calculated over each month and then averaged	(Eyring et al., 2006); Waugh and Eyring (2008)
		Climatological zonal mean, vertical tracer profiles		CH ₄ (ppm), 80° S, October	ch4-SH	
	CH ₄ (ppm), 10°S-10°N, annual mean			ch4-EQ	30/50 hPa	
	Climatological zonal mean, meridional tracer profiles	H ₂ O (ppm), 50 hPa, March / October		HALOE (1991-2005)	h2o-Subt	
Climatological zonal mean, vertical tracer profiles			h2o-SH		30/50 hPa	
			h2o-EQ		30/50 hPa	
Climatological zonal mean, vertical tracer profiles	H ₂ O (ppm), 10°S-10°N, annual mean	HALOE (1991-2005)	h2o-NH	No Grading		
Entry of water vapour into the stratosphere	Climatological zonal mean tropical water vapour	H ₂ O (ppm) 10°S-10°N, 100 hPa	HALOE (1991-2005)	h2o100-EQ	Applied for each month, then averaged	(Eyring et al., 2006); Waugh and Eyring (2008)
Tropical tropopause	Climatological zonal mean tropical temperature at tropopause	Temperature (K) 10°S-10°N, 100 hPa	ERA-Interim (1995-2005), NCEP (1995-2005)	ta-Trop	Applied for each month, then averaged.	(Eyring et al., 2006)

Tropical as- cent	Water Va- pour Tape Recorder Amplitude	H2O Tape Recorder Amplitude at 10N -10S	HALOE (1991- 2005)	tape-R	Applied for each month, then aver- aged	(Eyring et al., 2006) Waugh and Eyring (2008)
	Water Va- pour Tape Recorder Phase Speed	H2O Tape Recorder Phase Speed (months) at 10N -10S	HALOE (1991- 2005)	tape-c	Applied for each month, then aver- aged	
Chlorine res- ervoirs	Clima- tological zonal mean, meridional HCl profiles	HCl (ppb), 50 hPa, March / October	HALOE (1991- 2005)	hcl50-Subt	0°N-30°N, for April 0°-30°S for November; calculated over each month and then aver- aged	(Eyring et al., 2006)
	Clima- tological zonal mean, vertical tracer pro- files	HCl (ppb), 80° S, Octo- ber		hcl-SP	No Grading	
		HCl (ppb), 10°S-10°N, annual mean		hcl -EQ	30/50 hPa	
Polar proc- esses in win- ter and spring	Time series of polar Cl _y	Cl _y (ppb), 80°S, 50 hPa, October	UARS HCl	cly-SP	30/50 hPa	(Eyring et al., 2006) Waugh and Eyring (2008)
	Time series of mid- latitude Cl _y	Cl _y (ppb), 35°- 60°N, 50 hPa, annual mean	multiple	cly-ML	30/50 hPa	
	Vertical profile of polar Cl _y	Cl _y (ppb), 80°S, Novem- ber	UARS HCl	cly-SP	No Grading	

4.2 Statistical Methods and Specific Choices for Quantitative Model Evaluation

As mentioned in section 2.3, model grading and the use of performance metrics is a challenging and important task in climate model evaluation. In this thesis, a statistical error assessment is performed, following Gleckler et al. (2008), using the root-mean-square difference (RMSD), the overall mean bias and Taylor diagrams.

The *RMSD*, which is commonly used to quantify performance of climate and numerical weather forecast models, is defined as follows:

$$RMSD_M = \sqrt{\frac{1}{IJK} \sum_i \sum_j \sum_k w_{ijk} \cdot (M_{ijk} - O_{ijk})^2}. \quad (21)$$

This metric has been considered (among others) by Taylor (2001), Jöckel et al. (2006), Gleckler et al. (2008), Reichler and Kim (2008), Karpechko et al. (2010) and Yokoi et al. (2011). While Taylor (2001) and Yokoi et al. (2011) resigned the weighting, Gleckler et al. (2008), Reichler and Kim (2008) and Karpechko et al. (2010) use the weighting described

above. Additionally, Reichler and Kim (2008) weight the sum also by a factor indirectly proportional to the variance from the observation (thus stressing the variables with lower variance), and Karpechko et al. (2010) by a factor indirectly proportional to the uncertainty in the observed variable (thus laying stress on more accurate observations). Jöckel et al. (2006) apply a weighting depending on the model error (standard deviation from the averaged value) and the measurement error (combination of instrumental error and variance), thereby giving more importance to values with a smaller total error. Although the latter weightings are reasonable, they are only applicable consistently if all the errors and uncertainties are known. This weighting is resigned in order to achieve a better interpretability of the statistics used in this thesis.

Additionally the overall mean bias is calculated according to:

$$b_M = \langle M_{ijk} \rangle - \langle O_{ijk} \rangle = \frac{1}{IJK} \sum_i \sum_j \sum_k w_{ijk} (M_{ijk} - O_{ijk}), \quad (22)$$

where the index M indicates the model simulation. The fields M_{ijk} and O_{ijk} are the model and observation fields, respectively. They can be a function of latitude (i), longitude (j) and time (k), depending on the diagnostic considered. I and J indicate the corresponding grid numbers and K the number of time intervals. Finally, w_{ijk} is a weight which is proportional to the grid area in case the considered diagnostic is a latitude-longitude map or proportional to the length of each month if the diagnostic is a monthly time-series (or monthly climatology) and K a multiple of 12. Hence, the overall mean bias b_M is the difference of the weighted means of the model and of observational fields. This performance metric was already considered by Taylor (2001) and Yokoi et al. (2011), who, however, did not apply the weighting (although it was already proposed by Taylor (2001)).

Finally, in order to be able to focus on relative performance between the four simulations, we normalize the RMSD and the overall mean bias by dividing through the average across the individual model simulations (model-mean, Eq. 23) similar to Reichler & Kim (2008) and Karpechko et al. (2010). This is different to Gleckler et al. (2008), who normalized their metrics by subtracting the model-mean-metric before dividing by the latter, and also different to Yokoi et al. (2011), who normalized the metrics by subtracting the model-mean and then dividing by the inter-model standard deviation. Although the two latter normalizations also qualify, again the straight-forward normalization is used for a better interpretability of the results:

$$norm = \frac{1}{N} \sum_1^N b. \quad (23)$$

A further possibility to graphically summarize how closely a set of modeled patterns matches observations is provided by the so called Taylor diagram, which was originally proposed by Taylor (2001) and used in many studies (e.g., IPCC, 2001; SPARC CCMVal, 2010) to judge the relative skills of many different models. Since then, it is routinely employed in comparison investigations (e.g. Jöckel et al., 2006; Gleckler et al., 2008). The Tay-

lor diagram is a polar grid plot where the radial coordinate refers to the standard deviation of the model (test) field:

$$\sigma_M = \sqrt{\frac{1}{IJK} \sum_i \sum_j \sum_k w_{ijk} \cdot (M_{ijk} - \langle M_{ijk} \rangle)^2}, \quad (24)$$

normalized to the standard deviation of the observed (reference) field:

$$\sigma_O = \sqrt{\frac{1}{IJK} \sum_i \sum_j \sum_k w_{ijk} \cdot (O_{ijk} - \langle O_{ijk} \rangle)^2}. \quad (25)$$

The angular coordinate is defined by the inverse cosine of the correlation R_M between model and observation which is defined as follows:

$$R_M = \frac{\frac{1}{IJK} \sum_i \sum_j \sum_k w_{ijk} \cdot (M_{ijk} - \langle M_{ijk} \rangle) \cdot (O_{ijk} - \langle O_{ijk} \rangle)}{\sigma_M \sigma_O}. \quad (26)$$

Thus, each model and each diagnostic will provide a distinct point on the diagram. The closer the position of this point to the reference position of the observation ($\sigma_M / \sigma_O = 1$, $R = 1$ and thus $\arccos(R) = 0$), the better the fit to the observation. The distance between this point and the reference position is thereby the *centred* root mean square difference $cRMSD_M$.

$$cRMSD_M = \sqrt{\frac{1}{IJK} \sum_i \sum_j \sum_k w_{ijk} \cdot \left((M_{ijk} - \langle M_{ijk} \rangle) - (O_{ijk} - \langle O_{ijk} \rangle) \right)^2}. \quad (27)$$

Note that the statistics given above are not independent, particularly, adding the centered $RMSD$ and the overall mean bias b quadratically gives the mean square difference:

$$RMSD_M^2 = b_M^2 + cRMSD_M^2. \quad (28)$$

The correlation R_M reaches its maximum value of 1 if the two fields have the same *pattern* of variation ($M_{ijk} - \langle M_{ijk} \rangle \propto O_{ijk} - \langle O_{ijk} \rangle$ for all i, j and k), however, it does not reveal whether the two fields have the same *amplitude* of variation (i.e. the proportionality constant between the variation patterns). This amplitude of variation is, however, determined by the

standard deviations σ_M and σ_O . Thus, the Taylor diagram contains all the information needed to compare the pattern and amplitude of variation of two fields, allowing to directly see which of them (the pattern or the amplitude) has a bigger share in the centred root mean square difference $cRMSD$.

The formulas employed in the presented thesis are the same as given by Taylor (2001), Jöckel et al. (2006) and Gleckler et al. (2008), apart from the weighting which, in order to make comparison to previous EMAC evaluations possible, is the same as used by Jöckel et al. (2006).

A schematic description of the Taylor diagram is given in the following:

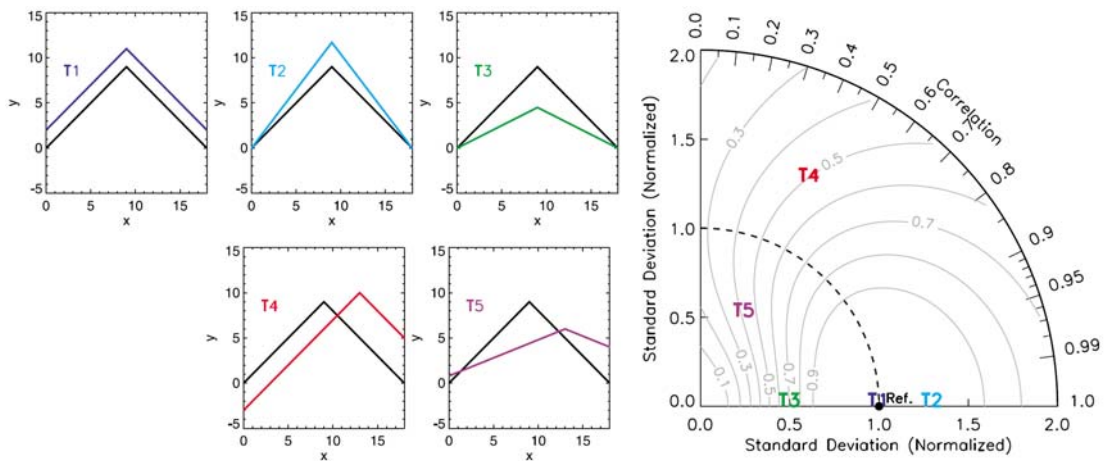


Figure 13. Taylor diagram: Illustrated are (left) examples of test (color coded) and reference fields (in black) and (right) their pattern statistics in the Taylor diagram. See text for explanation. From Hegglin et al. (2010), their Figure 2.

Figure 13 shows idealized different examples for the interpretation of a Taylor diagram. On the left side, different test fields (T1, T2, etc., colored) which are varying in amplitude and correlation (phase) and a reference field (black) are shown and plotted into the Taylor diagram (right).

T1: This test field is in phase with the reference field and has the same amplitude. Therefore, the correlation is 1 and the variation in the amplitude, represented by the normalized standard deviation, is 1. T1 is therefore found on the x-axis and the normalized standard deviation of value 1. The difference in the absolute values is not addressed by the Taylor diagram.

T2: This test field shows the same phase, but higher amplitude than the reference field. Therefore, the normalized standard deviation is higher than 1, but the correlation R still has its maximum value.

T3: Again, the reference field and the test field are in phase, but the amplitude of the reference field is lower. Therefore the normalized standard deviation has to be less than 1.

T4 and T5: Those fields have different phases and amplitudes, therefore the correlation decreases and the centered pattern RMSD increases.

Additionally to the already mentioned statistics, a so-called *t-test* or *Student's test* is performed on certain diagnostics. This test shows whether two univariate variables have an equal mean via a null hypothesis (Storch and Zwiers 1984). Different variations of this test exist. Here, the Welch's test is applied, as the standard deviations of the model and the observation may differ.

The difference of the mean is expressed in dimensionless units as:

$$t = \frac{\bar{\mu}_X - \bar{\mu}_Y}{\sqrt{\frac{S_X^2}{n_X} + \frac{S_Y^2}{n_Y}}}, \quad (29)$$

with $\bar{\mu}_X - \bar{\mu}_Y$ being the difference of the mean, S_X^2 and S_Y^2 being the variances and n_X and n_Y being the sample size. The degrees of freedom ν , which are associated with the variances, can be calculated as follows Storch and Zwiers 1984:

$$\nu = \frac{\left(\frac{S_X^2}{n_X} + \frac{S_Y^2}{n_Y}\right)^2}{\frac{\left(\frac{S_X^2}{n_X}\right)^2}{n_X - 1} + \frac{\left(\frac{S_Y^2}{n_Y}\right)^2}{n_Y - 1}} \quad (30)$$

The hypothesis is then tested by comparing the critical values of the t-distribution with ν degrees of freedom and a chosen level of significance with the computed t-value.

The above mentioned statistics are used on selected variables and diagnostics. A summary showing the specific choices of variables and domains is given in Table 4, Table 5 and Table 6.

5 Observational Data and the CCMVal-Diagnostic Tool

The model evaluation strategy described in Chapter 4 has been implemented by extending the *Chemistry Climate Model Validation Diagnostic* (CCMVal-Diagnostic) tool (Gettelman et al., 2011, in prep.) and developing a new routine for the statistical assessment. In the following Section 5.1.1 further information about the CCMVal-Diagnostic tool is given and Section 5.1.2 describes the extension of the tool with new diagnostics that have been added as part of this thesis.

Section 5.2 describes the observations that were newly collected and processed for the use in the CCMVal-Diagnostic tool in this work. Observational data are essential for the evaluation of CCMs. Many different types of observational data are available today, including meteorological reanalyses, ground-based and aircraft measurements, ozonesondes, and satellite data. Particularly the availability of satellite data since the 1970s expanded the world wide observational records for the atmosphere. In this thesis a variety of different observations are used for model evaluation, which are described in this section. For most variables a reference dataset and an alternate dataset was chosen in order to estimate differences and uncertainties in observations.

5.1 Diagnostics and Performance Metrics Evaluation Tool for EMAC

5.1.1 The CCMVal Diagnostic Tool

The CCMVal-Diagnostic tool is written in Python and in *NCAR Command Language* (NCL). It has a modular structure based on a main Python script which calls a number of functions specifying variables, diagnostics, models and observations (Figure 14). The tool is designed to compare models among each other and to observational data. One or more diagnostics and variables can be chosen at once. The code produces postscript figures and output in netCDF format containing time series and climatological data of the chosen variable(s) (Gettelman et al., 2011, in prep.).

The main script (main.py) reads in climate model output which is converted into the CCMVal standard format. This standard format (Climate and Forecast (CF) netCDF) includes for example standard pressure levels, specific names for variables, specific names for the variable-fields (e.g. for 2d or 3d fields) and specific structure for the filename. The tool is designed to process model output in the CCMVal-2 data standard (Eyring et al., 2008). A number of standard diagnostics have already been included, most of them based on diagnostics of stratospheric evaluation as in Eyring et al. (2006). The model output used for a specific diagnostic is specified in the namelist, e.g. one or more models and the time-period for the evaluation for each model can be chosen. Additionally, the path to the model output directories is given. In the directory “diag_att”, another file specifies the diagnostics and variables to be looked at. Then, the corresponding program for the chosen diagnostic is called from the directory “plot_type”. In a next step, this program gets further information from the “var_att” directory, which specifies the processing. In this directory, a file for each variable exists, specifying e.g. observations, levels or latitudes to be used for the diagnostic. Finally, figures and netCDF output files are produced by the CCMVal-Diagnostic tool.

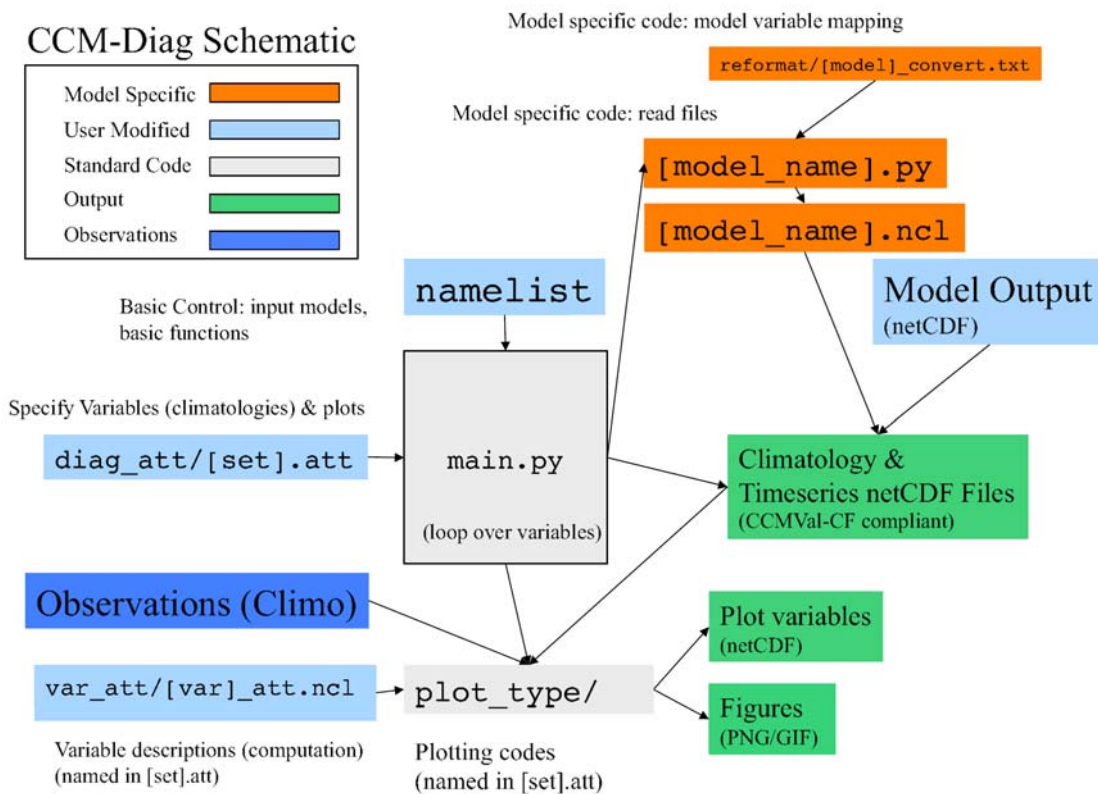


Figure 14. Schematic figure, showing the processes and components of the CCMVal-Diagnostic tool. From Gettelman et al. (2011, in prep.), their Figure 1.

5.1.2 Extension of the CCMVal Diagnostic Tool

The numerical codes for the calculation of diagnostics and the statistical assessment of this thesis have been implemented in the CCMVal-Diagnostic tool (Gettelman et al., 2011, in prep.) which is an open source tool designed for global chemistry-climate model evaluation (see Section 5.1.1). The first step was to extend the CCMVal diagnostic tool so that it could be used for the evaluation of EMAC. To do this, a routine that converts the EMAC output into the standard CCMVal CF (*Climate and Forecast*) compliant netCDF format has been implemented. For the use of EMAC in this thesis, a variety of new diagnostics were implemented into the tool, for the evaluation of the troposphere and basic climate parameters and some of the existing ones were modified (see Table 7). The original data files of the new observations (c.f. Section 5.2) needed for the model evaluation was processed according to the CCMVal-2 standard in order to be used within the CCMVal-Diagnostic tool.

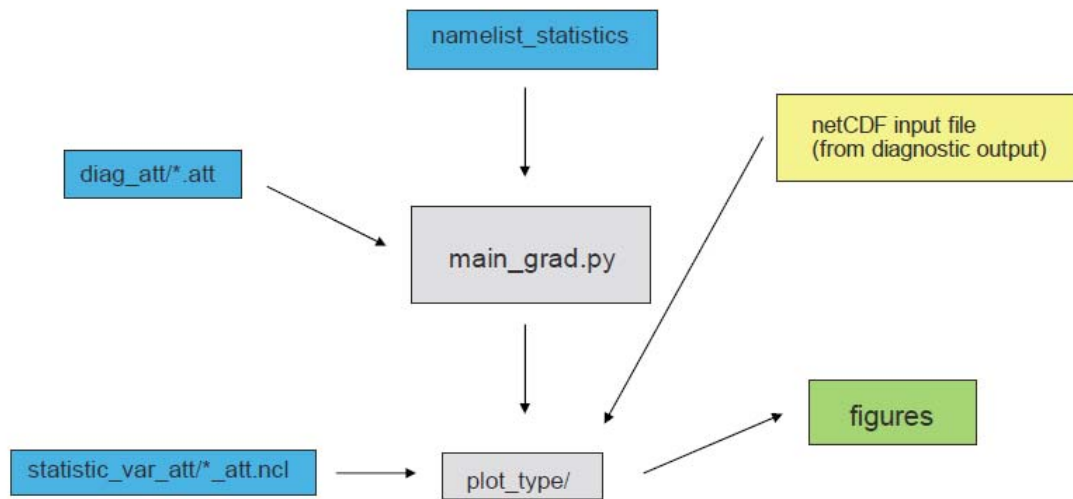


Figure 15. Schematic figure, showing the processes and components of the statistical routine implemented into the CCMVal-Diagnostic tool.

Next to additional diagnostics, a new feature for statistical evaluation of the model was added to the tool as part of this thesis. This routine is implemented within the original CCMVal-Diagnostic tool but is run independently. The “core” of the statistical routine is, similar to the original tool, a python script called “main_grad.py”, which calls namelists and specific information (such as latitudes or time-periods) from the “grading_var_att” folder for which the statistics are calculated. The data for the calculation is read from the netCDF files which were produced when applying the diagnostics of the original tool. In order to get these files, the netCDF-file output in the already existing diagnostics had to be modified and was newly implemented within new diagnostic codes. The produced netCDF files contain the model and observation names, and the absolute values and the standard deviation of the diagnostic variable and the specific attributes (levels, latitude, longitude, time).

Two new programs for the statistical evaluation exist by now. In the first program, the RMSD or the overall mean bias statistic is calculated (Section 4.2). It can be chosen in one of the input files which statistical measure should be used. Within the routine calculating the RMSD and the overall mean bias, a choice between two different types of figures/diagrams exists, each showing the RMSD or the overall mean bias of the selected diagnostics, but in different design. The second program calculates so-called Taylor diagrams (Taylor 2001). This diagrams can be shown either weighted (as done e.g. by Jöckel et al., 2010, see Section 4.2) or unweighted. A further description on the statistical methods mentioned here is given in Section 4.2.

Table 7 Extensions of the CCMVal-Diagnostic tool for the evaluation of EMAC in this thesis

Variable of interest /Statistic	Type of Plot	Extension
Basic climate parameters	Annual Cycle Panels	New
	Map Panels	
	Meridional Cross Section	
	Meridional Cross Section Differences	
Tropospheric ozone	Vertical Profiles (Emmons et al., 2000)	New
	Vertical Profiles of ozone (Tilmes et al., 2011)	
	Tropospheric column ozone	
	Overview maps for the chosen regions	
Stratospheric ozone	CO annual cycle (NOAA GLOBALview)	Modification of netCDF output-files Color-coding for the model simulations
	Already existing diagnostics for process-oriented evaluation of stratospheric ozone	
Quantitative Model Evaluation	Zonal mean total ozone for different seasons (Loyola et al., 2009)	New
	RMSD & Overall mean bias	New
	Taylor diagrams	New

5.2 Observational Data for Model Evaluation

As society and economies become more and more affected by climate variability and climate change, today's demand for information on climate is greater than ever. As pointed out by the IPCC AR4 (*Fourth Assessment Report*), changes of the climate system can be observed by monitoring the Earth. Hence, for future research as well as for politics, long-term, high-quality and continuous observations of the atmosphere, land and the ocean are needed. Without observations, the effectiveness of implemented policies to diminish climate change and predictions of future climate can not be evaluated (GCOS 2010).

A variety of different observational data sets have already been included in the original CCMVal-Diagnostic tool. However, these datasets couldn't be used for this work, as the time period of the model simulations between those used in the CCMVal project and the EMAC simulations used here differ. Therefore, new observational data were collected. In order to use the CCMVal-Diagnostic tool, these data had to be processed. This processing includes creating netCDF files, renaming variables and attributes according to the CCMVal standard and renaming the files themselves. For this processing, routines were written.

5.2.1 Observational Data for the Evaluation of Basic Climate Parameters

5.2.1.1 Temperature, Winds, Geopotential Height and Specific Humidity

For temperature, winds and geopotential height, meteorological reanalysis are taken as reference data. Meteorological reanalyses are assimilations of historical observational data that span an extended period of time, using a single consistent assimilation scheme and is therefore not affected by changes in the assimilation method (Dee et al., 2011). Reanalysis projects provide spatially complete and coherent records of atmospheric variables. Given the improvements of models, input data and assimilation methods, reanalyses have significantly improved in reliability, cover longer time-periods and have increased in spatial and temporal resolution (Dee et al., 2011).

Two different reanalysis datasets (ERA-Interim and NCEP/NCAR, see below) are used for the comparisons to simulated temperature, wind, specific humidity, and geopotential height. The differences between the climatologies derived from these fields are an indicator of the uncertainties in the meteorological analyses, although some products are known to be superior to others. ERA-Interim reanalyses are produced by the *European Centre for Medium-Range Weather Forecast* (ECMWF). ERA-Interim reanalysis data cover the period from 1989 to present (Dee et al., 2011). In the ERA-Interim reanalysis several weaknesses of the ERA-40 reanalysis⁵ were addressed, as e.g. the hydrological cycle or the quality of the stratospheric circulation. All observations used in the reanalysis are underlying quality control, selection steps (e.g. to sort out duplicate reports or data that is known to have large errors) and bias corrections (Dee et al., 2011). Therefore ERA-Interim is used as the main reference dataset for meteorological fields in this thesis.

In addition, the NCEP/NCAR reanalysis is applied in this thesis, which in a first attempt covered data from 1957 to the present (Kalnay et al., 1996) and was then extended back to 1948. Over the reanalysis period, developments in the observation system took place, particularly when satellite observations became available in the 1970s.

For specific humidity, as in Gleckler et al. (2008), observations from the *Atmospheric Infrared Sounder* (AIRS) experiment (Aumann et al., 2003) is used as our reference data set and ERA-Interim as alternate. AIRS data are available from the middle of 2002 to the middle of 2011. The data used in this thesis cover the years 2003 to 2010.

5.2.1.2 Radiation

For radiation the primary dataset is taken from the *Surface Radiation Budget Project* (SRB, GEWEX-news February 2011) and the alternate dataset is taken from the *Clouds and the Earth's Radiant Energy System* (CERES, Wielicki et al., 1996) experiment. The SRB dataset in its current version (version 3.0) covers the period from July 1983 to December 2007. The dataset provides surface and top of the atmosphere longwave and shortwave fluxes derived from a variety of satellite-observed parameters (e.g. cloud parameters and ozone fields, reanalysis meteorology). Quality checks have been made, e.g. surface fluxes have been compared to ground-based measurements (GEWEX-news February 2011, web2).

⁵ ECMWF 40 Year Re-analysis (ERA-40), covering the period from mid-1957 to mid-2002

The CERES experiment products include information about solar and longwave radiation from the surface and top of the atmosphere. The CERES experiment follows the *Earth Radiation Budget Experiment* (ERBE, Barkstrom, 1984). The first CERES instrument was launched in 1997. CERES data seems to have improved considerably compared to ERBE data, with a factor of 2-3 less error for radiative fluxes at the top of the atmosphere (web3, Wielicki et al., 1996). The aim of CERES is a long term record of radiative and cloud properties for climate analyses (web3, Wielicki et al., 1996).

5.2.2 Observational Data for the Evaluation Stratospheric Ozone

5.2.2.1 Datasets for Stratospheric Ozone

For the evaluation of total column ozone, the NIWA combined total column ozone dataset (Bodeker et al., 2005) is used as reference dataset and a combined dataset from the *Global Ozone Monitoring Experiment* (GOME) and GOME-2 as alternate. GOME was launched in April 1995 and deactivated in July 2011, its follow-up GOME-2 was launched on October 2006. The GOME dataset used here covers the period July 1995 to December 2010, however, only the data within 1996 to 2006 are used for the evaluation. The NIWA dataset is an assimilated database that covers the period from 1979 to 2005. It combines TOMS (*Total Ozone Mapping Spectrometer*), GOME and SBUV (*Solar Backscatter Ultra-Violet*) data. In order to obtain a global homogeneous dataset, ground-based data from the Dobson spectrophotometer network are used, removing differences between the individual input data or filling existing gaps.

As in Eyring et al. (2006), vertical and meridional profiles of climatological zonal mean ozone mixing ratios from different EMAC simulations are compared to measurements taken by the *HALogen Occultation Experiment* (HALOE) on board of the *Upper Atmosphere Research Satellite* (UARS), launched in 1991 (Russell et al., 1993). Model climatologies are formed for the period 1991-2005, based on extended data from Grooß and Russell III (2005). For the measurements, four infrared wavelengths are used. HALOE measurements range from 15 to 60-130 km altitude (depending on the species) and cover 80°S to 80°N in latitude within one year. Uncertainties of single profile HALOE retrievals have been estimated in several studies (Brühl et al., 1996, Harries et al., 1996, Park et al., 1996, Russell et al., 1996). For all measured species the accuracy of the HALOE retrievals decreases near the tropopause. In addition, sparse coverage of the polar regions increases the uncertainty in the HALOE climatologies there. In all intercomparisons the HALOE climatological mean and the interannual standard deviation (1σ) are shown.

5.2.2.2 Datasets for Key Processes that Determine Stratospheric Ozone

After quantifying deviations in stratospheric ozone to observations with the diagnostics described in Section 4.2.1, process-oriented diagnostics are applied in a second step. To do this, key diagnostics for process-oriented evaluation of stratospheric ozone that were defined by the CCMVal Activity (CCMVal, Eyring et al., 2005) were selected. In particular those diagnostics are selected that were defined as key diagnostics in the 2006 Scientific Assessment of Ozone Depletion (WMO 2007) and in Eyring et al. (2006). Several other diagnostics were applied to CCMs as part of the SPARC CCMVal Report on CCM Evaluation (SPARC CCMVal, 2010), but applying them all here is beyond the scope of this thesis.

This is subject to further work, once the CCMVal diagnostic tool (Gettelman et al., 2011, in prep.) is further developed.

To evaluate subtropical and polar stratospheric mixing barriers, the entry of water vapour into the stratosphere and tropical ascent, data from the HALOE experiment is used again, in this case methane (CH_4) and water vapour (H_2O). One of the aims of the HALOE experiment was an improvement in the understanding of stratospheric ozone depletion. For this reason, information on important species other than ozone was also collected.

The accumulation of halogenated compounds in the stratosphere over the past 40 years has been the primary driver of stratospheric ozone depletion. It is therefore important to assess how realistic is the representation of inorganic chlorine (Cl_y)⁶ in the CCMs, with a particular focus on polar spring Cl_y in the southern hemisphere. There are only limited observational data available for Cl_y (i.e. not enough to form climatology). As in Eyring et al. (2006), vertical and meridional profiles of simulated hydrogen chloride (HCl) with HALOE measurements. HCl is one of the principal components of inorganic chlorine (Cl_y). For the evaluation of Cl_y , not enough observations are available to form a global climatology. However, measurements in single years exist that can be used for assessing the simulations.

5.2.3 Observational Data for the Evaluation Tropospheric Ozone

5.2.3.1 Datasets for Tropospheric Ozone

For the evaluation of tropospheric column ozone a global climatology based on the *Aura Ozone Monitoring Instrument* (OMI) and *Microwave Limb Sounder* (MLS) ozone measurements for the period 2005 to 2009 (Ziemke et al., 2011) is used. The OMI/MLS gridded ozone climatology data are made available to the science community via the NASA Goddard Space Flight Center ozone and air quality website (<http://ozoneaq.gsfc.nasa.gov/>). As there seems to be no other climatology of tropospheric column ozone of comparable quality freely available, no alternate dataset is used for this quantity.

For the comparison of vertical profiles in the troposphere, a recently updated global climatology by Tilmes et al. (2011) is used, who constructed a climatology based on ozone sounding for the last 15 years that focuses on the troposphere and the lower stratosphere. This is an important extension to the Logan et al. (1999) climatology that was used by Jöckel et al. (2006), in particular for the time period that is evaluated here which covers the more recent years that are not included in the Logan et al. (1999) climatology. Vertical ozone profiles for 41 stations around the globe have been compiled and averaged for the years 1980–1994 and 1995–2009. The climatology provides information about the median and the width of the ozone probability distribution function, as well as interannual variability of ozone between 1995 and 2009, in pressure and tropopause-referenced altitudes. In addition to single stations, regional aggregates are included, combining stations with similar ozone characteristics. These regional aggregates for model evaluation and focus on the 1995–2009 time period are used here since this covers the time period simulated.

In addition, ozone from a collection of aircraft campaigns (Emmons et al., 2000) is used. These data are particularly valuable because in addition to ozone other species are measured at the same location and time, allowing a more detailed analysis of reasons why the

⁶ $\text{Cl}_y = \text{HCl} + \text{ClNO}_3 + \text{HOCl} + \text{ClO} + \text{Cl} + 2\text{Cl}_2\text{O}_2 + 2\text{Cl} + \text{OCIO} + \text{BrCl}$

model agrees or disagrees (see Section 3.3.2). These data are provided as global distribution and vertical profiles and were validated against ozonesondes and commercial aircraft measurements. Data files contain information on minimum and maximum values, the median, mean, standard deviation, and quartiles. The ozone data cover only selected regions of the Earth (corresponding to the location of the aircraft experiments) and time periods vary for each region (Emmons et al., 2000). Since this work was published already in 2000 the observational data do not exactly match the simulation periods. More recent campaigns were added to the dataset after publication, but no campaign later than 2001 is included in the dataset.

5.2.3.2 Datasets for Ozone Precursors and the Hydroxyl Radical

In addition to the evaluation of tropospheric ozone with aircraft campaigns and ozonesonde data, the performance of the model simulations are evaluated by comparing simulated ozone precursors and the hydroxyl radical (OH) to observations. For this evaluation, the Emmons et al. (2000) dataset is used again, which contains information about a variety of species in addition to ozone, including methane (CH_4), carbon monoxide (CO), nitrogen oxides (NO_x) and non-methane hydrocarbons (NMHCs).

For the evaluation of CO, observations are additionally taken as part of the NOAA GLOBALVIEW dataset. The goal of the GLOBALVIEW initiative was to get data products with a large spatial and temporal resolution. The data products, which include atmospheric constituents like CO_2 , CH_4 and CO, were meant to support carbon cycle modelling studies based on measurements from land-surface, ship, aircraft, and tower observations. GLOBALVIEW-CO is an observational dataset provided by the Cooperative Atmospheric Data Integration Project for Carbon Monoxide which is coordinated by NOAA (*National Oceanic and Atmospheric Administration*), ESRL (*Earth System Research Laboratory*) and, GMD (*Global Monitoring Division*). The data is derived from ESRL-measurements and therefore does not contain actual measurements. The processing includes smoothing, interpolation and extrapolation following Masarie and Tans (1995), resulting in an extended record. The data is updated annually. The dataset used in this thesis is the 4th annual update, 2009, covering the period from January 1991 to January 2009 (GLOBALVIEW-CO 2009).

6 Results and Discussion of Model Evaluation

As discussed in Section 4.1, a qualitative and quantitative evaluation of the four EMAC simulations described in Section 3 is performed. The results of this evaluation for basic climate parameters, tropospheric and stratospheric ozone and related processes are presented in Sections 6.1, 6.2 and 6.3, respectively.

6.1 Basic Climate Parameters

In the following subsections, the mean climate state in selected basic climate parameters such as temperature, wind, specific humidity, radiation, and geopotential height is evaluated in the four EMAC simulations, focusing primarily on global and regional scales of the simulated mean annual cycle. The choice of the tropospheric diagnostics and performance metrics follows those that were applied by Gleckler et al. (2008), with periods changed to represent 2000 conditions. Since the EMAC2-EVAL and the EMAC-QCTM simulations are both nudged by meteorological reanalysis up to ~ 100 hPa, a generally better agreement with meteorological reanalyses compared to the free-running timeslice simulations (EMAC-TS2000 and EMAC-ACCMIP) could be expected. However, since the nudging is relatively weak and is restricted to the troposphere (see Section 3.2.1), differences could still occur.

To assess performance in the stratosphere, the tropospheric levels used by Gleckler et al. (2008), i.e. 850 hPa and 200 hPa, were extended with two additional levels at 30 hPa and 5 hPa. The same observational data are used as for the tropospheric levels and the same regions (e.g. global, tropics, northern and southern hemispheric extratropics) are evaluated.

The variables temperature and zonal wind are discussed more precisely than the other basic climate parameters as differences in these variables can be more directly related to differences in ozone. The other basic climate variables (meridional wind, geopotential height, specific humidity and radiation) are discussed with a focus of the performance of the different EMAC setups, mainly to investigate whether the overall mean climate is correctly simulated.

6.1.1 Temperature

6.1.1.1 Detecting Temperature Biases

In a first step, temperature is evaluated by investigating the annual cycle of climatological mean temperatures at the four selected levels 850, 200, 30 and 5 hPa (Figure 16) and the meridional cross-section of the annual mean temperature as differences of the EMAC-simulation to the reference data set (Figure 17). To address uncertainties in the observations, or in this case meteorological reanalyses, differences are also shown between the reference dataset (ERA-Interim) and the alternate dataset (NCEP). In Figure 17, only differences which are statistically significant at a 95% confidence level in the t-test (Section 4.2) are shown, while differences that are not significant at this confidence level are marked white.

At 850 hPa all EMAC simulations are in good agreement with ERA-Interim and NCEP/NCAR and lie generally within the interannual variability of the meteorological reanalyses, with the exception of EMAC-ACCMIP which shows a small positive bias (~ 1 K) in the tropical summer months (Mai, June, July, August). The annual cycle is reproduced

in all regions. The interannual variability is, as in the meteorological reanalyses, very small at this level (Figure 16).

At 200 hPa, all EMAC simulations have a cold bias of around 5 K in all regions compared to the meteorological reanalyses and are well outside the interannual variability. This bias is particularly pronounced in the tropics in the two nudged simulations, whereas the nudged simulations are in better agreement with ERA-Interim than the free-running timeslice simulations in the extratropics in both hemispheres. The annual cycle at 200 hPa on the other hand is well represented in all simulations, with the exception of the tropics.

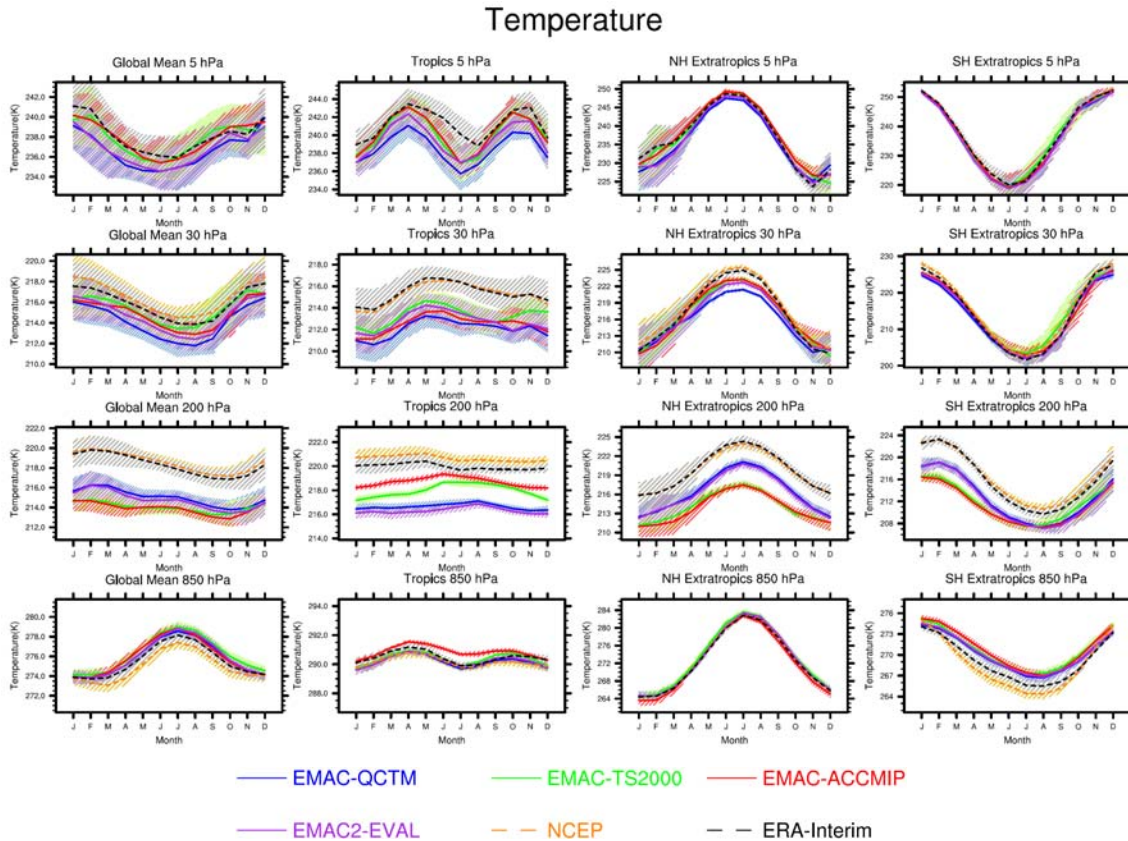


Figure 16. Annual cycle of temperature climatology at 5, 30, 200 and 850 hPa averaged globally, over the tropics (20°S-20°N), northern extratropics (20°N-90°N) and southern extra tropics (20°S-90°S) for different EMAC simulations in comparison to ERA-Interim and NCEP/NCAR reanalysis data. Grey shaded area indicates the ± 1 standard deviation. Note that the vertical scales are varying, to make differences between the EMAC simulations visible.

Stratospheric temperatures at 30 and 5 hPa (Figure 16, upper two rows) are within one standard deviation of ERA-Interim in the extratropics in all simulations, with the exception of the summer months in the northern hemisphere. In the tropics, a cold bias of around 2 K is simulated. The annual cycle is captured at these levels. At 5 hPa, EMAC-ACCMIP is in better agreement with the others in the tropics. In general the agreement looks much better in the lower troposphere, where the simulated temperature deviations from ERA-Interim are of

Annual Mean Temperature [K] (95% c.l.)

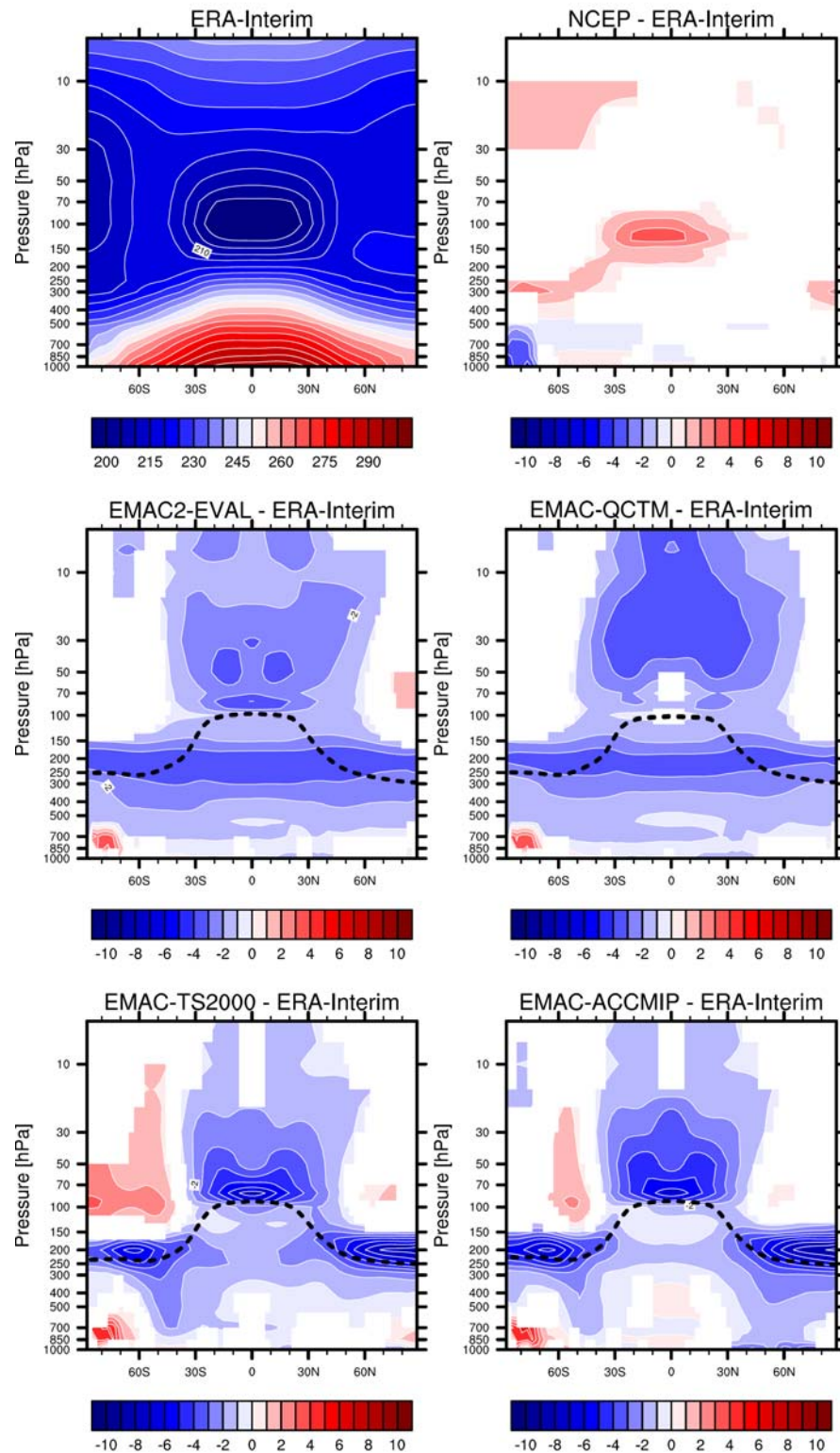


Figure 17. Annual mean zonally averaged temperature profile climatology for four different EMAC simulations in comparison to ERA-Interim and NCEP/NCAR reanalysis data. The upper left plot shows ERA-Interim absolute values; all other plots show differences between the NCEP reanalysis / the model simulations and ERA-Interim. The black dashed line in the model simulations shows the WMO tropopause height. Differences between the two fields that are not statistically significant according to the 95% confidence level are marked white.

similar magnitude than the differences between the two reanalysis datasets, which are anyway small and suggest therefore low uncertainties in the reference and alternate dataset.

Some of the already mentioned deviations from meteorological reanalysis can also be seen in the meridional cross-section of the annual mean temperature differences (Figure 17). The upper left plot, showing the total annual mean temperature values of the ERA-Interim reanalysis shows the common features of the temperature distribution with high temperatures at ground levels in the tropics, a decrease of temperature with height and towards the poles and a new increase with height towards the tropopause. Overall, the EMAC simulations capture these features, as can be seen by the small differences of about 1-2 K in most parts of the atmosphere.

Some differences exist, however, which are also seen in Figure 16. However, as only selected height levels are shown in Figure 16, Figure 17 additionally reveals some broader aspects which are:

- A warm bias in the tropics in the EMAC-ACCMIP simulation at 850 hPa.
- A warm bias in the polar southern hemisphere stratosphere (between about 100 hPa and 50 hPa) in the free-running simulations. This bias is particularly strong in the EMAC-TS2000 simulations. The nudged simulations on the other hand perform better at this height.
- Too cold temperatures in the tropical stratosphere. This bias is again particularly present in the free-running timeslice simulations.
- A cold bias in the extratropical lowermost stratosphere of the free-running simulations (EMAC-TS2000 and EMAC-ACCMIP). This feature is common to many of the CMIP3 and CCMVal models (IPCC, 2007; SPARC CCMVal, 2010). The nudged simulations show a continuing cold bias in the extratropical lowermost stratosphere and tropical upper troposphere. This underestimation of the temperatures is also seen in the 200 hPa level annual cycle (Figure 16).

These biases are further discussed in the following section.

6.1.1.2 Understanding Temperature Biases

The overestimation of the temperature at 850 hPa in the tropics in the free-running EMAC-ACCMIP simulation can be explained by the positive bias of the SSTs in the tropics in the prescribed dataset, which in the EMAC-ACCMIP simulation is taken from a historical simulation with the CMCC Climate Model (see Section 3.2.4).

The warm-bias in the southern hemispheric polar stratosphere in the free-running simulations is related to a too weak representation of the polar vortex and an underestimation of the ozone hole. The too weak polar vortex and the underestimation of the ozone hole are particularly prominent in the EMAC-TS2000 simulation, which will be further addressed in Section 6.3. In addition to the annual mean, the seasonal mean temperatures for this simulation are shown in Figure 18, confirming that this warm bias is mainly present in the JJA and SON seasons and thus related to the representation of the polar vortex and the ozone hole.

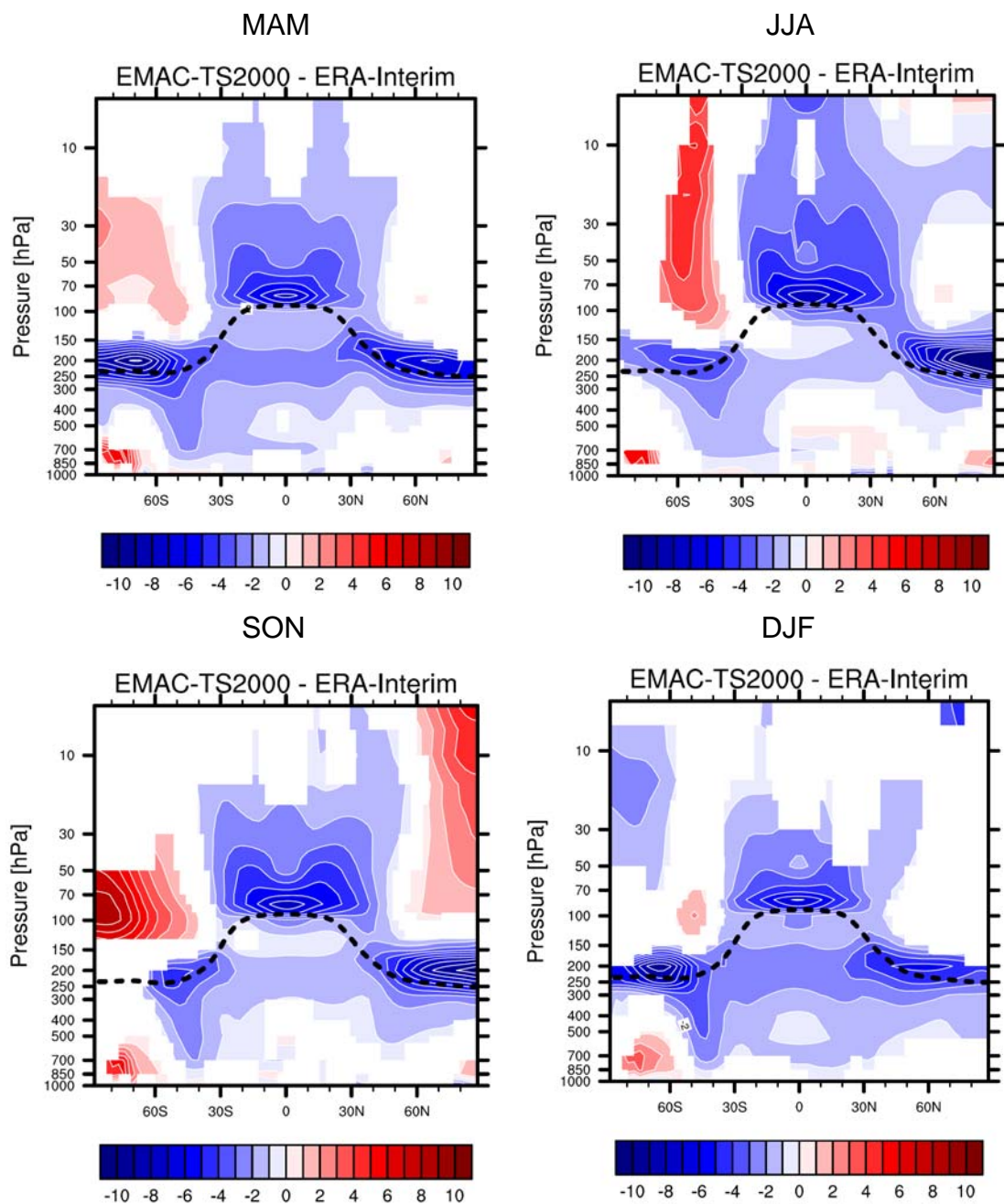


Figure 18. Seasonal mean zonally averaged temperature profile climatology for the EMAC-TS2000 simulations in comparison to ERA-Interim. The upper left plot shows the seasonal mean of MAM, the upper right of JJA. On the bottom the seasonal mean of SON (left) and DJF (right) is shown. The black dashed line in the model simulations shows the WMO tropopause height. Differences between the two fields that are not statistically significant according to the 95% confidence level, are marked white.

The cold bias in the lowermost extratropical stratosphere that can be seen in Figure 17 and Figure 16 is related to the wet bias (an overestimation of the water vapour concentrations) that is present in all four simulations. This wet bias is shown in Figure 19 which displays the annual cycle of water vapour in the EMAC simulations compared to HALOE data at 200 hPa in the extratropics. Water vapour is a greenhouse gas. In the stratosphere, greenhouse gases are known to have a cooling effect. Greenhouse gases absorb and emit infrared

radiation. In the stratosphere, more infrared radiation is emitted into space than upwelling IR-radiation from the troposphere is absorbed. This causes a net cooling. Overall, too high concentrations of water vapour in the extratropical lowermost stratosphere lead to too high infrared radiative cooling, which results into too low temperatures. This relation between the cold bias and the wet bias in the extratropical lowermost stratosphere has been shown in previous studies for example in Stenke et al. (2008) for the ECHAM4.L39(DLR) E39 model.

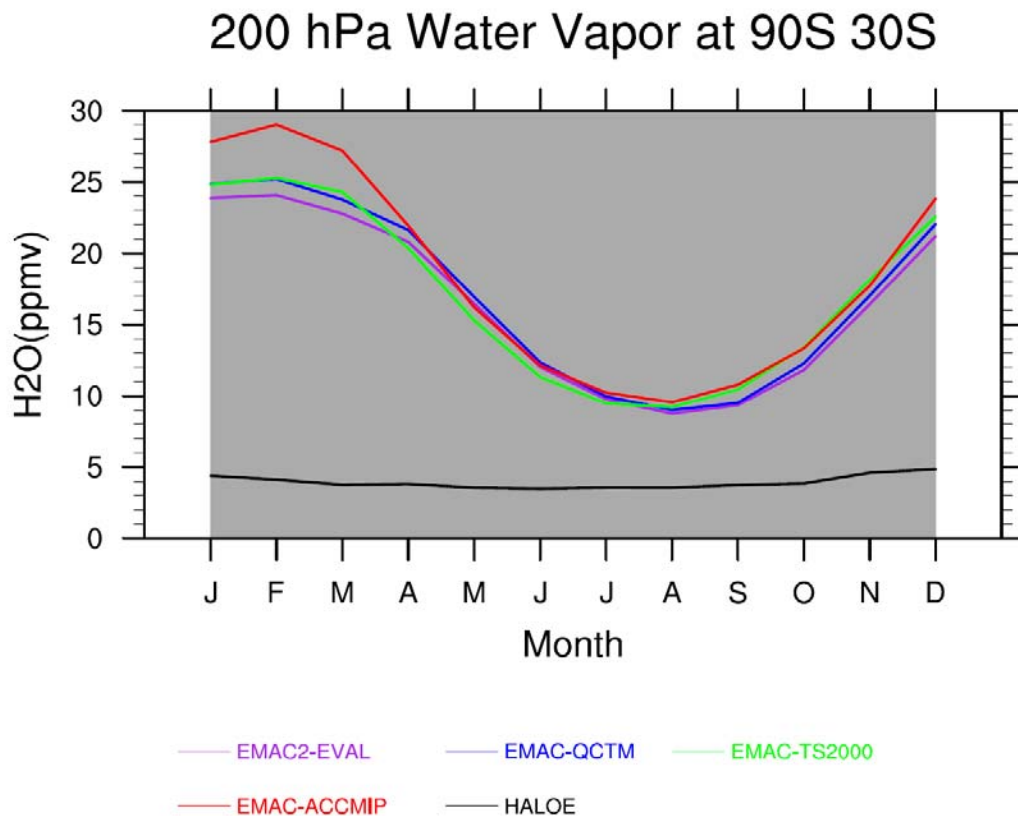


Figure 19. Seasonal variation of climatological means at 200 hPa in the southern hemisphere extratropics for water vapour for different EMAC simulations. Modeled water vapour fields are compared to the 1991-2005 water vapour climatology from HALOE.

The difference plots (Figure 17) and the plots of the annual cycle (Figure 16) also reveal biases in the temperature above the tropopause in the tropics. This bias has been examined already in Jöckel et al. (2006) and has been related to a slightly too strong Brewer-Dobson-Circulation (BDC) in the EMAC model, indicating deficiencies related to the wave forcing and adiabatic cooling/warming rates. This temperature bias in the lower stratosphere could be responsible for the shift in the tropical tropopause height in the two free-running simulations, which is shown in Figure 20. Here, the tropopause height is calculated following the definition of the World Meteorological Organization (WMO). According to this definition, the tropopause is defined as the lowest level at which the lapse-rate decreases to $2^{\circ}\text{C}/\text{km}$ or less, provided that the average lapse-rate between this level and all higher levels within 2 km does not exceed $2^{\circ}\text{C}/\text{km}$.

The temperature of the tropical tropopause layer (T_{TTL}) is an important aspect of model representation since it has strong implications for the water vapour distribution in the stratosphere. The lower-stratospheric water vapour mixing ratios are generally a function of

the model temperature near the tropical tropopause at 100 hPa, because low temperatures at the tropical tropopause cause condensation, dry the air and therefore less water vapour enters the stratosphere. Eyring et al. (2006) showed that model-model variations in tropical tropopause temperatures can indeed explain much of the variation in tropical lower-stratospheric water vapour in the CCMVal-1 simulations.

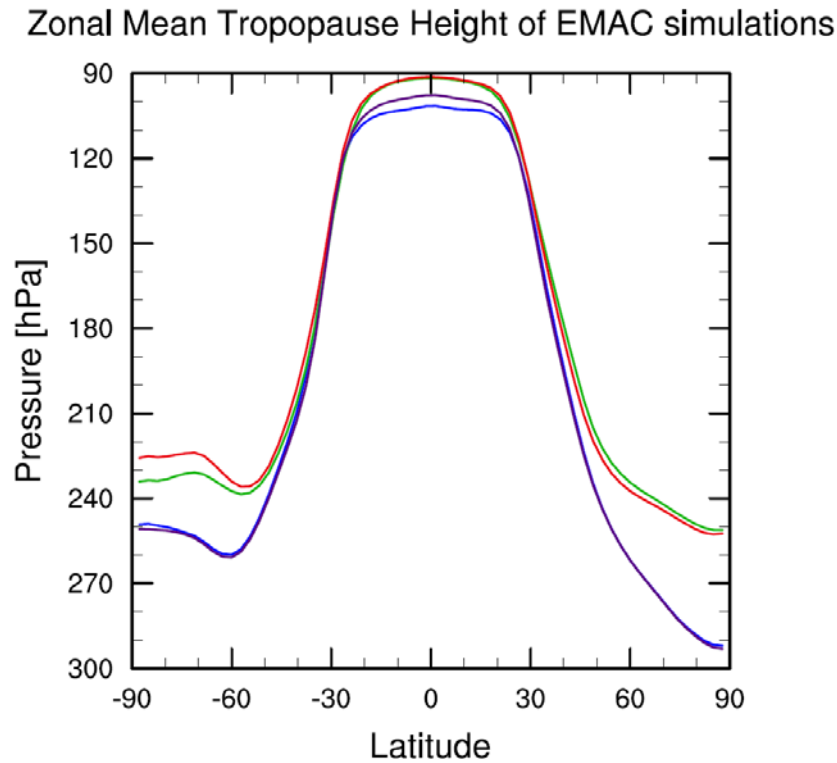


Figure 20. Tropopause height for the four EMAC simulations in comparison. The tropopause is calculated following the WMO definition, see details in the text.

This is similar to the behaviour in the four EMAC simulations, where smaller biases in temperatures compared to ERA-Interim in 100 hPa (EMAC2-EVAL and EMAC-QCTM) relate to smaller biases in water vapour at this level compared to HALOE observations (Figure 21). Not surprisingly, the nudged simulations EMAC2-EVAL and EMAC-QCTM represent the simulated annual cycle and absolute temperature values at 100 hPa remarkably well compared to ERA-Interim, while EMAC-TS2000 and EMAC-ACCMIP show about 1 to 4 K lower values and a reasonable annual cycle. Correspondingly the water vapour at 100 hPa is close to HALOE in the nudged simulations (within interannual variability except in September and October) and lower in the two free-running simulations throughout most of the year. The phase of the annual cycle water vapour cycle in the tropics at 100 hPa is well captured by all model simulations, but as for temperature, it is slightly weaker than ERA-Interim for the free-running simulations EMAC-TS2000 and EMAC-ACCMIP (Figure 21).

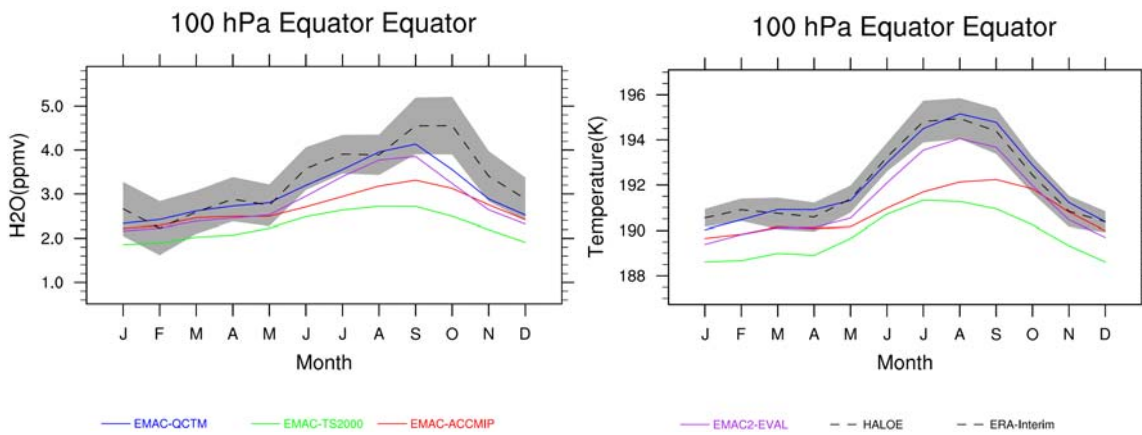


Figure 21. Seasonal variation of climatological means at 100 hPa at the equator for temperature (right) and water vapour (left) for different EMAC simulations. Modeled water vapour fields are compared to the 1995-2005 temperature climatology from ERA-Interim and the 1991-2005 water vapour climatology from HALOE.

6.1.2 Zonal Mean Wind

6.1.2.1 Detecting Zonal Mean Wind Biases

The zonal mean wind as simulated by EMAC is in good agreement with both reanalysis datasets at 850 hPa in the tropics and extratropics, where all simulations lie within the interannual variability of the reanalyses and reproduce the annual cycle very well (Figure 22). The nudged simulations (EMAC2-EVAL and EMAC-QCTM) perform remarkably better at this level.

The agreement is still good at 200 hPa, with the nudged simulations again performing better, especially in the tropics, where EMAC-TS2000 and EMAC-ACCMIP, on the other hand, slightly overestimate the winds by about 3 m/s. All simulations reproduce the annual cycle quite precisely at this level.

In the stratosphere, where the nudging is much weaker, all the simulations show a similar behaviour, and no significant improvement is obtained from the nudged simulations with respect to the free ones. On the contrary, the EMAC-QCTM simulation has some problems in reproducing the annual cycle in the tropics in particular at the 5 hPa level. The other simulations reproduce the annual cycle quite well and are within the interannual variability of the observations. In the NH extratropics, a small negative bias is found in winter for all simulations, in particular at 30 hPa.

Figure 23 and Figure 24 show the difference plots of the seasonal mean of the zonal mean wind in DJF and JJA. Generally good agreement between the EMAC simulations and ERA-Interim is simulated, and especially the summertime stratospheric easterlies are well represented in all simulations. Some weaknesses are found however in the simulations of westerlies, in particular:

- In DJF (Figure 23), the subtropical jet is underestimated at about 60°S in the free-running simulations (EMAC-TS2000 and EMAC-ACCMIP), while the nudged simulations capture the jet. However, the nudged simulations underestimate the polar night jet in the northern polar regions.

- In JJA, the westwind jet at 60°S is underestimated severely by the free-running simulations throughout the entire atmosphere, while the nudged simulations underestimate westerlies in the stratosphere.

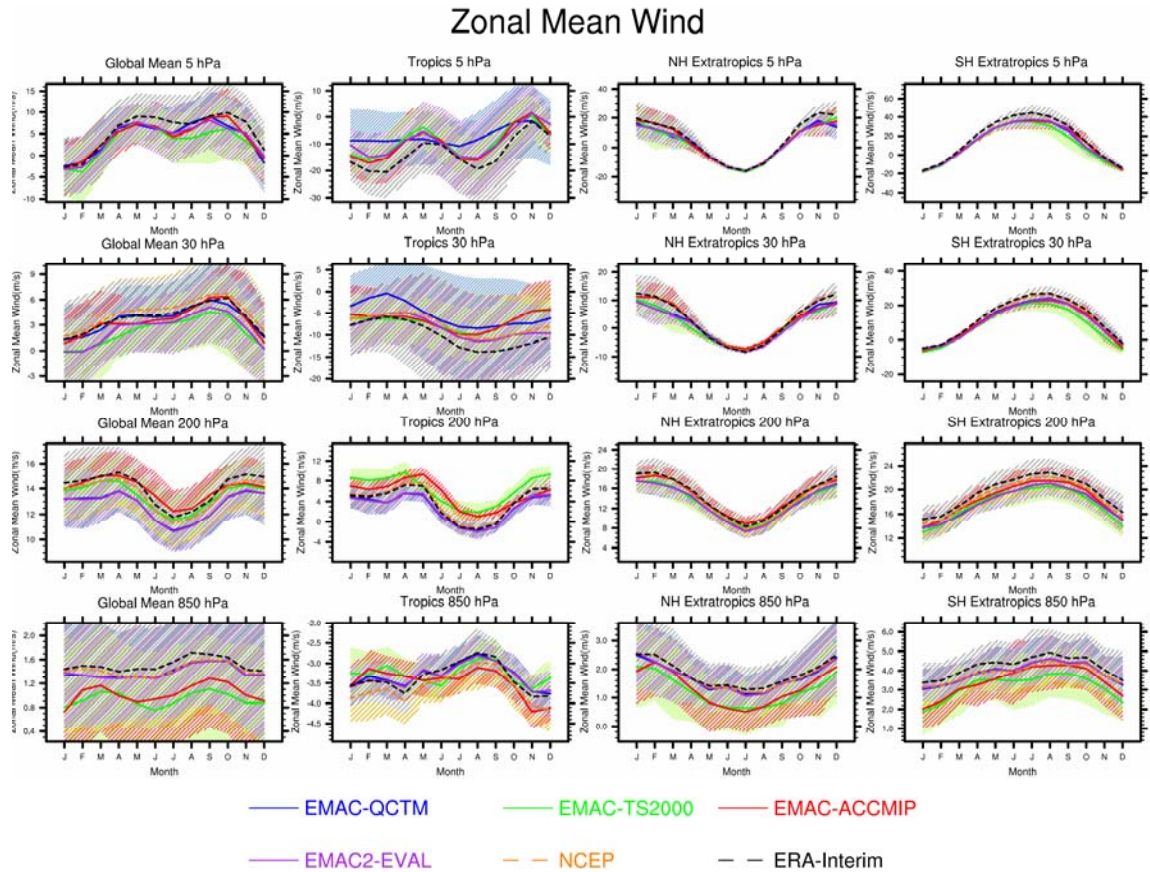


Figure 22. Same as Figure 16, but for zonal mean wind

6.1.2.2 Understanding Zonal Mean Wind Biases

In DJF, the underestimation of the polar night jet on the northern hemisphere in the nudged simulations might be related to a weak representation of the polar vortex in the northern hemisphere. The temperature profiles for DJF (not shown) for the nudged simulations show a warm bias in this specific region, which might be an indication for a too weak polar vortex. An explanation for the underestimation of the subtropical jet at 60°S by the free-running simulations is missing.

The underestimation of the west wind jets in JJA at 60°S in the free-running simulations (EMAC-TS2000 and EMAC-ACCMIP) might again be related to a too weak polar vortex. As shown in Section 6.1.1.2, the seasonal mean of the temperature (Figure 18) showed the warm bias in this region. Both, the weaker winds and the higher temperatures are an indication of an underestimation of the polar vortex. Other diagnostics related to the polar vortex will be shown in Section 6.3.

DJF Mean Zonal Mean Wind [m/s] (95% c.i.)

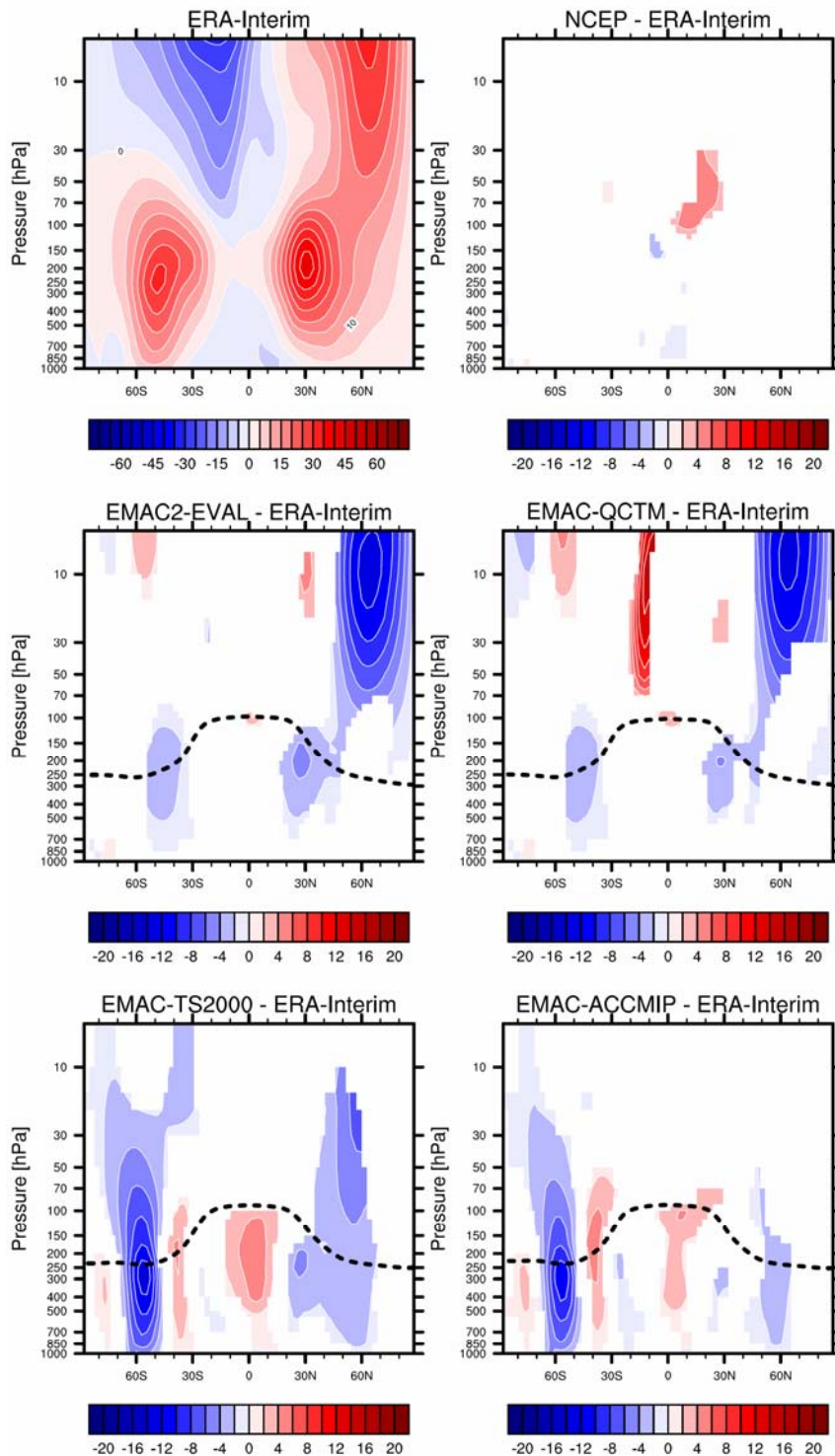


Figure 23. Seasonal (DJF) mean zonal mean wind profile climatology for four different EMAC simulations in comparison to ERA-Interim and NCEP/NCAR reanalysis data. The upper left plot shows ERA-Interim absolute values; all other plots show differences between the model simulations/NCEP reanalysis and ERA-Interim. The black dashed line in the model simulations shows the WMO tropopause height. Only differences which are statistically significant within a 95% confidence interval (t-test) are shown.

JJA Mean Zonal Mean Wind [m/s] (95% c.I.)

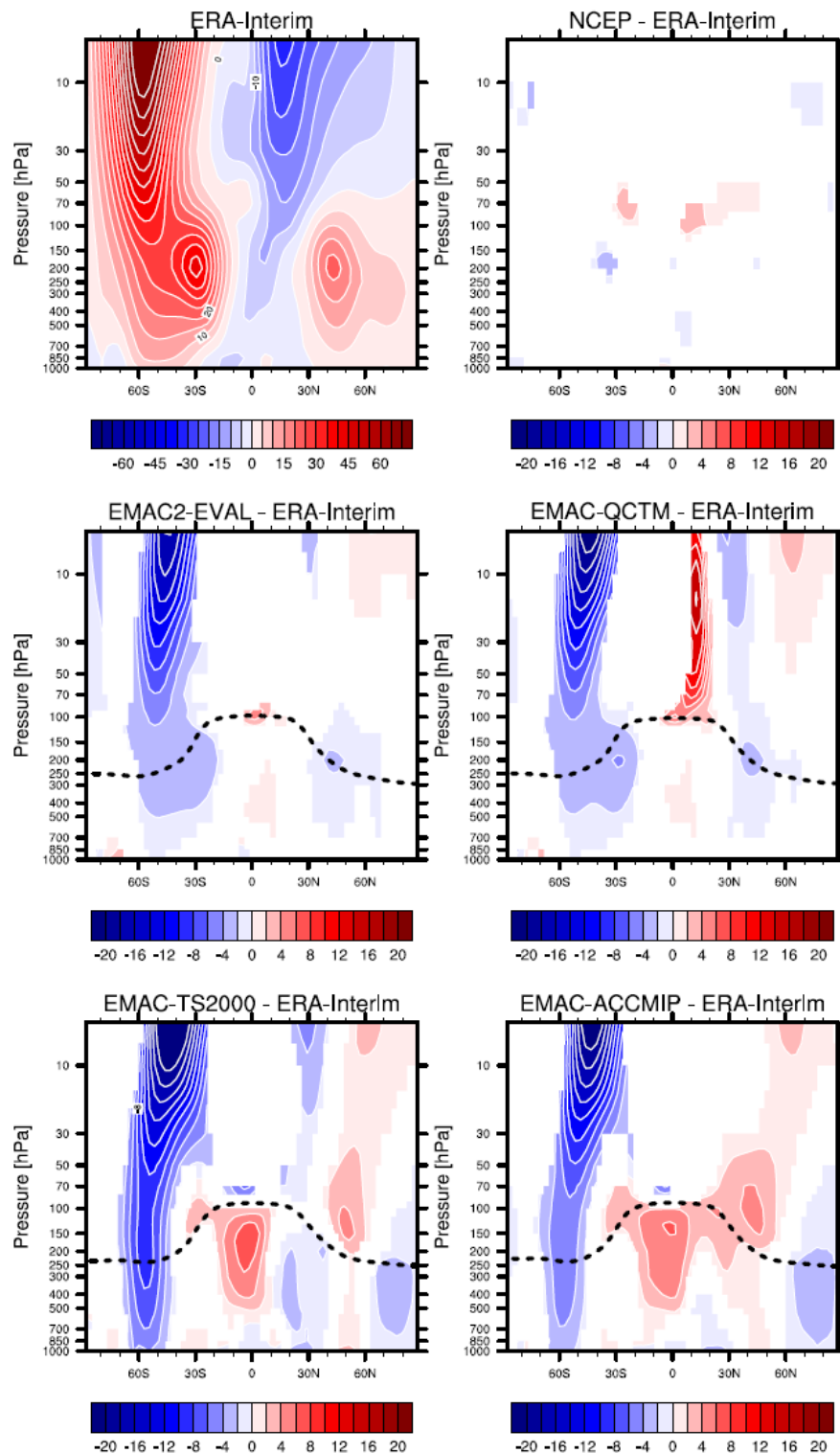


Figure 24. Seasonal (JJA) mean zonal mean wind profile climatology for four different EMAC simulations in comparison to ERA-Interim and NCEP/NCAR reanalysis data. The upper left plot shows ERA-Interim absolute values; all other plots show differences between the model simulations/NCEP reanalysis and ERA-Interim. The black dashed line in the model simulations shows the WMO tropopause height. Only values within a 95% significance interval (t-test) are shown for the difference plots. Values which are not significant are marked white.

6.1.3 Meridional Wind, Specific Humidity, Geopotential Height and Radiation

As mentioned before, meridional wind, specific humidity, geopotential height and radiation are evaluated mainly to assess whether there are some serious limitations in the simulation of the mean climate which in the case of radiation for example, could have been partly introduced due to the tuning of the model simulations. Therefore, in the following, the overall performance of these variables is summarized only briefly. One example showing the annual mean specific humidity profile climatology is shown in Figure 26, while for the latter variables similar figures can be found in the Appendix.

Overall, the meridional wind is similar to the reanalyses data in all simulations: all the major features are well reproduced by all model configurations. The meridional wind at the four selected levels (850, 200, 30, and 5 hPa) mostly lies within the interannual variability of the ERA-Interim reanalysis, with differences between ERA-Interim and NCEP reanalyses being in the same order or larger than differences to the model simulations (Figure A1).

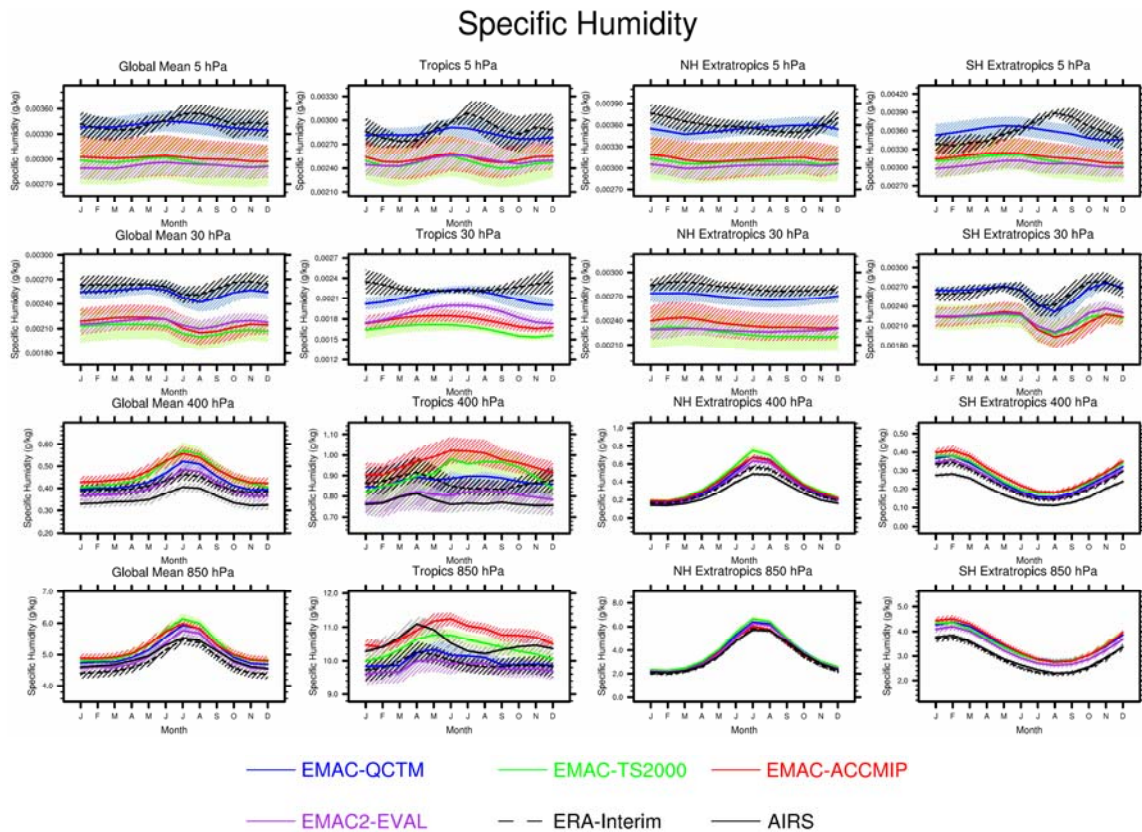


Figure 25. Same as Figure 16, but for specific humidity. Instead of the 200 hPa level, the 400 hPa level is shown, following Gleckler et al. (2008).

The annual cycle is mostly reproduced (Figure 25). Following Gleckler et al. (2008), the 400 hPa instead of 200 hPa level is shown which is more significant for the evaluation of specific humidity in the troposphere. In the extratropics the annual cycle shows a clear maximum in the summer months, following the change in incoming solar radiation during the year which affects water evaporation. In the tropics, on the other hand, the annual cycle shows a much smaller variation with time, since in this region the change in incoming radiation during the year is much less pronounced. The nudged simulations, which are driven by ECMWF operational analysis data, are generally closer to ERA-Interim than to AIRS

data, while the free-running simulations simulate monthly mean values closer to the AIRS data in the lower troposphere. The general pattern of the specific humidity profile climatology is characterized by a maximum over the equator at the surface, decreasing with latitude and altitude, and is reproduced by all simulations. This can be seen in corresponding difference plots in Figure 26. Small differences of 1-2% are found.

The comparison of simulated geopotential height and observations shows generally good agreement (see Figure A3 and Figure A4 in the Appendix), with relative differences of the order of 1-2%. The annual cycle is mostly captured. Differences of the same order, however, can be found also when comparing ERA-Interim with NCEP data, revealing some uncertainties also in the meteorological reanalyses.

Climatological mean maps of outgoing longwave clear-sky radiation at the top of the atmosphere, compared with SRB and CERES are shown in Figure 27. The total values of the observation (Figure 27, upper row, left) displays highest values in the tropics (about 300 W/m²) and two clear minima over the poles (around 150 W/m² at the South and 200 W/m² at the North). The EMAC simulations capture these features as can be seen in the differences plots (Figure 27), which indicate a better agreement of the model when compared to SRB than to CERES. For SRB, variations smaller than 20 W/m² are found everywhere on the globe, with a clear overestimation over the South polar regions (about 10 W/m², 5-10%), which is stronger in the free-running simulations and a underestimation over the highest mountain ridges (Andes and Himalaya, deviations higher than 30 W/m², 10%), which is stronger in the nudged simulations. For CERES, the difference pattern is very similar, but with slightly larger deviations.

The outgoing longwave (all-sky) radiation at the top of the atmosphere is compared again to SRB and CERES (Figure A5 in the Appendix). There are no significant differences among the EMAC simulations. The observation shows a maximum value over the tropics (250-300 W/m²) and two extended minima over the polar regions (about 100 W/m² for the South and 150 W/m² for the North). In general, the radiation values are lower than for clear-sky conditions (Figure 27), as expected due to the presence of clouds. The comparison with observations shows an excellent agreement of the EMAC simulations with both SRB and CERES (deviations mostly below 10-15 W/m²), which are also in agreement with each other, unlike in the clear-sky case. The nudged simulations perform slightly better than the free-running simulations, having only few localized spots of biases over the ITCZ and over the Himalaya (around 30 W/m², 10-20%). Biases of about 10-20 W/m² were also found for the CMIP3 models when compared to ERBE data, although some had very large deviation (up to about 50 W/m²), mostly concentrated in the tropics (IPCC 2007).

Another important quantity for the radiation budget evaluation is the reflected shortwave (all-sky) radiation (Figure A6 in the Appendix). The net shortwave radiation is primarily determined by solar incoming radiation and by the presence of clouds. The general pattern is therefore a combination of the variation of incoming solar radiation with latitude and season and of cloud cover. The EMAC simulations reproduce this pattern well. The observation shows the highest values (around 120-150 W/m²) over regions of high surface albedo or significant cloud cover (deserts, snow covered areas, Himalaya and Sahara), while the strongly absorbing ocean surface have lower values (60-80 W/m²). The comparison of EMAC simulations

Annual Mean Specific Humidity [kg/kg] (95% c.l.)

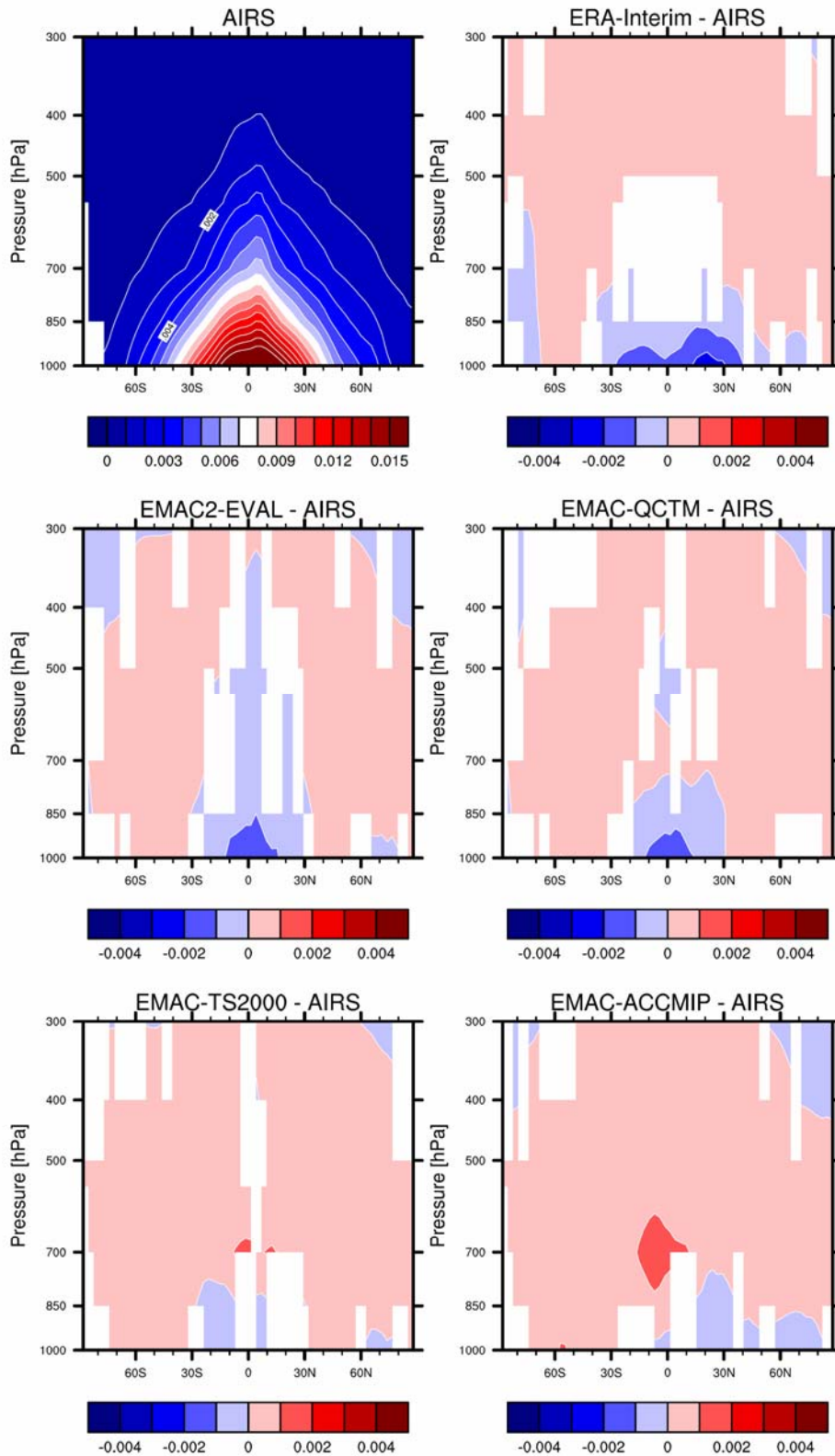


Figure 26. Annual mean specific humidity profile climatology for four different EMAC simulations in comparison to AIRS and ERA-Interim reanalysis data. The upper left plot shows AIRS absolute values; all other plots show differences between the ERA-Interim / the model simulations and AIRS. Differences between the two fields that are not statistically significant according to the 95% c.l. are marked white.

with SRB and CERES data shows that EMAC simulations overestimate shortwave outgoing radiation at mid-latitudes and in polar regions while it is underestimated in the tropics and subtropics. The EMAC simulations overestimate the reflected shortwave radiation particularly in northern higher latitudes (Alaska, North-East Russia), about 30-40 W/m^2 (10-20 %), whereas they underestimate it in the ITCZ, about 20-30 W/m^2 (20-30%). EMAC2-EVAL performs remarkably better than the others. Clouds are responsible for about half of the reflected radiation and cloud formation is one of the most difficult processes for global models in their current status (IPCC 2007), therefore most of the above deviations are likely attributable to uncertainties in cloud parameterizations, which are not further examined here.

Clear Sky TOA Outgoing Longwave Radiation [W/m^2]

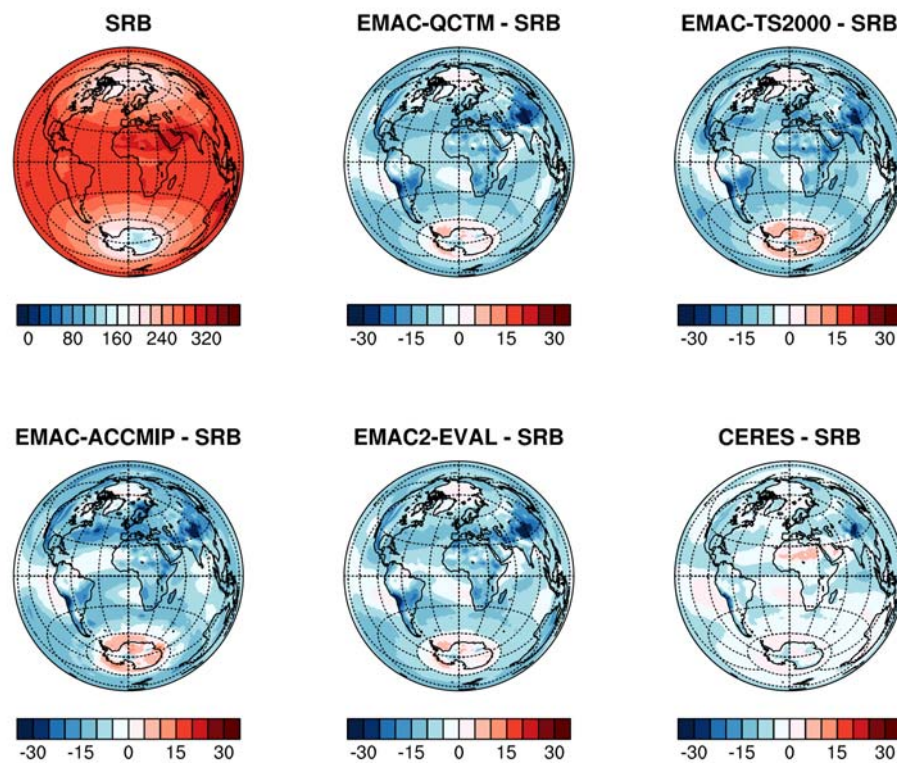


Figure 27. Annual mean values of clear sky outgoing longwave radiation at TOA [W/m^2] from SRB (upper left), differences from SRB data to CERES data and to the four EMAC simulations.

6.1.4 Quantifying Biases in Basic Climate Parameters

As described in Chapter 1, the overall mean bias, the root mean square difference and Taylor diagrams (see Section 4.2) are calculated to quantitatively assess how the ability of the four EMAC simulations to represent key features of observed climate compare to each other

Following Gleckler et al. (2008) the root mean square difference (RMSD) and overall mean bias in the annual cycle of different mean climate parameters at particular heights is calculated within four different domains (global, tropics, northern hemisphere extra tropics and southern hemisphere extra tropics). The results of the quantitative evaluation are displayed

in so-called portrait diagrams which are arranged such that the rows are labeled by the variable/diagnostic considered (see Table 4) and the columns by the four EMAC simulations (Figure 28). Each grid cell in the portrait diagram is split by a diagonal in order to show the model performance compared to the primary (lower triangle) and alternate (upper triangle) observation, if available. If no observation is available, the triangles are filled white. The corresponding diagnostic figures of the annual cycles in basic climate parameters and the map projections have been shown and discussed in Section 6.1.

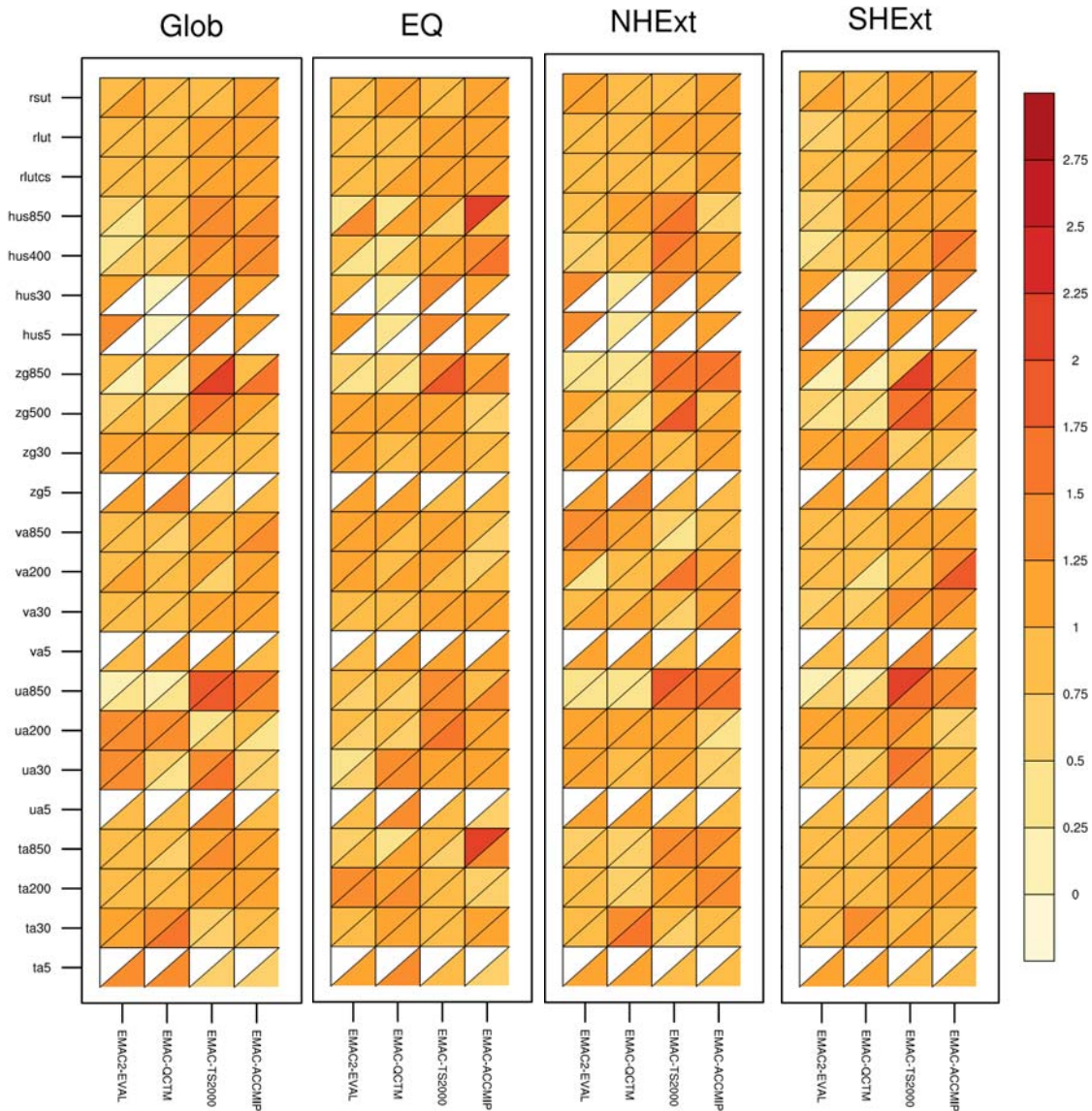


Figure 28. Portrait diagrams showing the root mean square difference (of the chosen basic climate parameters over the global domain, the tropics, and the northern and southern extratropics.)

For the interpretation of the figures shown in this section, note that due to the squaring, the RMSD gives positive values only, whereas the overall mean bias is not only sensitive to the absolute deviation from the observations, but also shows whether a model over- or underestimates the observations. Hence, the bias can be positive (overestimation) or nega-

tive (underestimation). The better the model performance, the smaller the absolute statistical values are.

When looking at temperature, at the four levels discussed in Section 6.1.1 (ta850, ta200, ta30 and ta5), nudged simulations (EMAC2-EVAL and EMAC-QCTM) perform slightly better than the two free-running ones (EMAC-TS2000 and EMAC-ACCMIP), but only in the lower levels, where the nudging is indeed strongest. In general, however, the four model simulations perform equally well, overestimating the temperature in the lower tropopause, and underestimating it at higher altitudes. The only exception, as discussed in Section 6.1.1, is a warm bias at 850 hPa in the tropics simulated by EMAC-ACCMIP. The difference in the performance with respect to the two observational datasets considered for the temperature (lower and upper triangles) is small, but still noticeable, revealing some uncertainties in the observations as well. The analysis with the Taylor diagram (Figure 30) confirms the good representation of the temperature in all model simulations, with all points lying above a correlation $R = 0.9$, showing that the phase of the annual cycle is very well captured. Deviations from the observation reference point (marked with OBS on the x-axis) are small, with the exception of ta200 in the global and tropical domains, which show a larger discrepancy, especially for the two free-running configurations (EMAC-TS2000 and EMAC-ACCMIP). In general, the extra-tropical regions are much better reproduced than the global and tropical domains by all model simulations, both in terms of correlation and normalized standard deviation.

The zonal mean winds are also better simulated by the nudged simulations than by the free-running ones, but only in the lower troposphere (ua850), as revealed by both RMSD (Figure 28) and overall mean bias diagrams (Figure 29). At this level, the wind speed is generally overestimated in the tropics and underestimated in the other regions. At 850 hPa, however, there are still large differences in the model performance with respect to the two observational datasets considered for the evaluation, which reveals potentially large uncertainties in the observational datasets. Such differences are significantly smaller at other levels, where also the performance of the different models is quite uniform. Zonal mean winds are generally underestimated in the extratropics and in the global domain, whereas they are overestimated in the tropics, especially in the stratosphere. These considerations are further supported by the Taylor diagram (Figure 30), which shows an excellent representation of the zonal mean winds in the extratropics by all model simulations: the value of the correlation is larger than $R = 0.9$ for all points in these domains and deviation from the reference point of the observations are mostly small, with the exception of the free-running simulations in the lower troposphere. In the global and tropical domain, variations in the phase and amplitude are larger than in the extratropics, but again the model simulations themselves perform similar. As for the extratropics, the 850 hPa wind speed (yellow dots) shows the lowest correlation and the largest deviation from the observations for the free-running simulations.

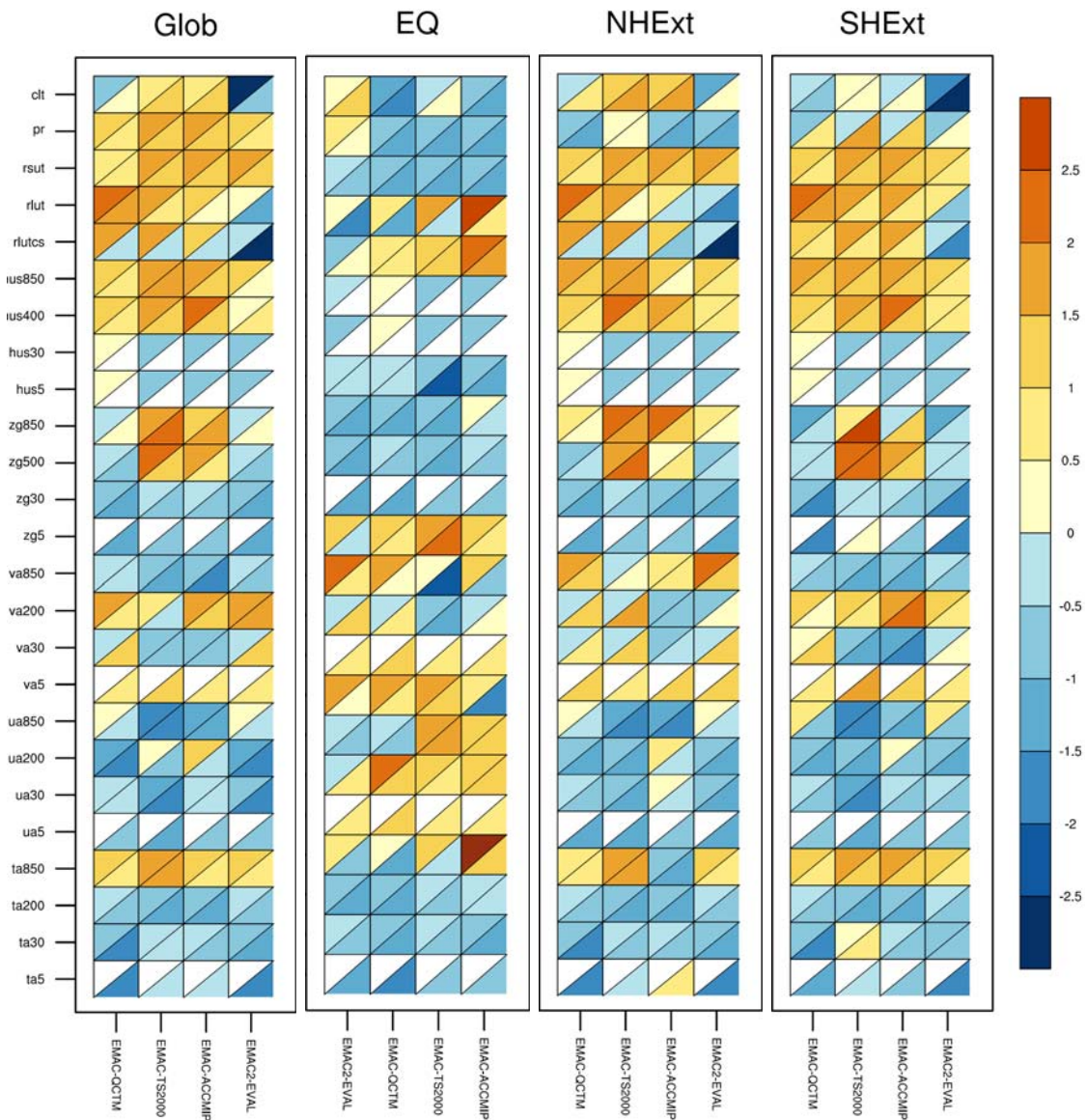


Figure 29. Portrait diagrams showing the overall mean bias (of the chosen basic climate parameters over the global domain, the tropics, and the northern and southern extratropics).

Concerning the remaining basic climate parameters, meridional wind (*va*) is generally well represented, with the nudged simulations performing slightly better. As revealed by the overall mean bias diagram, meridional winds are either overestimated or underestimated depending on the considered observational datasets, although deviations are generally quite small (light colors). The performance of the nudged simulations is also noticeably better when considering the geopotential height (*zg*), which is overall underestimated by all model simulations, with the exception of EMAC-TS2000, which overestimates this parameter in the extratropics. The specific humidity (*hus*) is remarkably better simulated by EMAC-QCTM than the other EMAC configurations, especially in the stratosphere, as it is clear from both the RMSD (Figure 28) and the overall mean bias diagrams (Figure 29). This could be a consequence of the decoupling of water vapour tendencies from chemical processes in this simulation, which could have an effect on the representation of specific humidity. Other model simulations perform equally well, with the nudged ones again looking

slightly better in the lowermost layers. Finally, radiation is equally represented by all model simulations in term of RMSD. Biases exist, with a general tendency of underestimating radiation in the tropics and overestimating it in the extratropics. EMAC2-EVAL shows an opposite behaviour and is characterized by larger deviations.

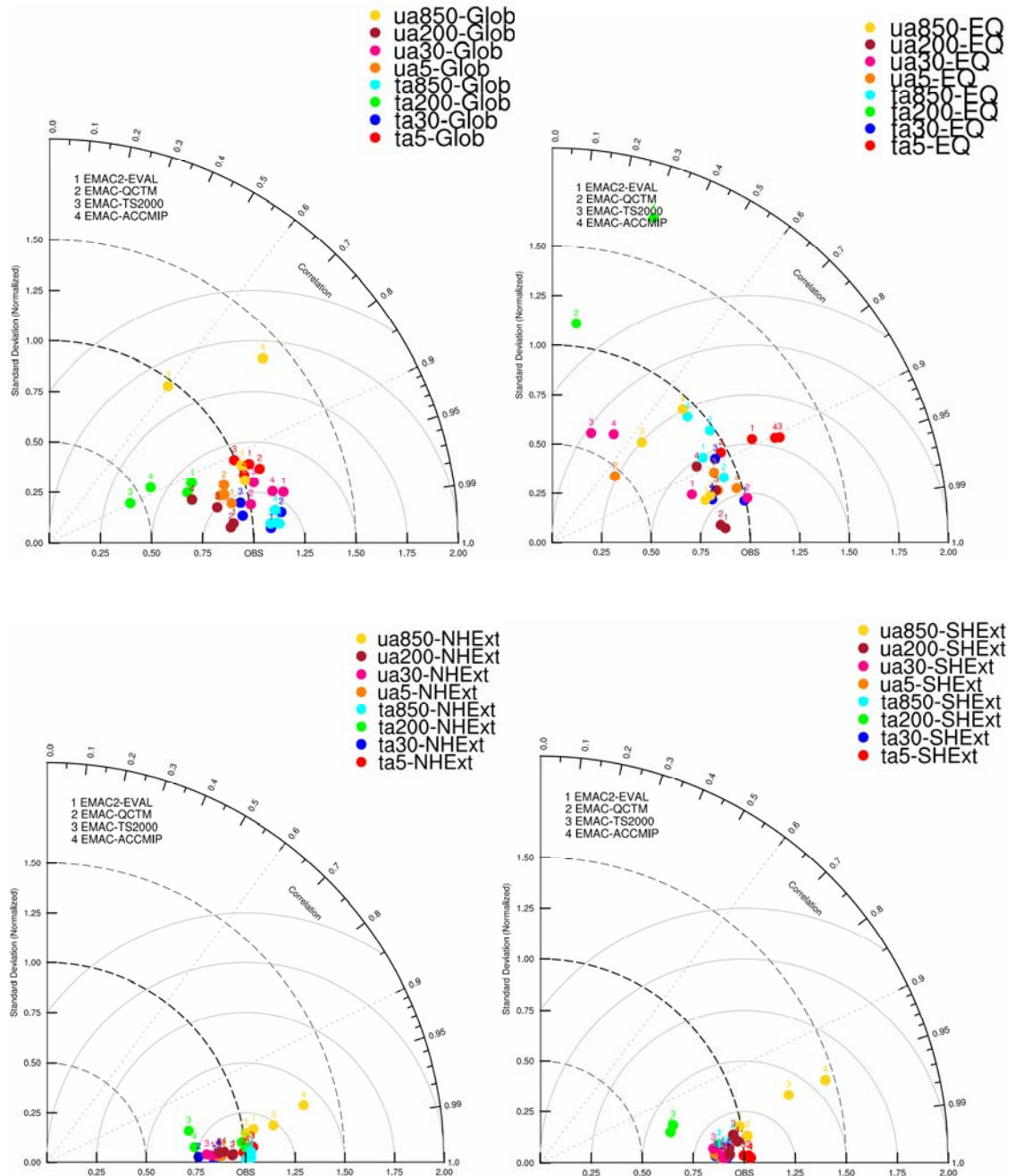


Figure 30. Taylor diagrams of selected basic climate parameters (temperature and zonal wind) over the four chosen domain and height-levels.

6.2 Tropospheric Ozone

A variety of different observations from satellite data (Ziemke et al., 2011), in-situ aircraft campaigns (Emmons et al., 2000), ozonesondes (Tilmes et al., 2011), and the NOAA GLOBALVIEW network (GLOBALVIEW-CO 2009) are used for the evaluation of simulated ozone and ozone precursors. These observations were described in more detail in Section 5.2. Although except for the satellite data the observations are localized, they still provide useful information on the model performance since they cover several years and can be used as a climatology. Figure 31 shows the areas covered by the observational campaigns and the location of measurement stations for the observations used in this chapter. The top panel shows ozonesonde stations from Tilmes et al. (2011): the locations and time periods were chosen in order to cover a variety of latitudes and to be as close as possible to the period simulated by the model. The middle panel shows regions of aircraft campaign data from Emmons et al. (2000) and the bottom one shows locations of NOAA GLOBALVIEW data stations. In order to compare our results to Pozzer et al. (2007), who evaluated organic species in a previous simulation with EMAC with a setup similar to EMAC2-EVAL to the Emmons et al. (2000) data, the same campaigns were chosen here.

6.2.1 Detecting Tropospheric Ozone Biases

Tropospheric column ozone values from the four EMAC simulations are compared to values derived from OMI and MLS instruments on board the Aura satellite averaged over the period 2005 to 2009 (Figure 32). Absolute values in the northern midlatitudes are slightly higher in the EMAC simulations compared to the OMI / MLS observations (as can be seen by comparing the middle row with the bottom-right panel of Figure 32). The calculation of tropospheric ozone column is sensitive to the tropopause height in the observations and in the model. In the OMI/MLS dataset, the vertically integrated MLS ozone profiles are subtracted from OMI total column ozone to derive the tropospheric column (Ziemke et al., 2011). The tropopause pressure separates tropospheric from stratospheric column ozone and is taken from NCEP using the WMO tropopause definition as in the EMAC simulations. If the tropopause is shifted towards too high (low) altitudes, this results into an overestimation (underestimation) of tropospheric column ozone, which could explain some of the differences between the observations and the EMAC simulations.

The pattern in the climatological mean on the other hand generally agrees well with observations, with lower values in the tropics and southern hemisphere than in the northern midlatitudes. The local maximum between Africa and South America, a region affected by biomass burning emission, is reproduced in all simulations although it is slightly underestimated by the EMAC-QCTM simulation and overestimated by all others. This is also visible in the annual cycle of the tropospheric column ozone (top row of Figure 32). Overall, the annual cycle is very well reproduced by the EMAC simulations (top row versus bottom-left panel of Figure 32), showing two distinct maxima during spring in the southern hemisphere and during spring/summer in the northern hemisphere. This seasonal increase in tropospheric column ozone is due to an increase of both photo-chemistry and stratosphere-troposphere exchange (de Laat et al., 2005, Ziemke et al., 2006). It varies among the EMAC simulations also because of the difference in emissions. Furthermore, single year emissions in the timeslice model simulations compared to transient emissions in the nudged and QCTM simulations lead to some differences in emission totals of ozone pre-

cursors (see Table 8 and Table 9), with subsequent impacts on tropospheric ozone formation.

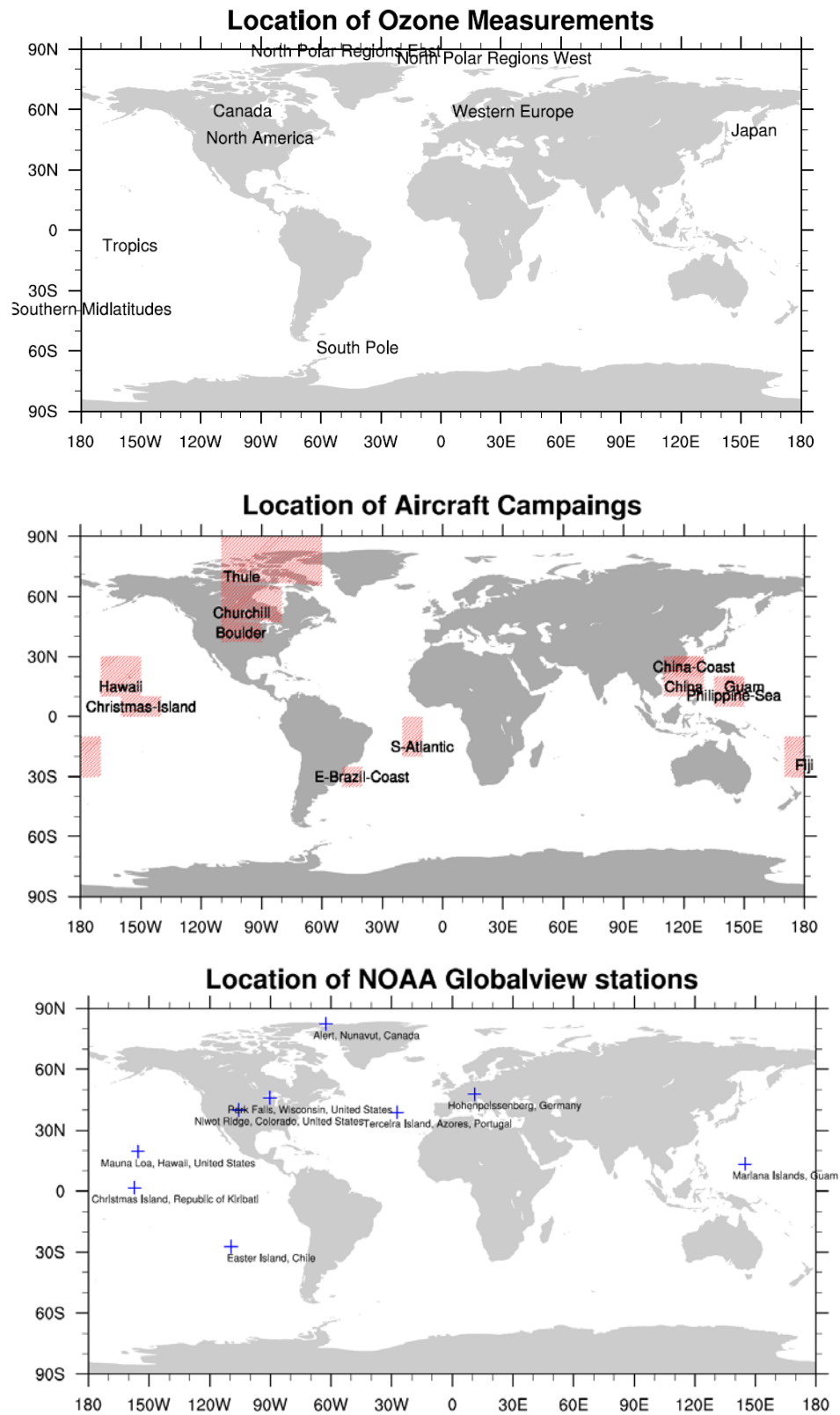


Figure 31. Locations of ozonesonde measurements (Tilmes et al. 2011, top panel), aircraft campaigns (Emmons et al., 2000, middle panel) and NOAA GLOBALVIEW stations (bottom panel) used for the model evaluation in this thesis.

To further evaluate ozone in the troposphere, the simulated vertical profiles are compared to ozonesondes data at selected stations from Tilmes et al. (2011) and to in situ measurements for selected aircraft campaigns from (Emmons et al., 2000).

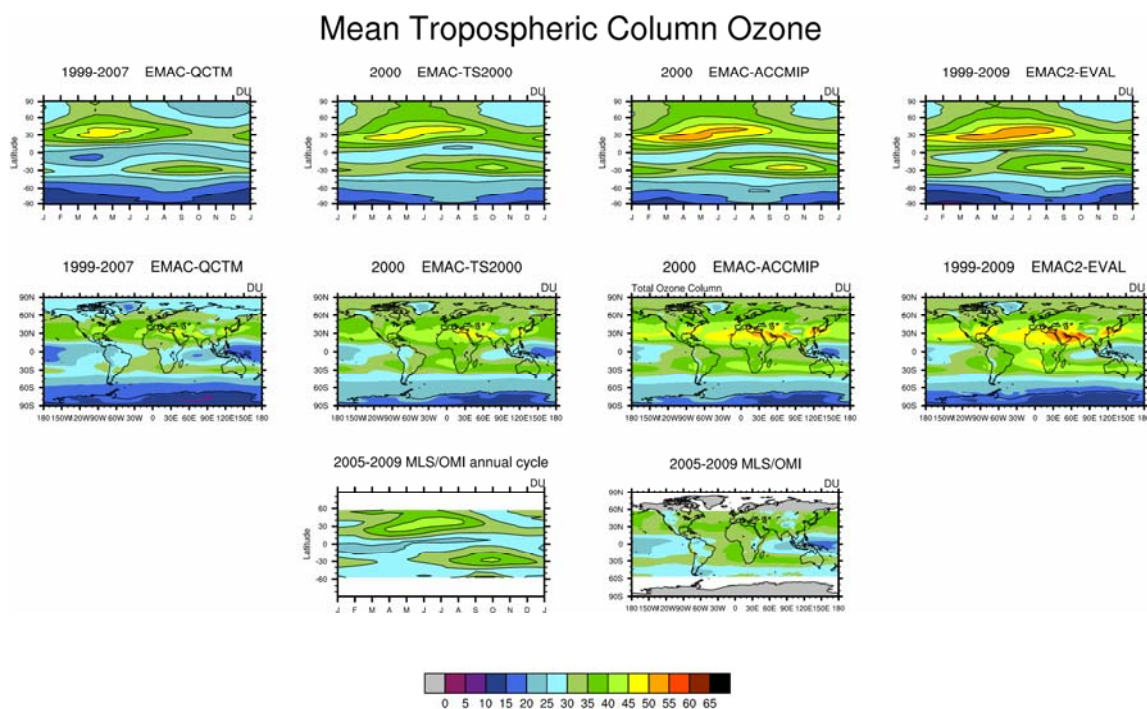


Figure 32. Tropospheric column ozone from the four EMAC simulations compared to MLS/OMI observations averaged between 2005 and 2009 (Ziemke et al., 2011). The first row shows the annual cycle of the tropospheric column at different latitudes in the four EMAC simulations. The second row the tropospheric ozone column in the four EMAC simulations. The last row contains the corresponding observations for the annual cycle (left panel) and for the tropospheric column (right panel).

The annual cycle of ozonesondes data according to Tilmes et al. (2011) is shown in Figure 33 for Western Europe and compared with the four model simulations. The general pattern is captured by EMAC, although a shift in the tropopause height during the year can be seen and the tropopause seems to be too low in this region compared to the observations. EMAC does not reproduce the higher ozone concentrations at the ground in the summer months. This might be related to lower concentrations of ozone precursors like CO or C₂H₆, especially in lower levels, as will be discussed in the next section. Figure 33 includes also a scatter plot (right column), comparing all points with their standard deviation. The points are plotted in red (purple) when the model overpredicts (underpredicts) the observations by more than one standard deviation and in blue otherwise. According to this color coding, the four model simulation are within one standard deviation of the observations for Western Europe.

Eight additional regions (not shown), namely Tropics, Canada, Japan, East and West North Polar regions, North America, Southern mid-latitudes and South Pole, each containing three or more ozonesondes stations and measurements from 1995 to 2009 were considered. Overall, there is good agreement between the ozonesondes measurements and the simulated ozone, but some deviations exist.

Western Europe

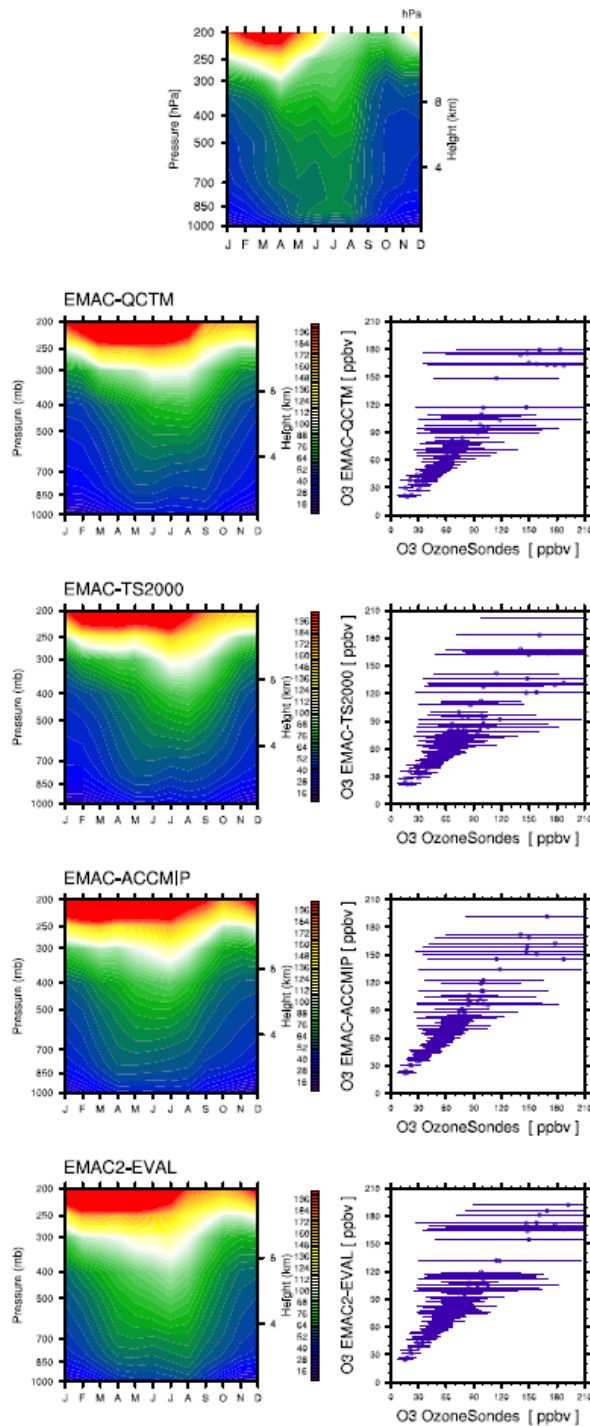


Figure 33. Comparison of tropospheric ozone (1000 hPa – 200 hPa) from different EMAC simulations with ozonesonde observations (Filmes et al., 2011) from Western Europe and Tropics. The first row shows the annual cycle in the observations. The other rows show the equivalent plot from the EMAC simulations (left column). The right column compares all points, with bars indicating the standard deviation in the observations: where the model overpredicts (underpredicts) the observations by more the one standard deviation, these points are plotted in red (purple) and then overplotted on the left column as solid (dashed) contours.

In particular, in the northern hemisphere, the EMAC simulations generally simulate ozone profiles similar to the observed ones, reproducing the main features: the low mixing ratios of ozone in winter and early spring between 1000-400 hPa, the rise of ozone mixing ratio in spring and summer months and the high values at 300-200 hPa. However, EMAC simulations slightly underestimate ozone mixing ratios above 250 hPa for the Canadian region and even more for Japan. In the North Polar Regions, differences are found between the East and the West. While EMAC simulations overestimate the ozone mixing ratios in 200-250 hPa in the East North Polar Region, they are underestimated in the West North Polar Region. Also, the rise in ozone mixing ratios in the summer months from the ground to the tropopause in the West North Polar Region is not reproduced by the EMAC simulations. This rise might be caused by the transport of polluted air masses from Western Europe to the Arctic. The model fails to reproduce ozone profiles in the Southern midlatitudes, in the South Polar Regions and in the Tropics, with severe underestimation of the ozone mixing ratios in the 300-200 hPa range and at the ground.

This section is concluded by showing the comparison of ozone vertical profiles with aircraft campaign data (Figure 34). Tropospheric ozone mixing ratios from a number of aircraft campaigns have been mapped onto a 5° longitude by 5° latitude grid by Emmons et al. (2000), with additional data from more recent campaigns (see <http://gctm.acd.ucar.edu/data>), including TRACE-P in 2001. For the present analysis, a subset of campaign to match the one discussed by Pozzer et al. (2007) for ozone precursors and other organic species were chosen.

In general, EMAC simulations show the same profile shape and ozone mixing ratios as the measured ozone with overall very good agreement. However, the comparison to in-situ measurements of vertical ozone profiles also reveals some deviations where the model simulations lie outside the 90% quantile of the mean of the observations. This is particularly the case for the measurements taken in remote areas at the Brazil-Coast and in Fiji at higher altitude levels.

Comparison with measurements from the TOPSE campaign during March 2000 at Boulder, Churchill, and Thule show excellent agreement, with model values mostly lying within the 90% quantile of the mean of the observations at all altitudes. According to (Emmons et al., 2003), ozone mixing ratios in these regions are mainly driven by photochemistry through the spring months. This comparison therefore reveals a good representation of the photochemical reactions by the model.

The PEM-Tropics campaign (1996) was a mission which provided the first detailed data on atmospheric composition over the South Pacific during the dry season (Hoell et al., 1999). Comparison between the simulations and flights over Fiji shows larger variations amongst the four EMAC-simulations, compared to the other ozone profiles shown. From about 2-6 km, the EMAC simulations lie outside or at the lower limit of the 90% interval of the observations, with the EMAC-QCTM simulation being lowest. The difference among the EMAC simulations could be related to different emissions of precursors in this region.

The comparison with TRACE-A between September and October shows good agreement between the model simulations and the observations for the Brazil-Coast for lower altitudes (< 4 km), but EMAC simulates higher ozone mixing ratios than observed above

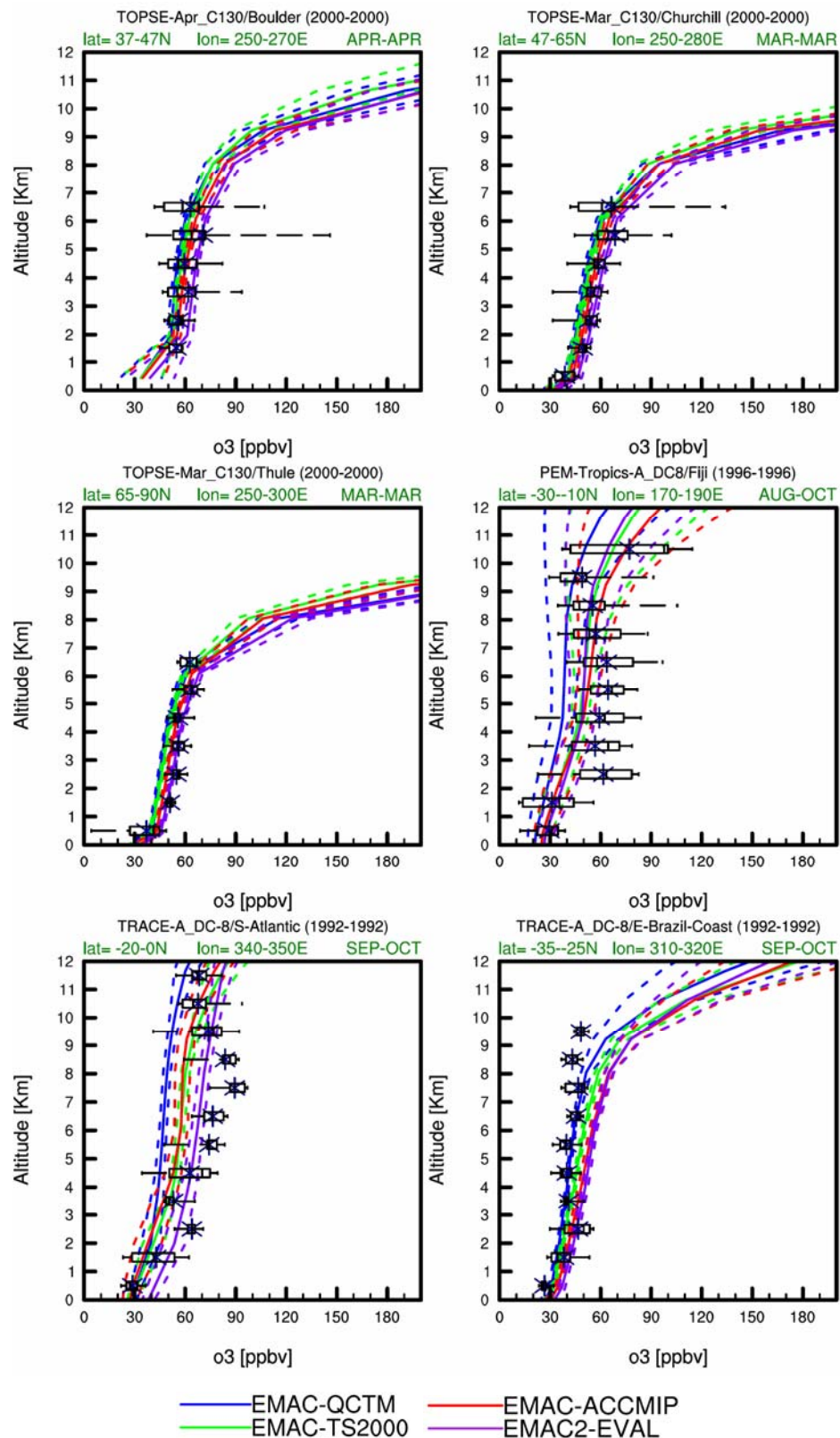


Figure 34. Vertical O_3 profiles from selected aircraft campaign observations by Emmons et al. (2000) and corresponding simulated values by the four EMAC simulations. Boxes and whiskers indicate the central 50% and 90% of the observations, respectively, with a vertical bar at the median and a star at the mean. The EMAC simulations are averaged over the same region as the observations. Mean and standard deviations over the same time period as the model runs are shown by the solid and dashed lines.

4 km. Here the EMAC-QCTM is closest to the observations. Larger variations for the simulations exist over the South Atlantic.

The EMAC simulations themselves show similar behaviour over the different locations, but in the EMAC2-EVAL simulation (purple) generally the highest ozone mixing ratios are simulated whereas in EMAC-QCTM generally the lowest mixing ratios are simulated. However, ozone precursor emissions vary substantially from year to year and the time periods between the EMAC simulations and the observations are not always the same. This could explain some of the disagreement between model and observations and indeed the three campaigns where the model performance appears to be not very good (Fiji, S-Atlantic and Brazil-Coast) have been conducted from 1992 to 1996, about a decade before the period simulated in the EMAC simulations considered here. Furthermore, these regions are quite sensitive to biomass burning emissions, which can vary quite strongly from year to year (see e.g. Van der Werf 2010).

To summarise the comparison with aircraft data, it can be concluded that there is overall very good agreement, with the model results mostly within 90% interval of the observational data. Larger deviations in some stations could be due to large difference between the time of the observations and the simulated period. It is worthy to note that exact agreement, especially near episodic sources of ozone precursors, cannot be expected from model simulations with relatively coarse spatial resolution and with climate conditions not fully constrained by meteorological re-analyses. Additional observations are needed before final conclusions for example on the chemistry scheme of the model can be made.

6.2.2 Understanding Tropospheric Ozone Biases

The aircraft campaign measurements from Emmons et al. (2000) are further used to evaluate ozone precursors like methane, nitrogen oxides, carbon monoxide and non-methane hydrocarbons (NMHCs), and to evaluate the hydroxyl radical (OH). In the following, the same regions as those used in Pozzer et al. (2007) are considered, although these are not always available for all species. In the latter case measurement campaigns that are closest to those used in the ozone evaluation are shown.

Methane

Vertical profiles of CH₄ mixing ratios in six selected regions (not shown) hardly reveal any disagreement among the EMAC simulations, which is not surprising, since the CH₄ lower boundary conditions are prescribed from the same observed data (AGAGE, Prinn et al. 2000) in all the EMAC simulations. The model generally agrees well with the observations, although it is not always within the the 90% quantil of the mean of the observational data. The differences in the mean values are of the order of 0.1 pptv and could be related to difference in the time periods between the model and the aircraft campaign or, more likely, to uncertainties in the data used to prescribe the lower boundary conditions.

Nitrogen oxides

Nitrogen oxides ($\text{NO}_x = \text{NO} + \text{NO}_2$) are, together with CO and NMHCs, important ozone precursors in the troposphere and serve as catalyst in the photochemical production cycles of tropospheric ozone (Jöckel et al. 2006). Vertical profiles for NO_x mixing ratios are presented in Figure 35. The vertical profiles simulated by EMAC show a similar shape to the observational data, being mainly characterized by a steep increase in the upper troposphere, and lie within the 90% observational interval in most cases. The NO_x profiles measured as part of the TOPSE campaign during March 2000 at Boulder, Churchill, and Thule show good agreement up to 7 km, while deviations exist for the PEM-Tropics and the TRACE-A campaign. This is similar to what was found for ozone in the above discussion. The spread among the mixing ratios simulated by the four EMAC simulations is very small in the lower and middle troposphere (up to about 7 km), whereas there are some important differences among the simulations in the upper troposphere. The EMAC-QCTM simulation, in particular, shows a different variation with altitude and simulates lower NO_x values in the upper troposphere compared to the other three model simulations, while EMAC-TS2000 and EMAC-ACCMIP usually simulate the highest mixing ratios. The higher NO_x emissions of EMAC2-EVAL in comparison to EMAC-QCTM are consistent with the results for ozone mixing ratios, given that NO_x is one of the main substances producing ozone via photochemical reactions in the troposphere. Between the two free-running simulations, EMAC-ACCMIP shows slightly higher NO_x concentrations, which was also noted for ozone.

Such differences among the different simulations cannot be explained with differences in the emissions, which are very similar (see Table 8 and Table 9), and would require a more detailed analysis of the involved chemical reactions, which is beyond the scope of this thesis.

Carbon monoxide

Another important species for tropospheric chemistry and for ozone formation is CO. The reaction between CO and the hydroxyl radical OH ($\text{CO} + \text{OH} \rightarrow \text{CO}_2 + \text{H}$) in the troposphere constitutes a sink of 90-95 % for CO and of about 41 % for OH (Logan et al., 1981; von Kuhlmann et al., 2003b). CO determines the oxidation capacity of the atmosphere by affecting the OH mixing ratios.

The evaluation of CO vertical profiles is shown in Figure 36. The EMAC simulations give similar results when compared to each other, with EMAC-ACCMIP having slightly higher values. This could be partly explained by the differences in total CO emissions, which are remarkably higher in this simulation because of the large contribution from biomass burning and traffic sources (Table 8). The model performs better, with deviations of the order of 10 ppbv, in remote locations like Guam, Philippine-Sea and Hawaii, where the effect of emissions is limited. In more polluted regions like China, the model simulations deviates significantly from the observations, especially in the lower and middle troposphere, while they improve in the upper levels, where again the effect of emissions is much smaller. A similar problem was pointed out also by the analysis of Pozzer et al. (2007) and they concluded that this is probably due to low fossil-fuel emissions in this region. However, the four simulations evaluated here still underestimate CO mixing ratios, although they have

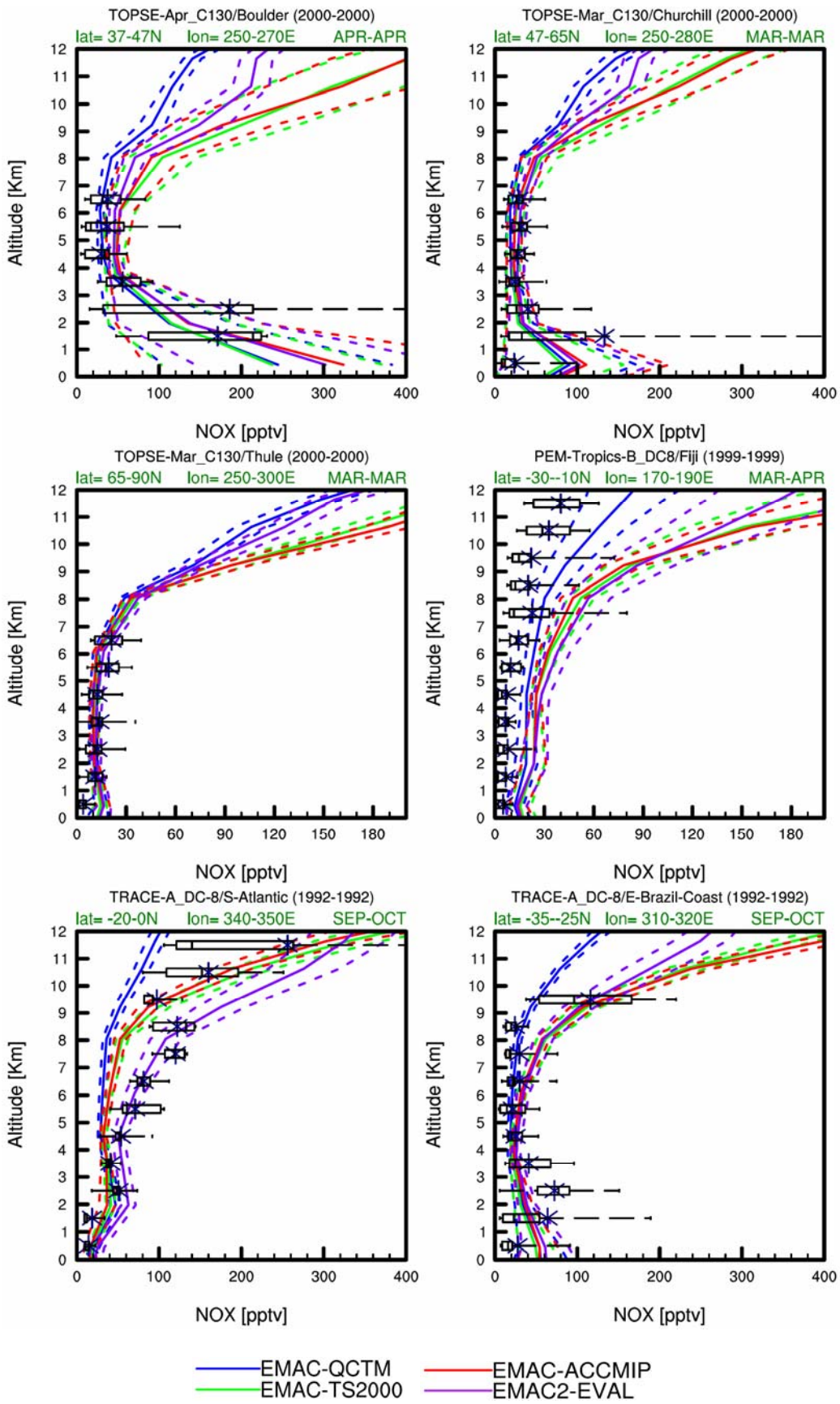


Figure 35. Similar to Figure 34, but for NO_x.

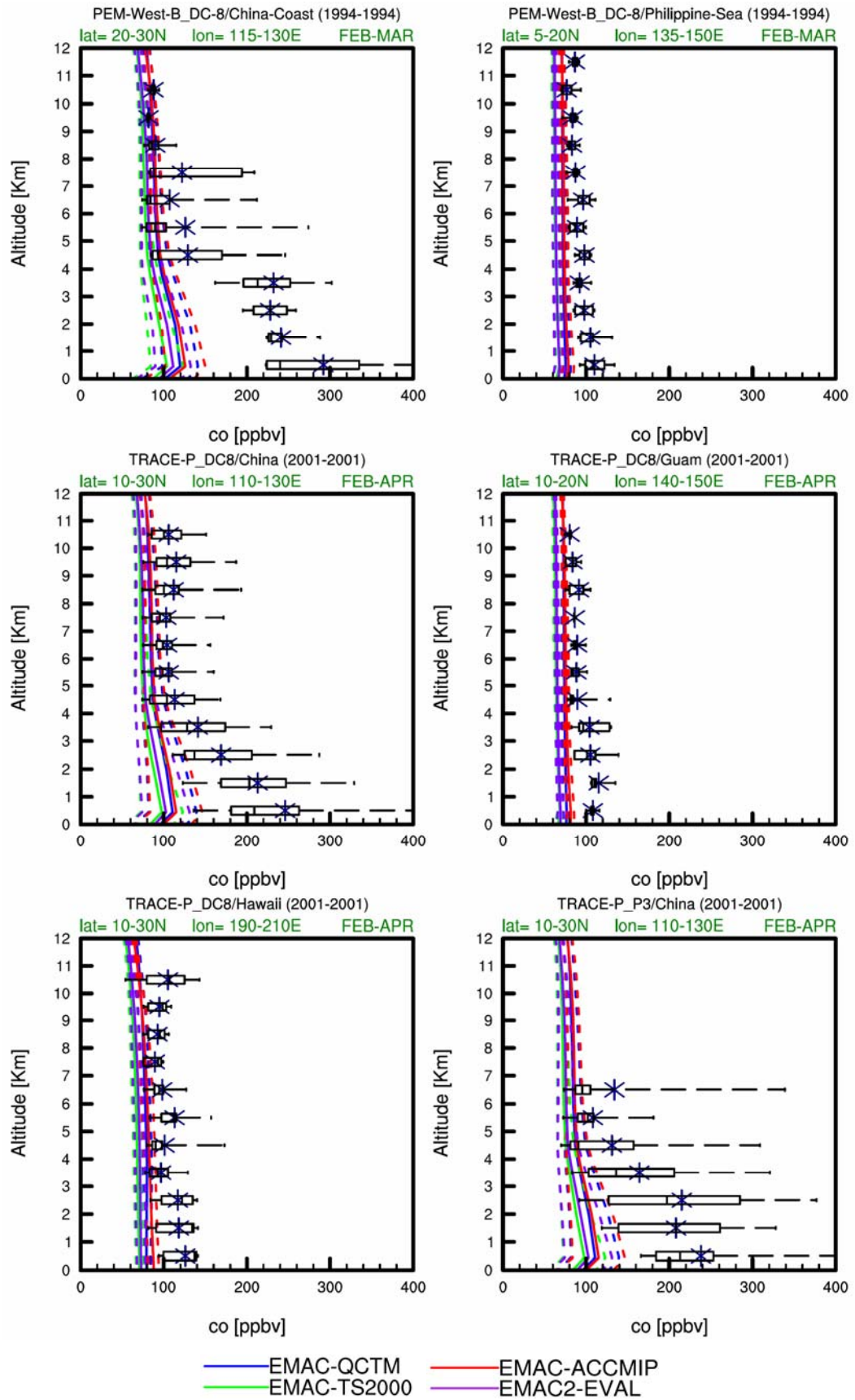


Figure 36. Similar to Figure 34, but for CO.

higher emissions from anthropogenic sources than Pozzer et al. (2007). Also the EMAC-ACCMIP simulation, which has twice as high CO emissions from traffic sources, does not perform better than the other simulations in this region. The representation of CO in South West Asia is a long-standing problem in many models and will require more extensive analysis in the future.

These considerations are further supported by the analysis of the CO annual cycle in various locations as observed by NOAA GLOBALVIEW (Figure 37). The EMAC-ACCMIP simulation again shows always a higher CO mixing ratio with respect to the other simulations. The annual cycle is reasonably well reproduced by all model simulations in all the 9 locations considered here, although a general underestimation of CO mixing ratios by the model is clearly visible. Also in this case, in remote locations, Christmas Island, Easter Island, Mariana Island and Hawaii, the agreement between model and observations is better than in more populated regions, Canada, Germany and United States, although important deviations are apparent also at the Azores site. Compared to Pozzer et al. (2007), the profiles show the same features, with higher variations between model simulations and observations in more polluted areas.

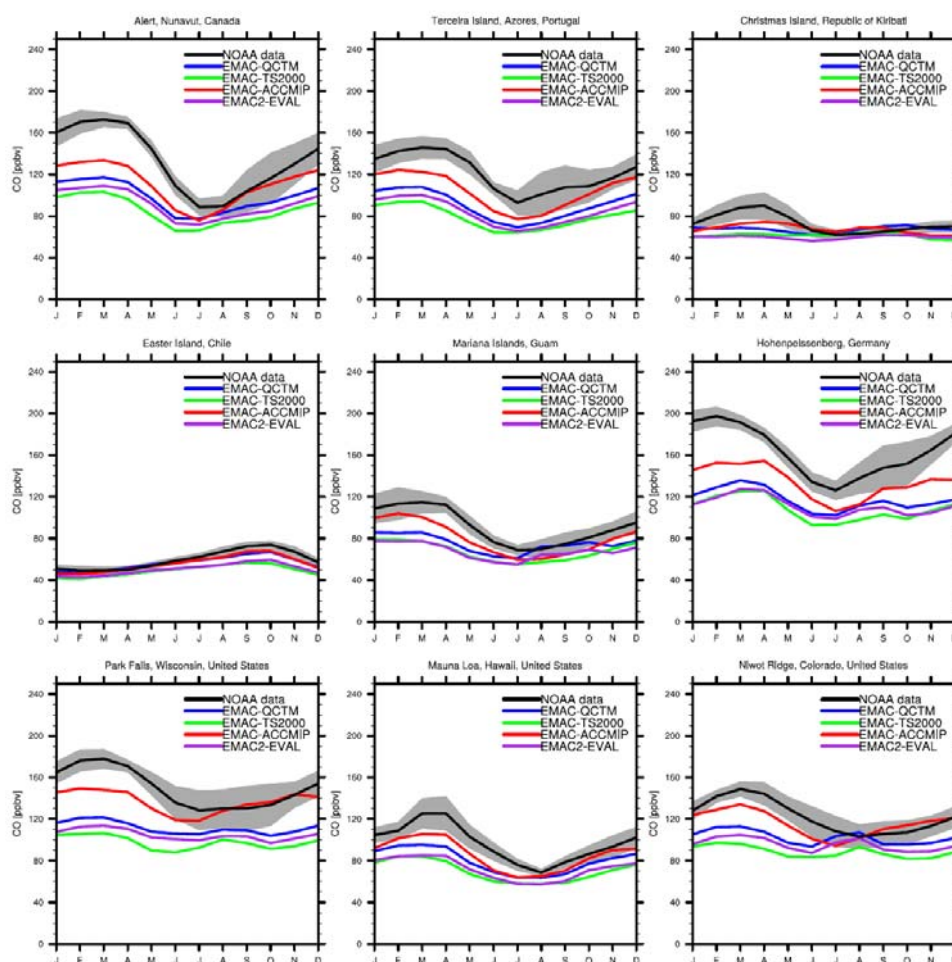


Figure 37. Annual cycle of the four EMAC simulations and NOAA GLOBALVIEW data for nine different stations world wide (see Figure 31, map at bottom). The grey shaded area shows the ± 1 standard deviation of the observation.

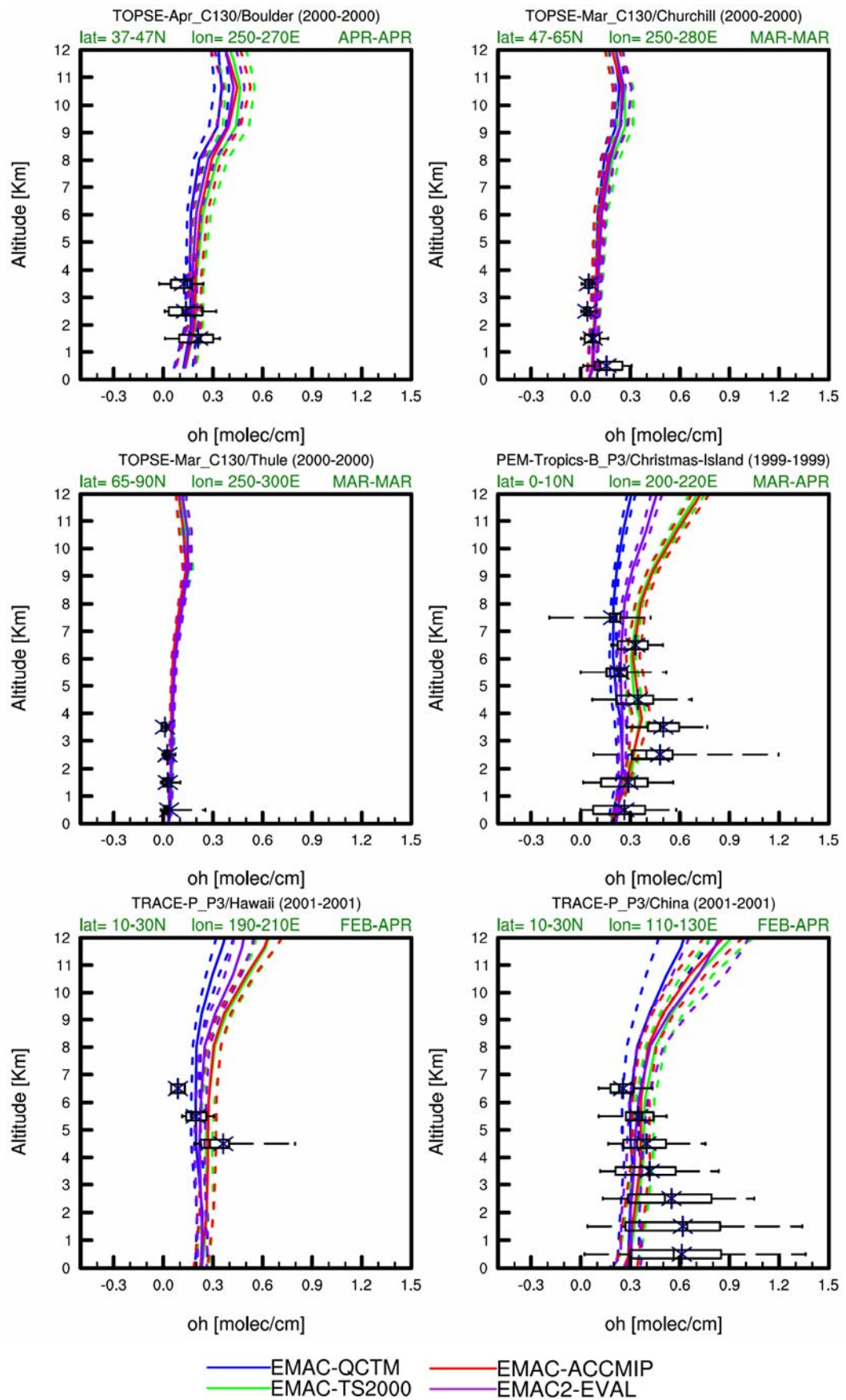


Figure 38. Similar to Figure 34, but for OH

An underestimation of CO could also be caused by differences in the OH concentration. As mentioned above, OH mixing ratios in the atmosphere are essential in determining the oxidation capacity. This compound plays also an essential role in the ozone photolysis with UV-radiation (von Kuhlmann et al., 2003). Vertical profiles for OH are reproduced very well by all model simulations, and in most cases lie within the observational error-bars (Figure 38). Small differences in the EMAC simulations can be seen in the upper levels. All four model simulations give similar results, with EMAC-ACCMIP showing slightly higher values in some regions. Overall, the agreement to the OH measurements is good so that at least for the regions and periods chosen here differences in OH are unlikely the reason for the underestimation of CO.

Non-methane hydrocarbons

Non-methane hydrocarbons (NMHCs) are also important ozone precursors and affect ozone chemistry through a large number of complex reactions. Several species of this family (ethylene (C_2H_4), ethane (C_2H_6), propene (C_3H_6), propane (C_3H_8) and acetone (CH_3COCH_3)) were analyzed and a reasonable agreement was found only for some of them in a few locations. In general, all model simulations have problems in reproducing the NMHCs.

The model performs well in reproducing the vertical profiles of C_2H_4 (Figure 39), with the model results being mostly within the 90% interval of the observations. The only exception is the Atlantic, where, similar to Pozzer et al. (2007), the model strongly underestimates the observations. In this region the effect of the emissions should be very limited, since no differences are found among the four model simulations, although EMAC-ACCMIP has higher biomass burning emissions, which should not be important in this region anyway. An improvement, compared to Pozzer et al. (2007) simulation, is found for the Thule and Boulder campaigns.

The vertical profiles for C_2H_6 (not shown) are strongly influenced by the emissions, since the EMAC-ACCMIP simulation is systematically higher than the other ones, having indeed twice as high emissions for this compound. On the other hand, the simulation of Pozzer et al. performs remarkably better, even with lower total C_2H_6 emissions. This could be related to a different geographical distribution of the emissions, as discussed by these authors in comparison with previous studies by von Kuhlmann et al. (2003b).

For C_3H_6 , all model simulations fail to reproduce the vertical profile above 2 km (not shown). The same problem exists also in the results of Pozzer et al. They pointed out that the removal of this tracer is due to chemical reactions with OH, NO_3 and O_3 , and that the chemical processes related to this tracer are probably not completely understood. They also performed sensitivity runs changing the reaction rates of the involved reactions, but found no improvements. This is an important issue that should be investigated in more detailed analysis of the chemical mechanism of EMAC.

EMAC simulations overestimate the C_3H_8 in the three analyzed areas (Tasmania, Hawaii and Christmas Island, not shown). Pozzer et al. (2007) claim to find a good match to the observations, thanks to a good representation of the emission. Our results, however, over

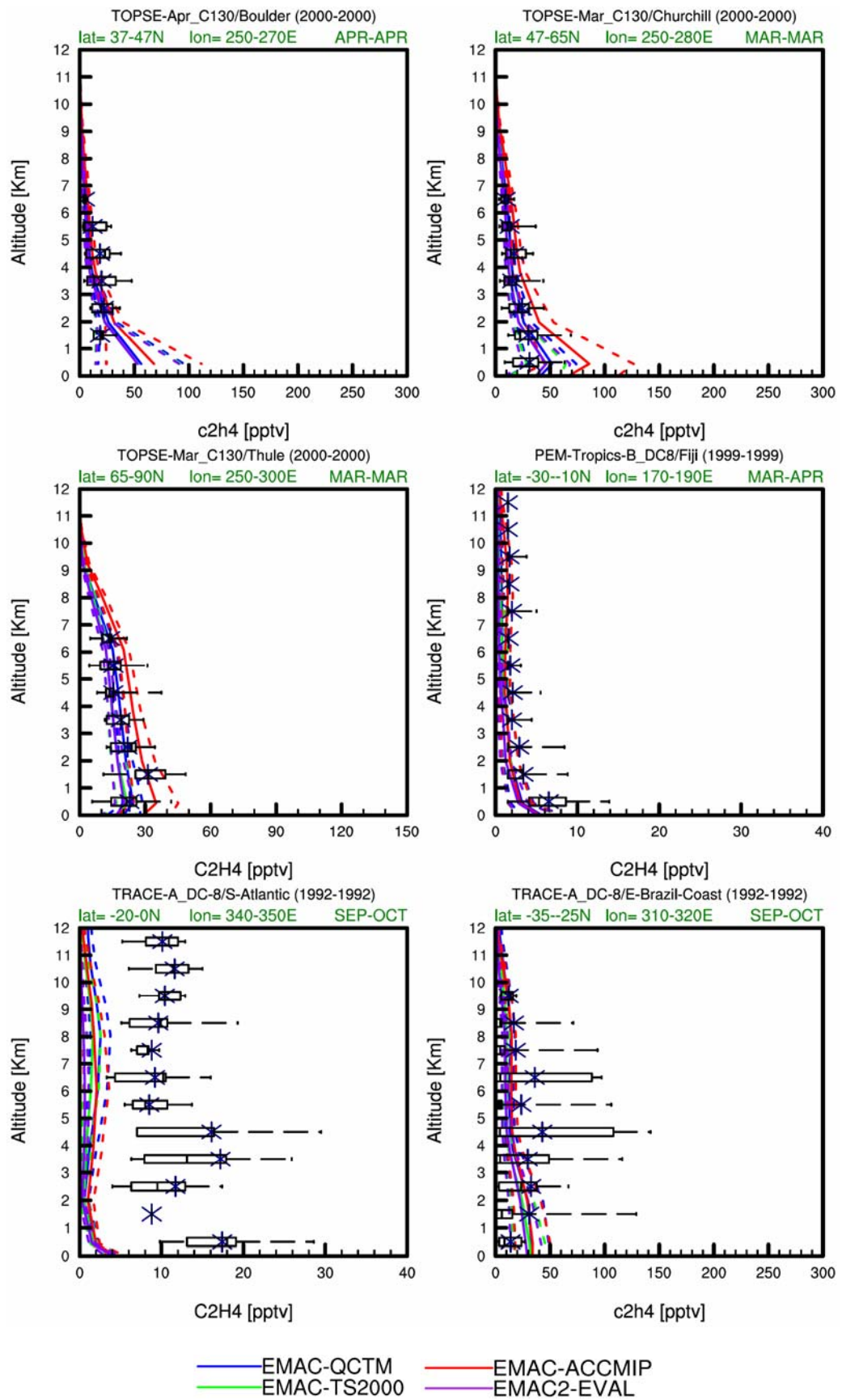


Figure 39. Similar to Figure 34, but for C₂H₄.

estimate the observations, although the emission totals are pretty similar. This points again to possible differences in the geographical distribution of the emissions or possibly to a wrong NMHC speciation. These however are quite remote areas, where the impact of the emissions should not be very high.

Finally, the analysis of CH_3COCH_3 (not shown) reveals a good agreement in both remote and polluted areas, with the model simulations mostly within the 90% interval of the observations, although often close to the lower end, and with significant improvements with respect to the simulation by Pozzer et al. (2007).

In conclusion, discrepancies between model and observations cannot always be ascribable to emissions, as it is clear when looking at vertical profiles in remote regions or when comparing model simulations with similar emission totals that lead to different results. The geographical distribution of the emissions might influence the representation of these species in the model simulations. Another issue is the speciation fraction adopted for the different NMHCs compounds. As discussed in Section 3.2, emission dataset usually provide total NMHC emissions. These are then split in the various compounds according to some speciation fractions, which have to be consistent with the chemical mechanism of the model. Here the same fractions as Pozzer et al. (2007) were used, therefore a comparison was not possible, but could be the subject of future sensitivity studies.

6.2.3 Quantifying Biases in Tropospheric Ozone and its Precursors

To summarize the findings of this chapter and to further highlight the differences between model and observations and among the four model simulations, a quantitative evaluation of tropospheric ozone and its precursors is performed. The normalized RMSD, the normalized overall mean bias and the Taylor diagram as statistical measures are considered, as for the quantitative evaluation of basic climate parameters (Section 6.1.4).

The normalized RMSD and overall mean bias for tropospheric ozone diagnostics are shown in Figure 40, including the evaluation of tropospheric column ozone (toztrop and toztrop_AC), the vertical profiles compared with observations by Tilmes et al. (2011) (O3-trop-VP) and Emmons et al. (2000) (O3-trop-ALL_regions). At a first glance, the performance of all model simulations in reproducing the tropospheric profiles of ozone and precursors from the observations is generally quite uniform, which is indicated by the very similar colors: none of the simulations performs significantly better than the others. The only exception is the tropospheric column ozone (toztrop) and the corresponding annual cycle (toztrop_AC), where EMAC-TS2000 and EMAC-QCTM perform slightly better, as it was also visible from Figure 32. These two simulations show a negative bias in the annual cycle, while EMAC-ACCMIP and EMAC2-EVAL have a positive bias. As discussed above, these differences could be related to the use of transient emissions in the nudged simulations versus single-year constant emissions in the free-running timeslice simulations. Also the difference in total emissions of ozone precursors (in particular in the EMAC-ACCMIP simulation) could play an important role in determining the tropospheric column ozone. As mentioned above, a correct representation of the tropopause height is also important for a correct simulation of tropospheric ozone columns.

A similar performance of the EMAC simulations in reproducing tropospheric ozone is confirmed also by the analysis of the Taylor diagram (Figure 41). The correlation values for

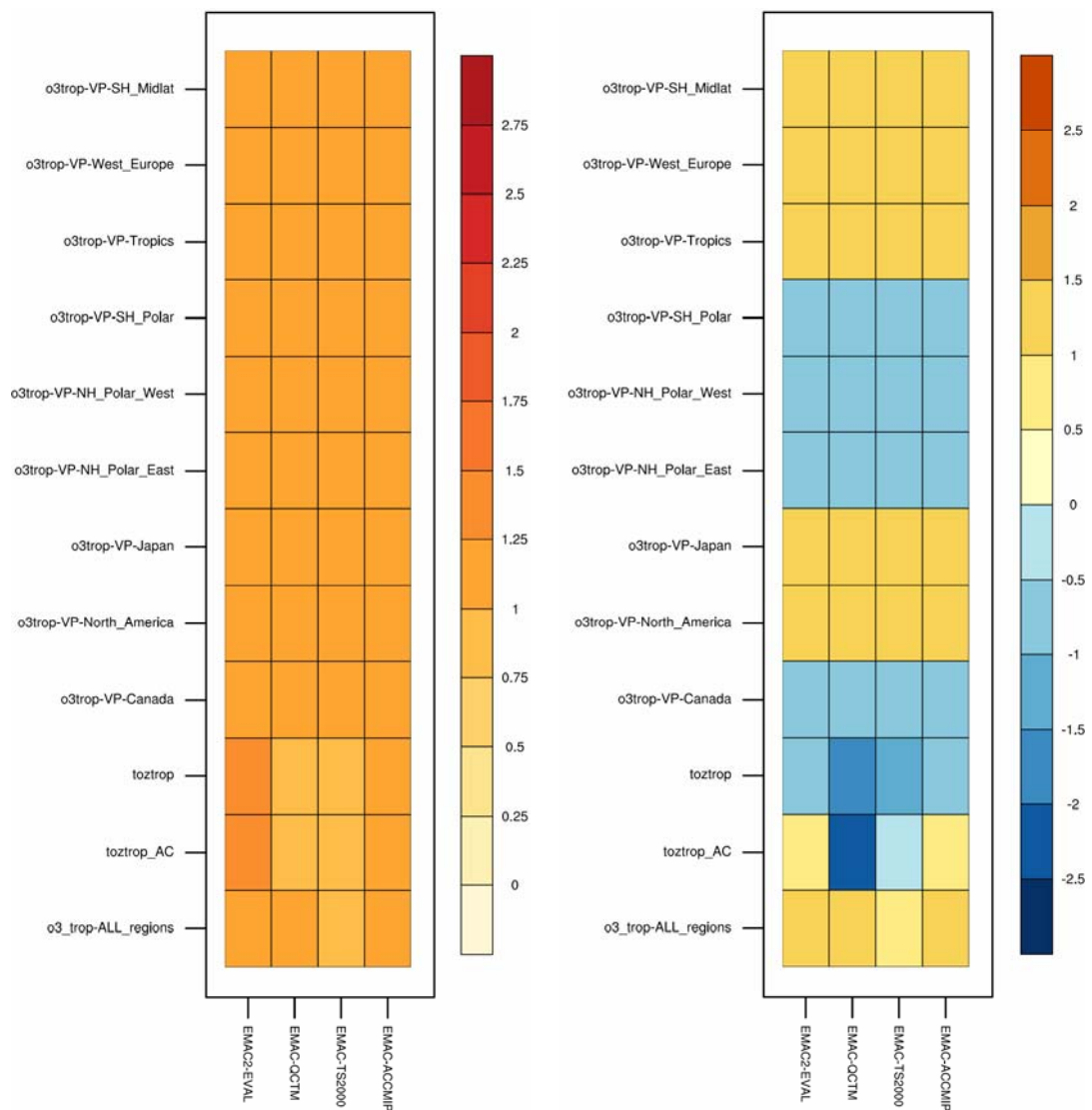


Figure 40. Portrait diagrams showing the root mean square difference (left) and the normalized overall mean bias (right) for chosen diagnostics of tropospheric ozone.

tropospheric column ozone and its annual cycle are about $R=0.6$ and $R=0.75$, respectively, and similar among all model simulations, meaning that the model is generally capturing the main features of the tropospheric column ozone pattern, as discussed in Section 6.2.1. Vertical profiles from station measurements (Filmes et al. 2011) show very high correlation (with the exception of the Tropics). This confirms the conclusion of Section 6.2.1, that the model reproduces well the ozone variations during the year (low values in winter and early spring at 1000-400 hPa, higher values in spring and summer months) and the general good agreement in the ozonesondes measurements with model simulations. The results are particularly good for the Western Europe station (see also Figure 33), which lies close to the reference point of the observations on the Taylor diagram. The other stations, on the other hand, have larger deviations from the observations in terms of amplitude, with the South Polar regions and the Tropics being the most problematic. The vertical ozone profile of the Emmons et al. (2000) data (o3_trop-All_regions) shows some deviations in terms of amplitude and correlation ($R\sim 0.7$). Note that the performance shown in the Taylor diagram for

the Emmons-profile cannot be directly compared to Figure 34 as all available observations for ozone were used for the calculation of the Taylor Diagram.

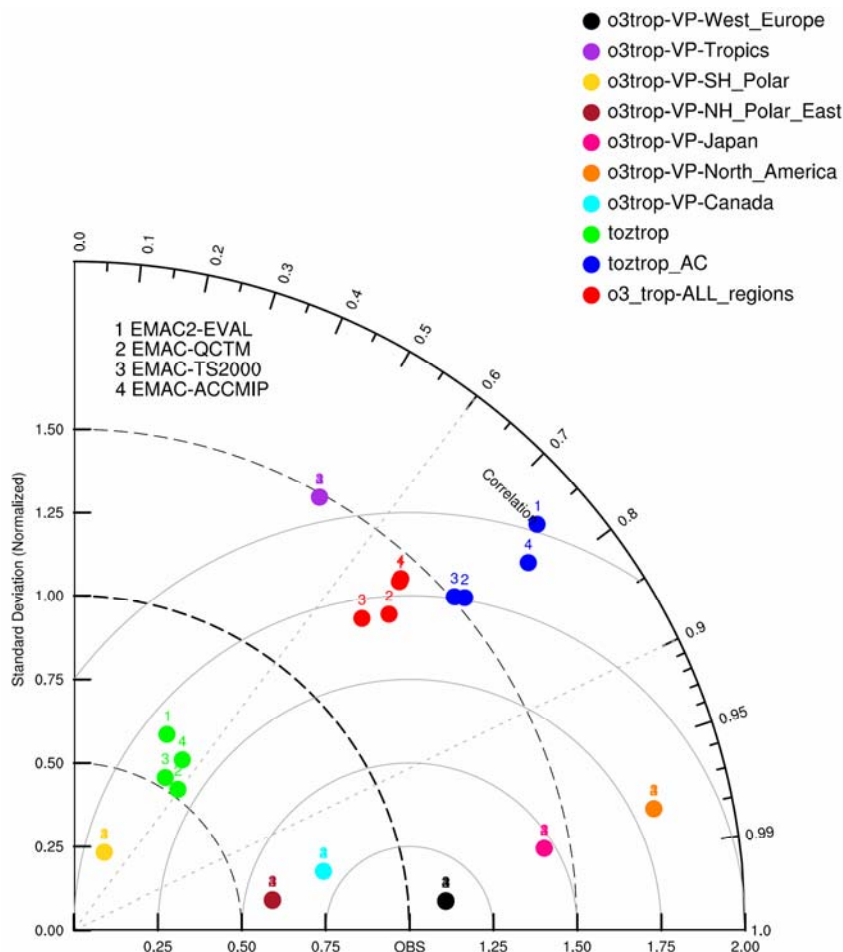


Figure 41. Taylor diagram of tropospheric ozone.

The diagnostic for ozone precursors (CO , NO_x , CH_4 and NMHCs) are summarized in Figure 42. Differences in the performance of the four EMAC simulations are more evident than in the case of ozone, since the mixing ratios of precursor species are more sensitive to the emission totals, as was discussed in detail in the previous section. The overall mean bias demonstrates that the model generally underestimates the concentration of these compounds, with the exception of NO_x . Another general feature is the systematic lower value of the RMSD and mean bias for the EMAC-ACCMIP simulation, which differs from the others mainly in the emission totals for all compounds. In this regard, it can be concluded that the emission inventories adopted for the EMAC-ACCMIP leads to a better performance of the model, in terms of vertical profiles of ozone precursor mixing ratios, although the impact of emissions in remote location is often found to be quite limited.

This analysis demonstrates the importance of having accurate emission inventories in order to reproduce the mixing ratios of certain compounds. However, large uncertainties in such inventories still exist and can be a large limitation in the performance of particular model simulations, regardless of the model's ability in simulating other processes (like chemistry and transport) that determines the vertical profiles of mixing ratios that are discussed here. In addition, as noted previously, deviations in the time period and location between aircraft

data and model contribute to deviations in this comparison. Further measurements and additional more process-oriented diagnostics are needed in order to fully understand and evaluate the model's tropospheric chemistry.

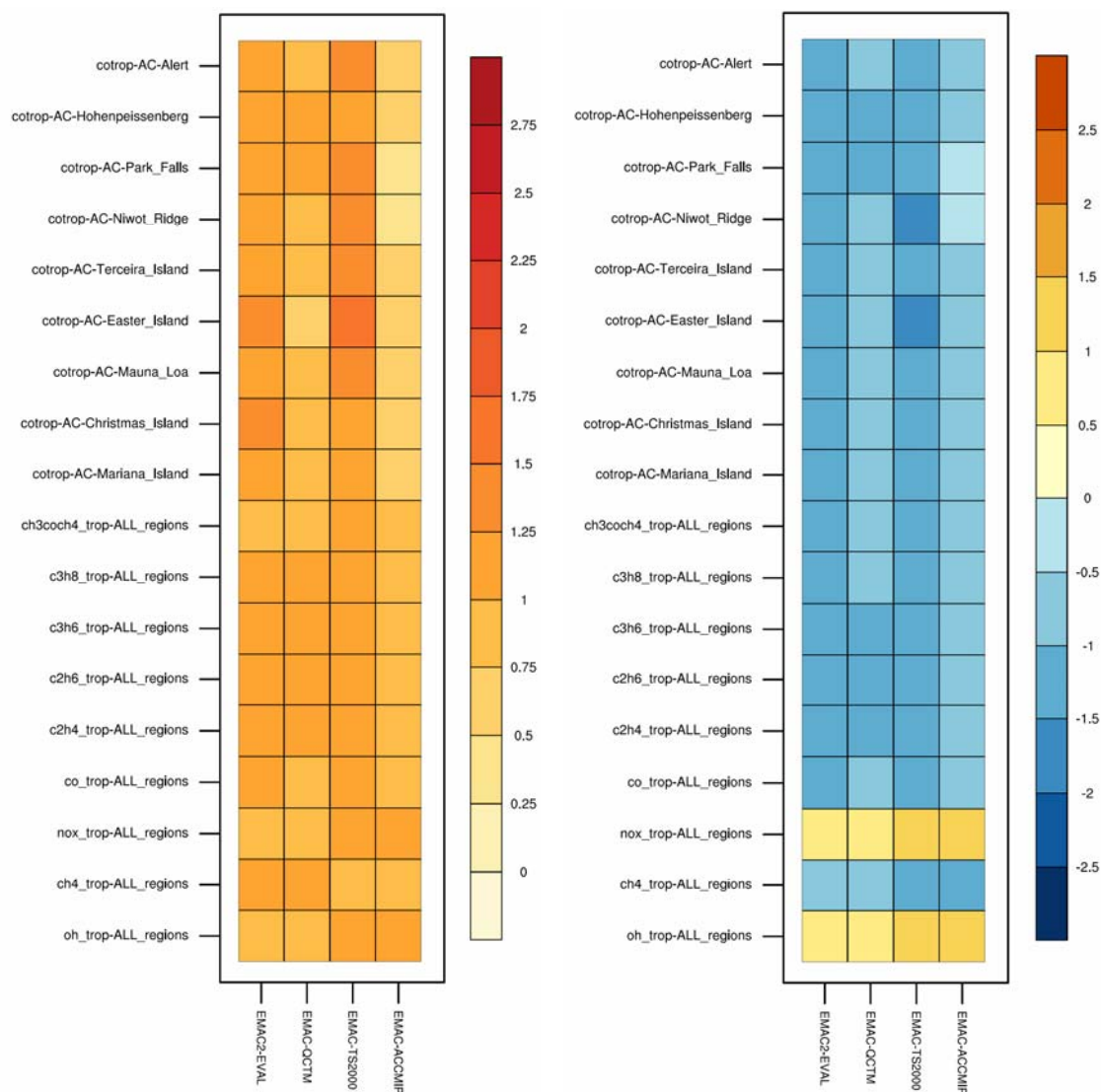


Figure 42. Portrait diagrams showing the root mean square difference (left) and the normalized overall mean bias (right) for chosen diagnostics of ozone precursors.

6.3 Stratospheric Ozone

In this section, simulated stratospheric ozone profiles and total column ozone from the EMAC simulation are first compared to different observations (Section 6.3.1). In order to better understand deviations from observations, a process-oriented evaluation is performed additionally, following the diagnostics that were applied by Eyring et al. (2006) as part of the CCMVal-1 comparison (Section 6.3.2).

6.3.1 Detecting Stratospheric Ozone Biases

Following Eyring et al. (2006), Figure 43 compares climatological mean vertical ozone profiles and latitudinal cross sections at 50 hPa from the four EMAC simulations to HALOE observations. In contrast to the Eyring et al. (2006) study, the HALOE observations have been extended to 2005, see details on the observations in Section 5.2.

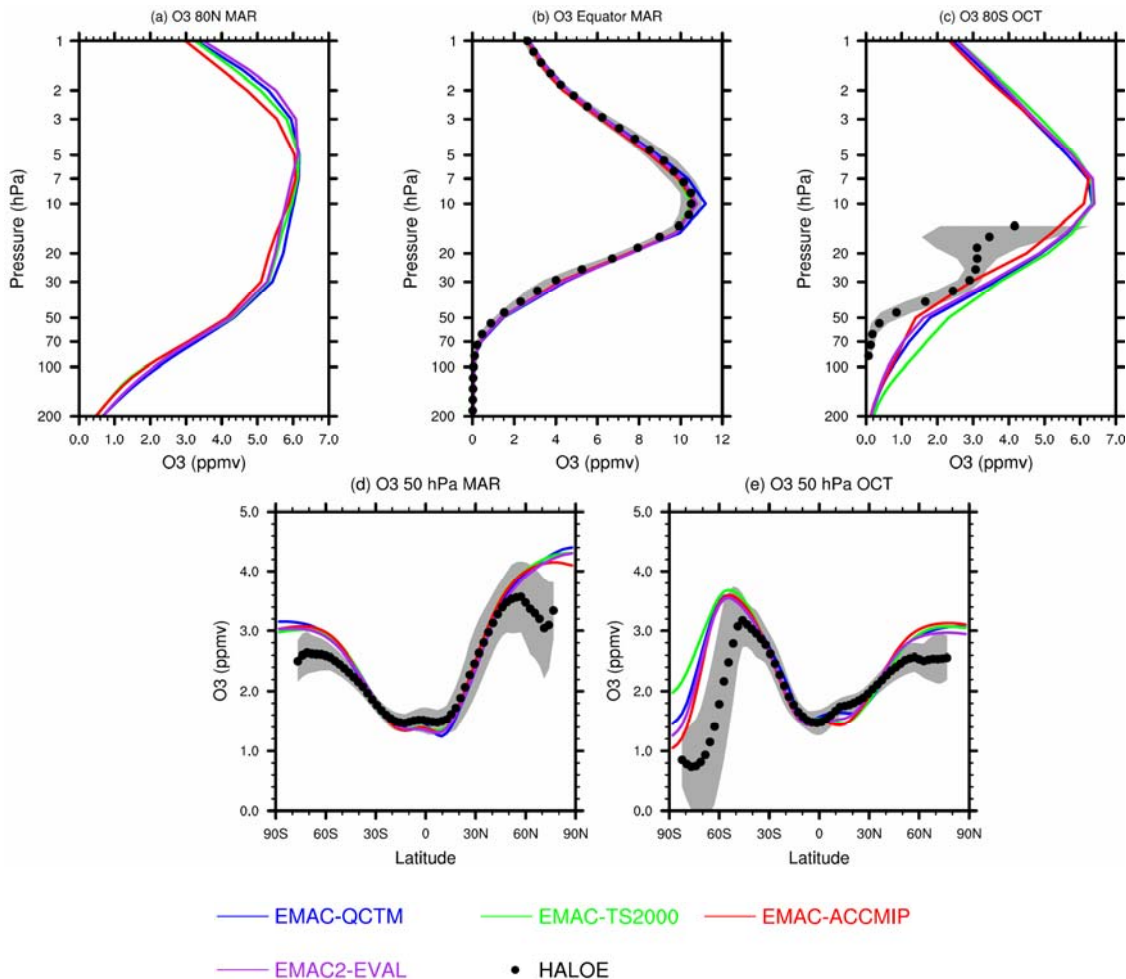


Figure 43. Climatological zonal mean O_3 mixing ratios from different EMAC simulations and HALOE in ppmv. Upper panels (a-c): Vertical profiles at 80°N in March (left), 0° in March (middle) and 80°S in October (right). Lower panels (d,e): Latitudinal profiles at 50 hPa in March (left) and October (right). The grey area shows HALOE plus and minus 1 standard deviation (σ) about the climatological zonal mean. Climatological means were calculated for the years 1999-2007 (EMAC-QCTM), 1999-2009 (EMAC2-EVAL), 10 years timeslice (EMAC-TS2000), 12 years timeslice (EMAC-ACCMIP) and 1991-2005 (HALOE).

In the tropics (Figure 43b), EMAC simulations are in very good agreement with each other and compared to HALOE observations and lie within the 1-sigma standard deviation of the observations. Only EMAC-QCTM shows slightly higher ozone mixing ratios of ~ 0.5 ppmv between 7 hPa and 15 hPa where ozone mixing ratios peak. In the southern hemispheric polar spring at 80°S (Figure 43c) all four model simulations simulate higher ozone mixing ratios compared to HALOE observations and lie outside the interannual variability of HALOE. Below 50 hPa, this is similar to CCMVal-1 models (Eyring et al., 2006), which

are also biased high compared to HALOE observations. In the lower stratosphere, between 50 and 20 hPa, the EMAC simulations do not deplete ozone to the extent seen in the observations and significantly overestimate ozone mixing ratios. This is particular the case for the EMAC-TS2000 simulation (see also Figure 43e), which out of the four simulations shows the largest biases over the entire altitude range between 200 and 15 hPa. In the northern hemispheric polar spring (Figure 43a and Figure 43d), ozone is again too high, but a quantitative comparison at this latitude is not possible because of missing observations from HALOE. Variations between the individual EMAC simulations in this region are up to 0.5 ppmv, with EMAC-ACCMIP showing the lowest mixing ratios which are closest to the HALOE observations at 50 hPa (Figure 43d).

To further evaluate stratospheric ozone, zonal mean total column ozone climatology from the different EMAC simulations is compared to the NIWA assimilated data (Bodeker et al., 2005) and observations from the GOME instrument in Figure 44 and Figure 45, respectively. The well-known features of highest ozone values in northern spring, low ozone values in the tropics, with a small seasonal cycle, the ozone maximum in the mid-latitudes of the Southern Hemisphere in late winter/early spring and the ozone hole above the Antarctic are well represented the EMAC simulations, but significant quantitative differences

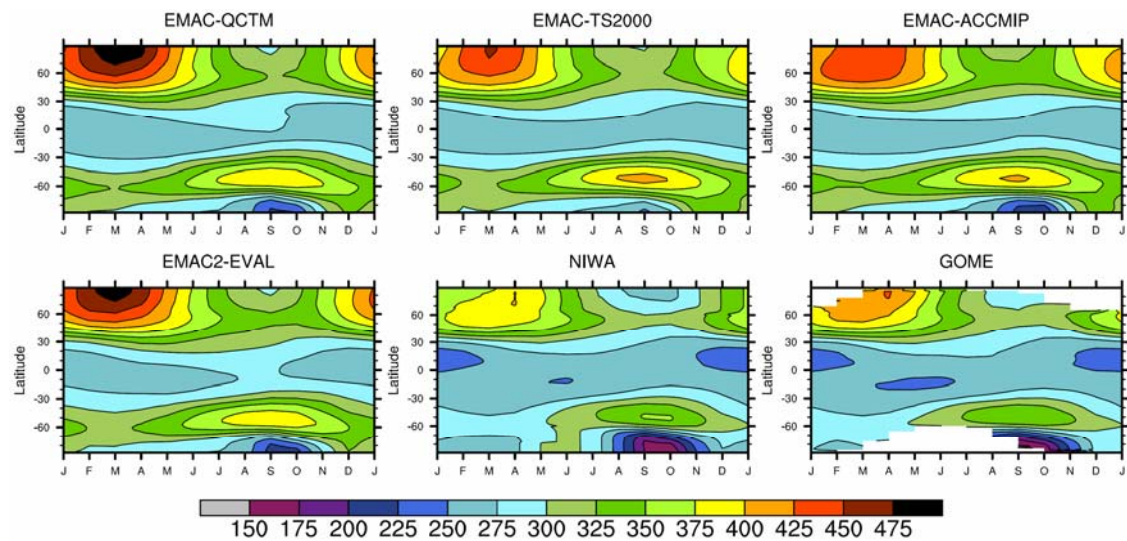


Figure 44. Total column ozone climatologies for different EMAC simulations (1999-2007 (QCTM), 1999-2009 (EMAC2-EVAL), 10 years timeslice (EMAC-TS2000), 5 years timeslice (EMAC-ACCMIP)) compared to the NIWA (1995-2005) combined total column ozone database (Bodeker et al., 2005) and GOME data (1996-2006).

compared to observations exist. The ozone hole is underestimated in all EMAC simulations, in particular in the EMAC-TS2000. This was also shown in Figure 43c, where ozone mixing ratios were overestimated throughout most of the lower stratosphere in southern hemispheric spring. In northern hemispheric winter, EMAC simulations overestimate ozone mixing ratios in the high latitudes, especially EMAC2-EVAL and EMAC-QCTM, a feature that is also visible in Figure 43. At about 50°-60°S, the midlatitude maximum in total column ozone mixing ratios in autumn is produced by all EMAC simulations, but is more pronounced than in the NIWA and GOME observations. This was also noticed for a

couple of CCMVal-1 models by Eyring et al. (2006). In the tropics the EMAC simulations show good agreement with NIWA and GOME observations. The different behaviour of total column ozone that was discussed above is also visible in the zonal mean total ozone values for the different seasons: December, January, February (DJF), March, April, May (MAM), June, July, August (JJA), September, October, November (SON), and the annual mean. Here it can be seen that the EMAC simulations overestimate total column ozone in all seasons and regions, pointing to a general high bias in ozone. The overestimation is most pronounced over Antarctica in spring (SON), with the EMAC-TS2000 simulation being far outside the interannual measurement uncertainty.

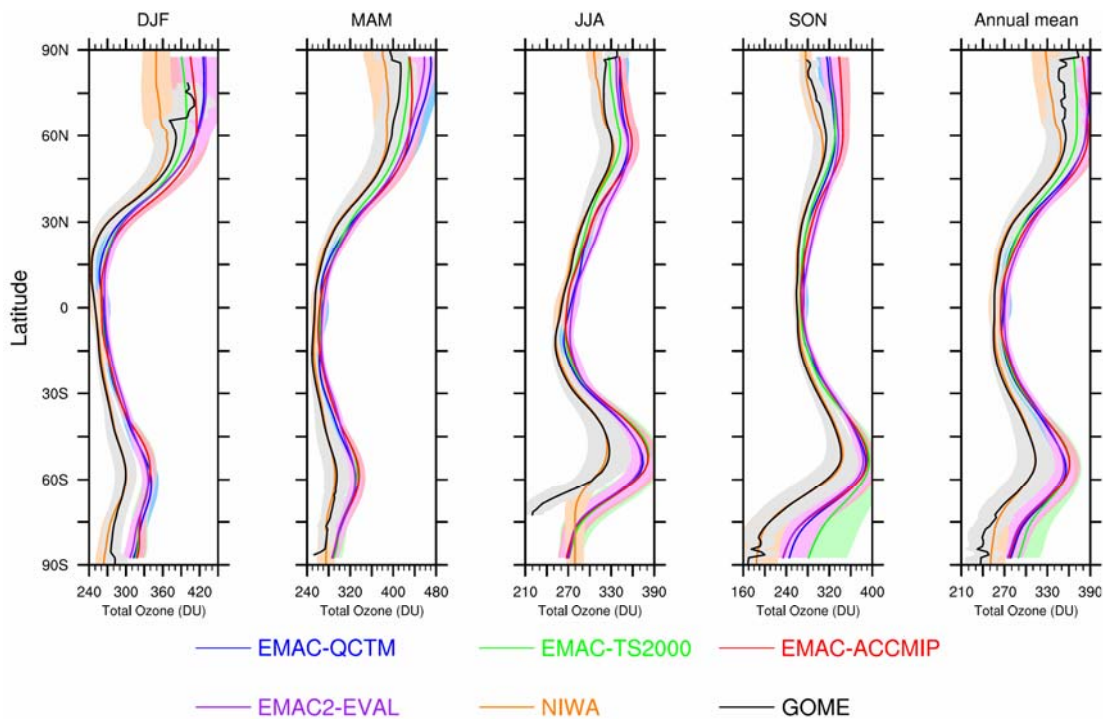


Figure 45. Zonal mean total ozone values for DJF, MAM, JJA, SON and the annual mean from GOME (mean values in black with standard deviations as background surfaces), NIWA (orange line indicating mean values and the shaded area the standard deviations), and results from the four EMCA simulations (blue, green, red and purple curves with mean and standard deviation).

6.3.2 Understanding Stratospheric Ozone Biases

To analyse the reasons for the differences in stratospheric ozone to observations, a process-oriented evaluation as done by Eyring et al. (2006) is performed. Some aspects of stratospheric dynamics have already been evaluated in Section 4.1. In the following, additional dynamics and transport processes as well as chemical species that are important for stratospheric ozone are examined.

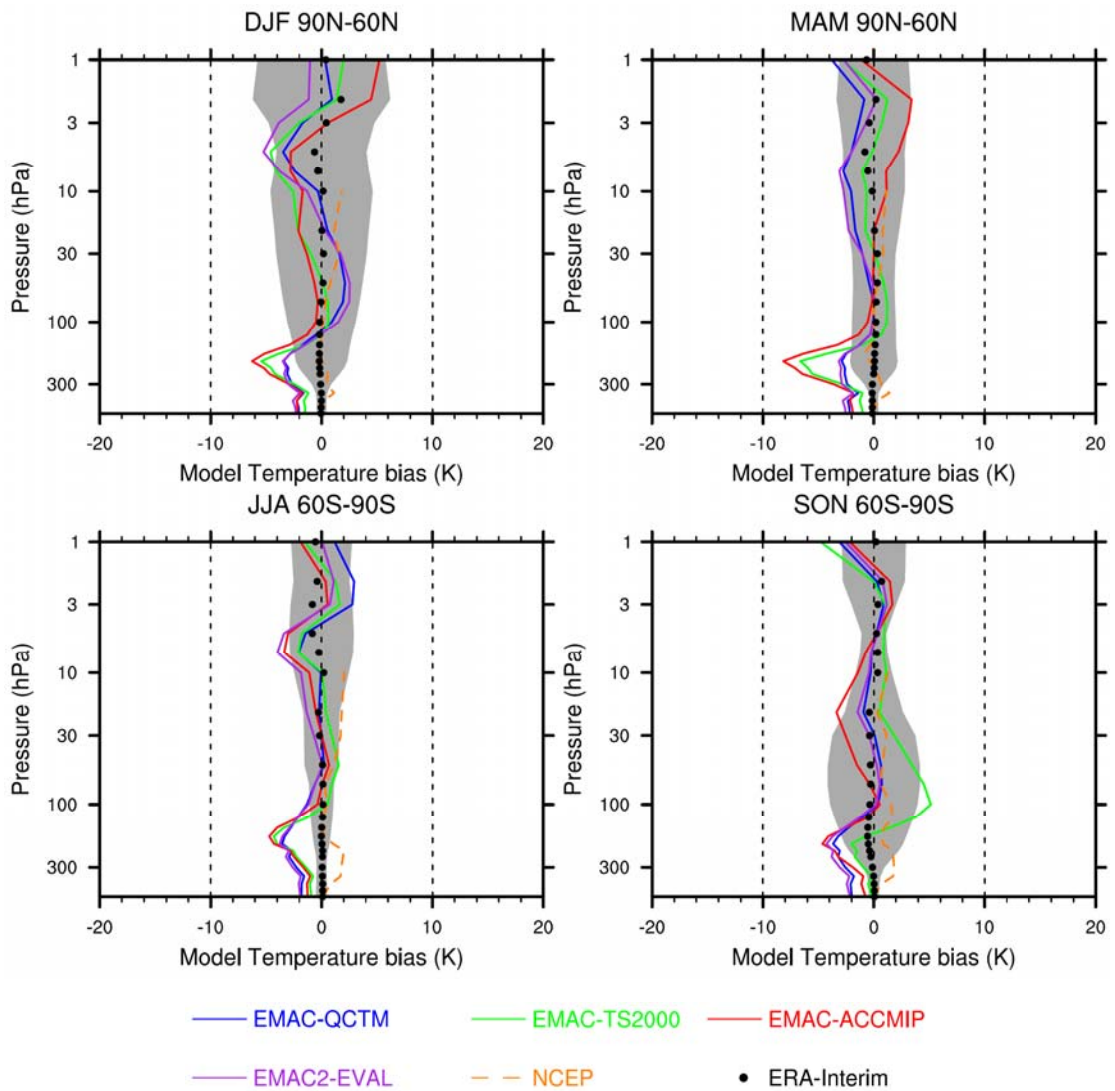


Figure 46. Climatological mean temperature biases for 60°-90°N (upper panels) and 60°-90°S (lower panels) for the winter (left) and spring seasons (right). The climatological means for the four EMAC simulations (1999-2007 (EMAC-QCTM), 1999-2009 (EMAC2-EVAL), 10 years timeslice (EMAC-TS2000), 12 years timeslice (EMAC-ACCMIP)), NCEP/NCAR and ERA-Interim data from 1995-2005 are considered. Biases are calculated relative to ERA-Interim reanalyses. The grey area shows ERA-Interim plus and minus 1 standard deviation (σ) about the climatological mean.

Stratospheric Temperatures

Many of the chemical reactions in the stratosphere that determine ozone are temperature dependent. Therefore, when assessing the ozone hole, it is necessary to assess the ability of a model to simulate temperatures. Figure 46 shows the mean winter and springtime climatological mean temperature biases poleward of 60°. Above 100 hPa, there is generally very good agreement between the EMAC simulations and the ERA-Interim reanalyses data, with the EMAC temperatures lying mostly within the interannual variability of ERA-Interim. In the lower stratosphere in winter and spring the model simulations have a cold bias of up to -5 K in the southern and up to -8 K in the northern hemisphere. It is notable that in the northern hemisphere the bias in the nudged simulations is around 6 K smaller

than in the free-running simulations, despite the fact that the stratosphere is not nudged. The bias in the lower southern hemispheric stratosphere in spring is however smaller than in the previously used E39C model and in many other CCMs evaluated in Eyring et al. (2006) and SPARC CCMVal (2010). The “cold-pole” problem overall is a long standing problem of stratospheric GCMs and CCMs that can be attributed in part to missing wave drag (Garcia and Boville 1994). EMAC-TS2000 on the other hand shows a positive bias which could be related to the missing ozone depletion (see Figure 44 and Figure 45). The causes and effects of the underestimation of the ozone hole in the EMAC-TS2000 simulation will be further examined in a follow up study. However, since the main difference between the EMAC-TS2000 and the EMAC-ACCMIP simulation is the difference in the prescribed SSTs, this points to the SSTs causing the main difference in performance between the two free-running model simulations. A key impact of SSTs on stratospheric ozone attributed to differences in the meridional circulation, which are in turn driven by differences in the wave forcing have already been identified by Garny et al. (2009). The SST signal propagates to the stratosphere by modulation of the planetary wave activity and thus the Brewer-Dobson-Circulation.

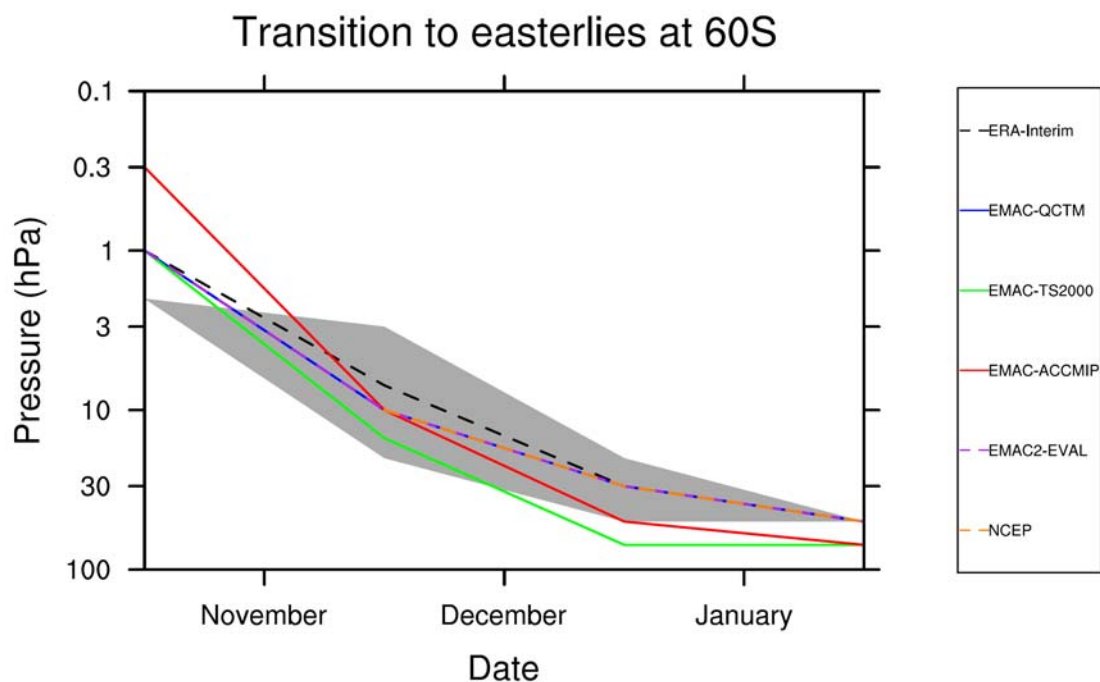


Figure 47. Descent of the zero zonal mean wind lines at 60°S based on the climatological mean annual cycle calculated from the monthly mean zonal mean winds for different EMAC simulations. The black dashed line shows the mean date of transition from easterlies to westerlies from ERA-Interim reanalysis, the grey area indicates the 1-sigma standard deviation. Tickmarks refer to the first day of the month. Climatological means are calculated as in Figure 3.

Stratospheric Winds

Zonal mean winds can be used to further investigate the cold bias problem in the polar regions discussed in Section 6.1.1. A cold bias could affect the duration of the Antarctic ozone hole and can be quantified by looking at the descent of the zero zonal mean wind lines at 60°S based on the climatological mean annual cycle calculated from the monthly mean zonal mean winds. The change from westerly winds to easterly winds (Figure 47) at

60°S in the stratosphere is an indication for the break up of the polar vortex, which represents a strong transport barrier in the stratosphere and goes along with low temperatures. While low temperatures in the polar vortex favour the formation of polar stratospheric clouds which lead to ozone depletion, the transport barrier inhibits the transport of ozone and chemically related substances from the midlatitudes into the polar regions. Unlike in many of the CCMs assessed in Eyring et al. (2006), the transition from westerlies to easterlies compared to ERA-Interim occurs at around the same time in the EMAC2-EVAL and EMAC-QCTM (notice that the lines for these two simulations are overlapping in the figure) and too early in the free-running simulations EMAC-TS2000 and EMAC-ACCMIP. The earlier transition could be due to the underestimation of the ozone hole, in particular in the EMAC-TS2000 simulation (see Section 6.3.1).

To zoom more closely into a region of importance for stratospheric ozone, Figure 48 shows the annual cycle of zonal mean wind and temperature in 30 hPa averaged over 55°-60° north and south for different EMAC simulations compared to ERA-Interim and NCEP/NCAR reanalysis data. Differences between the two reanalyses datasets are generally very small. The model simulations reproduce hemispheric differences of the mean value, annual cycle and dynamical variability changes. The annual cycle is well captured in both hemispheres in all except the EMAC-QCTM simulation, and the mean values in the Northern Hemisphere agree well with meteorological reanalyses. In contrast to simulations with the previous E39C model (Dameris et al., 2005) three of the four model simulations, namely EMAC2-EVAL, EMAC-QCTM, and EMAC-ACCMIP, simulate zonal mean winds in the southern hemisphere in agreement with ERA-Interim. This could be related to a reduced cold bias compared to ERA-Interim (Figure 46, upper right panel). The EMAC-TS2000 slightly underestimates wind speeds at these altitudes, and lies mostly outside the interannual variability of ERA-Interim. EMAC-TS2000 and EMAC-ACCMIP show slightly negative wind speeds (east wind) from the middle of November to January/February, which is in agreement with Figure 47, where the transition from westerlies to easterlies already took place at this height. In the northern hemisphere, wind speeds are weaker than in southern hemisphere, which is expected as the polar vortex is usually weaker in the Arctic, due to stronger perturbation by atmospheric waves. All model simulations lie within interannual variability of ERA-Interim over the year. The maximum differences between the EMAC simulations and meteorological reanalyses are ~ 10 m/s and differences between the individual EMAC simulations as well as EMAC simulations and reanalyses are generally small.

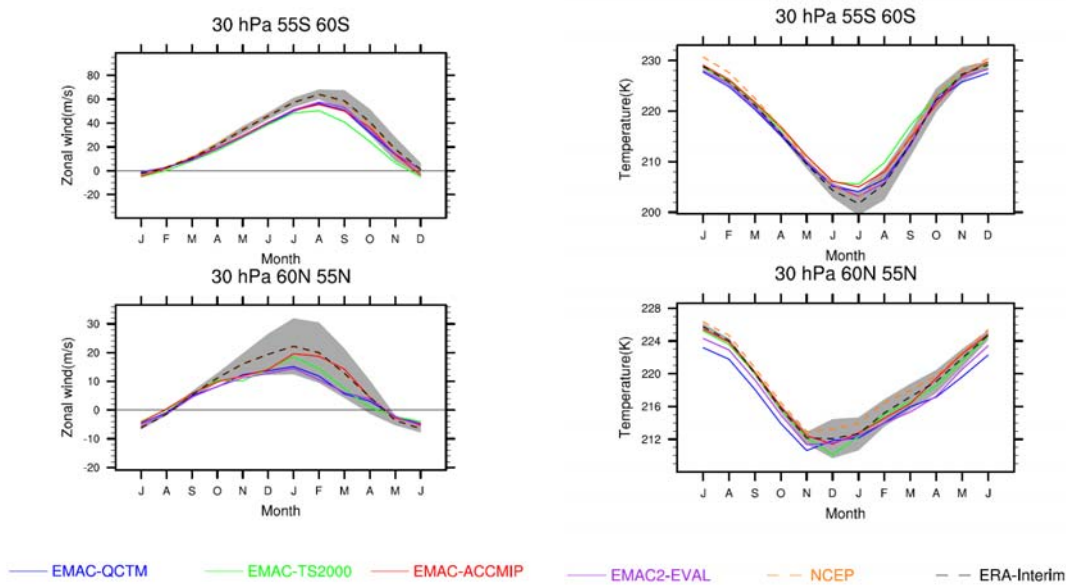


Figure 48. Annual cycle of zonal wind (left) and temperature (right) at 30 hPa at 55–60°S and 55–60°N from different EMAC simulations in comparison to ERA-Interim and NCEP/NCAR reanalysis data. The grey shaded area indicates the ± 1 standard deviation of ERA-Interim.

Transport properties

Transport in the stratosphere involves both meridional overturning (the residual circulation) and mixing, which together represent the Brewer-Dobson circulation. The most important aspects are the vertical (diabatic) mean motion and the horizontal mixing. Horizontal mixing is highly inhomogeneous, with transport barriers in the subtropics and at the edge of the wintertime polar vortex; mixing is most intense in the wintertime “surf zone” and is comparatively weak in the summertime extratropics. Accurate representation of this structure is important for the ozone distribution itself, as well as for the distribution of chemical families and species that affect ozone chemistry (NO_y , Cl_y , H_2O , CH_4). Within both the tropics and the polar vortex, the key physical quantities to represent are the degree of isolation and the diabatic ascent or descent, respectively. Useful information can be obtained from instantaneous snapshots of tracer fields, such as CH_4 (Eyring et al., 2005).

Figure 49 therefore compares climatological mean vertical CH_4 profiles and latitudinal cross sections at 50 hPa from the EMAC simulations to HALOE. In the tropics the vertical CH_4 profile agrees well with HALOE measurements and is within 1σ of the observations (Figure 49b), but in the southern hemispheric polar spring at 80°S and below 15 hPa (Figure 49c) all four EMAC simulations show higher CH_4 mixing ratios than HALOE, outside the interannual variability. This bias was also present in many CCMVal-1 models (Eyring et al., 2006) but is much smaller than in the previous model version E39C. In northern hemispheric spring (Figure 49a), observational data are missing. Still, the latitudinal cross section (Figure 49) indicates that at least at 50 hPa EMAC simulations overestimate CH_4 mixing ratios and exceed the HALOE interannual standard deviation. However, except the biases in the polar regions, the meridional gradients are very well simulated in all EMAC simulations, indicating generally good transport properties of the model in the tropics and midlatitudes.

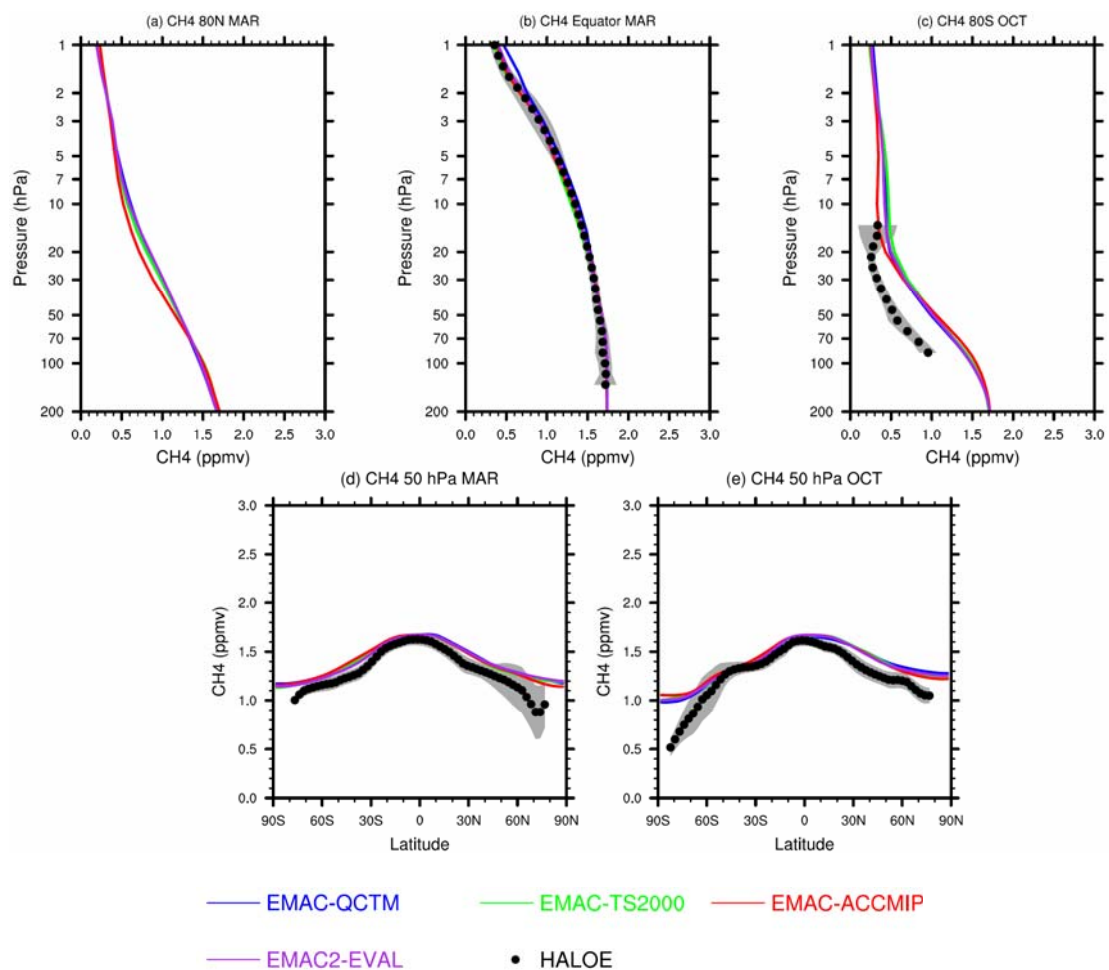


Figure 49. Same as Figure 43, but for CH₄ in ppmv.

Another transport diagnostic is the vertical propagation of the annual cycle of water vapour (the so called “tape recorder”) which can be used to get information on vertical transport in the tropics as well as mixing in tropical and mid-latitude stratospheric regions (Eyring et al., 2006). Figure 50 shows vertical propagation of water vapour mixing ratios into the stratosphere as a deviation from the time-mean profile, averaged between 10°S and 10°N. Two cycles are shown. Comparison of the amplitudes of the mixing ratio from the four different EMAC simulations and the HALOE data shows similarities between the two nudged simulations EMAC2-EVAL and EMAC-QCTM, and similarities between the two free-running simulations EMAC-TS2000 and EMAC-ACCMIP. The EMAC2-EVAL and EMAC-QCTM simulations agree better with the HALOE observations, although the model simulations simulate the amplitude above 100 hPa whereas HALOE observations shows the maximum amplitude in around 100 hPa (Figure 51). EMAC-TS2000 and EMAC-ACCMIP show lower amplitudes (maximum at 0.6 ppmv). Positive values are found from June to September/October and negative values from December/January to April. With increasing height the amplitude decreases. The decrease is stronger for model simulations as for HALOE data. The propagation of water vapour can be seen as well. Propagation pattern (shift in time and height) show similarities between model simulations and HALOE data but the magnitude of transported water vapour is less for the EMAC simulations. Overall, the comparison shows again good transport properties of the model.

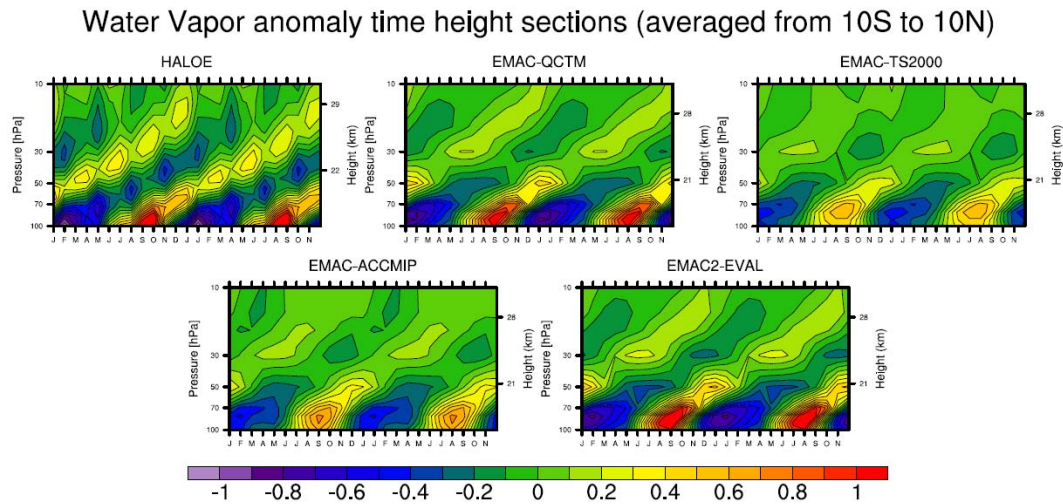


Figure 50. Time-height sections of water vapour mixing ratio shown as the deviation (ppmv) from the time-mean profile, averaged between 10°S and 10°N (‘tape recorder’) for different EMAC simulations and HALOE data. Two consecutive cycles are shown.

Water vapour

Water vapour also plays an important role in stratospheric chemistry and can have significant impacts on ozone, through changes in HO_x , as well as changes in the radiative balance because water vapour is one of the main greenhouse gases, and the formation of PSCs. Figure 52 compares climatological mean vertical profiles and latitudinal cross sections of H_2O at 50 hPa derived from different EMAC simulations and HALOE. EMAC simulations underestimate water vapour throughout the stratosphere above 100 hPa, except above around 3 hPa in the tropics. Compared to CH_4 (Figure 49) the spread between the model simulations is larger, with the nudged simulations generally lying much closer to ERA-Interim data than the free-running simulations. This is related to the more accurate temperatures that are simulated around the tropical tropopause that determines the entry of stratospheric water vapour, see Figure 21 and corresponding discussion in Section 6.1. Above around 2 hPa, the water vapour concentrations of all simulations are in agreement with HALOE observations.

At 50 hPa, in northern and southern spring, water vapour is underestimated by 1-2 ppm (Figure 52d and e). In the southern hemispheric polar spring at 80°S (Figure 52c) all four model simulations again show lower mixing ratios above 70 hPa up to 20 hPa and lie outside the interannual variability of HALOE observations. The EMAC simulations show minimum concentrations at the tropopause height (200-100 hPa) around the tropical cold point. It is noted that EMAC-QCTM and EMAC-ACCMIP as well as EMAC2-EVAL and EMAC-TS2000 agree well with each other, particularly in upper polar regions. Underestimation of water vapour in the polar stratosphere can have an impact on the formation of PSCs, which in turn impacts on ozone depletion. Less water vapour reduces the possibility of the formation of PSCs, which in turn weakens ozone depletion. In addition, an underestimation of water vapour in the stratosphere reduces the radiative heating and lower temperatures weaken chemical reactions related to ozone depletion. This is in agreement with Figure 46, where small cold biases were found.

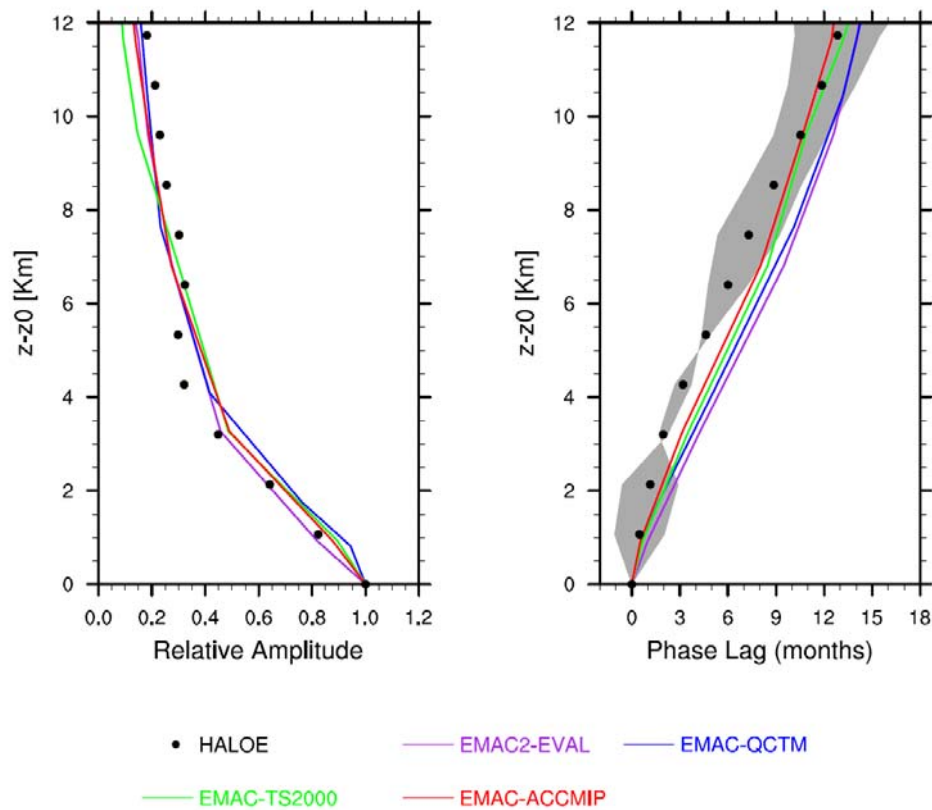


Figure 51. Vertical variation of (left) amplitude and (right) phase lag of annual cycle of water vapour averaged between 10°S and 10°N . The amplitude is normalized to unity and phase lag is set to zero at the level where the amplitude is maximum (between 16 and 20 km). The vertical axis in both plots is the distance from level of maximum amplitude. Solid circles are HALOE observations.

Chlorine Species

Ozone depletion in the last decades was mainly caused by a rise of concentration of halogenated compounds in the stratosphere (particularly in southern hemispheric spring). Therefore, it is important to assess model performance in reproducing the distribution of these species. Halogenated compounds include inorganic chlorine (Cl_y), which again contains HCl.

Figure 43 compares climatological mean vertical profiles and latitudinal cross sections of HCl at 50 hPa derived from different EMAC simulations and HALOE. Following Eyring et al. (2006), in this figure April and November have been chosen instead of March and October as in the previous plots, because the HCl/Cl_y ratio is generally higher in these months. In general, HCl is simulated very well by all EMAC simulations. A spread of about 0.3 ppbv can be found between the model simulations at 50 hPa at 80°S in November (Figure 53c and e), but comparison to observations is not possible as no observations are available. In the tropics, mixing ratios of EMAC simulations are slightly higher than HALOE observations (Figure 53). EMAC-TS2000 shows lowest mixing ratios at 50 hPa in the Antarctic (Figure 53) which could be an indication for the poorly simulated ozone hole in this simulation.

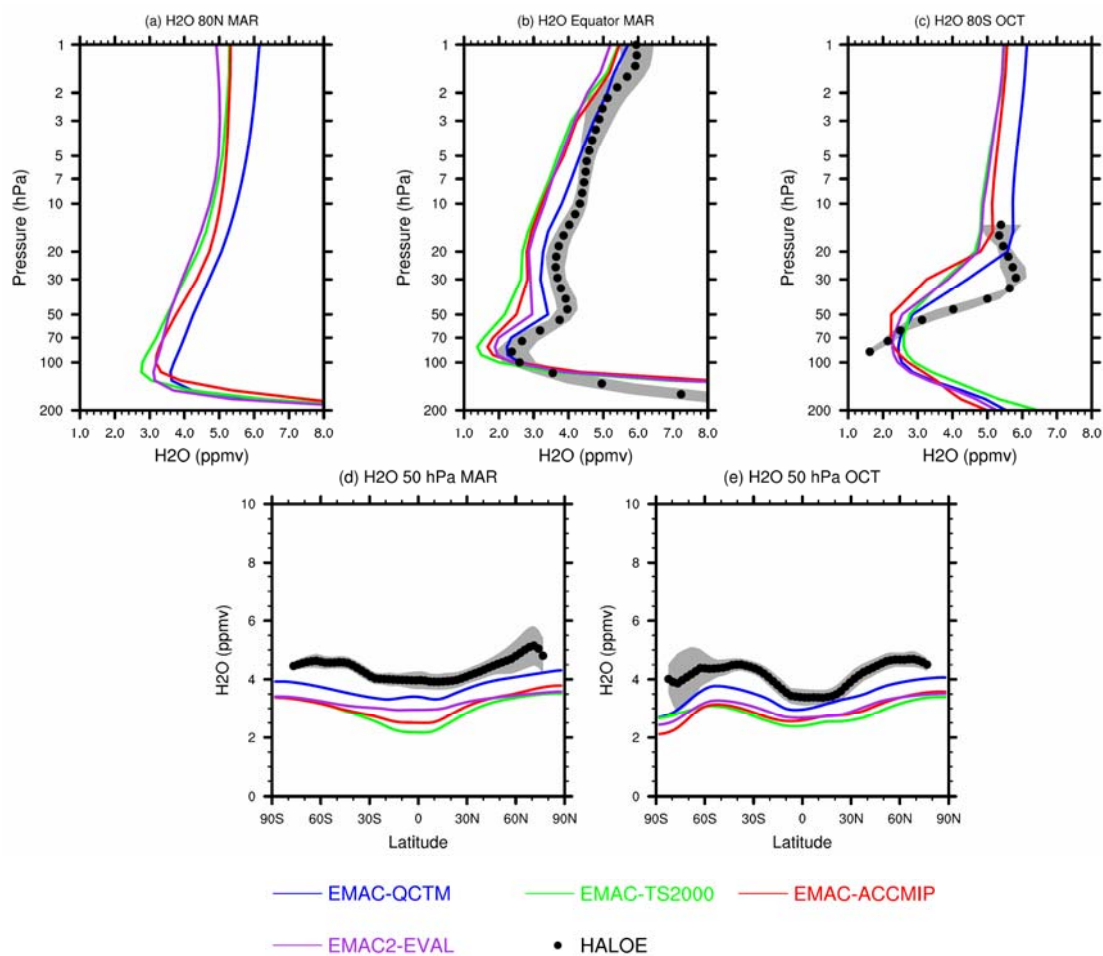


Figure 52. Same as Figure 43, but for H₂O in ppmv.

To further evaluate chlorine species, the climatological mean vertical profiles and time series of Cl_y derived from different EMAC simulations are compared to observations (Figure 54). Most apparent in this figure are the missing observations which limit quantitative conclusions on the model behaviour. In the Antarctic, only one single observation is available for the year 2005, which shows that EMAC simulations underestimate Cl_y by around 0.5 ppbv. Compared to the E39C model that was previously used and assessed in Eyring et al. (2006), the agreement with observations for Cl_y is much better in the simulations that are evaluated here, however biases of around 0.3-5 ppbv remain, see also SPARC CCMVal (2010). In the midlatitudes the model simulations agree even better with observations and lie within the uncertainty of the observations throughout the analyzed time period (1999-2007).

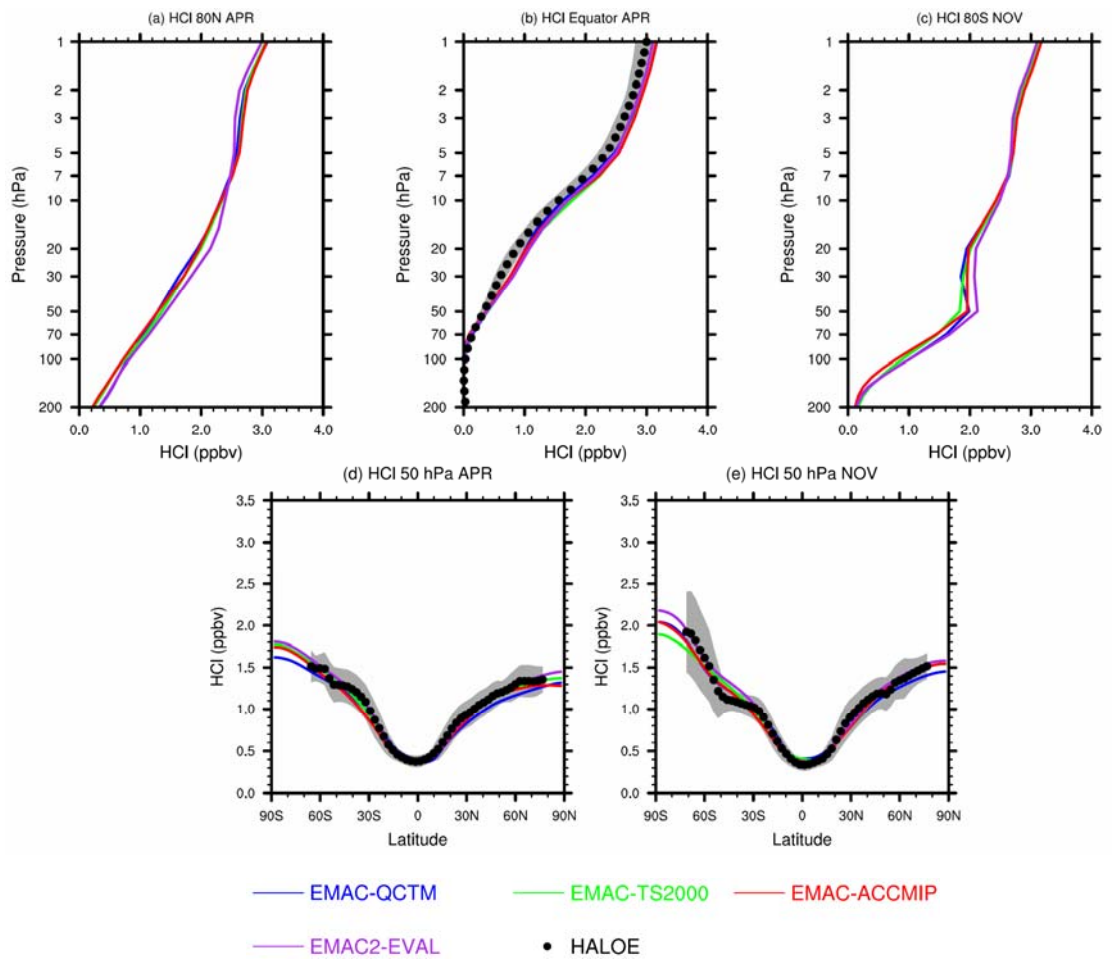


Figure 53. Same as Figure 43, but for HCl in ppbv.

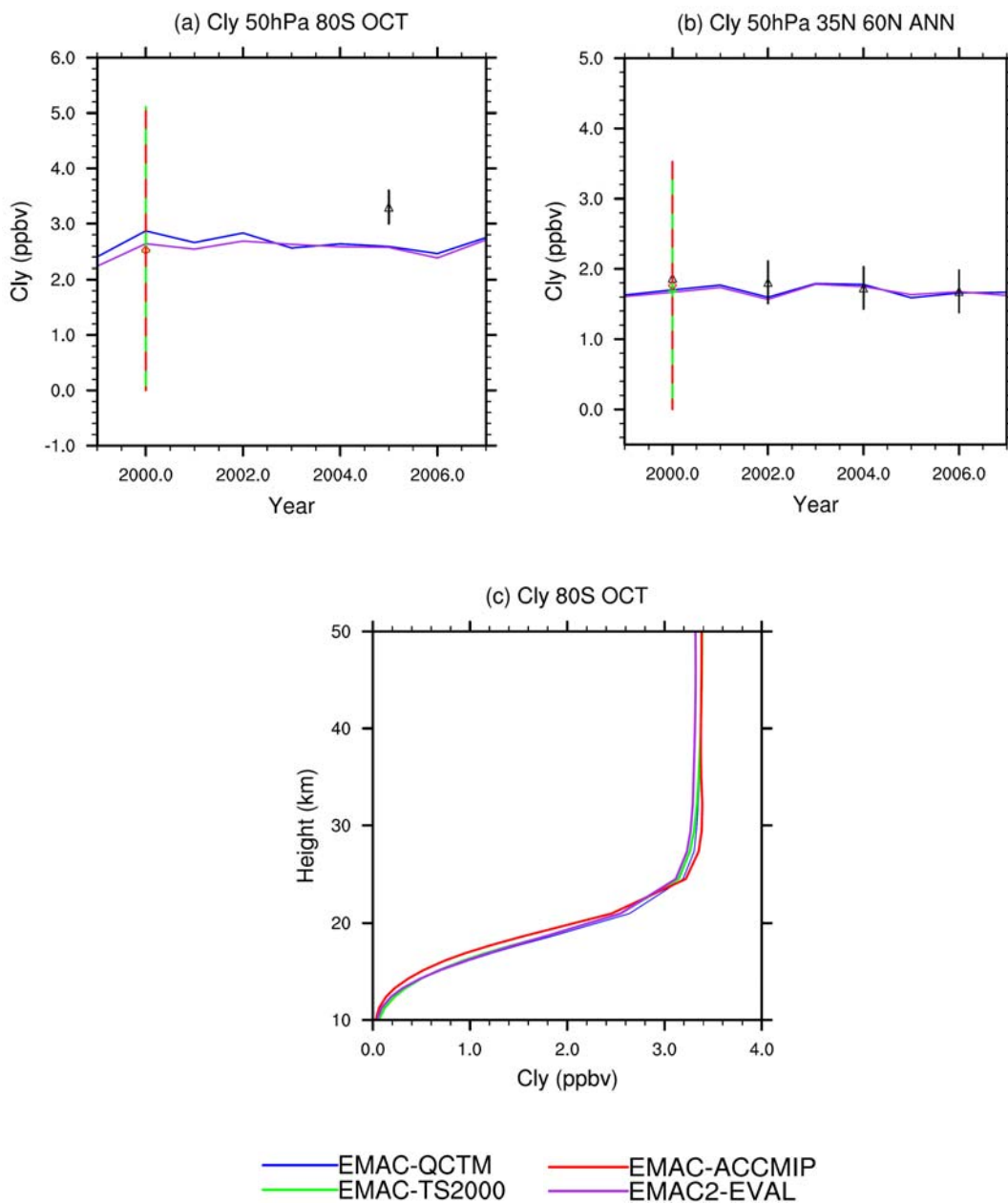


Figure 54. (a) Climatological mean vertical profiles (1999-2007 (EMAC-QCTM), 1999-2009 (EMAC2-EVAL), 10 years timeslice (EMAC-TS2000), 12 years timeslice (EMAC-ACCMIP)) at 80°S in November for Cl_y in ppbv. (b) and (c) Time series of October mean Antarctic Cl_y at 80°S from different EMAC simulations ((1998-2007 (QCTM), 1998-2007 (EMAC2-EVAL)) at 50 hPa and annual mean time series of Cl_y at mid-latitudes in 50 hPa. Estimates of Cl_y from Aura MLS HCl in 2005 [M. Santee, pers. communication] are shown in addition.

6.3.3 Quantifying Biases in Stratospheric Ozone and Related Processes

To summarize the evaluation of stratospheric ozone in the four EMAC simulations with a particular focus on how the simulations compare to each other, a quantitative comparison is performed, using the normalized RMSD, the normalized overall mean bias, and the Taylor diagram (see description in Section 4.2) as statistical measures.

Regarding the choice of diagnostics as well as the selection of regions and altitude ranges over which the diagnostics are averaged, this work follows the study by Waugh and Eyring (2008). In addition, a quantitative evaluation of ozone itself similar to Karpetchko et al. (2010) is added, except that trend diagnostics are not included since here time slice or short nudged simulations are evaluated. A summary of the stratospheric diagnostics and performance metrics is given in Table 6.

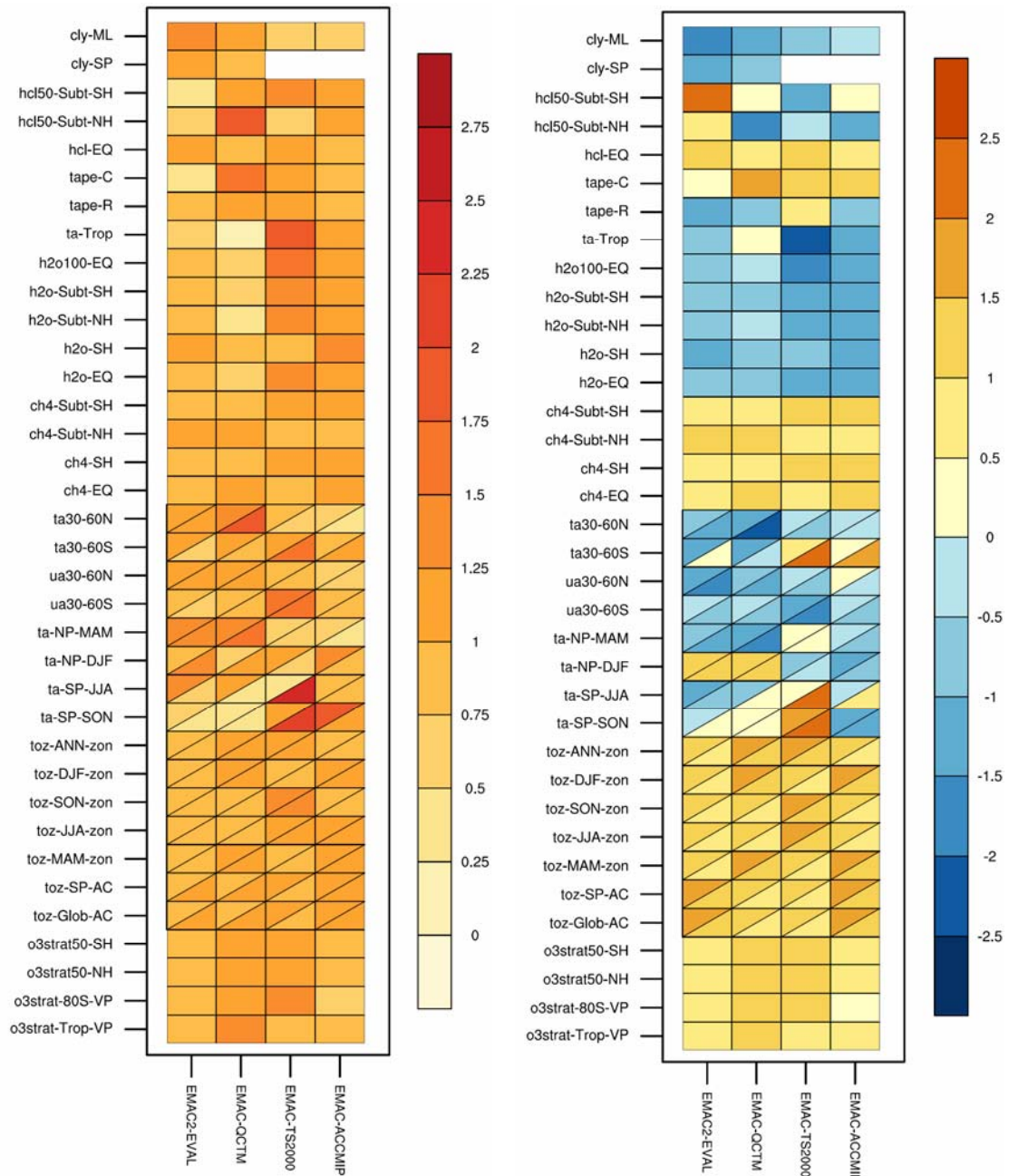


Figure 55. Portrait diagrams showing the normalized root mean square difference (left) and overall mean bias (right) of chosen diagnostics for stratospheric ozone and related key processes. For an explanation of the abbreviations for each performance metrics see Table 6.

Similar to the results presented in the mean climate and tropospheric ozone evaluation sections (Sections 6.1 and 6.2), for some diagnostics (temperature (ta), zonal wind (ua) and

total column ozone (toz)), two observational datasets are used to estimate observational uncertainty and the performance metrics are shown with respect to both observations. The lower triangle in Figure 55 which shows the RMSD (left) and the overall mean bias (right) refers to the primary observation, and the upper triangle to the alternate observational dataset.

The overestimation of total column ozone (toz) compared to both observations (NIWA and GOME) and stratospheric ozone compared to HALOE (o3strat) as discussed in Section 6.1 is clearly apparent in the overall mean bias (Figure 55, right panel, 11 lowermost metrics, all orange color). The larger bias in EMAC-TS2000 compared to the other three EMAC simulations even in the annual mean in SON is also visible (toz-SON-zon). This larger bias can be attributed to the differences in prescribed SSTs, see discussion in Section 6.3.2. Apart from this, no clear differences in ozone biases can be found between the different model setups (nudged versus free-running) or between the simulations using different emissions inventories (EMAC-ACCMIP simulations versus the three others). The latter was expected since the emissions affecting stratospheric ozone are particularly those from long-lived species (CO_2 , CH_4 , N_2O , CFCs, HCFCs, halons, H_2), and these are prescribed from AGAGE observations as lower boundary conditions in all four simulations. Similarly, the RMSD (Figure 55, left) and the Taylor diagram (Figure 56) reveal, apart from the issues discussed above, no large differences for total column ozone and the vertical profile (VP) of ozone, with the RMSD lying within 0.75 and 1.25 scattered around the mean RMSD calculated from all four simulations (which is indicated by the 1 in Figure 39, left), and all four simulations lying close to each other in the Taylor diagram. All ozone diagnostics in the Taylor diagram show a very good correlation with the observations ($R > 0.95$), except for total column ozone in JJA (toz-JJA-zon) and MAM (toz-MAM-zon) as well as for ozone at 50 hPa in the southern hemisphere (o3strat50-SH), where the normalized standard deviation has to high values (> 2) and therefore these diagnostics lie outside of the range of the diagram. The deviation from the observation in terms of amplitude is otherwise quite small.

Larger differences among the simulations exist for the performance metrics calculated for key processes determining stratospheric ozone. For example, the climatological mean temperature averaged over 60° - 90°S in JJA and SON at 50 hPa (ta-SP-JJA and ta-SP-SON) is overestimated in the EMAC-TS2000 simulation as discussed in previous sections (see also Figure 46), whereas temperature is generally within the interannual standard deviation of the observations in the other three simulations. Similarly, there is an overall bias in the temperature at 100 hPa in the tropics which is most pronounced in the free-running simulations. Although nudging is applied only up to 200 hPa, the nudged simulations are in better agreement for the temperature at these altitudes.

Tropical temperature in the tropopause determines the entry level of stratospheric water vapour. As a result of the temperature bias in particular in the free-running simulations stratospheric water vapour (H_2O) is underestimated in all simulations, displayed by the blue colours in the right panel of Figure 55, with the free-running simulations having slightly larger biases. CH_4 shows very similar results in all model simulations indicating good transport properties in the stratosphere in the tropics and midlatitudes (see Section 2.2.1 for the description).

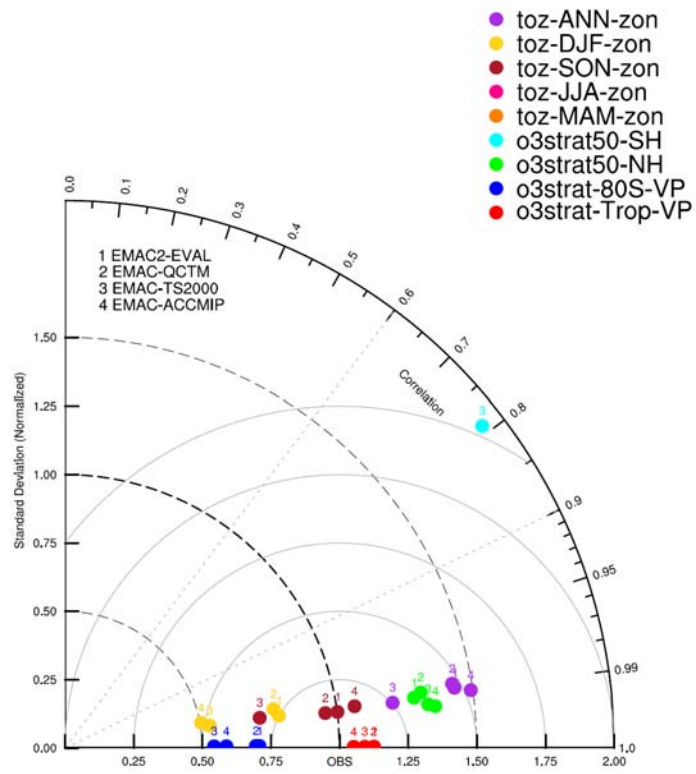


Figure 56. Taylor diagrams of stratospheric ozone.

7 Summary and Outlook

7.1 Summary

Four present-day simulations with different setups of the *ECHAM/MESy Atmospheric Chemistry* (EMAC) model have been evaluated in this thesis through a comprehensive comparison to observations. In particular, results from a previous EMAC evaluation of a model simulation with a weak nudging towards realistic meteorology in the troposphere from Jöckel et al. (2010) have been compared to new simulations with different model setups and emissions datasets in free-running timeslice and nudged *Quasi Chemistry-Transport Mode* (QCTM, Deckert et al., 2011). The latter two configurations are important for chemistry-climate projections and the quantification of individual sources (e.g. transport sector) that lead to small chemical perturbation of the climate system, respectively. The goal of this thesis was to compare the EMAC simulations to each other with a focus on how well ozone and selected climate parameters are represented in the different setups (nudged versus free-running) and simulations with different boundary conditions (emissions and sea surface temperatures (SSTs) / sea ice concentrations (SICs)).

The four EMAC simulations used in this work differ from each other in their setup. The two nudged simulations (EMAC2-EVAL and EMAC-QCTM) are transient and driven by the same SSTs and (transient where available) emission inventories. The previously evaluated EMAC2-EVAL simulation that covers the time period 1998-2009 (Jöckel et al., 2010) serves as the reference simulation. In the QCTM simulation (EMAC-QCTM, 1998-2007)) the chemistry is decoupled from radiation and dynamics, thus omitting feedback mechanisms between these fundamental aspects of a chemistry-climate model. The setups of the free-running timeslice simulations (EMAC-TS2000 and EMAC-ACCMIP) differ from each other in the emission inventories and the SSTs. To follow the specification of the *Atmospheric Chemistry and Climate Model Intercomparison Project* (ACCMIP), emissions from Lamarque et al. (2010) and modeled SSTs and SICs from the *Centro Euro-Mediterraneo per i Cambiamenti Climatici* (CMCC) climate model are used as input parameters in the EMAC-ACCMIP simulation. The boundary conditions in the EMAC-TS2000 simulation are more similar to the nudged simulations, except that emissions and SSTs are climatological means instead of transient datasets. All four EMAC simulations are carried out in T42-L90MA resolution, i.e. with a spherical truncation of T42 (corresponding to a quadratic Gaussian grid of approximately $2.8^\circ \times 2.8^\circ$ degrees in latitude and longitude) with 90 vertical hybrid pressure levels up to 0.01 hPa.

In addition to a qualitative evaluation showing figures for a variety of different selected diagnostics, a quantitative evaluation has been performed to summarize the results. In particular, the normalized root-mean square difference (RMSD) between model simulation and observations as well as the overall mean bias have been calculated for certain domains and height-levels. Where possible, an alternate observational dataset was used in addition to the reference dataset to consider observational uncertainty that is introduced by differences between different instruments or meteorological reanalyses. In addition, Taylor diagrams which are a common graphical summary to evaluate climate models have been shown. These diagrams display the normalized standard deviation, the centered RMSD and the pattern correlation between the model simulation and observation.

The main differences due to the setup of the simulations (free-running versus nudged) are introduced through differences in the meteorology. The evaluation of the mean state of basic climate parameters is therefore important in addition to the evaluation of ozone. This work could show that the mean state of temperature, zonal wind, meridional wind, geopo-

tential height, specific humidity, and radiation is in general well represented by the four EMAC simulations. Some differences exist in specific regions and altitudes which are, except for the warm bias in the tropics and the polar southern hemispheric lower stratosphere in spring in the EMAC-ACCMIP simulation, related to the different setups (nudged versus free-running). These include:

- A warm bias ($\sim 0.5\text{-}1$ K) in the tropics in the EMAC-ACCMIP simulation at 850 hPa, which is related to the warm bias in the prescribed SSTs that are taken from a simulation with the CMCC climate model.
- A warm bias ($\sim 3\text{-}5$ K) in the polar southern hemispheric lower stratosphere (between about 100 hPa and 50 hPa) in spring in the free-running EMAC-TS2000 simulation, which is likely related to an underestimation of the ozone hole in this simulation. The nudged and the free-running EMAC-ACCMIP simulations produce an ozone hole closer to observations (see further discussion below) and thus no significant biases in the same region in the seasonal mean (JJA and SON).
- Too cold temperatures ($\sim 4\text{-}8$ K) in the tropical stratosphere. This bias is particularly present in the free-running timeslice simulations and might be related to a too strong Brewer-Dobson-Circulation (Jöckel et al., 2010).
- A cold bias ($\sim 3\text{-}7$ K) in the extratropical lowermost stratosphere in the free-running simulations (EMAC-TS2000 and EMAC-ACCMIP). This feature is common to many of the CMIP3 and CCMVal models (IPCC, 2007; SPARC CCMVal, 2010). This cold bias is related to the wet bias, an overestimation of water vapour in this region by around a factor of 2-10, depending on the season, leading to a too high infrared radiative cooling. The nudged simulations show the same wet bias but due to the assimilation of the temperature towards realistic meteorology, a reduced cold bias in the extratropical lowermost stratosphere.
- An underestimation of zonal wind by $\sim 10\text{-}20$ m/s (depending on the season) at 60°S in all four EMAC simulations in JJA and SON, which is more pronounced in the free-running simulations. These differences indicate a too weak polar vortex in the southern hemisphere.
- An underestimation of the polar night jet ($\sim 5\text{-}10$ m/s) in DJF on the northern hemisphere in the nudged simulations which indicates a too weak polar vortex in the northern hemisphere.
- An underestimation of the subtropical jet ($\sim 10\text{-}15$ m/s) at 60°S in DJF from the ground up to around 50 hPa in the free-running simulations.
- Biases in other climate parameters (meridional wind, specific humidity, geopotential height and radiation) were quantified and while quantitative differences to observations exist in certain regions, in general good agreement exists among the four model simulations and the observations.

The evaluation of tropospheric ozone and ozone precursors (nitrogen oxides (NO_x), carbon monoxide (CO) and non-methane hydrocarbons (NMHCs)) showed that generally only small differences exist among the four model simulations that are related to the model setup, but differences due to the use of different emissions in the EMAC-ACCMIP simulation exist:

- Tropospheric column ozone is generally slightly overestimated compared to observations, but the annual cycle of total column ozone is well represented. These differences could partly be related to uncertainties in the tropopause height of the model and the MLS/OMI observations, and to observational uncertainties.
- The ability of the EMAC simulations to reproduce observations from ozonesondes and insitu measurements depends on the region. Ozone profiles on the northern hemisphere are generally reproduced well and are within the interannual standard deviation (1σ), while all EMAC simulations do not reproduce the profiles in the tropics, the southern midlatitudes and the southern polar region. In these regions ozone concentrations are severely underestimated and the annual cycle is not captured.
- The EMAC simulations have problems in representing surface ozone. Depending on the region, over- or underestimations are found. The Western Europe region, for example shows an overestimation in the summer month, while surface ozone is underestimated in the tropics and North America. This is likely related to the emissions of ozone precursors. The new emissions inventory from Lamarque et al. (2010) used in the EMAC-ACCMIP simulations does only partly improve this problem despite the higher emission totals, which could be related to the geographical distribution of the emissions.
- The vertical profiles of NO_x for the selected regions are simulated well by EMAC and are broadly within the 90% quantile of the observations except for the upper tropospheric levels, where differences between the EMAC simulations themselves and the observations exist.
- The evaluation of CO showed an underestimation compared to observations in all EMAC simulations, particularly in regions with anthropogenic influence. Better results were achieved in remote locations. The EMAC-ACCMIP simulation with its different emission inventory that includes a factor of 2 higher CO emissions than the inventory used in the other three simulations is in better agreement with the observations.
- All four EMAC simulations have difficulties in simulating NMHCs in the chosen regions. This could be due to the NMHC totals in the inventories, but also due to a wrong NMHC speciation. While the EMAC simulations fail in reproducing C_3H_6 (propene) which is underestimated severely, C_3H_8 (propane) is mostly overestimated and outside the 90% quantile of the observations.

Stratospheric ozone and selected key processes are generally well simulated compared to different observational datasets, but large differences in the representation of the ozone hole between the two free-running simulations exist, pointing to the importance of the prescribed SSTs for stratospheric performance:

- The ozone hole is underestimated in all EMAC simulations, which is apparent in the comparison of total column ozone. The annual cycle in total column ozone is well represented, but total column ozone values are overestimated in the northern hemispheric spring and the ozone hole is underestimated in the southern hemispheric spring in all model simulations, but particularly in the EMAC-TS2000 simulation. The other free-running simulation (EMAC-ACCMIP) has a better representation of the ozone hole, which is likely related to the modeled SSTs prescribed in this simulation.

- Simulated vertical ozone profiles in the stratosphere are in good agreement with the observations and generally lie within the interannual standard deviation (1σ) in the tropics. An overestimation of the mixing ratios is found however in the southern polar region at 50 hPa in spring, which again shows the problem of the EMAC simulations in representing the ozone hole.
- Except for the EMAC-TS2000 simulation, a small cold bias ($\sim 1-5$ K) in the southern hemispheric polar ($60^\circ-90^\circ$ S) winter and spring seasons is found. The warm bias above 200 hPa ($\sim 1-6$ K) in the SON seasonal mean in the southern polar regions in the EMAC-TS2000 is likely related to the missing ozone depletion.
- Evaluating stratospheric winds shows that the transition to easterlies occurs too early in the two free-running simulations, but is simulated correctly in the nudged simulations. Additionally, the zonal mean wind at 60° S is underestimated in southern hemispheric spring, particularly by the EMAC-TS2000 simulation. This again indicates a too weak polar vortex, which would be in agreement with the underestimation of the ozone hole.
- Stratospheric transport processes evaluated by gradients in methane (CH_4) concentrations are represented well in the tropics and midlatitudes, but too high tracer concentrations and not steep enough latitudinal gradients in CH_4 are found in the polar regions, where CH_4 concentrations lie outside 1σ of the observation.
- HCl is simulated well by all EMAC simulations. EMAC-TS2000 shows lowest mixing ratios at 50 hPa in the Antarctic. The other chlorine species evaluated in this thesis was inorganic chlorine (Cl_y) which shows good agreement with the observations at 50 hPa in the northern midlatitudes, while Cl_y is underestimated by around 0.3 to 0.5 ppbv in 80° S in 50 hPa. However, observations for this species are sparse.
- Water vapour is underestimated throughout the stratosphere above 100 hPa, except above around 3 hPa in the tropics. This is related to the more accurate temperatures, simulated by the nudged simulations around the tropical tropopause that determines the entry of stratospheric water vapour.

7.2 Conclusion and Outlook

In general, no large differences were identified that were related to the different setup of the model (nudged versus free-running). This opens the possibility to evaluate the overall model performance with the help of shorter nudged simulations in comparison to observations in particular years to learn something about the free-running simulation that is used for chemistry-climate projections and that has to be evaluated in a statistical manner. However, some differences due to the setup that were identified in Section 7.1 have been found, and in many cases the two corresponding simulations of one setup (nudged or free-running) are more alike.

The difference in boundary conditions (emissions and SSTs/SICs) leads to differences between the EMAC-ACCMIP and the other three simulations. In particular, the role of the prescribed SSTs on the ability of the model to realistically simulate the ozone hole was identified through a comparison of the two free-running simulations, with one (EMAC-TS2000) prescribing observed and the other one (EMAC-ACCMIP) modeled SSTs. The EMAC-TS2000 simulation has major problems representing the ozone hole with observed

SSTs, whereas the EMAC-ACCMIP simulation that used modeled SSTs showed a much better agreement with the observations, similar to the representation of the ozone hole in the nudged simulations. For the temperature at 850 hPa in the tropics, the EMAC-ACCMIP simulation shows a warm bias compared to ERA-Interim and NCEP due to the bias in the tropics in the prescribed modeled SSTs.

The new emission inventory of Lamarque et al. (2010) used for the EMAC-ACCMIP simulation improves the representation of certain tropospheric ozone precursors (like CO or C₂H₆). However, an improvement in the representation of tropospheric ozone is not clearly apparent.

Overall, as summarized in Section 7.1, this thesis has identified differences between the EMAC simulations and observations. While several of these biases could be quantified and explained, further analysis and sensitivity studies are required to fully understand all the deviations from observations, for example:

- Differences in the temperature and zonal wind could partly be explained, while the other basic climate parameters (meridional wind, specific humidity, geopotential height and radiation) were only briefly evaluated and reasons for the differences to observations could be further investigated.
- The importance of ozone precursors and other processes (e.g. stratosphere-troposphere exchange) in the context of the ability of the model to realistically simulate tropospheric ozone needs to be further investigated. The differences of NO_x in the upper troposphere cannot be explained with differences in the emissions and would therefore require a more detailed analysis of the involved chemical reactions. The representation of CO, particularly in South West Asia is a long-standing problem in many models and will require more extensive analysis in the future. Also, the different representation of the NMHCs which might be due to the speciation fraction adopted for the different NMHCs compounds could be the subject of future sensitivity studies.
- The dynamical aspects of the underestimation of the ozone hole in particular in the free-running EMAC-TS2000 timeslice simulation is further investigated in a follow up study.
- The influence of different emission inventories could be identified by a comparison of the EMAC-ACCMIP simulation to the other three simulations. This analysis demonstrates the importance of accurate emission inventories. However, large uncertainties in emission inventories still exist and might require further analysis. If the emissions are wrong, a correct simulation of ozone is obviously not possible. The new emission inventory of Lamarque et al. (2010) improves the performance, as can be seen in the EMAC-ACCMIP simulation for the tropospheric variables related to ozone. Especially CO and some of the NMHCs (like C₂H₆) perform better with this new emission inventory. Similar to the emissions, the different SSTs and SICs in the EMAC-ACCMIP simulation have an influence on the ability of the model to reproduce observations.

In addition, the model evaluation itself can be improved or made more robust by considering additional observational datasets and their uncertainties. Examples include comparison to the MERRA reanalysis or the climatologies that are currently established by the SPARC Data and the ESA Climate Change Initiative. The quantitative model evaluation can be improved by considering the results of the t-test in the overall mean bias and root mean square calculation or by applying other statistical methods.

The results of this thesis are important for several follow-up studies in particular because the model simulations evaluated here are reference simulations for several sensitivity studies that are currently underway. The EMAC-QCTM simulation is the reference simulation of the DLR project VEU (*Verkehrsentwicklung und Umwelt*), where the influence of traffic emissions is investigated. The EMAC-ACCMIP simulation is one of the simulations within the ACCMIP-project covering the period from 1850 to 2100. Apart from the direct use of this evaluation for upcoming projects, the evaluation can be used to guide further model improvements.

And finally, the CCMVal-Diagnostic tool, an open source tool for the evaluation of climate models, has been extended with new observations and new routines for the troposphere and a quantitative model evaluation. The extended version can be used to routinely evaluate EMAC simulations and forms the basis for the evaluation tool in the DLR ESMVal (*Earth System Model Validation*) project. In follow up studies this evaluation tool can be further developed by implementing new diagnostics or additional observations. The evaluation tool will significantly facilitate the complex evaluation of EMAC on the long-term.

A publication that summarizes the results presented in this thesis is in preparation for submission to a peer-reviewed journal.

References

- Allen, D. J., and K. E. Pickering, 2002: Evaluation of lightning flash rate parameterizations for use in a global chemical transport model. *J. Geophys. Res.*, 107, 4711.
- Arrhenius, S., 1896b: On the Influence of Carbonic Acid in the Air upon the Temperature of the Ground. London, Edinburgh, and Dublin Philosophical Magazine and Journal of Science (fifth series) April 1896, vol 41, pages 237–275.
- Aumann, H. H., M. T. Chahine, C. Gautier, M. D. Goldberg, E. Kalnay, L. M. McMillin, H. Revercomb, P. W. Rosenkranz, W. L. Smith, D. H. Staelin, L. L. Strow, and J. Susskind, 2003: AIRS/AMSU/HSB on the Aqua mission: design, science objectives, data products and processing system. *EEE Trans. Geosci. and Remote Sensing*, 41, 253-264.
- Barkstrom, B. R., 1984: The Earth Radiation Budget Experiment (ERBE). *Bulletin of the American Meteorological Society*, 65, 1170-1185.
- Bodeker, G. E., H. Shiona, and H. Eskes, 2005: Indicators of Antarctic ozone depletion. *Atmos. Chem. Phys.*, 5, 2603-2615.
- Borken-Kleefeld, J., H. Steller, G. D. Ceuster, F. Vanhove, M. Eide, O. Endresen, H. Behrens, D. Lee, B. Owen, T. Meretei, K. Rypdal, R. B. Skeie, J. v. Aardenne, G. Erhardt, and R. Sausen, 2010: QUANTIFY transport emission scenarios up to 2100. *Environmental Science and Technology*, in preparation.
- Boyer, T., C. Stephens, J. Antonov, M. Conkright, R. Locarnini, T. O'Brien, and H. Garcia, 2002: World Ocean Atlas 2001, Volume 2 Salinity p. 167 pp. NOAA Atlas NESDIS 50, U.S. Government Printing Office.
- Broadgate, W. J., P. S. Liss, and S. A. Penkett, 1997: Seasonal emissions of isoprene and other reactive hydrocarbon gases from the ocean. *Geophys. Res. Lett.*, 24, 2675-2678.
- Brühl, C., S. R. Drayson, J. M. Russell, III, P. J. Crutzen, J. M. McInerney, P. N. Purcell, H. Claude, H. Gernandt, T. J. McGee, I. S. McDermid, and M. R. Gunson, 1996: Halogen Occultation Experiment ozone channel validation. *J. Geophys. Res.*, 101, 10217-10240.
- Buchholz, J., 2005: Simulations of physics and chemistry of polar strato- spheric clouds with a general circulation model, Ph.D. thesis, University of Mainz, Germany, <http://nbn-resolving.de/urn/resolver.pl?urn=urn:nbn:de:hebis:77-8187>.
- Cagnazzo, C., E. Manzini, M. A. Giorgetta, P. M. D. F. Forster, and J. J. Morcrette, 2007: Impact of an improved shortwave radiation scheme in the MAECHAM5 General Circulation Model. *Atmos. Chem. Phys.*, 7, 2503-2515.
- Chapman, S., 1930: A theory of upper atmosphere ozone. *Memoirs of the Royal Meteorological Society*, pp.103–125.
- Cionni, I., V. Eyring, J. F. Lamarque, W. J. Randel, D. S. Stevenson, F. Wu, G. E. Bodeker, T. G. Shepherd, D. T. Shindell, and D. W. Waugh, 2011: Ozone database in support of CMIP5 simulations: results and corresponding radiative forcing. *Atmos. Chem. Phys.*, 11, 11267-11292.
- de Laat, A. T. J., I. Aben, and G. J. Roelofs, 2005: A model perspective on total tropospheric O₃ column variability and implications for satellite observations. *J. Geophys. Res.*, 110, D13303.

- Deckert, R., P. Jöckel, V. Grewe, K. D. Gottschaldt, and P. Hoor, 2011: A quasi chemistry-transport model mode for EMAC. *Geosci. Model Dev.*, 4, 195-206.
- Dee, D. P., S. M. Uppala, A. J. Simmons, P. Berrisford, P. Poli, S. Kobayashi, U. Andrae, M. A. Balmaseda, G. Balsamo, P. Bauer, P. Bechtold, A. C. M. Beljaars, L. van de Berg, J. Bidlot, N. Bormann, C. Delsol, R. Dragani, M. Fuentes, A. J. Geer, L. Haimberger, S. B. Healy, H. Hersbach, E. V. Hólm, L. Isaksen, P. Kållberg, M. Köhler, M. Matricardi, A. P. McNally, B. M. Monge-Sanz, J. J. Morcrette, B. K. Park, C. Peubey, P. de Rosnay, C. Tavolato, J. N. Thépaut, and F. Vitart, 2011: The ERA-Interim reanalysis: configuration and performance of the data assimilation system. *Quarterly Journal of the Royal Meteorological Society*, 137, 553-597.
- Dentener, F., S. Kinne, T. Bond, O. Boucher, J. Cofala, S. Generoso, P. Ginoux, S. Gong, J. J. Hoelzemann, A. Ito, L. Marelli, J. E. Penner, J. P. Putaud, C. Textor, M. Schulz, G. R. van der Werf, and J. Wilson, 2006: Emissions of primary aerosol and precursor gases in the years 2000 and 1750 prescribed data-sets for AeroCom. *Atmos. Chem. Phys.*, 6, 4321-4344.
- Emmons, L. K., D. A. Hauglustaine, J.-F. Müller, M. A. Carroll, G. P. Brasseur, D. Brunner, J. Staehelin, V. Thouret, and A. Marengo, 2000: Data composites of airborne observations of tropospheric ozone and its precursors. *J. Geophys. Res.*, 105, 20497-20538.
- Emmons, L. K., P. Hess, A. Klonecki, X. Tie, L. Horowitz, J. F. Lamarque, D. Kinnison, G. Brasseur, E. Atlas, E. Browell, C. Cantrell, F. Eisele, R. L. Mauldin, J. Merrill, B. Ridley, and R. Shetter, 2003: Budget of tropospheric ozone during TOPSE from two chemical transport models. *J. Geophys. Res.*, 108, 8372.
- Eyring, V., M. P. Chipperfield, M. A. Giorgetta, D. E. Kinnison, E. Manzini, K. Matthes, P. A. Newman, S. Pawson, T. G. Shepherd, and D. W. Waugh, 2008: Overview of the New CCMVal Reference and Sensitivity Simulations in Support of Upcoming 460 Ozone and Climate Assessments and the Planned SPARC CCMVal. *SPARC Newsletter*, pp. 20–26.
- Eyring, V., I. S. A. Isaksen, T. Berntsen, W. J. Collins, J. J. Corbett, O. Endresen, R. G. Grainger, J. Moldanova, H. Schlager, and D. S. Stevenson, 2010a: Transport impacts on atmosphere and climate: Shipping. *Atmospheric Environment*, 44, 4735-4771.
- Eyring, V., I. Cionni, J. F. Lamarque, H. Akiyoshi, G. E. Bodeker, A. J. Charlton-Perez, S. M. Frith, A. Gettelman, D. E. Kinnison, T. Nakamura, L. D. Oman, S. Pawson, and Y. Yamashita, 2010b: Sensitivity of 21st century stratospheric ozone to greenhouse gas scenarios. *Geophys. Res. Lett.*, 37, L16807.
- Eyring, V., N. R. P. Harris, M. Rex, T. G. Shepherd, D. W. Fahey, G. T. Amanatidis, J. Austin, M. P. Chipperfield, M. Dameris, P. M. D. F. Forster, A. Gettelman, H. F. Graf, T. Nagashima, P. A. Newman, S. Pawson, M. J. Prather, J. A. Pyle, R. J. Salawitch, B. D. Santer, and D. W. Waugh, 2005: A Strategy for Process-Oriented Validation of Coupled Chemistry–Climate Models. *Bulletin of the American Meteorological Society*, 86, 1117-1133.
- Eyring, V., N. Butchart, D. W. Waugh, H. Akiyoshi, J. Austin, S. Bekki, G. E. Bodeker, B. A. Boville, C. Brühl, M. P. Chipperfield, E. Cordero, M. Dameris, M. Deushi, V. E. Fioletov, S. M. Frith, R. R. Garcia, A. Gettelman, M. A. Giorgetta, V. Grewe, L. Jourdain, D. E. Kinnison, E. Mancini, E. Manzini, M. Marchand, D. R. Marsh, T. Nagashima, P. A. Newman, J. E. Nielsen, S. Pawson, G. Pitari, D. A. Plummer, E. Rozanov, M. Schraner, T. G. Shepherd, K. Shibata, R. S. Stolarski, H. Struthers, W.

- Tian, and M. Yoshiki, 2006: Assessment of temperature, trace species, and ozone in chemistry-climate model simulations of the recent past. *J. Geophys. Res.*, 111, D22308.
- Fahey, D. W., and M. I. Hegglin, 2011: Twenty Questions and Answers About the Ozone Layer: 2010 Update.
- Fichefet, T., and M. A. M. Maqueda, 1997: Sensitivity of a global sea ice model to the treatment of ice thermodynamics and dynamics. *J. Geophys. Res.*, 102, 12609-12646.
- Fogli, P. G., and Coauthors, 2009: INGV-CMCC Carbon: A Carbon Cycle Earth System Model, CMCC online RP0061: <http://www.cmcc.it/publications-meetings/publications/research-papers/rp0061-ingvcmcc-carbon-icc-a-carbon-cycle-earth-system-model><http://www.cmcc.it/publicationsmeetings/publications/research-papers/rp0061-ingv-cmcc-carbon-icc-a-carbon-cycle-earth-systemmodel>.
- Fortuin, P. J. F., and H. Kelder, 1998: An ozone climatology based on ozonesonde and satellite measurements. *J. Geophys. Res.*, 103, 31709-31734.
- Fourier, J., 1824: Remarques Générales Sur Les Températures Du Globe Terrestre Et Des Espaces Planétaires. *Annales de Chimie et de Physique*, Vol. 27, pp. 136–167.
- Ganzeveld, L. N., J. A. van Aardenne, T. M. Butler, M. G. Lawrence, S. M. Metzger, P. Stier, P. Zimmermann, and J. Lelieveld, 2006: Technical Note: Anthropogenic and natural offline emissions and the online Emissions and dry DEPosition submodel EMDEP of the Modular Earth Submodel system (MESSy). *Atmos. Chem. Phys. Discuss.*, 6, 5457-5483.
- Garcia, R. R., and B. A. Boville, 1994: “Downward Control” of the Mean Meridional Circulation and Temperature Distribution of the Polar Winter Stratosphere. *Journal of the Atmospheric Sciences*, 51, 2238-2245.
- Garny, H., M. Dameris, and A. Stenke, 2009: Impact of prescribed SSTs on climatologies and long-term trends in CCM simulations. *Atmos. Chem. Phys.*, 9, 6017-6031.
- GCOS, 2010 Implementation Plan for the Global Observing System for Climate in Support of the UNFCCC, August 2010.
- Gottelman, A., V. Eyring, C. Fischer, H. Shiona, I. Cionni, M. Neish, G. Bodeker, and S. W. Wood, 2011, in prep.: A Community Diagnostic Tool for Chemistry Climate Model Validation. *Atmos. Chem. Phys.*
- GEWEX-news, February 2011, Vol. 21, No. 1.
- Giorgetta, M. A., and L. Bengtsson, 1999: Potential role of the quasi-biennial oscillation in the stratosphere-troposphere exchange as found in water vapor in general circulation model experiments. *J. Geophys. Res.*, 104, 6003-6019.
- Gleckler, P. J., K. E. Taylor, and C. Doutriaux, 2008: Performance metrics for climate models. *J. Geophys. Res.*, 113, D06104.
- GLOBALVIEW-CO, 2009: Cooperative Atmospheric Data Integration Project - Carbon Monoxide. CD-ROM. NOAA ESRL, [Also available on Internet via anonymous FTP to <ftp.cmdl.noaa.gov>, Path: [ccg/co/GLOBALVIEW](ftp://ftp.cmdl.noaa.gov/ccg/co/GLOBALVIEW)].
- Grewe, V., D. Brunner, M. Dameris, J. L. Grenfell, R. Hein, D. Shindell, and J. Staehelin, 2001: Origin and variability of upper tropospheric nitrogen oxides and ozone at northern mid-latitudes. *Atmospheric Environment*, 35, 3421-3433.

- Groß, J. U., and J. M. Russell III, 2005: Technical note: A stratospheric climatology for O₃, H₂O, CH₄, NO_x, HCl and HF derived from HALOE measurements. *Atmos. Chem. Phys.*, 5, 2797-2807.
- Harries, J. E., J. M. Russell, III, A. F. Tuck, L. L. Gordley, P. Purcell, K. Stone, R. M. Bevilacqua, M. Gunson, G. Nedoluha, and W. A. Traub, 1996: Validation of measurements of water vapor from the Halogen Occultation Experiment (HALOE). *J. Geophys. Res.*, 101, 10205-10216.
- Hartmann, D. L., Ed., 1994: *Global Physical Climatology*. Academic Press.
- Hegglin, M. I., A. Gettelman, P. Hoor, R. Krichevsky, G. L. Manney, L. L. Pan, S. W. Son, G. Stiller, S. Tilmes, K. A. Walker, V. Eyring, T. G. Shepherd, D. Waugh, H. Akiyoshi, J. A. Añel, J. Austin, A. Baumgaertner, S. Bekki, P. Braesicke, C. Brühl, N. Butchart, M. Chipperfield, M. Dameris, S. Dhomse, S. Frith, H. Garny, S. C. Hardiman, P. Jöckel, D. E. Kinnison, J. F. Lamarque, E. Mancini, M. Michou, O. Morgenstern, T. Nakamura, D. Olivie, S. Pawson, G. Pitari, D. A. Plummer, J. A. Pyle, E. Rozanov, J. F. Scinocca, K. Shibata, D. Smale, H. Teysse, W. Tian, and Y. Yamashita, 2010: Multimodel assessment of the upper troposphere and lower stratosphere: Extratropics. *J. Geophys. Res.*, 115, D00M09.
- Hoell, J. M., D. D. Davis, D. J. Jacob, M. O. Rodgers, R. E. Newell, H. E. Fuelberg, R. J. McNeal, J. L. Raper, and R. J. Bendura, 1999: Pacific Exploratory Mission in the tropical Pacific: PEM-Tropics A, August-September 1996. *J. Geophys. Res.*, 104, 5567-5583.
- Hoor, P., J. Borken-Kleefeld, D. Caro, O. Dessens, O. Endresen, M. Gauss, V. Grewe, D. Hauglustaine, I. S. A. Isaksen, P. Jöckel, J. Lelieveld, G. Myhre, E. Meijer, D. Olivie, M. Prather, C. Schnadt Poberaj, K. P. Shine, J. Staehelin, Q. Tang, J. van Aardenne, P. van Velthoven, and R. Sausen, 2009: The impact of traffic emissions on atmospheric ozone and OH: results from QUANTIFY. *Atmos. Chem. Phys.*, 9, 3113-3136.
- IPCC, 2007: Intergovernmental Panel on Climate Change (IPCC), *Climate Change 2007: The Physical Science Basis. Contribution of Working Group I to the Fourth Assessment Report of the Intergovernmental Panel on Climate Change*.
- IPCC, 2001: Intergovernmental Panel on Climate Change (IPCC), *Climate Change 2001: The Physical Science Basis Contribution of Working Group I to the Third Assessment Report of the Intergovernmental Panel on Climate Change*.
- Jacob, D. J., 1999: *Introduction to Atmospheric Chemistry*. Princeton Univ. Press.
- Jeuken, A. B. M., P. C. Siegmund, L. C. Heijboer, J. Feichter, and L. Bengtsson, 1996: On the potential of assimilating meteorological analyses in a global climate model for the purpose of model validation. *J. Geophys. Res.*, 101, 16939-16950.
- Jöckel, P., A. Kerkweg, J. Buchholz-Dietsch, H. Tost, R. Sander, and A. Pozzer, 2008: Technical Note: Coupling of chemical processes with the Modular Earth Submodel System (MESSy) submodel TRACER. *Atmos. Chem. Phys.*, 8, 1677-1687.
- Jöckel, P., A. Kerkweg, A. Pozzer, R. Sander, H. Tost, H. Riede, A. Baumgaertner, S. Gromov, and B. Kern, 2010: Development cycle 2 of the Modular Earth Submodel System (MESSy2). *Geosci. Model Dev.*, 3, 717-752.
- Jöckel, P., H. Tost, A. Pozzer, C. Brühl, J. Buchholz, L. Ganzeveld, P. Hoor, A. Kerkweg, M. Lawrence, G. R. Sander, B. Steil, G. Stiller, M. Tanarhte, D. Taraborrelli, J. van Aardenne, and J. Lelieveld, 2006: The atmospheric chemistry general circulation

- model ECHAM5/MESSy1: consistent simulation of ozone from the surface to the mesosphere. *Atmos. Chem. Phys.*, 6, 5067-5104.
- Kalnay, E., M. Kanamitsu, R. Kistler, W. Collins, D. Deaven, L. Gandin, M. Iredell, S. Saha, G. White, J. Woollen, Y. Zhu, A. Leetmaa, R. Reynolds, M. Chelliah, W. Ebisuzaki, W. Higgins, J. Janowiak, K. C. Mo, C. Ropelewski, J. Wang, R. Jenne, and D. Joseph, 1996: The NCEP/NCAR 40-Year Reanalysis Project. *Bulletin of the American Meteorological Society*, 77, 437-471.
- Karpechko, A. Y., N. P. Gillett, B. Hassler, K. H. Rosenlof, and E. Rozanov, 2010: Quantitative assessment of Southern Hemisphere ozone in chemistry-climate model simulations. *Atmos. Chem. Phys.*, 10, 1385-1400.
- Kerkweg, A., R. Sander, H. Tost, and P. Jöckel, 2006b: Technical note: Implementation of prescribed (OFFLEM), calculated (ONLEM), and pseudo-emissions (TNUDGE) of chemical species in the Modular Earth Submodel System (MESSy). *Atmos. Chem. Phys.*, 6, 3603-3609.
- Kerkweg, A., J. Buchholz, L. Ganzeveld, A. Pozzer, H. Tost, and P. Jöckel, 2006a: Technical Note: An implementation of the dry removal processes DRY DEposition and SEDimentation in the Modular Earth Submodel System (MESSy). *Atmos. Chem. Phys.*, 6, 4617-4632.
- Kettle, A. J., and M. O. Andreae, 2000: Flux of dimethylsulfide from the oceans: A comparison of updated data sets and flux models. *J. Geophys. Res.*, 105, 26793-26808.
- Kirner, O., R. Ruhnke, J. Buchholz-Dietsch, P. Jöckel, C. Brühl, and B. Steil, 2011: Simulation of polar stratospheric clouds in the chemistry-climate-model EMAC via the submodel PSC. *Geosci. Model Dev.*, 4, 169-182.
- Knutti, R., 2010: The end of model democracy? *Climatic Change*, 102, 395-404.
- Knutti, R., R. Furrer, C. Tebaldi, J. Cermak, and G. A. Meehl, 2010a: Challenges in Combining Projections from Multiple Climate Models. *Journal of Climate*, 23, 2739-2758.
- Knutti, R., G. Abramowitz, Collins, V. Eyring, P. J. Gleckler, B. Hewitson, and L. Mearns., 2010b: Good Practice Guidance Paper on Assessing and Combining Multi Model Climate Projections 0165-0009.
- Lamarque, J. F., T. C. Bond, V. Eyring, C. Granier, A. Heil, Z. Klimont, D. Lee, C. Liousse, A. Mieville, B. Owen, M. G. Schultz, D. Shindell, S. J. Smith, E. Stehfest, J. Van Aardenne, O. R. Cooper, M. Kainuma, N. Mahowald, J. R. McConnell, V. Naik, K. Riahi, and D. P. van Vuuren, 2010: Historical (1850–2000) gridded anthropogenic and biomass burning emissions of reactive gases and aerosols: methodology and application. *Atmos. Chem. Phys.*, 10, 7017-7039.
- Landgraf, J., and P. J. Crutzen, 1998: An Efficient Method for Online Calculations of Photolysis and Heating Rates. *Journal of the Atmospheric Sciences*, 55, 863-878.
- Lawrence, M. G., and P. J. Rasch, 2005: Tracer Transport in Deep Convective Updrafts: Plume Ensemble versus Bulk Formulations. *Journal of the Atmospheric Sciences*, 62, 2880-2894.
- Lean, J., 2000: Evolution of the Sun's Spectral Irradiance Since the Maunder Minimum. *Geophys. Res. Lett.*, 27, 2425-2428.
- Lin, S.-J., and R. B. Rood, 1996: Multidimensional Flux-Form Semi-Lagrangian Transport Schemes. *Monthly Weather Review*, 124, 2046-2070.

- Logan, J. A., 1999: An analysis of ozonesonde data for the troposphere: Recommendations for testing 3-D models and development of a gridded climatology for tropospheric ozone. *J. Geophys. Res.*, 104, 16115-16149.
- Madec, G., P. Delecluse, I. Imbard, and C. Levy, 1999: OPA 8.1 Ocean General Circulation Model reference manual. Note du Pôle de modélisation No. 11, Inst. Pierre-Simon Laplace (IPSL), France, 91pp.
- Manzini, E., M. A. Giorgetta, M. Esch, L. Kornbluh, and E. Roeckner, 2006: The Influence of Sea Surface Temperatures on the Northern Winter Stratosphere: Ensemble Simulations with the MAECHAM5 Model. *Journal of Climate*, 19, 3863-3881.
- Masarie, K. A., and P. P. Tans, 1995: Extension and integration of atmospheric carbon dioxide data into a globally consistent measurement record. *J. Geophys. Res.*, 100, 11593-11610.
- Moss, R. H., J. A. Edmonds, K. A. Hibbard, M. R. Manning, S. K. Rose, D. P. van Vuuren, T. R. Carter, S. Emori, M. Kainuma, T. Kram, G. A. Meehl, J. F. B. Mitchell, N. Nakicenovic, K. Riahi, S. J. Smith, R. J. Stouffer, A. M. Thomson, J. P. Weyant, and T. J. Wilbanks, 2010: The next generation of scenarios for climate change research and assessment. *Nature*, 463, 747-756.
- Nakicenovic, N., J. Alcamo, G. Davis, B. de Vries, J. Fenhann, S. Gaffin, K. Gregory, A. Grubler, T. Y. Jung, T. Kram, E. L. La Rovere, L. Michaelis, S. Mori, T. Morita, W. Pepper, H. M. Pitcher, L. Price, K. Riahi, A. Roehrl, H.-H. Rogner, A. Sankovski, M. Schlesinger, P. Shukla, S. J. Smith, R. Swart, S. van Rooijen, N. Victor, and Z. Dadi, 2000: Special Report on Emissions Scenarios: A Special Report of Working Group III of the Intergovernmental Panel on Climate Change.
- Naujokat, B., 1986: An Update of the Observed Quasi-Biennial Oscillation of the Stratospheric Winds over the Tropics. *Journal of the Atmospheric Sciences*, 43, 1873-1877.
- Nordeng, T.-E., 1994: Extended versions of the convection parametrization scheme at ECMWF and their impact upon the mean climate and transient activity of the model in the tropics. Research Dept Technical Memorandum No. 206, ECMWF, Shinfield Park, Reading RG2 9AX, United Kingdom.
- Park, J. H., J. M. Russell, III, L. L. Gordley, S. R. Drayson, D. C. Benner, J. M. McInerney, M. R. Gunson, G. C. Toon, B. Sen, J. F. Blavier, C. R. Webster, E. C. Zipf, P. Erdman, U. Schmidt, and C. Schiller, 1996: Validation of Halogen Occultation Experiment CH4 measurements from the UARS. *J. Geophys. Res.*, 101, 10183-10203.
- Pozzer, A., P. Jöckel, R. Sander, J. Williams, L. Ganzeveld, and J. Lelieveld, 2006: Technical Note: The MESSy-submodel AIRSEA calculating the air-sea exchange of chemical species. *Atmos. Chem. Phys.*, 6, 5435-5444.
- Pozzer, A., P. Jöckel, H. Tost, R. Sander, L. Ganzeveld, A. Kerkweg, and J. Lelieveld, 2007: Simulating organic species with the global atmospheric chemistry general circulation model ECHAM5/MESSy1: a comparison of model results with observations. *Atmos. Chem. Phys.*, 7, 2527-2550.
- Price, C., and D. Rind, 1994: Modeling Global Lightning Distributions in a General Circulation Model. *Monthly Weather Review*, 122, 1930-1939.
- Prinn, R. G., R. F. Weiss, P. J. Fraser, P. G. Simmonds, D. M. Cunnold, F. N. Alyea, S. O'Doherty, P. Salameh, B. R. Miller, J. Huang, R. H. J. Wang, D. E. Hartley, C. Harth,

- L. P. Steele, G. Sturrock, P. M. Midgley, and A. McCulloch, 2000: A history of chemically and radiatively important gases in air deduced from ALE/GAGE/AGAGE. *J. Geophys. Res.*, 105, 17751-17792.
- Rayner, N. A., D. E. Parker, E. B. Horton, C. K. Folland, L. V. Alexander, D. P. Rowell, E. C. Kent, and A. Kaplan, 2003: Global analyses of sea surface temperature, sea ice, and night marine air temperature since the late nineteenth century. *J. Geophys. Res.*, 108, 4407.
- Reichler, T., and J. Kim, 2008: How Well Do Coupled Models Simulate Today's Climate? *Bulletin of the American Meteorological Society*, 89, 303-311.
- Roeckner, E., R. Brokopf, M. Esch, M. Giorgetta, S. Hagemann, L. Kornbluh, E. Manzini, U. Schlese, and U. Schulzweida, 2006: Sensitivity of Simulated Climate to Horizontal and Vertical Resolution in the ECHAM5 Atmosphere Model. *Journal of Climate*, 19, 3771-3791.
- Russell, J. M., III, L. L. Gordley, J. H. Park, S. R. Drayson, W. D. Hesketh, R. J. Cicerone, A. F. Tuck, J. E. Frederick, J. E. Harries, and P. J. Crutzen, 1993: THE HALOGEN OCCULTATION EXPERIMENT. *J. Geophys. Res.*, 98, 10777-10797.
- Russell, J. M., III, L. E. Deaver, M. Luo, J. H. Park, L. L. Gordley, A. F. Tuck, G. C. Toon, M. R. Gunson, W. A. Traub, D. G. Johnson, K. W. Jucks, D. G. Murcray, R. Zander, I. G. Nolt, and C. R. Webster, 1996: Validation of hydrogen chloride measurements made by the Halogen Occultation Experiment from the UARS platform. *J. Geophys. Res.*, 101, 10151-10162.
- Sander, R., A. Kerkweg, P. Jöckel, and J. Lelieveld, 2005: Technical note: The new comprehensive atmospheric chemistry module MECCA. *Atmos. Chem. Phys.*, 5, 445-450.
- Sander, R., A. Baumgaertner, S. Gromov, H. Harder, P. Jöckel, A. Kerkweg, D. Kubistin, E. Regelin, H. Riede, A. Sandu, D. Taraborrelli, H. Tost, and Z. Q. Xie, 2011: The atmospheric chemistry box model CAABA/MECCA-3.0. *Geosci. Model Dev.*, 4, 373-380.
- Sandu, A., and R. Sander, 2006: Technical note: Simulating chemical systems in Fortran90 and Matlab with the Kinetic PreProcessor KPP-2.1. *Atmos. Chem. Phys.*, 6, 187-195.
- Santer, B. D., K. E. Taylor, T. M. L. Wigley, T. C. Johns, P. D. Jones, D. J. Karoly, J. F. B. Mitchell, A. H. Oort, J. E. Penner, V. Ramaswamy, M. D. Schwarzkopf, R. J. Stouffer, and S. Tett, 1996: A search for human influences on the thermal structure of the atmosphere. *Nature*, 382, 39-46.
- Schlesinger, M. E., Ed., 1988: *Physically-Based Modelling and Simulation of Climate and Climatic Change, Part 1*. Kluwer Academic Publishers.
- Schmitt, A., and B. Brunner, 1997: Emissions from aviation and their development over time, in: *Pollutants from air traffic results of atmospheric research 1992-1997. Final Report on the BMBF Verbundprogramm Schadstoffe in der Luftfahrt*, Tech. report, DLR-Mitteilung 97-04, pp. 1301.
- Shaw, T. A., and T. G. Shepherd, 2008: Atmospheric science: Raising the roof. *Nature Geosci*, 1, 12-13.
- SPARC CCMVal, Ed., 2010: *SPARC Report on the Evaluation of Chemistry-Climate Models*, V. Eyring, T. G. Shepherd, D. W. Waugh (Eds.). SPARC Report No. 5, WCRP-132, WMO/TD-No. 1526, <http://www.atmosph.physics.utoronto.ca/SPARC>.

- Spiro, P. A., D. J. Jacob, and J. A. Logan, 1992: Global Inventory of Sulfur Emissions With $1^{\circ}\times 1^{\circ}$ Resolution. *J. Geophys. Res.*, 97, 6023-6036.
- Steil, B., C. Brühl, E. Manzini, P. J. Crutzen, J. Lelieveld, P. J. Rasch, E. Roeckner, and K. Krüger, 2003: A new interactive chemistry-climate model: 1. Present-day climatology and interannual variability of the middle atmosphere using the model and 9 years of HALOE/UARS data. *J. Geophys. Res.*, 108, 4290.
- Stenke, A., V. Grewe, and M. Ponater, 2008: Lagrangian transport of water vapor and cloud water in the ECHAM4 GCM and its impact on the cold bias. *Climate Dynamics*, 31, 491-506.
- Storch, H. v., and F. W. Zwiers, 1984: *Statistical Analysis in Climate Research*. Cambridge University Press.
- Tanre, D., J.-F. Geleyn, and J. M. Slingo, 1984: First results of the introduction of an advanced aerosol-radiation interaction in the ECMWF low resolution global model. In: *Aerosols and their climatic effects* pp. 133-177, H. Gerber and A. Deepak, Eds., A. Deepak, Hampton, VA.
- Taylor, K. E., 2001: Summarizing multiple aspects of model performance in a single diagram. *J. Geophys. Res.*, 106, 7183-7192.
- Thompson, D. W. J., and S. Solomon, 2002: Interpretation of Recent Southern Hemisphere Climate Change. *Science*, 296, 895-899.
- Thompson, D. W. J., and S. Solomon, 2005: Recent stratospheric climate trends as evidenced in radiosonde data: Global structure and tropospheric linkages. *J. Climate*, 18, 4785-4795.
- Thompson, D. W. J., M. P. Baldwin, and S. Solomon, 2005: Stratosphere–Troposphere Coupling in the Southern Hemisphere. *Journal of the Atmospheric Sciences*, 62, 708-715.
- Tiedtke, M., 1989: A Comprehensive Mass Flux Scheme for Cumulus Parameterization in Large-Scale Models. *Monthly Weather Review*, 117, 1779-1800.
- Tilmes, S., J. F. Lamarque, L. K. Emmons, A. Conley, M. G. Schultz, M. Saunio, V. Thouret, A. M. Thompson, S. J. Oltmans, B. Johnson, and D. Tarasick, 2011: Ozone sonde climatology between 1995 and 2009: description, evaluation and applications. *Atmos. Chem. Phys. Discuss.*, 11, 28747-28796.
- Tost, H., P. Jöckel, A. Kerkweg, R. Sander, and J. Lelieveld, 2006: Technical note: A new comprehensive SCAVenging submodel for global atmospheric chemistry modelling. *Atmos. Chem. Phys.*, 6, 565-574.
- Valcke, S., 2006: OASIS3 User Guide (prism_2-5), PRISM Report No 2, 6th Ed., CERFACS, Toulouse, France, 64 pp.
- van Aalst, M. K., M. M. P. van den Broek, A. Bregman, C. Brühl, B. Steil, G. C. Toon, S. Garcelon, G. M. Hansford, R. L. Jones, T. D. Gardiner, G. J. Roelofs, J. Lelieveld, and P. J. Crutzen, 2004: Trace gas transport in the 1999/2000 Arctic winter: comparison of nudged GCM runs with observations. *Atmos. Chem. Phys.*, 4, 81-93.
- van Aardenne, J. A., F. Dentener, J. G. G. Olivier, J. A. H. W. Peters, and L. N. Ganzeveld, 2005: The EDGAR3.2 Fast Track 2000 dataset (32FT2000), Tech. rep., Joint Research Centre, Institute for Environment and Sustainability (JRC-IES), Climate Change Unit, TP280, 21020, Ispra (Va), Italy, <http://www.mnp.nl/edgar/model/v32ft2000edgar/docv32ft2000/>.

- van der Werf, G. R., J. T. Randerson, L. Giglio, G. J. Collatz, M. Mu, P. S. Kasibhatla, D. C. Morton, R. S. DeFries, Y. Jin, and T. T. van Leeuwen, 2010: Global fire emissions and the contribution of deforestation, savanna, forest, agricultural, and peat fires (1997–2009). *Atmos. Chem. Phys.*, 10, 11707-11735.
- van Vuuren, D., K. Riahi, S. Smith, M. Meinshausen, M. Mastrandrea, and R. Moss, 2009: RCP Extension White Paper.
- von Kuhlmann, R., M. G. Lawrence, P. J. Crutzen, and P. J. Rasch, 2003: A model for studies of tropospheric ozone and nonmethane hydrocarbons: Model evaluation of ozone-related species. *J. Geophys. Res.*, 108, 4729.
- Wallace, J. M., and P. V. Hobbs, 2006: *Atmospheric Science, 2nd Edition An Introductory Survey*.
- Waugh, D. W., and V. Eyring, 2008: Quantitative performance metrics for stratospheric-resolving chemistry-climate models. *Atmos. Chem. Phys.*, 8, 5699-5713.
- web1: <http://www.srh.noaa.gov/jetstream//global/images/jetstream3.jpg>.
- web2: http://eosweb.larc.nasa.gov/PRODOCS/srb/table_srb.html.
- web3: <http://ceres.larc.nasa.gov/>.
- Wielicki, B. A., B. R. Barkstrom, E. F. Harrison, R. B. Lee, G. Louis Smith, and J. E. Cooper, 1996: Clouds and the Earth's Radiant Energy System (CERES): An Earth Observing System Experiment. *Bulletin of the American Meteorological Society*, 77, 853-868.
- WMO, 2002: (World Meteorological Organization) Scientific Assessment of Ozone Depletion: Global Ozone Research and Monitoring Project—Report, No. 47, 498pp., Geneva 2003.
- WMO, 2007: (World Meteorological Organization) Scientific Assessment of Ozone Depletion: 2006. Global Ozone Research and Monitoring Project - Report No. 50, 572pp, Geneva.
- WMO, 2011: (World Meteorological Organization), Scientific Assessment of Ozone Depletion: 2010. Global Ozone Research and Monitoring Project—Report, No. 52, 516pp. Geneva, Switzerland.
- Yokoi, S., Y. N. Takayabu, K. Nishii, H. Nakamura, H. Endo, H. Ichikawa, T. Inoue, M. Kimoto, Y. Kosaka, T. Miyasaka, K. Oshima, N. Sato, Y. Tsushima, and M. Watanabe, 2011: Application of Cluster Analysis to Climate Model Performance Metrics. *Journal of Applied Meteorology and Climatology*, 50, 1666-1675.
- Ziemke, J. R., S. Chandra, G. J. Labow, P. K. Bhartia, L. Froidevaux, and J. C. Witte, 2011: A global climatology of tropospheric and stratospheric ozone derived from Aura OMI and MLS measurements. *Atmos. Chem. Phys.*, 11, 9237-9251.
- Ziemke, J. R., S. Chandra, B. N. Duncan, L. Froidevaux, P. K. Bhartia, P. F. Levelt, and J. W. Waters, 2006: Tropospheric ozone determined from Aura OMI and MLS: Evaluation of measurements and comparison with the Global Modeling Initiative's Chemical Transport Model. *J. Geophys. Res.*, 111, D19303.

Abbreviations

ACCMIP	Atmospheric Chemistry Climate Model Intercomparison Project
AeroCom	Aerosol Comparisons between Observations and Models
AGAGE	Advanced Global Atmospheric Gases Experiment
AGCM	Atmosphere General Circulation Model
AIRS	Atmospheric Infrared Sounder
AIRSEA	MESSy submodel
AMIP	Atmospheric Model Intercomparison Project
BDC	Brewer Dobson Circulation
Br _x	Bromines
CCM	Chemistry-Climate Model
CMCC	Centro Euro-Mediterraneo per I Cambiamenti Climatici
CCMVal	Chemistry-Climate Model Validation Activity
CMIP	Climate Model Intercomparison Project
CERES	Clouds and the Earth's Radiant Energy System
CFC	Chlorofluorocarbon
CH ₄	Methane
CLOUD	Messy submodel
Cl _x	Chlorines
Cl _y	Inorganic Chlorine
CMAP	CPC Merged Analysis of Precipitation
CO	Carbon Monoxide
CO ₂	Carbon Dioxide
CONVECT	Messy submodel
CPC	Climate Prediction Center
cRMSD	Centered Pattern Root Mean Square Difference
CVTRANS	MESSy submodel
DJF	December January February (Seasonal Mean)
DMS	Dimethyl sulfide
DLR	Deutsches Zentrum für Luft- und Raumfahrt
DRYDEP	MESSy submodel
DU	Dobson Unit
E39C	ECHAM4.L39(DLR) model
ECMWF	European Center for Medium-Range Weather Forecasts
ECHAM	ECMWF Hamburg (General Circulation Model)
ECHAM5	5th Generation European Centre Hamburg General Circulation Model
ECV	Essential Climate Variable
EDGAR	Emissions Database for Global Atmospheric Research
EDM	Energy Balance Model
EMAC	ECHAM/MESSy Atmospheric Chemistry (Model)
EMEP	Co-operative Programme for Monitoring and Evaluation of the Long-range Transmission of Air Pollutants in Europe
EMIC	Earth Model of Intermediate Complexity
ERA-40	ECMWF Reanalysis (40 years reanalysis since 1957)
ERA-Interim	ECMWF Reanalysis (time period from 1989 to present)
ERBE	Earth Radiation Budget Experiment
ESM	Earth System Model

ESRL	Earth System Research Laboratory
GCM	General Circulation Model / Global Circulation Model
GCOS	Global Climate Observing System
GCPP	Global Precipitation Climatology Centre
GEWEX	Global Energy and Water Cycle Experiment
GFED	Global Fire Emissions Database
GLOBALVIEW	NOAA ESRL data products
GMD	Global Monitoring Division
GOME	Global Ozone Monitoring Experiment
GPCP	Global Precipitation Climatology Project
HALOE	Halogen Occultation Experiment
HadISST	Global sea-Ice coverage and SST, Met Office
HETCHEM	MESSy submodel
HCl	Hydrogen Chloride
HF	Hydrogen Fluoride
HNO ₃	Nitric Acid
H ₂ O	MESSy submodel; H ₂ O as a tracer
H ₂ O	Water / Water Vapour
H _x O _y	Hydrogen Oxides
ITCZ	Inter Tropical Convergence Zone
IPCC	Intergovernmental Panel on Climate Change
IPCC AR4	Intergovernmental Panel on Climate Change Assessment Report 4
IPCC AR5	Intergovernmental Panel on Climate Change Assessment Report 5
JJA	June July August (Seasonal Mean)
JVAL	MESSy submodel
L2010	Emission Inventory, Lamarque et al., 2010
LNOX	MESSy submodel
MAECHAM4/CHEM	MESSy submodel
MAM	March April Mai (Seasonal Mean)
MECCA	MESSy submodel
MESSy	Modular Earth Submodel System
MLS	Microwave Limb Sounder
N ₂	Nitrogen (molecule)
NCAR	National Center for Atmospheric Research
NCEP	National Center for Environmental Prediction
NCL	NCAR Command Language
netCDF	Network Common Data Format
NH	Northern Hemisphere
NIWA	National Institute of Water and Atmospheric Research
NMHCs	None-methane Hydrocarbons
NO	Nitrogen Monoxide
NO ₂	Nitrogen Dioxide
NO _x	Nitrogen Oxides
NOAA	National Oceanic and Atmospheric Administration
O	Oxygen (atom)
O ₂	Oxygen (molecule)
O ₃	Ozone
ODS	Ozone Depleting Substance

OFFEMIS	MESSy submodel
OFFLEM	MESSy submodel
OH	Hydroxyl Radical
OMI	Aura Ozone Monitoring Instrument
PAN	Peroxyacetylnitrat
PEM	Pacific Exploration Mission
PSC	Polar Stratospheric Cloud
PSC	MESSy submodel
PTRAC	MESSy submodel
QUANTIFY	Quantifying the Climate Impact of Global and European Transport System
QCTM	Quasi Chemical-Transport Mode
QBO	MESSy submodel
QBO	Quasi-Biannual Oscillation
RAD4ALL	MESSy submodel
RC	Radiative-Convective Model
RF	Radiative Forcing
RCP	Representative Concentration Pathways
RMSD	Root Mean Square Difference
SB97	Emissions, Schmitt & Brunner., 1997
SBUV	Solar Backscatter Ultraviolet Spectral Radiometer
SCAV	MESSy submodel
SD	Statistical Dynamical Model
SEDI	MESSy submodel
SH	Southern Hemisphere
SIC	Sea Ice Cover
SON	September October November (Seasonal Mean)
SPARC	Stratospheric Processes and their Role in Climate
SRB	Surface Radiation Budget Project
SRES	Special Report on Emissions Scenarios
SST	Sea Surface Temperature
TNUDGE	MESSy submodel
TOMS	Total Ozone Mapping Spectrometer
TOPSE	Tropospheric Ozone Production about the Spring Equinox (Campaign)
TOZ	Total Column Ozone
TRACE-A	Transport and Atmospheric Chemistry near the Equator-Atlantic (Experiment)
TRACE-P	Transport and Chemical Evolution over the Pacific (Mission)
TROPOP	MESSy submodel
TTL	Tropical Tropopause Layer
UARS	Upper Atmosphere Research Satellite
UNFCCC	United Nations Framework Convention on Climate Change
UV	Ultra-Violet (radiation)
VP	Vertical Profile
WMO	World Meteorological Organization
WRCP	World Climate Research Programme

List of Figures

- Figure 1.** Decadal mean tropospheric column ozone, in the RCPs 2.6 and 8.5 at the end of the 21st century. From Cionni et al. (2011), their Figure 9.....5
- Figure 2.** 1980 baseline-adjusted annual mean global total ozone column from 17 CCM simulations. The thick black line shows the multi-model mean and the light- and dark-grey shaded regions show the 95% confidence and 95% prediction intervals, respectively. The red vertical dashed line indicates the year when the multi-model mean returns to 1980 values and the blue vertical dashed lines indicate the uncertainty in these return dates. The green horizontal dashed line refers to the 1980 baseline. From Eyring et al. (2010b), their Figure 1.....6
- Figure 3.** Components of the Earth’s system, interactions and processes. From IPCC 2007, Chapter 1, FAQ 1.2, Figure 1.....9
- Figure 4.** Global mean energy balance showing the equilibrium between incoming solar and outgoing longwave radiation. About half of the incoming solar radiation is absorbed by the Earth’s surface. This energy is transferred to the atmosphere by warming the air in contact with the surface (thermals), by evapotranspiration and by longwave radiation that is absorbed by clouds and greenhouse gases. The atmosphere in turn radiates longwave energy back to Earth as well as out to space. From IPCC 2007, Chapter 1, FAQ 1.1, Figure 1.....10
- Figure 5.** Idealized meridional cross section of the temperature distribution (schematic). Contour intervals of 20°C, pink regions show warmer, blue regions cooler areas. From Wallece and Hobbs (2006), their Figure 1.11.13
- Figure 6.** Midlatitude temperature profile from U.S. Standard Atmosphere. From Wallece and Hobbs (2006), their Figure 1.09.....14
- Figure 7.** Schematic description of the Earth’s wind patterns and pressure belts. Hadley cell and subtropical jets (J) are shown as well. From Wallece and Hobbs (2006), their Figure 1.15.16
- Figure 8.** Meridional cross section of the atmospheric cells and jet streams (web2).....16
- Figure 9.** Idealized meridional cross section of the wind strength and direction (contours of 10 m/s) for the summer and winter hemisphere. Yellow areas indicate regions of easterlies, red areas regions of westerlies. The more intensive the color, the stronger the winds are. Small differences in northern and southern hemispheric seasons are neglected. From Wallece and Hobbs (2006), their Figure 1.11.17
- Figure 10.** Longitudinally averaged cross-section of the atmosphere showing the Brewer–Dobson circulation (black arrows), and the ozone distribution as measured by the OSIRIS satellite instrument in March 2004. The circulation is forced by waves propagating up from the troposphere (orange arrows), especially in the winter hemisphere, and it strongly shapes the distribution of ozone by transporting it from its source region in the tropical upper stratosphere to the high-latitude lower stratosphere. The dashed line represents the tropopause. From Shaw and Shepherd (2008), their Figure 1.18
- Figure 11.** Stratospheric ozone production. Fahey and Hegglin (2011), their Figure Q2-1.19

- Figure 12.** Schematic illustration of tropospheric O₃ chemistry showing the coupling between the chemical cycles of ozone, HO_x and NO_x. From Jacob (1999), their Figure 1 (modified). 21
- Figure 13.** Taylor diagram: Illustrated are (left) examples of test (color coded) and reference fields (in black) and (right) their pattern statistics in the Taylor diagram. See text for explanation. From Hegglin et al. (2010), their Figure 2. 41
- Figure 14.** Schematic figure, showing the processes and components of the CCMVal-Diagnostic tool. From Gettelman et al. (2011, in prep.), their Figure 1. 44
- Figure 15.** Schematic figure, showing the processes and components of the statistical routine implemented into the CCMVal-Diagnostic tool..... 45
- Figure 16.** Annual cycle of temperature climatology at 5, 30, 200 and 850 hPa averaged globally, over the tropics (20°S-20°N), northern extratropics (20°N-90°N) and southern extra tropics (20°S-90°S) for different EMAC simulations in comparison to ERA-Interim and NCEP/NCAR reanalysis data. Grey shaded area indicates the ± 1 standard deviation. Note that the vertical scales are varying, to make differences between the EMAC simulations visible. 52
- Figure 17.** Annual mean zonally averaged temperature profile climatology for four different EMAC simulations in comparison to ERA-Interim and NCEP/NCAR reanalysis data. The upper left plot shows ERA-Interim absolute values; all other plots show differences between the NCEP reanalysis / the model simulations and ERA-Interim. The black dashed line in the model simulations shows the WMO tropopause height. Differences between the two fields that are not statistically significant according to the 95% confidence level are marked white..... 53
- Figure 18.** Seasonal mean zonally averaged temperature profile climatology for the EMAC-TS2000 simulations in comparison to ERA-Interim. The upper left plot shows the seasonal mean of MAM, the upper right of JJA. On the bottom the seasonal mean of SON (left) and DJF (right) is shown. The black dashed line in the model simulations shows the WMO tropopause height. Differences between the two fields that are not statistically significant according to the 95% confidence level. are marked white..... 55
- Figure 19.** Seasonal variation of climatological means at 200 hPa in the southern hemisphere extratropics for water vapour for different EMAC simulations. Modeled water vapour fields are compared to the 1991-2005 water vapour climatology from HALOE. 56
- Figure 20.** Tropopause height for the four EMAC simulations in comparison. The tropopause is calculated following the WMO definition, see details in the text..... 57
- Figure 21.** Seasonal variation of climatological means at 100 hPa at the equator for temperature (right) and water vapour (left) for different EMAC simulations. Modeled water vapour fields are compared to the 1995-2005 temperature climatology from ERA-Interim and the 1991-2005 water vapour climatology from HALOE. 58
- Figure 22.** Same as Figure 16, but for zonal mean wind..... 59
- Figure 23.** Seasonal (DJF) mean zonal mean wind profile climatology for four different EMAC simulations in comparison to ERA-Interim and NCEP/NCAR reanalysis data. The upper left plot shows ERA-Interim absolute values; all other plots show differences between the model simulations/NCEP reanalysis and ERA-Interim. The black dashed line in the model simulations shows the WMO tropopause height. Only differences which are statistically significant within a 95% confidence interval (t-test) are shown..... 60

- Figure 24.** Seasonal (JJA) mean zonal mean wind profile climatology for four different EMAC simulations in comparison to ERA-Interim and NCEP/NCAR reanalysis data. The upper left plot shows ERA-Interim absolute values; all other plots show differences between the model simulations/NCEP reanalysis and ERA-Interim. The black dashed line in the model simulations shows the WMO tropopause height. Only values within a 95% significance interval (t-test) are shown for the difference plots. Values which are not significant are marked white.....61
- Figure 25.** Same as Figure 16, but for specific humidity. Instead of the 200 hPa level, the 400 hPa level is shown, following Gleckler et al. (2008).....62
- Figure 26.** Annual mean specific humidity profile climatology for four different EMAC simulations in comparison to AIRS and ERA-Interim reanalysis data. The upper left plot shows AIRS absolute values; all other plots show differences between the ERA-Interim / the model simulations and AIRS. Differences between the two fields that are not statistically significant according to the 95% c.l. are marked white.....64
- Figure 27.** Annual mean values of clear sky outgoing longwave radiation at TOA [W/m^2] from SRB (upper left), differences from SRB data to CERES data and to the four EMAC simulations.....65
- Figure 28.** Portrait diagrams showing the root mean square difference (of the chosen basic climate parameters over the global domain, the tropics, and the northern and southern extratropics.)66
- Figure 29.** Portrait diagrams showing the overall mean bias (of the chosen basic climate parameters over the global domain, the tropics, and the northern and southern extratropics.68
- Figure 30.** Taylor diagrams of selected basic climate parameters (temperature and zonal wind) over the four chosen domain and height-levels.....69
- Figure 31.** Locations of ozonesonde measurements (Tilmes et al. 2011, top panel), aircraft campaigns (Emmons et al., 2000, middle panel) and NOAA GLOBALVIEW stations (bottom panel) used for the model evaluation in this thesis.....71
- Figure 32.** Tropospheric column ozone from the four EMAC simulations compared to MLS/OMI observations averaged between 2005 and 2009 (Ziemke et al., 2011). The first row shows the annual cycle of the tropospheric column at different latitudes in the four EMAC simulations. The second row the tropospheric ozone column in the four EMAC simulations. The last row contains the corresponding observations for the annual cycle (left panel) and for the tropospheric column (right panel).....72
- Figure 33.** Comparison of tropospheric ozone (1000 hPa – 200 hPa) from different EMAC simulations with ozonesonde observations (Tilmes et al., 2011) from Western Europe and Tropics. The first row shows the annual cycle in the observations. The other rows show the equivalent plot from the EMAC simulations (left column). The right column compares all points, with bars indicating the standard deviation in the observations: where the model overpredicts (underpredicts) the observations by more the one standard deviation, these points are plotted in red (purple) and then overplotted on the left column as solid (dashed) contours.73
- Figure 34.** Vertical O_3 profiles from selected aircraft campaign observations by Emmons et al. (2000) and corresponding simulated values by the four EMAC simulations. Boxes and whiskers indicate the central 50% and 90% of the observations, respectively, with a vertical bar at the median and a star at the mean. The EMAC simulations are averaged over the

same region as the observations. Mean and standard deviations over the same time period as the model runs are shown by the solid and dashed lines.....	75
Figure 35. Similar to Figure 34, but for NO _x	78
Figure 36. Similar to Figure 34, but for CO.....	79
Figure 37. Annual cycle of the four EMAC simulations and NOAA GLOBALVIEW data for nine different stations world wide (see Figure 31, map at bottom). The grey shaded area shows the ± 1 standard deviation of the observation.....	80
Figure 38. Similar to Figure 34, but for OH.....	81
Figure 39. Similar to Figure 34, but for C ₂ H ₄	83
Figure 40. Portrait diagrams showing the root mean square difference (left) and the normalized overall mean bias (right) for chosen diagnostics of tropospheric ozone.	85
Figure 41. Taylor diagram of tropospheric ozone.	86
Figure 42. Portrait diagrams showing the root mean square difference (left) and the normalized overall mean bias (right) for chosen diagnostics of ozone precursors.	87
Figure 43. Climatological zonal mean O ₃ mixing ratios from different EMAC simulations and HALOE in ppmv. Upper panels (a-c): Vertical profiles at 80°N in March (left), 0° in March (middle) and 80°S in October (right). Lower panels (d,e): Latitudinal profiles at 50 hPa in March (left) and October (right). The grey area shows HALOE plus and minus 1 standard deviation (σ) about the climatological zonal mean. Climatological means were calculated for the years 1999-2007 (EMAC-QCTM), 1999-2009 (EMAC2-EVAL), 10 years timeslice (EMAC-TS2000), 12 years timeslice (EMAC-ACCMIP) and 1991-2005 (HALOE).	88
Figure 44. Total column ozone climatologies for different EMAC simulations (1999-2007 (QCTM), 1999-2009 (EMAC2-EVAL), 10 years timeslice (EMAC-TS2000), 5 years timeslice (EMAC-ACCMIP)) compared to the NIWA (1995-2005) combined total column ozone database (Bodeker et al., 2005) and GOME data (1996-2006).....	89
Figure 45. Zonal mean total ozone values for DJF, MAM, JJA, SON and the annual mean from GOME (mean values in black with standard deviations as background surfaces), NIWA (orange line indicating mean values and the shaded area the standard deviations), and results from the four EMCA simulations (blue, green, red and purple curves with mean and standard deviation).	90
Figure 46. Climatological mean temperature biases for 60°-90°N (upper panels) and 60°-90°S (lower panels) for the winter (left) and spring seasons (right). The climatological means for the four EMAC simulations (1999-2007 (EMAC-QCTM), 1999-2009 (EMAC2-EVAL), 10 years timeslice (EMAC-TS2000), 12 years timeslice (EMAC-ACCMIP)), NCEP/NCAR and ERA-Interim data from 1995-2005 are considered. Biases are calculated relative to ERA-Interim re-analyses. The grey area shows ERA-Interim plus and minus 1 standard deviation (σ) about the climatological mean.....	91
Figure 47. Descent of the zero zonal mean wind lines at 60°S based on the climatological mean annual cycle calculated from the monthly mean zonal mean winds for different EMAC simulations. The black dashed line shows the mean date of transition from easterlies to westerlies from ERA-Interim reanalysis, the grey area indicates the 1-sigma standard deviation. Tickmarks refer to the first day of the month. Climatological means are calculated as in Figure 3.	92

- Figure 48.** Annual cycle of zonal wind (left) and temperature (right) at 30 hPa at 55-60°S and 55-60°N from different EMAC simulations in comparison to ERA-Interim and NCEP/NCAR reanalysis data. The grey shaded area indicates the ± 1 standard deviation of ERA-Interim.....94
- Figure 49.** Same as Figure 43, but for CH₄ in ppmv.....95
- Figure 50.** Time-height sections of water vapour mixing ratio shown as the deviation (ppmv) from the time-mean profile, averaged between 10°S and 10°N ('tape recorder') for different EMAC simulations and HALOE data. Two consecutive cycles are shown.96
- Figure 51.** Vertical variation of (left) amplitude and (right) phase lag of annual cycle of water vapour averaged between 10°S and 10°N. The amplitude is normalized to unity and phase lag is set to zero at the level where the amplitude is maximum (between 16 and 20 km). The vertical axis in both plots is the distance from level of maximum amplitude. Solid circles are HALOE observations.97
- Figure 52.** Same as Figure 43, but for H₂O in ppmv.....98
- Figure 53.** Same as Figure 43, but for HCl in ppbv.....99
- Figure 54.** (a) Climatological mean vertical profiles (1999-2007 (EMAC-QCTM), 1999-2009 (EMAC2-EVAL), 10 years timeslice (EMAC-TS2000), 12 years timeslice (EMAC-ACCMIP)) at 80°S in November for Cl_y in ppbv. (b) and (c) Time series of October mean Antarctic Cl_y at 80°S from different EMAC simulations ((1998-2007 (QCTM), 1998-2007 (EMAC2-EVAL)) at 50 hPa and annual mean time series of Cl_y at mid-latitudes in 50 hPa. Estimates of Cl_y from Aura MLS HCl in 2005 [M. Santee, pers. communication] are shown in addition. 100
- Figure 55.** Portrait diagrams showing the normalized root mean square difference (left) and overall mean bias (right) of chosen diagnostics for stratospheric ozone and related key processes. For an explanation of the abbreviations for each performance metrics see Table 6..... 101
- Figure 56.** Taylor diagrams of stratospheric ozone..... 103
- Figure A1.** Same as Figure 16, but for meridional wind.xiii
- Figure A2.** Annual mean zonally averaged meridional wind profile climatology for four different EMAC simulations in comparison to ERA-Interim and NCEP/NCAR reanalysis data. The upper left plot shows ERA-Interim absolute values; all other plots show differences between the NCEP reanalysis / the model simulations and ERA-Interim. The black dashed line in the model simulations shows the WMO tropopause height. Differences between the two fields that are not statistically significant according to the 95% c.l. are marked white.....xiv
- Figure A3.** Same as **Figure 16** ,but for geopotential height. Instead of the 200 hPa level, the 500 hPa level is shown, following Gleckler et al. (2008).....xv
- Figure A4.** Annual mean zonally averaged geopotential height profile climatology for four different EMAC simulations in comparison to ERA-Interim and NCEP/NCAR reanalysis data. The upper left plot shows ERA-Interim absolute values; all other plots show differences between the NCEP reanalysis / the model simulations and ERA-Interim. The black dashed line in the model simulations shows the WMO tropopause height. Differences between the two fields that are not statistically significant according to the 95% c.l. are marked white.xvi

-
- Figure A5.** Annual mean values of all sky outgoing longwave radiation at TOA [W/m^2] from SRB (upper left), differences from SRB data to CERES data and to the four EMAC simulations.xvii
- Figure A6.** Annual mean values of of all sky TOA outgoing shortwave radiation [W/m^2] from SRB (upper left), differences from SRB data to CERES data and to the four EMAC simulations.....xviii

List of Tables

Table 1 List of the MESSy submodels that have been used in the simulations of this thesis	28
Table 2 Details of the four EMAC simulations evaluated in this thesis	29
Table 3 Boundary conditions and emission datasets for the simulations considered in this thesis. References to each dataset/inventory are given in the text. Below a specification whether data are used in transient or in constant (2000) mode, is given for each dataset. The Lamarque et al. (2010) inventory is abbreviated with L2010.	30
Table 4 List of core processes to evaluate basic mean climate state. Diagnostics for the evaluation are given along with the variable, observations, the short name and period / domain for the performance metric and references.	32
Table 5 List of core processes to evaluate tropospheric ozone. Diagnostics for the evaluation are given along with the variable, observations, the short name and period / domain for the performance metric and references.	34
Table 6 List of core processes to evaluate stratospheric ozone. Diagnostics for the evaluation are given along with the variable, observations, the short name and period / domain for the performance metric and references.	36
Table 7 Extensions of the CCMVal-Diagnostic tool for the evaluation of EMAC in this thesis.	46
Table 8 Total offline emissions for different species and sectors in the 4 runs. For transient emissions, minimum and maximum values for the simulated period (excluding the spin-up year) are given. For constant emission, the value refers to the year 2000. Units are Tg(species)/yr and Tg(NO)/yr for NO _x . See Table 3 for the corresponding emission inventories. NH ₃ emissions per sector are available only for the ACCMIP run, in the other cases only the total value is given in the last row.	xix
Table 9 Table 8 continued	xx

Appendix

A1 Figures

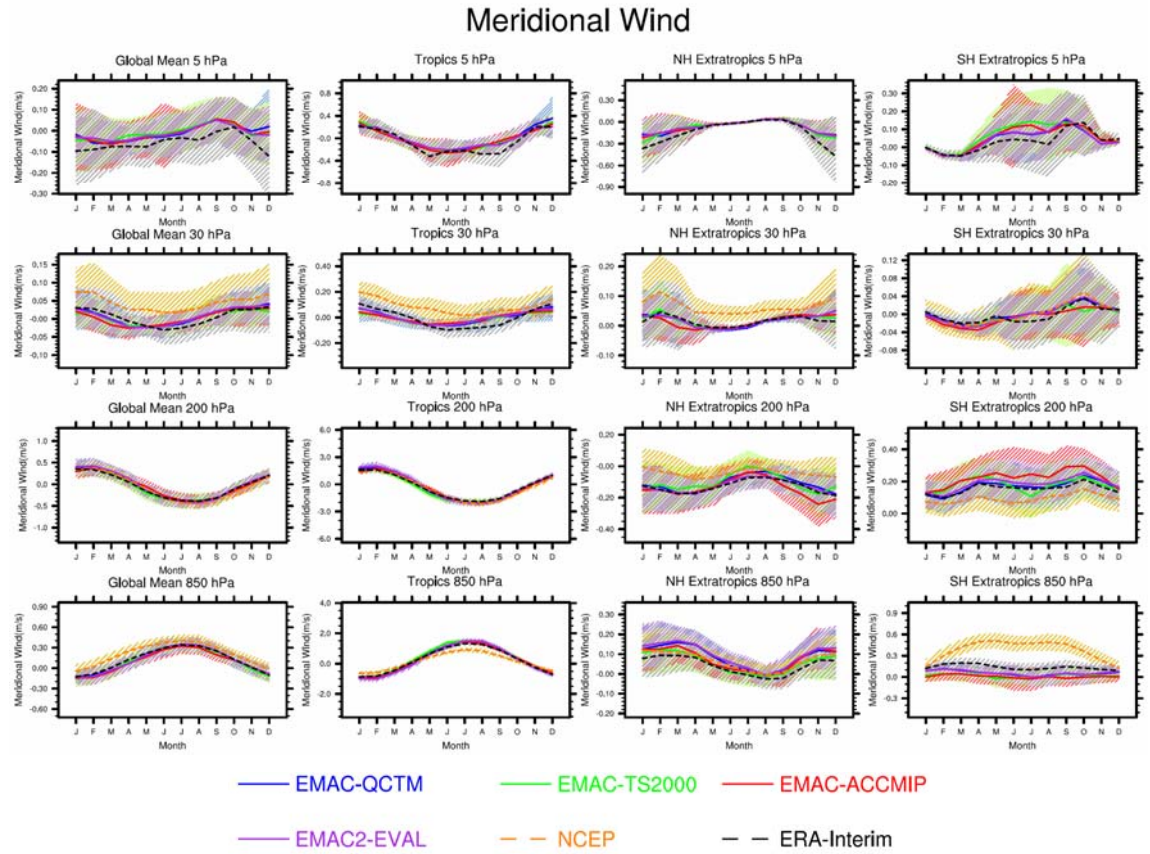


Figure A1. Same as Figure 16, but for meridional wind.

Annual Mean Meridional Wind [m/s] (95% c.l.)

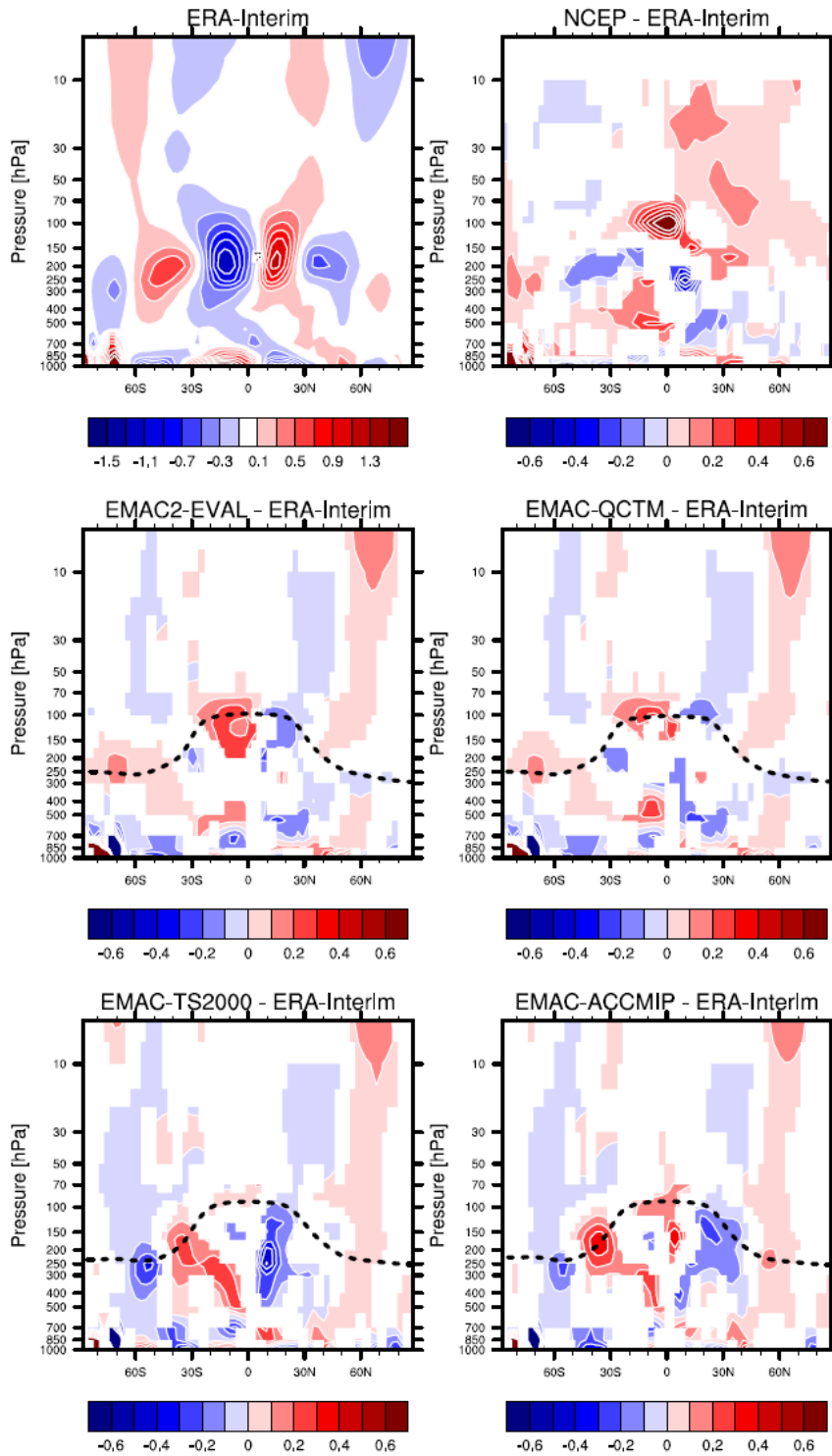


Figure A2. Annual mean zonally averaged meridional wind profile climatology for four different EMAC simulations in comparison to ERA-Interim and NCEP/NCAR reanalysis data. The upper left plot shows ERA-Interim absolute values; all other plots show differences between the NCEP reanalysis / the model simulations and ERA-Interim. The black dashed line in the model simulations shows the WMO tropopause height. Differences between the two fields that are not statistically significant according to the 95% c.l. are marked white.

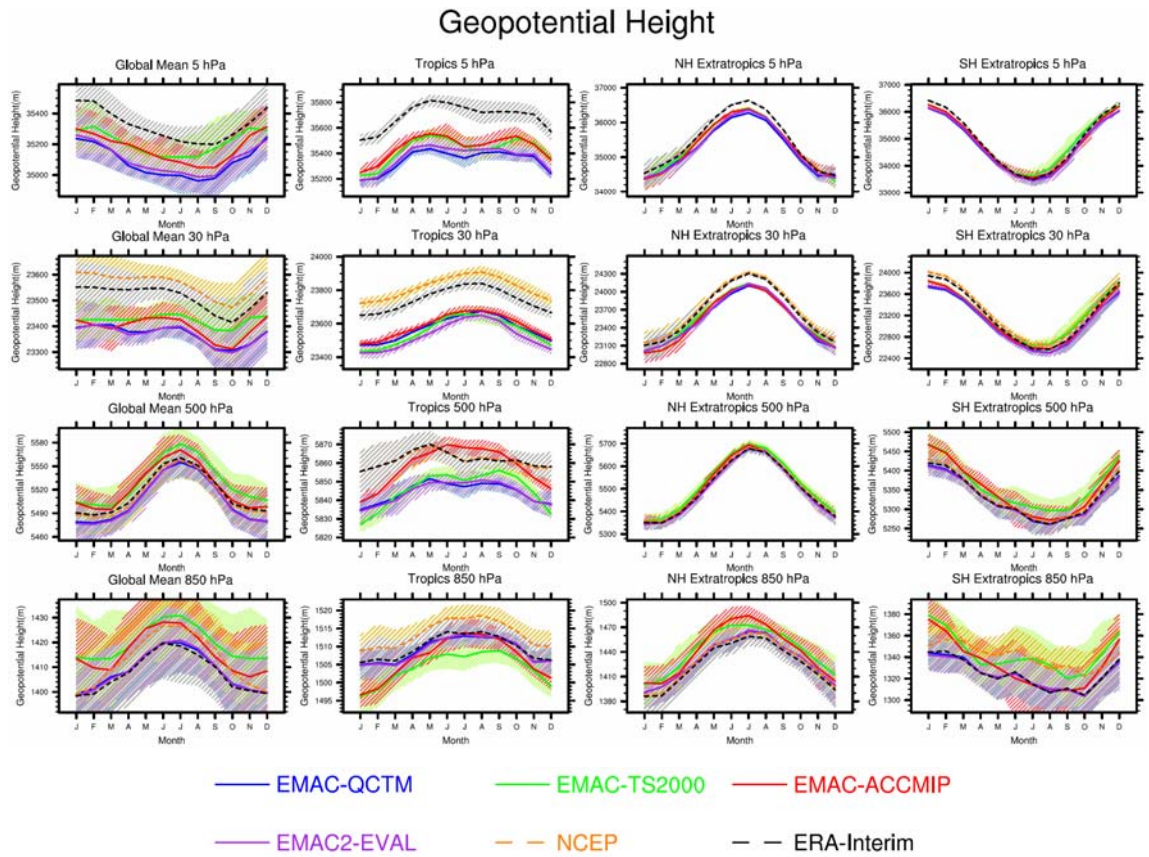


Figure A3. Same as Figure 16, but for geopotential height. Instead of the 200 hPa level, the 500 hPa level is shown, following Gleckler et al. (2008).

Annual Mean Geopotential Height [m] (95% c.l.)

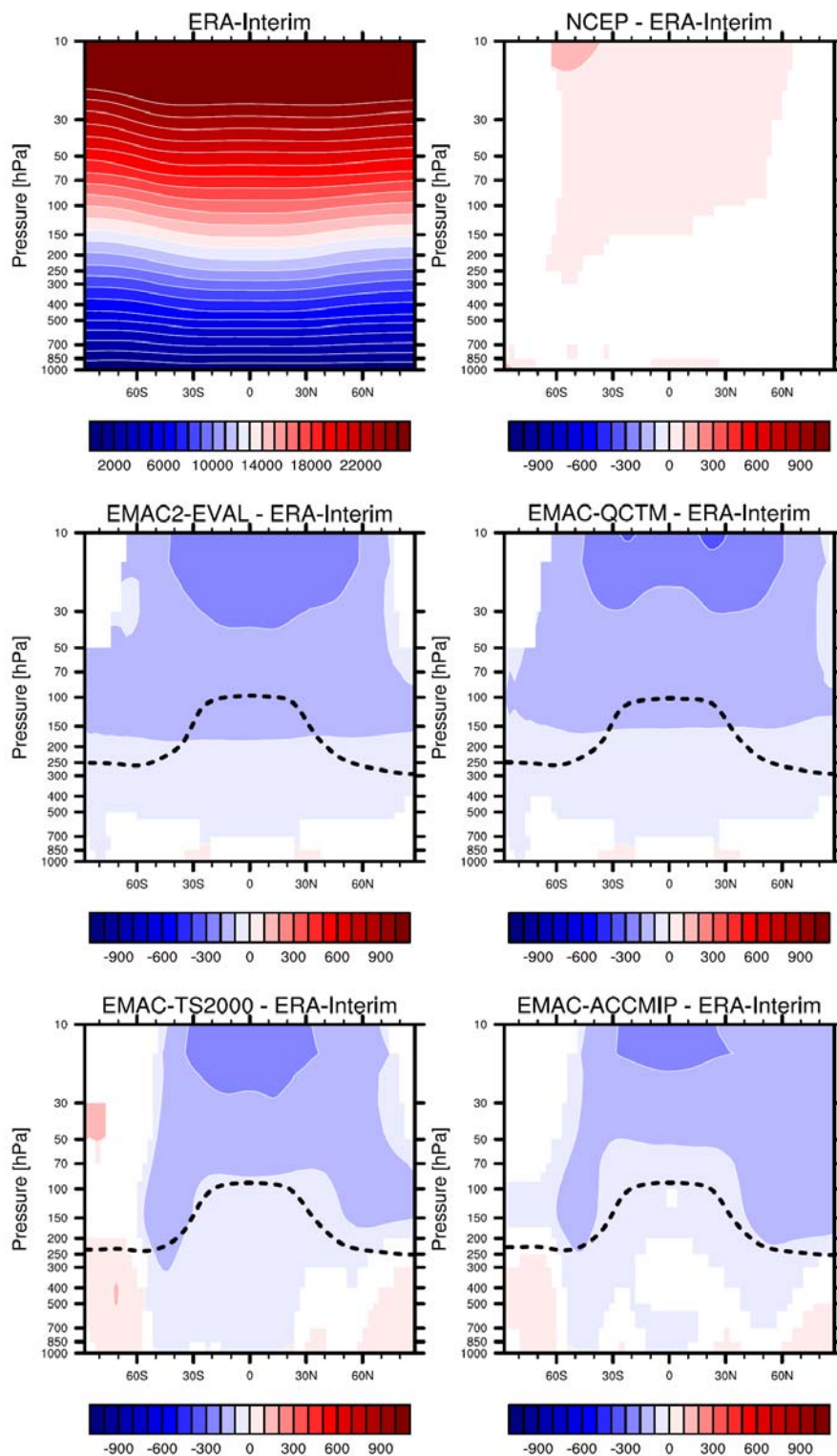


Figure A4. Annual mean zonally averaged geopotential height profile climatology for four different EMAC simulations in comparison to ERA-Interim and NCEP/NCAR reanalysis data. The upper left plot shows ERA-Interim absolute values; all other plots show differences between the NCEP reanalysis / the model simulations and ERA-Interim. The black dashed line in the model simulations shows the WMO tropopause height. Differences between the two fields that are not statistically significant according to the 95% c.l. are marked white.

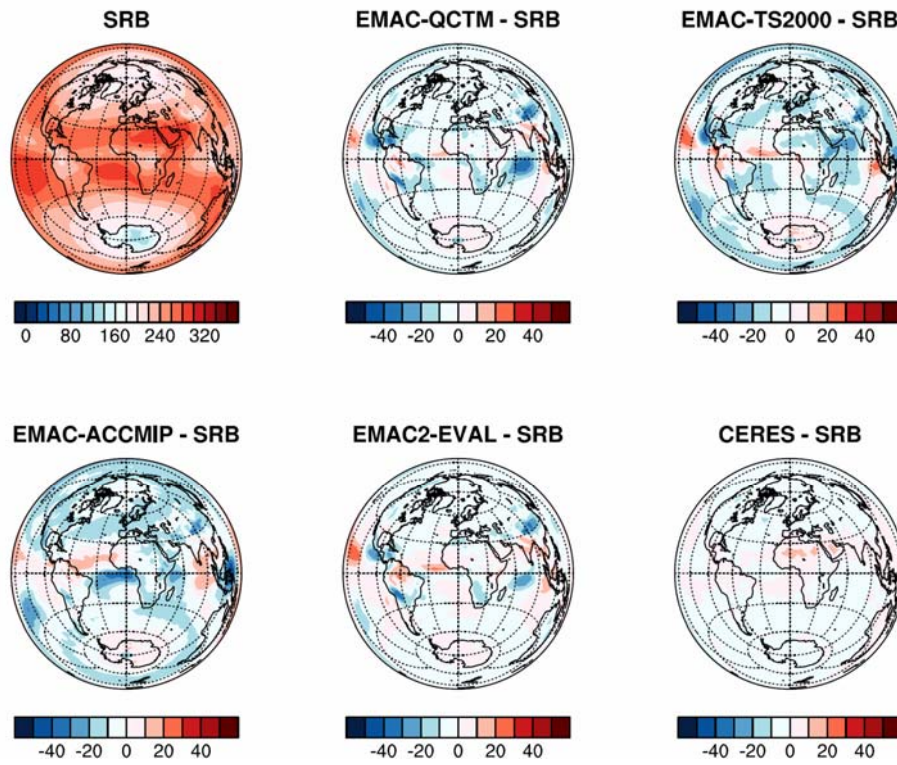
All Sky TOA Outgoing Longwave Radiation [W/m^2]

Figure A5. Annual mean values of all sky outgoing longwave radiation at TOA [W/m^2] from SRB (upper left), differences from SRB data to CERES data and to the four EMAC simulations.

All-Sky TOA Upward Shortwave Radiation [W/m^2]

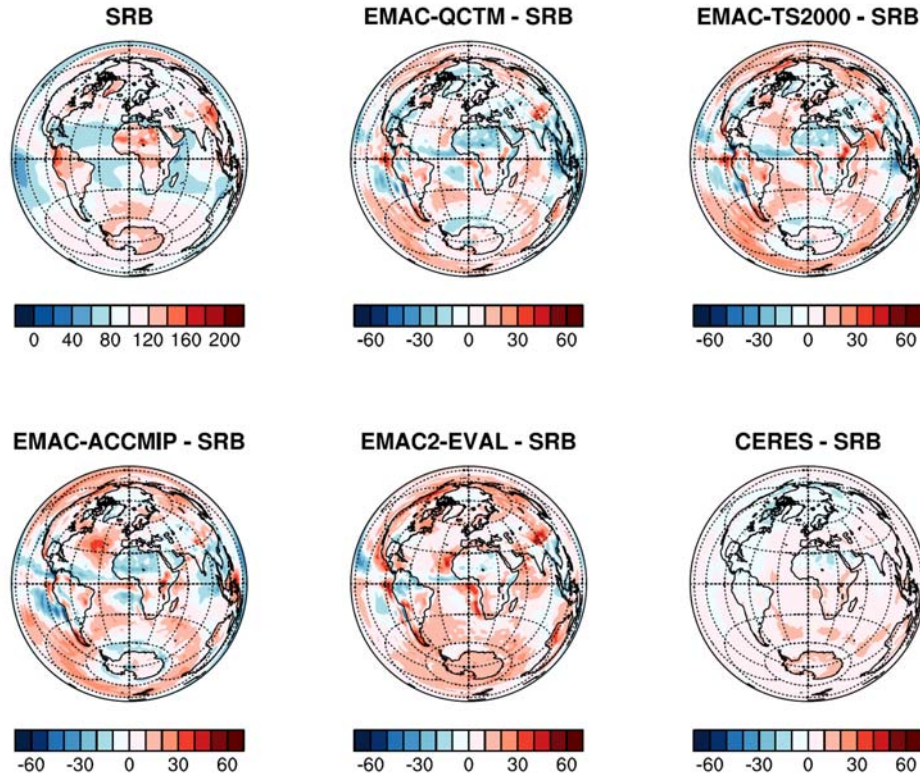


Figure A6. Annual mean values of of all sky TOA outgoing shortwave radiation [W/m^2] from SRB (upper left), differences from SRB data to CERES data and to the four EMAC simulations.

A2 Tables

Table 8 Total offline emissions for different species and sectors in the 4 runs. For transient emissions, minimum and maximum values for the simulated period (excluding the spin-up year) are given. For constant emission, the value refers to the year 2000. Units are Tg(species)/yr and Tg(NO)/yr for NO_x. See Table 3 for the corresponding emission inventories. NH₃ emissions per sector are available only for the ACCMIP run, in the other cases only the total value is given in the last row.

Sector	Experiment	NO _x	CO	SO ₂	NH ₃	C ₂ H ₄	C ₂ H ₆	C ₃ H ₆	C ₃ H ₈
Biomass burning and agricultural waste burning	Eval	7.87 – 11.19	270.74 – 403.71	1.85 – 2.80	-	3.08 – 4.25	1.75 – 2.42	1.38 – 1.90	0.55 – 0.75
	QCTM	7.87 – 11.19	270.74 – 403.71	1.85 – 2.80	-	3.08 – 4.25	1.75 – 2.42	1.38 – 1.90	0.55 – 0.75
	TS2000	8.54	285.31	2.04	-	3.27	1.86	1.47	0.58
	ACCMIP	12.06	476.76	4.03	11.73	13.73	7.83	6.13	2.44
Anthropogenic non-traffic sources	Eval	32.88	364.66	88.03	-	3.15	5.43	1.33	8.40
	QCTM	32.88	364.66	88.03	-	3.15	5.43	1.33	8.40
	TS2000	32.88	364.66	88.03	-	3.15	5.43	1.33	8.40
	ACCMIP	32.88	364.66	88.03	36.27	3.15	5.43	1.33	8.40
Traffic sources	Eval	32.01 – 36.82	111.23 – 111.82	12.12 – 16.69	-	0.59 – 0.63	1.01 – 1.08	0.25 – 0.26	1.57 – 1.68
	QCTM	32.01 – 36.82	111.23 – 111.82	12.12 – 16.69	-	0.59 – 0.63	1.01 – 1.08	0.25 – 0.26	1.57 – 1.68
	TS2000	32.93	111.62	12.94	-	0.60	1.03	0.25	1.59
	ACCMIP	36.78	223.55	15.33	0.47	1.16	2.00	0.49	3.09
Natural sources	Eval	-	112.80	30.69	-	11.38	0.54	3.42	0.35
	QCTM	-	112.80	30.69	-	11.38	0.54	3.42	0.35
	TS2000	-	112.80	30.69	-	11.38	0.54	3.42	0.35
	ACCMIP	-	112.80	30.69	-	11.38	0.54	3.42	0.35
Total	Eval	73.60 – 79.77	858.42 – 991.64	132.75 – 137.56	65.27	18.17 – 19.37	8.74 – 9.44	6.36 – 6.89	10.87 – 11.14
	QCTM	73.60 – 79.77	858.42 – 991.64	132.75 – 137.56	65.27	18.17 – 19.37	8.74 – 9.44	6.36 – 6.89	10.87 – 11.14
	TS2000	74.36	874.38	133.69	65.27	18.40	8.86	6.46	10.92
	ACCMIP	81.73	1177.77	138.08	48.46	29.43	15.80	11.36	14.28

Table 9 Table 8 continued

Sector	Experiment	C ₄ H ₁₀	CH ₃ CHO	CH ₃ COCH ₃	CH ₃ COOH	CH ₃ OH	HCHO	HCOOH	MEK
Biomass burning and agricultural waste burning	Eval	0.69 – 0.96	1.23 – 1.69	1.12 – 1.55	3.93 – 5.43	3.96 – 5.47	2.10 – 2.90	2.15 – 2.96	2.66 – 3.67
	QCTM	0.69 – 0.96	1.23 – 1.69	1.12 – 1.55	3.93 – 5.43	3.96 – 5.47	2.10 – 2.90	2.15 – 2.96	2.66 – 3.67
	TS2000	0.74	1.31	1.19	4.18	4.21	2.23	2.28	2.82
	ACCMIP	3.12	5.48	4.99	17.54	17.71	9.40	9.57	11.88
Anthropogenic non-traffic sources	Eval	62.82	-	2.78	-	2.78	0.87	-	3.75
	QCTM	62.82	-	2.78	-	2.78	0.87	-	3.75
	TS2000	62.82	-	2.78	-	2.78	0.87	-	3.75
	ACCMIP	62.82	-	2.78	-	2.78	0.87	-	3.75
Traffic sources	Eval	11.74 – 12.55	-	0.52 – 0.55	-	0.52 – 0.55	0.16 – 0.17	-	0.70 – 0.75
	QCTM	11.74 – 12.55	-	0.52 – 0.55	-	0.52 – 0.55	0.16 – 0.17	-	0.70 – 0.75
	TS2000	11.91	-	0.53	-	0.53	0.17	-	0.72
	ACCMIP	23.13	-	1.03	-	1.03	0.32	-	1.39
Natural sources	Eval	0.40	-	55.82	3.39	150.71	-	5.59	-
	QCTM	0.40	-	55.82	3.39	150.71	-	5.59	-
	TS2000	0.40	-	55.82	3.39	150.71	-	5.59	-
	ACCMIP	0.40	-	55.82	3.39	150.71	-	5.59	-
TOTAL	Eval	75.65 – 76.54	1.23 – 1.69	60.12 – 60.58	7.32 – 8.82	157.63 – 159.16	3.13 – 3.94	7.72 – 8.54	7.11 – 8.15
	QCTM	75.65 – 76.54	1.23 – 1.69	60.12 – 60.58	7.32 – 8.82	157.63 – 159.16	3.13 – 3.94	7.72 – 8.54	7.11 – 8.15
	TS2000	75.87	1.31	60.32	7.57	158.22	3.27	7.87	7.29
	ACCMIP	89.48	5.48	64.61	20.93	172.22	10.59	15.16	17.02

Acknowledgments

This work was performed as part of the ESMVal (Earth System Model Validation) project that is funded by the German Aerospace Center (DLR).

The biggest thanks ever to Veronika Eyring for supervising me, for her help and believe in me, the many laughs and a work-intensive but great year at DLR. A big “Thank you” to Mattia Righi and Irene Cionni for help and advice during the whole year. Don’t know what I would have done without you!

Again, thanks to Veronika Eyring and Mattia Righi for advice and help with the interpretation of the results of this work.

Thanks to Bernhard Mayer for being my supervisor at LMU and his believe in me.

I thank Hanna Kotarba for her help with some of the plotting routines. Thanks also go to Jens-Uwe Grooss for extending the HALOE observational dataset until 2005, to Simone Tilmes for providing me with an up-to-date ozonesondes climatology and to Diego Loyola for the GOME data.

I also want to thank everyone at the Meteorological Institute of Munich (MIM) and my fellow students for five fantastic years of studying, the “next-to-studying” fun-activities and all the support I got! You guys are great!

Furthermore, thanks to my parents and a number of friends (I won’t mention names, as there are a too many of them) for every kind of support I got!

Declaration

I hereby declare that this master thesis is my own work, except where explicitly stated otherwise in the text or in the bibliography.

Erklärung

Hiermit erkläre ich, die vorliegende Arbeit selbständig verfasst zu haben und keine anderen als die in der Arbeit angegebenen Quellen und Hilfsmittel benutzt zu haben.

München,
